

# Chemodynamical Properties of Simulated Late-type Galaxies

Kate Pilkington

A THESIS SUBMITTED IN PARTIAL FULFILMENT  
OF THE REQUIREMENTS FOR THE DEGREE OF  
DOCTOR OF PHILOSOPHY

Jeremiah Horrocks Institute for Astrophysics and Supercomputing  
University of Central Lancashire

May 2013

# Declaration

The work presented in this thesis was carried out at the Jeremiah Horrocks Institute, University of Central Lancashire.

I declare that while registered as a candidate for the research degree, I have not been a registered candidate or enrolled student for another award of the University or other academic or professional institution.

I declare that no material contained in the thesis has been used in any other submission for an academic award. All the work presented here is my own, with the exception of analysis described in Chapter 4, which was a collaborative effort with C.G. Few, who was responsible for analysing his RaDES simulations, while I was responsible for the particle-based simulations.

The simulations used in Chapter 2 were run by Chris Brook and described in Governato et al. (2010). The simulations of Chapter 3 were run by Chris Brook and Greg Stinson, and presented in Brook et al. (2012a). For the simulations used in Chapter 4, the MUGS suite was generated by Greg Stinson (Stinson et al. 2010), Gal1 was run by Daisuke Kawata and presented in Rahimi et al. (2011), Kob11 was run by Chiaki Kobayashi and described in Kobayashi & Nakasato (2011), the RaDES suite was run by Gareth Few (Few et al. 2012b), and the MaGICC simulations were run by Chris Brook and Greg Stinson (Brook et al. 2012a); the chemical evolution codes used were described by Chiappini et al. (2001) and Mollá & Díaz (2005). Finally, in Chapter 5, I ran the chemical evolution models, using the `GETool` code originally written by Brad Gibson and Yeshe Fenner (Fenner & Gibson 2003).

# Abstract

The chemistry of galaxies provides a powerful probe of the underlying physics driving their evolution, complementing the traditional tools of morphology, kinematics, and colours. This dissertation examines several aspects of the galactic chemical evolution of late-type galaxies - both disc-like and dwarf - using a suite of cosmological hydrodynamical simulations, which incorporate the nucleosynthetic pollution of the interstellar medium, supplemented with classical analytical models of Local Group dwarfs. Throughout the work, these models are confronted with extant observations of both local and high-redshift systems, in order to identify both the strengths and weaknesses of the current generation of galaxy models. The work here has been presented across four primary science chapters which follow on from the Introduction and Motivation, prior to closing with the Conclusions and Future Directions.

The first science result (Chapter 2) derives from an examination of the cold (neutral) gas content of the first-ever simulated bulgeless dwarf disc galaxies (Governato et al. 2010), and builds upon the work first presented in Pilkington et al. (2011). The focus of the work is on comparing the observables inferred from the simulated interstellar media, with those seen in nature (including The HI Nearby Galaxies Survey and the Magellanic Clouds), including their velocity dispersion profiles, disc flaring, and the distribution of power within the ISM's structure, on different scales. Going beyond the work in Pilkington et al. (2011), two additional simulations from the Governato et al. (2010) suite are included, and the original work has been extended to include an analysis of the chemical properties of the dwarf galaxies.

The second science result (Chapter 3) examines the role of feedback, metal diffusion, and initial mass function selection, on the resulting chemistry of a new grid of M33-like disc simulations. The emphasis of the analysis is upon the resulting age-metallicity relations and metallicity distribution functions (in particular, the extreme metal-poor tail). Aspects of the work have been presented by Pilkington et al. (2012b), enhanced here by a further examination of the satellites associated with their respective host galaxies. The satellites are seen to be free of gas, with star formation histories which make them not unlike Local Group dwarf spheroidals.

The third science result (Chapter 4) is based upon an analysis of the temporal evolution of metallicity gradients in Milky Way-like systems, and derives from the work presented in Pilkington et al. (2012d). A large suite of simulations, sampling a range of numerical codes (particle- and grid-based, in addition to classical Galactic Chemical Evolution (GCE) models), each with different treatments of star formation, energy feedback, and assembly histories, was employed. The analysis focussed on both the radial and vertical abundance gradients, emphasising the role of feedback in shaping the gradients, and demonstrates the critical role that new observations of *in situ* gradients at high-redshift can play in constraining the uncertain nature of feedback within simulations. This work has been complemented by a brief examination of the azimuthal abundance variations in the massive discs.

The fourth science result (Chapter 5) expands upon our earlier exploration of the chemical properties of *simulated* dwarf galaxies, but now employs a classical semi-numerical GCE approach. By coupling colour-magnitude diagram-constrained star formation histories with our `GEtool` GCE code, we attempt to constrain the relative rates of gas infall and outflow, for the Carina, Fornax, and Sculptor Local Group dwarfs, in order to match their empirical chemical abundance patterns and metallicity distribution functions. This builds upon the preliminary work, as presented by Pilkington & Gibson (2012a).

# Contents

<b>Declaration</b>	<b>2</b>
<b>Abstract</b>	<b>3</b>
<b>Acknowledgements</b>	<b>15</b>
<b>List of Publications</b>	<b>16</b>
<b>1 INTRODUCTION</b>	<b>20</b>
1.1 Dwarf Galaxies . . . . .	21
1.2 The Milky Way . . . . .	23
1.2.1 The Bulge . . . . .	24
1.2.2 The Disk . . . . .	25
1.2.3 The Halo . . . . .	26
1.3 The Local Group . . . . .	28
1.4 Origin of the Elements . . . . .	29
1.5 Galaxy Simulations . . . . .	30
1.6 Chemical Evolution Models . . . . .	31
1.7 Aims of this Thesis . . . . .	34
1.8 Thesis Outline . . . . .	35
<b>2 The Cold Gas Content of Bulgeless Dwarf Galaxies</b>	<b>36</b>

2.1	Abstract . . . . .	36
2.2	Introduction . . . . .	37
2.3	Method . . . . .	39
	2.3.1 Simulations . . . . .	39
	2.3.2 Analysis . . . . .	43
2.4	Results . . . . .	47
	2.4.1 Radial Density Profiles . . . . .	47
	2.4.2 Flaring . . . . .	52
	2.4.3 Velocity Dispersion . . . . .	55
	2.4.4 Power Spectrum and Superbubbles . . . . .	59
	2.4.5 DG2 and DG3 . . . . .	65
2.5	Discussion . . . . .	70
2.6	Chemistry of Dwarf Galaxies . . . . .	76
	2.6.1 Introduction . . . . .	76
	2.6.2 The Mass-Metallicity relation . . . . .	78
	2.6.3 MDFs . . . . .	83
2.7	Summary . . . . .	90
<b>3</b>	<b>The Distribution of Metals in Cosmological Simulations of Dwarf</b>	
	<b>Disc Galaxies</b>	<b>92</b>
3.1	Abstract . . . . .	92
3.2	Introduction . . . . .	93
3.3	Simulations . . . . .	96
3.4	Age-Metallicity Relations . . . . .	105
3.5	Metallicity Distribution Functions . . . . .	108
3.6	Summary . . . . .	129
3.7	Satellite Galaxies . . . . .	131
	3.7.1 Conclusions . . . . .	141

<b>4</b>	<b>Metallicity Gradients in Disk Galaxies</b>	<b>146</b>
4.1	Abstract . . . . .	146
4.2	Introduction . . . . .	147
4.3	Simulations . . . . .	151
4.3.1	MUGS . . . . .	151
4.3.2	Gal1 . . . . .	154
4.3.3	KN11 . . . . .	155
4.3.4	RaDES . . . . .	156
4.3.5	Chemical Evolution Models . . . . .	158
4.4	Present-Day Gradients . . . . .	160
4.4.1	Radial Gradients . . . . .	160
4.4.2	Vertical Gradients . . . . .	167
4.5	Evolution of the Radial Gradients . . . . .	169
4.6	Effects of Feedback on the Evolution of Metallicity Gradients . . . . .	179
4.7	Summary . . . . .	180
4.8	Azimuthal Variations . . . . .	184
4.8.1	Overview and Results . . . . .	184
4.8.2	Conclusions . . . . .	191
<b>5</b>	<b>Chemical Evolution of the Local Group Dwarf Spheroidals</b>	<b>192</b>
5.1	Abstract . . . . .	192
5.2	Introduction . . . . .	193
5.3	The Code . . . . .	194
5.3.1	Stellar Yields . . . . .	197
5.4	Carina . . . . .	198
5.4.1	Inflows and Outflows . . . . .	200
5.4.2	Abundance Patterns . . . . .	201
5.4.3	Metallicity Distribution Function . . . . .	206

5.4.4	Choice of Yields . . . . .	209
5.4.5	Discussion . . . . .	214
5.5	Sculptor . . . . .	215
5.5.1	Inflows and Outflows . . . . .	216
5.5.2	Abundance Patterns . . . . .	220
5.5.3	Metallicity Distribution Function . . . . .	222
5.5.4	Discussion . . . . .	226
5.6	Fornax . . . . .	226
5.6.1	Inflows and Outflows . . . . .	227
5.6.2	Abundance Patterns . . . . .	228
5.6.3	Metallicity Distribution Function . . . . .	231
5.6.4	Discussion . . . . .	234
5.7	Conclusions . . . . .	234
<b>6</b>	<b>Conclusions</b>	<b>236</b>
6.1	The Chemistry and Cold Gas Content of Bulgeless Dwarf Galaxies . .	237
6.2	The Distribution of Metals in Cosmological Simulations of Dwarf Disk Galaxies . . . . .	238
6.3	Metallicity Gradients in Disk Galaxies . . . . .	239
6.4	Chemical Evolution Models of Local Group Dwarf Spheroidal Galaxies	240
6.5	Future Work . . . . .	241

# List of Tables

2.1	Integrated Properties of the Governato et al. (2010) Dwarfs . . . . .	80
3.1	Parameters for the five 11m galaxies . . . . .	102
3.2	Raw MDF characteristics for the five 11m galaxies . . . . .	118
3.3	MDF characteristics for the five 11m galaxies . . . . .	119
4.1	Present day characteristics of the 25 simulated disks . . . . .	152

# List of Figures

1.1	Map of the Local Group of Galaxies . . . . .	28
1.2	A Comparison of Various Initial Mass Function Forms . . . . .	33
2.1	Cold Gas (HI) Mass - Stellar Luminosity Relation for the Governato et al. (2010) Dwarfs . . . . .	41
2.2	Star Formation Rates of DG1, DG1LT and nDG1 . . . . .	45
2.3	HI moment zero maps for DG1LT, DG1 and nDG1 . . . . .	46
2.4	Gas and Stellar Radial Density Profiles for DG1, nDG1, and DG1LT	50
2.5	Radial HI Column Density Profiles for DG1, nDG1, and DG1LT . . .	51
2.6	Neutral Hydrogen Column Density Map of DG1 . . . . .	52
2.7	Neutral Hydrogen Column Density Map of nDG1 . . . . .	53
2.8	Vertical Surface Density Profiles of DG1 and nDG1 . . . . .	54
2.9	Velocity Dispersion Profiles for DG1, nDG1, and DG1LT . . . . .	58
2.10	Radial, Azimuthal, and Vertical Velocity Dispersions for the Simu- lated HI in DG1 . . . . .	60
2.11	Radial, Azimuthal, and Vertical Velocity Dispersions for the Simu- lated HI in DG1, Including Thermal Broadening . . . . .	61
2.12	Radial, Azimuthal, and Vertical Velocity Dispersions for the Simu- lated HI in nDG1 . . . . .	62
2.13	Radial, Azimuthal, and Vertical Velocity Dispersions of the Simulated HI in nDG1, Including Thermal Broadening . . . . .	63

2.14	Spatial Power Spectra of the Cold ISM of DG1, nDG1, DG1LT, and the SMC . . . . .	66
2.15	Moment Zero Maps of the Cold ISM of DG2 and DG3 . . . . .	67
2.16	Star Formation Rates for DG2 and DG3 . . . . .	68
2.17	Radial Density Profiles for DG2 and DG3 . . . . .	69
2.18	Power Spectra for the Cold ISM of DG2, DG3, and the SMC . . . . .	71
2.19	Velocity Dispersion Profiles for the Cold ISM of DG2 and DG3 . . . . .	72
2.20	Mass Metallicity Relation . . . . .	81
2.21	Luminosity Metallicity Relation . . . . .	82
2.22	MDFs of the Governato et al. (2010) Simulated Dwarf Galaxies . . . . .	85
2.23	Cumulative MDFs of the Governato et al. (2010) Simulated Dwarf Galaxies . . . . .	86
2.24	Stellar Abundance Ratios in nDG1 Compared to Empirical DART Data . . . . .	88
2.25	Stellar Oxygen-to-Iron Ratios for the Governato et al. (2010) Dwarfs . . . . .	89
2.26	Age-Metallicity Relations for the Governato et al. (2010) Dwarfs . . . . .	90
3.1	Radial Metallicity Gradients of the MaGICC Simulations . . . . .	100
3.2	Vertical Metallicity Gradients of the MaGICC Simulations . . . . .	101
3.3	Star formation histories of the MaGICC galaxies . . . . .	104
3.4	Age metallicity relations of the MaGICC galaxies . . . . .	109
3.5	MDF's of the MaGICC galaxies . . . . .	112
3.6	Cumulative MDF for 11mKroupa . . . . .	113
3.7	Cumulative MDF for 11mChab . . . . .	114
3.8	Cumulative MDF for 11mNoDiff . . . . .	115
3.9	Cumulative MDF for 11mNoRad . . . . .	116
3.10	Cumulative MDF for 11mNoMinshut . . . . .	117
3.11	MDF split by age of 11mKroupa . . . . .	123

3.12	MDF of the bulge of 11mKroupa . . . . .	124
3.13	Cumulative MDFs of the Disc Stars of the MaGICC Galaxies . . . . .	127
3.14	Cumulative MDFs of the Solar Neighbourhoods of the MaGICC Galaxies . . . . .	128
3.15	Star Formation History of the Satellite Associated with 11mKroupa . . . . .	133
3.16	Star Formation History of the Satellite Associated with 11mChab . . . . .	134
3.17	Star Formation History of the Satellite Associated with 11mNoRad . . . . .	135
3.18	MDF of the Satellite Associated with 11mKroupa . . . . .	135
3.19	MDF of the Satellite Associated with 11mChab . . . . .	136
3.20	MDF of the Satellite Associated with 11mNoRad . . . . .	137
3.21	Age-Metallicity Relation for the Satellite Associated with 11mKroupa . . . . .	138
3.22	Age-Metallicity Relation for the Satellite Associated with 11mChab . . . . .	139
3.23	Age-Metallicity Relation for the Satellite Associated with 11mNoRad . . . . .	140
3.24	Abundance Ratios for the Satellite Associated with 11mKroupa . . . . .	141
3.25	Abundance Ratios for the Satellite Associated with 11mChab . . . . .	142
3.26	Abundance Ratios for the Satellite Associated with 11mNoRad . . . . .	143
4.1	Radial Metallicity Gradients for g15784 and Apollo . . . . .	162
4.2	Radial Metallicity Gradients for the MUGS Simulations . . . . .	163
4.3	Star Formation Rate as a Function of Radius for g15784, Apollo, and Two Chemical Evolution Models . . . . .	166
4.4	Vertical Metallicity Gradients for g15874 and Apollo . . . . .	170
4.5	Vertical Metallicity Gradients for the MUGS Simulations . . . . .	171
4.6	Radial Metallicity Gradients as a Function of Redshift for g15784 and Apollo . . . . .	177
4.7	Metallicity Gradient as a Function of Redshift for all Simulations . . . . .	178
4.8	Metallicity Gradient vs Redshift for Conventional (MUGS) and Enhanced (MaGICC) Feedback Simulations . . . . .	181

4.9	Distribution of Young Stars in g15784 . . . . .	186
4.10	Young Stellar Density Distribution in g15784 . . . . .	187
4.11	Young Stellar and Cold Gas Density Distribution of g15784 . . . . .	188
4.12	Azimuthal Density Distribution of g15784 . . . . .	189
4.13	Azimuthal Metallicity Distribution of g15784 . . . . .	190
5.1	Representative Stellar Yields used for Modelling the Chemical Evolution of Local Group dSphs . . . . .	199
5.2	Empirical Star Formation History for the Carina dSph . . . . .	200
5.3	Adopted Inflow and Outflow Patterns for the Carina Model . . . . .	202
5.4	Galactic Wind Components for the Carina dSph Model . . . . .	203
5.5	Predicted Abundance Patterns for Carina dSph Chemical Evolution Model . . . . .	207
5.6	Predicted MDF for the Chemical Evolution Model of Carina . . . . .	208
5.7	Stellar Yields Adopted for Modeling Carina: SNeII from Kobayashi et al. (2006) . . . . .	210
5.8	Predicted Abundance Pattern for the Carina dSph using the SNeII Yields of Kobayashi et al. (2006) . . . . .	212
5.9	Predicted MDF for the Carina Dwarf using the Kobayashi et al. (2006) SNeII Yields . . . . .	213
5.10	Star Formation History of the Sculptor dSph from de Boer et al. (2012a)	217
5.11	Gas Inflows and Outflows for the Sculptor Chemical Evolution Model	218
5.12	Stellar Wind Sub-Components Associated with the Sculptor dSph Model . . . . .	219
5.13	Predicted Abundance Ratios for the Chemical Evolution Model for Sculptor . . . . .	221
5.14	Predicted MDF for the Chemical Evolution Model of the Sculptor dSph	223

5.15	Surface Density of Lost and Re-accreted Gas for the Model Sculptor dSph . . . . .	224
5.16	Metallicity Distribution Function of the Sculptor dSph in the Absence of Re-accretion . . . . .	225
5.17	Star Formation History of the Fornax dSph from de Boer et al. (2012b)	228
5.18	Predicted Gas Inflow and Outflow Rates for the Chemical Evolution Model of Fornax . . . . .	229
5.19	Contributions to the SN-driven Winds of the Fornax Model . . . . .	230
5.20	Predicted Abundance Patterns for the Fornax Chemical Evolution Model . . . . .	232
5.21	Predicted and Empirical MDFs for the Fornax dSph . . . . .	233

# Acknowledgements

I would like to thank the STFC for its financial support throughout the course of this PhD. The support of my collaborators, Chris Brook, Francesco Calura, Brad Gibson, and Greg Stinson, is also acknowledged. I am grateful to Saint Mary's University and Monash University for their hospitality and invitations to visit.

The help of Rob Thacker, Mercedes Mollá, Daisuke Kawata and Dimitris Stamatellos in proof reading and providing insightful comments on this thesis is gratefully acknowledged.

For my friends who have been there to listen to every up and down I am very grateful, the many nights out and distractions proved very useful to the writing of this thesis.

Finally I would like to dedicate this thesis to my parents Alison and Len Walters. Without their continued support and encouragement I could not have made it this far.

# List of Publications

Refereed Journals:

1. **Constraining Sub-Grid Physics with High-Redshift Spatially-Resolved Metallicity Distributions<sup>1</sup>**

B.K. Gibson, K. Pilkington, C.B. Brook, G.S. Stinson & J.Bailin

2013, A&A, in press

2. **Decoding the Message from Meteoritic Stardust Silicon Carbide Grains**

Karen M. Lewis, Maria Lugaro, Brad K. Gibson & Kate Pilkington

2013, ApJ, in press

3. **The Stellar Metallicity Distribution of Disc Galaxies and Bulges in Cosmological Simulations**

Calura, F., Gibson, B.K., Michel-Dansac, L., Stinson, G.S., Cignoni, M., Dotter, A., Pilkington, K., House, E.L., Brook, C.B., Few, C.G., Bailin, J., Couchman, H.M.P. & Wadsley, J.

2012, MNRAS, 427, 1401

---

<sup>1</sup>Forms part of Chapter 4

**4. Thin Disc, Thick Disc and Halo in a Simulated Galaxy**

Brook, C.B., Stinson, G.S., Gibson, B.K., Kawata, D., House, E.L., Miranda, M.S., Maccio, A.V., Pilkington, K., Roskar, R., Wadsley, J. & Quinn, T R.  
2012, MNRAS, 429, 690

**5. The Distribution of Metals in Cosmological Hydrodynamical Simulations of Dwarf Disc Galaxies<sup>2</sup>**

Pilkington, K., Gibson, B.K., Brook, C.B., Calura, F., Stinson, G.S., Thacker, R. J., Michel-Dansac, L., Bailin, J., Couchman, H.M.P., Wadsley, J., Quinn, T.R. & Maccio, A.  
2012, MNRAS, 425, 969

**6. Metallicity Gradients in Disks. Do Galaxies Form Inside-Out?<sup>3</sup>**

Pilkington, K., Few, C.G., Gibson, B.K., Calura, F., Michel-Dansac, L., Thacker, R.J., Molla, M., Matteucci, F., Rahimi, A., Kawata, D., Kobayashi, C., Brook, C.B., Stinson, G.S., Couchman, H.M.P., Bailin, J. & Wadsley, J.  
2012, A&A, 540, A56

**7. The Chemical Evolution of Globular Clusters -II. Metals and Fluorine**

Sanchez-Blazquez, P., Marcolini, A., Gibson, B.K., Karakas, A.I., Pilkington, K. & Calura, F.  
2012, MNRAS, 419, 1379

---

<sup>2</sup>Forms part of Chapter 3

<sup>3</sup>Forms part of Chapter 4

8. **The Cold Gas Content of Bulgeless Dwarf Galaxies**<sup>4</sup>

Pilkington, K., Gibson, B.K., Calura, F., Brooks, A.M., Mayer, L., Brook, C.B., Stinson, G.S., Thacker, R.J., Few, C.G., Cunnama, D. & Wadsley, J.  
2011, MNRAS, 417, 2891

9. **Hierarchical Formation of Bulgeless Galaxies: Why Outflows Have Low Angular Momentum**

Brook, C.B., Governato, F., Roskar, R., Stinson, G., Brooks, A.M., Wadsley, J., Quinn, T., Gibson, B.K., Snaith, O., Pilkington, K., House, E. & Pontzen, A.  
2011, MNRAS, 415, 1051

Conference Proceedings:

1. **The Role of Feedback in Shaping the Abundance Gradients and Age-Metallicity Relations of Galaxies**<sup>5</sup>

Gibson, B.K., Pilkington, K., Bailin, J., Brook, C.B. & Stinson, G.S.  
2013, Nuclei in the Cosmos XII, Cairns, Australia.

2. **The Chemical Evolution of the Carina Dwarf Spheroidal**<sup>6</sup>

Pilkington, K. & Gibson, B.K.  
2013, Nuclei in the Cosmos XII, Cairns, Australia.

3. **Decoding the Message from Silicon in Stardust Mainstream Silicon Carbide Grains**

Lewis, K.M., Lugaro, M., Gibson, B.K. & Pilkington, K.  
2012, 75th Annual Meeting of the Meteoritical Society, Cairns, Australia.

---

<sup>4</sup>Forms part of Chapter 2

<sup>5</sup>Forms part of Chapter 4

<sup>6</sup>Forms part of Chapter 5

4. **The Distribution of Young Stars and Metals in Simulated Cosmological Disk Galaxies** <sup>7</sup>

Pilkington, K., Gibson, B.K. & Jones, D. H.

2013, From the First Structures to the Universe Today; Proceedings of 2nd Workshop on Numerical and Observational Astrophysics; Buenos Aires, Argentina.

5. **Metallicity Gradients in Simulated Disk Galaxies** <sup>8</sup>

Pilkington, K. & Gibson, B.K.

2012, Proceedings of 3rd Subaru International Conference; Shuzenji, Japan.

6. **The Chemical and Dynamical Evolution of Isolated Dwarf Galaxies**<sup>9</sup>

Pilkington, K., Gibson, B.K., Calura, F., Stinson, G.S., Brook, C.B. & Brooks, A.

2012, Dwarf Galaxies: Keys to Galaxy Formation and Evolution, JENAM, Lisbon, Portugal. Astrophysics and Space Science Proceedings, p47

---

<sup>7</sup>Forms part of Chapter 4

<sup>8</sup>Forms part of Chapter 4

<sup>9</sup>Forms part of Chapter 2

# Chapter 1

## INTRODUCTION

The favoured  $\Lambda$ CDM cosmological framework predicts the hierarchical assembly of galaxies. Large galaxies are formed from the more significant over densities within the initial matter distribution, with continual accretion of smaller satellites or galaxies resulting in a steady build-up of mass. In this paradigm, dwarf galaxies can be viewed as the building blocks of the massive galaxies we see today. The underlying physics governing galaxy formation and evolution is probed observationally through a combination of morphological structure, internal kinematics, colours, and most recently, chemistry. This thesis provides one of the most comprehensive analyses of the underlying stellar chemistry of late-type dwarfs and massive galaxies; indeed, it is the first of its sort to do so using successful cosmological hydrodynamical simulations of bulgeless disc galaxies. This preliminary chapter will provide an introduction to the empirical properties of dwarf galaxies, followed by those of more massive spirals such as our own Milky Way (and their satellites, such as those permeating our Local Group); the final sub-section will outline the characteristics of the simulations and analytical models employed in this thesis, linking back to the aforementioned empirical properties against which they are calibrated.

## 1.1 Dwarf Galaxies

Dwarf galaxies are the most common type of galaxy in the local Universe. While ubiquitous, these dwarfs are not distributed randomly but are, instead, highly clustered, found preferentially in the vicinity of more massive hosts. Upwards of 40-50 dwarfs have been discovered orbiting the Milky Way (Belokurov et al. 2010), although both the interpretation of high-resolution N-body simulations (Klypin et al. 1999) and extrapolation of satellite luminosity functions (Sawala et al. 2010) suggest that there may be 1-2 orders-of-magnitude more companions yet to be discovered. Due to their low surface brightness and low intrinsic luminosity, detailed studies (and, indeed, discovery) of dwarfs has been a challenge. The past decade, particularly due to the advent of the 8-10m class era of optical astronomy, has relaxed these restrictions to detailed analyses. Recent studies such as PAndAS (Pan Andromeda Archaeological Survey) are discovering new dwarf galaxies (e.g. Richardson et al. 2011) orbiting M31, and finding that they have similar chemical properties to our own Milky Way’s satellites. The Local Group of galaxies is dominated by the two massive spirals (M31 and the Milky Way), and most of the Local Group dwarfs are associated closely with one of these two massive discs; interestingly, there are only two dwarfs (so far) which have been shown to be truly isolated: Cetus (Whiting et al. 1999) and Tucana (McConnachie et al. 2006).

Beyond their numbers, dwarf galaxies are particularly exciting galactic laboratories, as they (or their ancestral cousins) are thought to be the building blocks of massive galaxies within the cosmological hierarchical clustering paradigm. Indeed, the belief that these dwarfs are galactic building blocks led to the prediction that the elemental abundance patterns in both dwarfs and their hosts should be similar. One of the more recent surprising discoveries in “galactic archaeology” was that this anticipated similarity was not confirmed (Venn et al. 2004) – i.e. the present-day dwarfs surrounding the Milky Way are not representative of the Galactic building

## CHAPTER 1

blocks which formed our Galaxy. Further, more recent comparisons of the metallicity distribution functions (MDFs) of neighbouring dwarf galaxies suggested that the relative proportion of extremely metal poor stars did not resemble that of the Milky Way halo (Helmi et al. 2006), suggesting (again) that our halo was not formed from the merger of such common dwarfs. This is discussed further in §1.2.3

In addition to these challenging “baryonic” problems, dwarf galaxies also possess amongst the highest mass-to-light ratios known, indicative of being highly dark matter-dominated, making them ideal “non-baryonic” (dark matter) laboratories. Aaronson (1983) made the first measurements of velocity dispersion for stars in Draco and Ursa Minor. The inferred mass to light ratio from his results showed significant amounts of “hidden matter”. With advances in observations it became easier to measure the mass of the Local Group dwarfs using the stellar velocity dispersions and the HI rotation curves, confirming his results. Most recently, it has been suggested that *all* low-mass dwarfs reside within identical dark mass halos of mass  $\sim 10^7 M_{\odot}$  (Gilmore et al. 2007)

Local Group dwarf galaxies are the closest extragalactic objects to us, with those associated with the Milky Way ranging from  $\sim 8$  kpc (Sagittarius) to 50-65 kpc (Magellanic Clouds) to  $\sim 80$  kpc (Draco/Sculptor/Sextans) to  $\sim 140$  kpc (Fornax) to  $\sim 450$  kpc (NGC 6822). They are the only extragalactic objects for which we have data for single stars’ abundance patterns and radial velocities. Projects such as DART (Dwarf Abundances and Radial-velocities Team), which aim to obtain detailed chemistry and kinematics from sampling the red giant branch stars in the central regions of Local Group dwarf spheroidals, are now greatly increasing the amount of high resolution observational data we have for dwarf galaxies.

In the Local Group there are three main types of dwarf galaxy present: dwarf spheroidals (dSph), dwarf irregulars (dIrr), and dwarf transitionals (dTrans). dSphs are mainly extremely gas poor, have little or no present-day star formation and are

## CHAPTER 1

found preferentially close to their host galaxy. dIrrs are found further away from the host (and in some cases appear isolated), possess a more significant gas reservoir, and more substantial present-day star formation. dTrans, as the name suggests, lie between the two with little recent star formation, but still showing the presence of an HI gas reservoir. The proximity of the dSphs to their host suggests that the latter has played an important role in stripping the former of their gas (e.g. Marcolini et al. 2003) thereby affecting their star formation and evolution.

### 1.2 The Milky Way

Our galaxy, the Milky Way, is currently undergoing (and will continue to do so for the coming decade) a comprehensive photometric, kinematic, and chemical ‘decomposition’, including current surveys such as RAVE (e.g. Siebert 2012, :the RAdial Velocity Experiment) and SEGUE (e.g. Yanny et al. 2009, :the Sloan Extension for Galactic Understanding and Exploration), and future experiments such as GAIA (e.g. Cacciari 2009) and HERMES (e.g. Zucker et al. 2012). Studies such as these provide us instantaneous ‘snapshots’ of the structure, kinematics, and chemistry of the Milky Way, but as will be discussed here, there are many unsolved puzzles remaining in the field (hence, the justification for experiments such as Gaia, HERMES, the Gaia-ESO Survey, and LAMOST).

In its broadest terms, we know that the Milky Way is a late-type spiral galaxy with a total mass of  $\sim 10^{12} M_{\odot}$ . Our solar system is situated  $\sim 8$  kpc from the Galactic centre, and orbits about the Galaxy every  $\sim 200$  Myr. Like other disc galaxies, the Milky Way is comprised of a number of baryonic sub-components: a centrally-concentrated spheroidal bulge (within which a bar or bars co-exist), a dominant disk (itself often sub-divided into co-spatial thin and thick discs), and a trace stellar halo extending to the outer reaches of the virial radius. Each of these components can be distinguished, to varying degrees of success, by their unique

## CHAPTER 1

kinematics and chemistry.

### 1.2.1 The Bulge

The central bulge of the Milky Way has been classically viewed as a near-spheroidal distribution of old and predominantly metal-rich stars whose (i) support is governed by velocity anisotropies (rather than the ordered rotation supporting the disc), and (ii) stellar content accounts for a substantial fraction of the Milky Way, as a whole; a detailed review for the Milky Way bulge can be found in Minniti & Zoccali (2008). Recent work has extended this classical picture, demonstrating the bulge is a more complex, and subtle, entity.

For example, Hill et al. (2011) analysed the chemistry of 219 bulge red clump stars and found a bimodal distribution in the metallicity. They interpreted this as indicating the presence of two separate stellar populations within the bulge, each following different formation scenarios. Bensby et al. (2011), with a sample of 26 microlensed dwarf and sub-giant stars in the bulge also found a bimodal MDF. However, the peaks of their MDF did not coincide with those of Hill et al. (2011). Both sets of authors conclude that the origin of these different metallicity peaks is unknown, and speculate it could be down to large uncertainties or contamination by disk stars. The two bulge populations have been confirmed in kinematics by Babusiaux et al. (2010), in which they show that the metal-rich population shows bar-like kinematics and the metal-poor population shows kinematics akin to an old spheroidal population. In addition to the dual populations, a radial metallicity gradient is also thought to exist. Zoccali et al. (2008) and Zoccali et al. (2009) show MDFs of different regions in the bulge, claiming a flattening in metallicity with increasing radius, concluding it is due to the most metal-rich stars becoming increasingly rare as one moves from the centre. That said, in the very inner regions of the bulge, Rich et al. (2007) finds no evidence for the existence of any metallicity

## CHAPTER 1

gradient.

More recently Ness et al. (2012) and Bensby et al. (2013) show observational results from bulge surveys. Bensby et al. (2013) adds to the data set presented in Bensby et al. (2011) and finds the MDF now has more complex features than the bimodality originally found in Bensby et al. (2011), the authors suggest the features could stem from different stellar populations. Ness et al. (2012) find a bimodal distribution spatially and kinematically from the ARGOS bulge survey. These recent results show there is still many observations needed until we have a clear picture of the formation of the Milky Ways bulge.

Semi-numerical chemical evolution models from, for example, Grieco et al. (2012), attempt to provide a coherent model for these multiple populations within the bulge (albeit, necessarily ignoring the aforementioned kinematic constraints). Using two different formation timescales for the differing populations (older, more metal-poor stars, form on an  $\sim 0.1$  Gyr timescale, while the younger, more metal-rich, component forms on the longer timescale of  $\sim 3$  Gyr), they obtain bimodal MDFs and gradients similar to those observed.

### 1.2.2 The Disk

Classically the disk of the Milky Way has been split into a (dominant) thin disc enshrouded by a (less dominant) thick disc. Identified by Gilmore & Reid (1983), the thick disc has been the subject of much recent controversy. It was thought originally to contain a distinct/discrete population of stars relative to those of the thin disk, whether viewed in luminosity (e.g. Yoachim & Dalcanton 2006), kinematics (e.g. Pasetto et al. 2012) or metallicity (e.g. Lee et al. 2011). Such a ‘discrete’ thick disc picture is consistent with evidence provided for some external disc galaxies (e.g. Yoachim & Dalcanton 2006; Freeman 2012). This picture has been called into question by Bovy et al. (2012), who claim a single, continuous, disc is in better

## CHAPTER 1

agreement with observations. At the time of writing of this thesis, the existence (or not) of a discrete thick disc in the Milky Way remains hotly debated, although Gaia and HERMES should resolve this issue over the coming decade.

Whether the stars seen well above the mid-plane (but still orbiting circularly about the Galaxy) should be thought of as part of a discrete or a semi-continuous structure, we will refer to them colloquially as ‘thick disc’ stars throughout this thesis. The origin of these thick disc stars remain a primary topic of debate in galactic structure, but the four primary scenarios can be categorised as:

- Brook et al. (2004) suggested thick discs form during an intense gas-rich merger phase at high-redshift; this scenario is supported by observations such as those of Wyse et al. (2006) and Gilmore et al. (2002).
- Abadi et al. (2003b) suggested that the thick disc formed from the direct accretion of debris from a now-disrupted SMC-mass satellite (that mass of satellite is required to give the correct stellar metallicities (Freeman 2012)).
- Kroupa (2002) favoured a scenario in which the thick disc originated from kinematic heating of a pre-existing thin disk.
- Schönrich & Binney (2009) suggest the thick disc might have formed from the radial migration of inner disc stars to the outer regions.

In order to understand which of these methods actually formed the thick disc and, importantly whether or not the thick and thin discs are discrete entities, additional data will be required. One can expect that Gaia will provide this necessary data (e.g. Robin et al. 2012).

### 1.2.3 The Halo

The stellar halo of the Milky Way is its most metal-poor baryonic component. As discussed in §1.1, attempts have been made to link dwarf galaxies with the halo in

## CHAPTER 1

terms of chemical abundances (e.g. Venn et al. 2004). Helmi et al. (2006) looked at the metal-poor tail of the metallicity distribution functions (MDFs) of several nearby dwarf galaxies and compared them to the galactic halo, concluding the latter could not have been made from the accretion of the former. A recent re-analysis, though, by Schörck et al. (2009) showed that the Helmi et al. conclusion was pre-mature (driven by CaT-[Fe/H] transformation issues).

Tolstoy et al. (2003) showed that the  $[\alpha/\text{Fe}]$  ratios in dSphs were lower at the same metallicity ( $[\text{Fe}/\text{H}]$ ) than what is seen in the halo of the Milky Way. Venn et al. (2004) found the same results except for the extreme retrograde orbiting stars in the halo were found to possess similar  $[\alpha/\text{Fe}]$  as that seen in dSphs (at the same  $[\text{Fe}/\text{H}]$ ). What fraction of the halo was formed from stars accreted directly from dwarf galaxies remains contentious, although as Venn et al. (2004) show, the merging of dwarfs similar to the present day dSphs could not have formed the halo, as their chemical signatures are too different. However many of the lowest metallicity stars in dSphs show similar chemical patterns to the lowest metallicity stars in our halo, meaning early merging of these systems could have contributed to the halo.

Carollo et al. (2007) found, from 17000 SDSS stars, that the halo could be separated into two different populations, an inner halo and an outer halo. The inner halo was found to be rotating with the disk of the Milky Way but much slower, while the outer halo was found to be rotating in a retrograde fashion. In addition to the separation in kinematics there was also a claimed separation in metallicity with the MDF of the inner halo peaking around  $[\text{Fe}/\text{H}] \sim -1.6$  and the outer halo peaking around  $[\text{Fe}/\text{H}] \sim -2.2$ . The characteristics of this ‘dual halo’ are further described by Beers et al. (2012). How an inner and outer halo might form with these characteristics is still a matter of debate, but Zolotov et al. (2009) and Zolotov et al. (2010) claim the outer halo is comprised only of accreted stars from disrupted satellites, while the stars of the inner halo formed *in situ* at high-redshift from

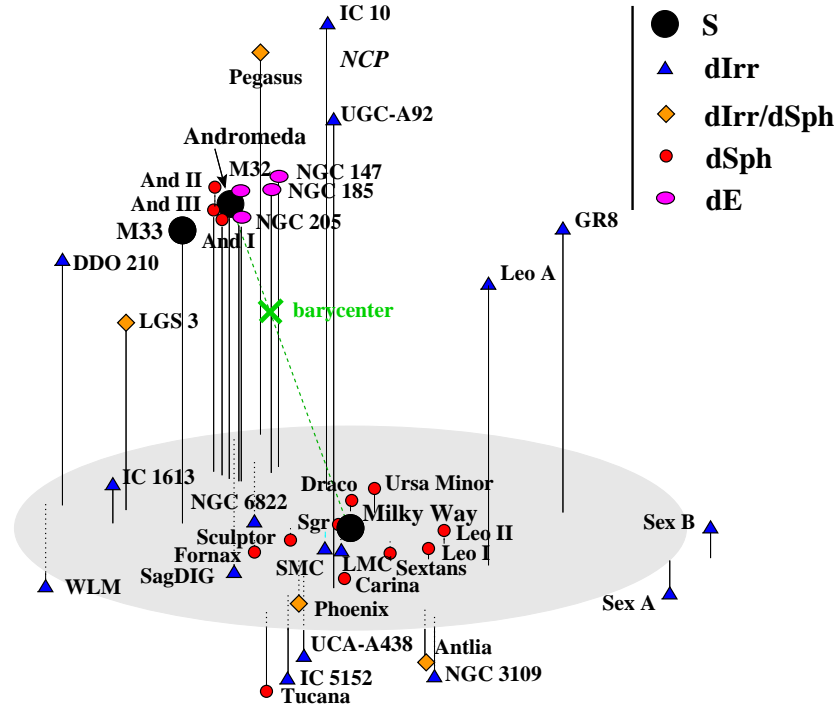


Figure 1.1: Approximate positions of many of the catalogued Local Group galaxies, taken from Grebel (1998). Spiral galaxies are represented as black circles, dwarf irregulars as blue triangles, dwarf spheroidals as red circles, dwarf ellipticals as magenta ellipses, and dwarf transitionals as yellow diamonds.

accreted gas, and the stars were then displaced to their current orbits.

### 1.3 The Local Group

Our local galactic environment is something called the Local Group (Figure 1.1), comprised of three primary spirals (the Milky Way, Andromeda (M31), and Triangulum (M33)). Upwards of 40 dwarf galaxies have also been catalogued around the Milky Way Belokurov et al. (2010), with many yet to be discovered; similar numbers are thought to be orbiting M31, with 27 currently catalogued (Richardson et al. 2011).

In passing, it can be noted that our Local Group itself is part of a collection of similar such groups which are embedded within what is called the Virgo Supercluster.

## 1.4 Origin of the Elements

It is widely accepted the Universe began with a Big Bang, resulting (over the next few minutes) in the nucleosynthesis of hydrogen, helium, and trace amounts of ‘metals’, in the form of lithium, with mass fractions, respectively, of  $X \sim 0.76$ ,  $Y \sim 0.24$ , and  $Z \sim 0.00$  (e.g. Jimenez et al. 2003). The rest of the elements that we see around us today have been created by nuclear reactions in stars (e.g. Burbidge et al. 1957). The first nuclear reactions in a star are hydrogen burning, converting hydrogen into helium via the proton-proton chain, and the CNO (carbon-nitrogen-oxygen) cycle. After most of the (core) hydrogen has been used up, the star will be left with a predominantly helium core, resulting in core contraction and an increase in temperature and density, and eventually in the ignition of helium. He-burning (into carbon) then proceeds via the triple- $\alpha$  process. Post-helium core burning, provided the star can reach sufficient temperatures, carbon-burning can begin, followed by neon burning, oxygen burning, and finally silicon burning. These latter burning cycles apply to massive Type II progenitors ( $>10 M_{\odot}$ ). Each stage creates progressively heavier elements, until the fusing elements no longer release energy, but instead the reactions require energy to be drawn from the surrounding environment (i.e., exothermic vs endothermic reactions).

For elements heavier than iron there therefore must be another route to their production. This process is called ‘neutron capture’, usually sub-divided into rapid- and slow-neutron capture (the r- and s-process, respectively). Both processes involve the capture of neutrons to increase the atomic mass with beta decay (eventually) increasing the atomic number.

A primary s-process site is the asymptotic giant branch (AGB) phase of low-to-intermediate mass stars, during the H- and He-shell burning stages. The primary r-process sites remain somewhat of a mystery, but whatever they might be, they require high neutron densities and high temperatures. Possible sites include neutrino

## CHAPTER 1

driven winds from core collapse supernova (Arcones & Thielemann 2013), neutron star mergers (Korobkin et al. 2012), and magnetorotationally driven supernovae (Winteler et al. 2012); a full review can be found in Thielemann et al. (2011). The pattern of r- and s-process nucleosynthesis differs, because of the differing timescales involved in the neutron capture; the s-process never wanders far from the valley stability in the chart of nuclides, while the r-process is the only process which allows the creation of neutron-rich isotopes to the right of the valley of stability.

### 1.5 Galaxy Simulations

Simulations of galaxies date back to the pre-computer era (Holmberg 1941), where light intensity was used as a proxy for gravity. The first simulations using computers (e.g. Toomre & Toomre 1972; White 1978) were pure gravitational N-body, modeling the dynamics of a system under (only) the influence of the inverse square law of gravity; for pure dark matter systems and/or pure stellar systems, such N-body simulations are invaluable. Significant advances including baryonic (gas-phase) physics became feasible with the advent of Smoothed Particle Hydrodynamics (SPH), first described by Gingold & Monaghan (1977) and Lucy (1977). SPH is used in galaxy simulations to model the gas dynamics, where the gas is discretised as a set of particles, and various thermodynamic properties of a given gas particle “shared” with its immediate neighbours within what is called a smoothing length  $h$ . SPH solves the ideal gas law in conjunction with the fundamental laws of hydrodynamics; a detailed overview of the mechanics of SPH is given in Monaghan (1992). Except where otherwise noted, the hydrodynamical simulations analysed in this thesis have all made use of the SPH + N-Body code GASOLINE (Wadsley et al. 2004).

A rich literature exists related to simulating the formation of dwarfs (e.g. Stinson et al. 2007, 2009; Governato et al. 2010; Sawala et al. 2010) and massive spirals (e.g. Governato et al. 2007; Stinson et al. 2010) with coupled gravitational N-body and

## CHAPTER 1

hydrodynamical codes . Much of this work has been necessarily undertaken within an idealised<sup>1</sup> framework and/or with limited treatment of chemical elemental (and isotopic) evolution, due to the relative difficulty of achieving the dynamic range necessary to resolve simultaneously both the dwarf and its host. A traditional problem plaguing the simulation of dwarf disc galaxies (e.g. Stinson et al. 2007, 2009; Sawala et al. 2010, and references therein) and massive spirals (e.g. Sommer-Larsen et al. 2003; Abadi et al. 2003a; Governato et al. 2004, 2007; Robertson et al. 2004; Bailin et al. 2005; Okamoto et al. 2005; Sánchez-Blázquez et al. 2009; Stinson et al. 2010, and references therein), within a cosmological context, has been the inability to recover successfully the properties of a truly “late-type” disk and, in particular, those with essentially no associated stellar bulge, similar to classical galaxies such as the Local Group’s M33.

### 1.6 Chemical Evolution Models

The origins, evolution and distribution of the chemical elements has long been studied in galaxies (e.g. Schmidt 1959). Without knowing information about the dynamical properties of galaxies, much can be learnt solely from its chemical properties. There are many different chemical evolution models in the literature (e.g. Chiappini et al. 2001; Mollá & Díaz 2005; Fenner & Gibson 2003) but they *all* make use of some variant of the same fundamental set of equations.

Usually, chemical evolution models assume, as an ‘initial condition’, primordial gas bearing the imprint of the aforementioned Big Bang Nucleosynthesis (BBN), although applications have been described in which some degree of ‘prompt initial enrichment’ has been imposed upon the BBN composition.

The underlying stellar evolution responsible for the subsequent generations of nucleosynthesis is obviously a critical component to any chemical evolution model.

---

<sup>1</sup>Ignoring the influence of large-scale structure - i.e., “non-cosmological”.

## CHAPTER 1

Stellar yields - the mass of any given element ejected from a star of a given mass and metallicity - is the specific ingredient required. Many different stellar evolution groups are involved in yield generation (e.g. Karakas 2010; Woosley & Weaver 1995). Each set of yields is slightly different, and with no set of yields available for every mass and every metallicity of star it becomes difficult to piece together results from different groups. Two new projects aimed at self-consistently producing full grids of yields for all stellar masses and metallicities are in progress now: **NuGrid** and **Monχey** are eagerly anticipated by the entire community.

The next critical ingredient is the initial mass function (IMF), which corresponds to the relative numbers of stars of a given mass born within a single generation. Again, the field of IMF determination has been (and still is, to some degree) fraught with controversy over the correct functional form (if there is but one), or if it varies for different types of galaxies (e.g. Brewer et al. 2012), different stellar ages (e.g. Zaritsky et al. 2012), or even different regions within a given galaxy (e.g. Matteucci & Brocato 1990). The most commonly used functional forms for the IMF are those of Salpeter (1955), Kroupa et al. (1993), and Chabrier (2003), but there are many others (Figure 1.2).

Chemical evolution models also need to adopt a parameterised star formation law, i.e the rate at which stars form from the gas reservoir. Many models assume a Kennicutt-Schmidt Law, first outlined by Schmidt (1959) where  $(\Sigma_{SFR}) \propto (\Sigma_{gas})^n$ . Here,  $(\Sigma_{SFR})$  is the star formation rate surface density,  $(\Sigma_{gas})$  the gas surface density, and  $n$  is taken from observations to be  $\sim 1.4$ , after Kennicutt (1998). Not surprisingly, given the need to parameterise the complex microphysics of star formation in a simple functional form, there are a wide variety of forms available to the modeler, including those of Dopita & Ryder (1994), where there is also a dependence on the total mass surface density and Oort (1974) where there is a dependence on rotation of the galaxy (such that when the orbiting gas crosses the spiral arms, the

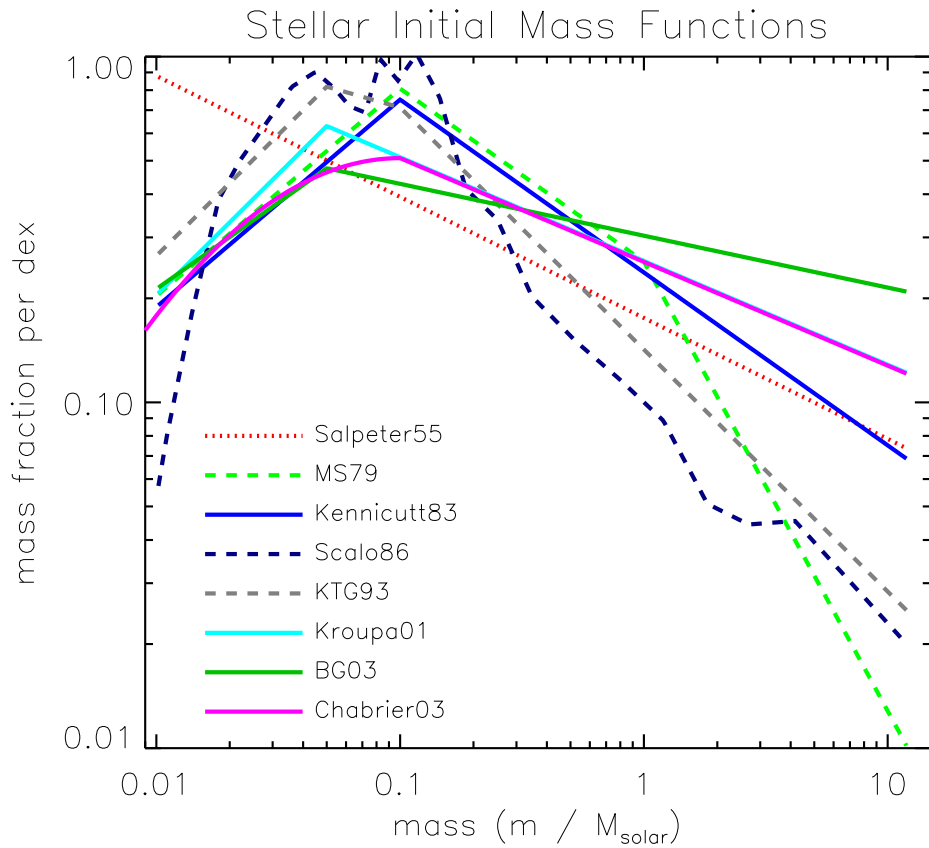


Figure 1.2: A literature survey of the most commonly used initial mass functions (IMFs). The red dotted line corresponds to the classic form of Salpeter (1955); the green dashed line shows that of Miller & Scalo (1979); the dark blue line shows that of Kennicutt (1983); the dark blue dashed line shows that of Scalo (1986); the grey dashed line shows that of Kroupa et al. (1993); the cyan line shows that of Kroupa (2001); the green lines shows that of Baldry & Glazebrook (2003); the magenta lines shows that of Chabrier (2003). For all simulations realised with the `Gasoline` code, the lower and upper mass limits for the IMF were  $0.1 M_{\odot}$  and  $40 M_{\odot}$ , respectively. Figure courtesy of Ivan Baldry.

## CHAPTER 1

star formation rate is taken to increase). These different star formation laws have been tested within chemical evolution models to quantify their impact; Portinari & Chiosi (1999) found that they needed further assumptions and not just the star formation law (such as infall rates and infall time scales) to reproduce metallicity gradients within the galaxy.

Finally, there needs to be a prescription for the lifetimes of the stars within the model. Schaller et al. (1992) shows how the stellar lifetimes depend on both stellar metallicity and stellar mass. High mass stars have much shorter lifetimes than low mass stars; also, for high mass stars ( $>6M_{\odot}$ ), higher metallicity stars have shorter lifetimes than their lower metallicity counterparts. For low mass stars ( $<6M_{\odot}$ ), the opposite is true - i.e., higher metallicity stars have longer lifetimes than lower metallicity stars.

Simple ‘closed-box’ models of chemical evolution do not include inflows and outflows of gas, although parameterisation of both are incorporated routinely into most chemical evolution models (e.g. Chiappini et al. 2001; Mollá & Díaz 2005; Fenner & Gibson 2003); the term ‘outflows’ can be broadly thought to include effects such as SNe- and stellar wind-driven outflows, and ram pressure stripping of gas. Specific parameterisations will be explored further in Chapter 5.

### 1.7 Aims of this Thesis

This thesis uses the first cosmological simulations that have been shown to match several properties of late type disk galaxies. With these simulations the aim of this thesis is to further constrain the uncertain physics within the modelling of galaxies, by using observational constraints. The constraints focused upon include, firstly chemistry of galaxies both in space and time, more specifically including the metallicity distribution functions and the evolution of the radial gradients. Secondly using the the ISM and in particular the velocity dispersion profiles and power spectra

## CHAPTER 1

of the simulations. Finally using chemical evolution models, inflows and outflows of gas are used to constrain the chemistry within local group dwarf galaxies.

### 1.8 Thesis Outline

This thesis provides an analysis of the chemistry within several different simulations of late type dwarf galaxies and the more massive spirals. The first chapter, §2, The Cold Gas Content of Bulgeless Dwarf Galaxies, shows an in depth analysis of the HI regions and the chemistry of several bulgeless dwarf galaxies from the Governato et al. (2010) sample. The second chapter, §3, The Distribution of Metals in Cosmological Simulations of Dwarf Disc Galaxies, shows a parameter study using five versions of one galaxy, with the aim to improve the short comings of the chemistry found in the previous chapter. The third chapter, §4, Metallicity Gradients in Disk Galaxies, uses simulations of massive sprial galaxies to examine the differences in the evolution of the radial metallicity gradient. The final chapter, §5, Chemical Evolution Models of Local Group Dwarf Spheroidals, shows chemical evolution models of three local group dwarf spheroidals.

## Chapter 2

# The Cold Gas Content of Bulgeless Dwarf Galaxies

### 2.1 Abstract

This chapter presents an analysis of the neutral hydrogen (HI) properties of several fully cosmological hydrodynamical dwarf galaxy simulations, realised with a range of sub-grid physics parameterisations. As reported by Governato et al. (2010), the high resolution, high star formation density threshold version of this galaxy is the first known simulation which successfully results in a dwarf spiral without any associated stellar bulge. The HI distribution and kinematics of this bulgeless disk are compared in detail with what is observed in a sample of nearby dwarfs. The focus here is on the radial gas density profiles, velocity dispersion (e.g. velocity ellipsoid, turbulence), and the power spectrum of structure within the cold interstellar medium. The highest resolution dwarf, when using a high density star formation threshold comparable to densities of giant molecular clouds, possesses bulk characteristics consistent with those observed in nature, though the cold gas is not as radially extended as that observed in nearby dwarfs, resulting in somewhat excessive surface densities. The

## CHAPTER 2

lines-of-sight velocity dispersion radial profiles have values that are in good agreement with observed dwarf galaxies, but due to the fact that only the streaming velocities of particles are tracked, a correction to include the thermal velocities can lead to profiles that appear too flat and isotropic relative to those seen in nature. The ISM power spectra of the simulations appear to possess more power on smaller spatial scales than that of the SMC. We conclude that unavoidable limitations remain due to the unresolved physics of star formation and feedback within pc-scale molecular clouds.

## 2.2 Introduction

The interstellar medium (ISM) of galaxies provides the fuel for star formation throughout the Universe, and is comprised of several phases, including/dominated by  $\text{H}_2$  (molecular hydrogen), HI (neutral hydrogen), and HII (ionised hydrogen) regions. These regions are well-defined in terms of their density, temperature, and spatial distribution. Neutral hydrogen (HI) is well-studied through the ubiquitous 21cm spin-flip transition of hydrogen; molecular hydrogen ( $\text{H}_2$ ) is studied indirectly via transitions associated with CO (e.g., the CO feature at  $\lambda=2.6\text{mm}$ ) and an empirically-derived scaling factor linking CO back to  $\text{H}_2$ ; ionised hydrogen (HII) is observed typically through the use of the  $\text{H}\alpha$  emission line associated with young, massive, stars.

The neutral hydrogen medium can be sub-divided further into two distinct phases, the cold neutral medium (CNM) and the warm neutral medium (WNM). About 60% of HI regions are WNM, possessing somewhat lower densities than the CNM ( $\sim 0.5 \text{ cm}^{-3}$ , as opposed to  $\sim 50 \text{ cm}^{-3}$ ), and (more importantly) show temperatures about  $100\times$  that of the CNM.

The cold gas in galaxies is linked directly to underlying star formation processes and associated ISM physics; any successful model of galaxy formation should adopt a

## CHAPTER 2

holistic approach, examining both the gas and star properties in consort. First, this chapter examines in detail the cold neutral hydrogen (HI) gas content of the simulated Governato et al. (2010) dwarfs. Initially, the focus is on the fiducial simulation therein, DG1, along with its low star formation threshold analog (DG1LT), in addition to an updated version of DG1 (nDG1) which employs both high-temperature metal-line cooling and enhanced supernova energy feedback. All three galaxies have the same initial conditions; minimal differences in the set-up are described in §2.3.1. In addition to these three realisations of one dwarf galaxy, we have added two additional ones from the Governato et al. (2010) sample - DG2 and DG3 (§2.4.5) - to test the consistency of the original conclusions based solely upon DG1. The focus of this chapter is to determine if the HI gas properties agree with recent observational data to an equally successful degree as the stellar component. Studies such as the The HI Nearby Galaxy Survey (THINGS) (Walter et al. 2008) provide excellent high resolution (spectral and spatial) data against which to compare the simulations. The gas properties of the simulations are compared directly with several of the most recent relevant empirical datasets (Tamburro et al. 2009; O’Brien et al. 2010; Stanimirovic et al. 1999), in order to assess both their strengths and weaknesses.

A traditional problem plaguing the simulation of disk galaxies (e.g. Thacker & Couchman 2001; Sommer-Larsen et al. 2003; Abadi et al. 2003a; Governato et al. 2004, 2007; Robertson et al. 2004; Bailin et al. 2005; Okamoto et al. 2005; Sánchez-Blázquez et al. 2009; Stinson et al. 2010, and references therein), within a cosmological context, has been the inability to recover successfully the properties of a truly “late-type” disk and, in particular, those with essentially no associated stellar bulge, similar to classical systems such as M33 and NGC 6503.

Recent work by Governato et al. (2010), though, has produced what appears to be exactly such a bulgeless dwarf, via the imposition of a higher density threshold for star formation ( $100 \text{ cm}^{-3}$ , as opposed to  $0.1 \text{ cm}^{-3}$ , as adopted in the aforementioned

## CHAPTER 2

earlier generations of simulations), and mass resolution that allows one to identify individual star forming regions.<sup>1</sup> The primary dwarf in their analysis (DG1) forms a shallow central dark matter profile and possesses a pure exponential stellar disk of radial scale  $r_d \sim 1$  kpc, with a stellar bulge-to-disk ratio  $B/D \approx 0.04$  as determined from the  $i$ -band light profile.

First, the basic properties of the simulations will be described (§2.3.1), before detailing the analyses undertaken for the fiducial DG1; §2.4 reports the main findings of this work, including: (i) the radial distribution of cold gas within the disks associated with DG1, DG1LT, and nDG1; (ii) the radial dependence of the vertical density distribution of the gas; (iii) spatially-resolved velocity dispersion maps of the cold gas; and (iv) the spatial distribution of power encoded within the structure of the ISM. Second, results are presented for the remaining dwarfs from the Governato et al. (2010) suite (DG2 and DG3). In §2.6, the chemistry of the full suite of simulations is analysed, complementing that of the cold ISM presented elsewhere. Finally, the chapter concludes with a summary of the findings, highlighting both the strengths *and* weaknesses of the current generation of simulations.<sup>2</sup>

## 2.3 Method

### 2.3.1 Simulations

This work makes use of the recent Governato et al. (2010) simulations which produced, for the first time, a late-type dwarf spiral with no associated stellar bulge. A full description of the simulations' characteristics is provided by Governato et al.

---

<sup>1</sup>The higher star formation density threshold can only be applied because the high resolution of the simulation, coupled with heating from the UV background, ensures fragmentation does not occur at unresolved scales.

<sup>2</sup>A complementary analysis of DG1, aimed *solely* at inferring its central dark matter distribution using the same methodology employed by observers, was presented by Oh et al. (2011).

## CHAPTER 2

(2010), but for context, it is useful to summarise their primary traits.

Using the N-body+SPH (Monaghan 1992) code GASOLINE (Wadsley et al. 2004), a low resolution (25 Mpc box, sufficient to provide realistic torques for these dwarfs), dark matter only simulation was used to identify  $3.5 \times 10^{10} M_{\odot}$  (virial) halos (with typical spin parameters  $\lambda=0.05$ ) for potential (high resolution) re-simulation using a volume renormalisation technique (i.e., “zoom-style” or “multi-resolution” simulation). New initial conditions were then re-constructed for the primary target halo (called “DG1”), using the relevant low-frequency waves associated with tidal torquing in the low resolution “parent” simulation, but now enhanced with higher spatial frequencies generated after tracing the present-day particles back to the relevant Lagrangian sub-region within the parent. The mass distribution was then sampled at higher resolution in the regions of interest, and more coarsely, further away from the identified halo. Both DG1 and nDG1 have a force resolution of 86pc, while that of DG1LT is somewhat lower (116pc); the initial baryonic (dark) particle mass for DG1 and nDG1 is  $3300 M_{\odot}$  ( $16000 M_{\odot}$ ), while for DG1LT it is  $7800 M_{\odot}$  ( $37000 M_{\odot}$ ). At  $z=0$ , the  $i$ -band luminosities of DG1, nDG1, and DG1LT are  $M_i=-16.5$ ,  $-15.8$ , and  $-19.1$ , respectively. Figure 2.1 shows the luminosity of the simulations as a function of HI mass; all the realisations lie well within the scatter of the observations from Verheijen et al. (2010).

The three primary realisations employed here (DG1, DG1LT, and nDG1) use the same dark matter halo / assembly history, differing only in their treatment of the baryonic physics associated with star formation - i.e., either supernova energy feedback efficiency (DG1 vs nDG1) or star formation density threshold (DG1 vs DG1LT). DG1 was simulated using a star formation density threshold of  $100 \text{ cm}^{-3}$ , typical of the densities encountered in giant molecular clouds, rather than the canonical value adopted in earlier simulations ( $0.1 \text{ cm}^{-3}$ ).<sup>3</sup> Other than the increased density

---

<sup>3</sup>GASOLINE employs an ideal gas law equation of state (Wadsley et al. 2004), and the mean molecular weight is implicitly solved for and allowed to vary (Shen et al. 2010a).

## CHAPTER 2

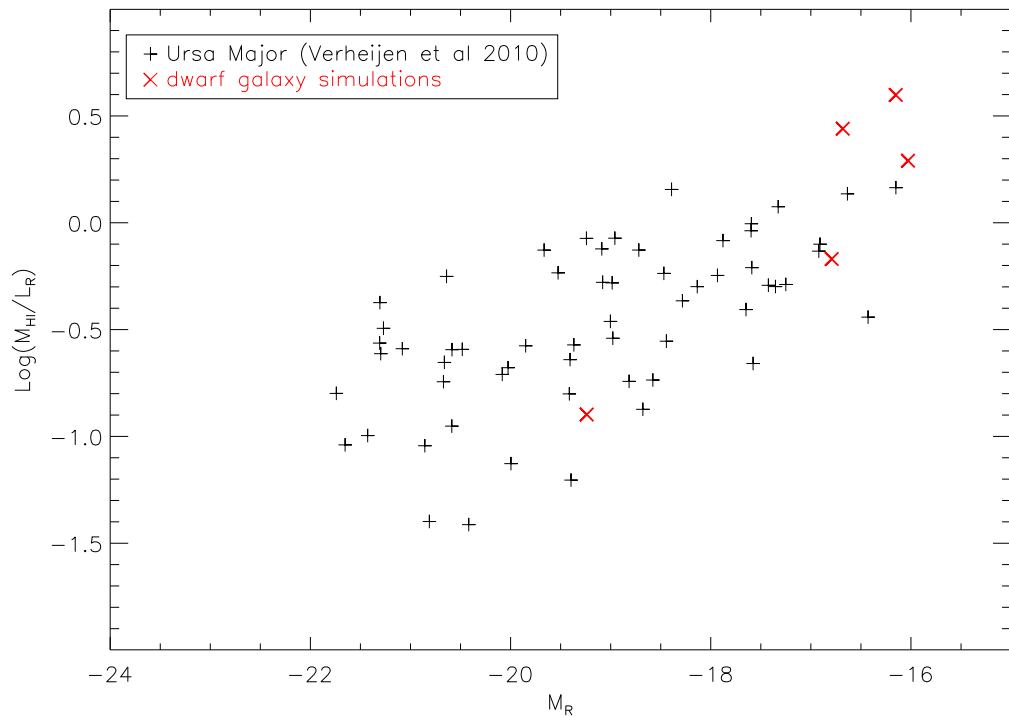


Figure 2.1: Relationship between HI mass and stellar luminosity for the five Governato et al. (2010) dwarfs employed in our analysis (nDG1, DG1, DG1LT, DG2 and DG3) with observational data (Verheijen et al. 2010) shown in black and the simulations in red.

## CHAPTER 2

threshold, two additional parameterisations were adopted, within the context of the feedback formalism employed: the star formation efficiency ( $\epsilon_{\text{SF}}=0.1$ ) and the fraction of supernova (SN) energy coupled to the ISM ( $\epsilon_{\text{SN}}=0.4$ ). The star formation and feedback are modelled as described in Stinson et al. (2009). Without any additional *ad hoc* adjustments, this high density threshold led to bulgeless dwarf spirals (akin to the classic prototype, M33) with flat (non-centrally concentrated) rotation curves (again, for the first time). Alongside our analysis of the high-threshold DG1 simulation, we provide a parallel analysis of two other simulated dwarfs, DG1LT (the lower-threshold analog, which uses the aforementioned canonical  $0.1 \text{ cm}^{-3}$  threshold, and a star formation efficiency  $\epsilon_{\text{SF}}=0.05$ , with the same initial conditions as that used for DG1), and an updated version of DG1, nDG1 (again with the same initial conditions as DG1 and high density threshold of  $100 \text{ cm}^{-3}$ , but now with high-temperature metal-line cooling, after Shen et al. (2010a), and increased thermal energy coupling to the ISM ( $\epsilon_{\text{SN}}=1$ )), in order to better assess the role played by star formation threshold and feedback in “setting” the gas properties of the respective simulations.

To foreshadow the discussion which will follow, perhaps the most problematic aspect of the current analysis is the uncertain numerical “leap-of-faith” that must be made in associating the typically 7000–8000K SPH gas particles, regardless of their local density ( $\sim 0.1\text{--}100 \text{ cm}^{-3}$ ), with star formation (which in nature occurs in clouds and cores with temperatures 2–3 orders-of-magnitude lower than this). Until the effects of cooling by molecular hydrogen are incorporated fully within GASOLINE, this remains an unavoidable limitation of our modeling. We return to this point in § 2.3.2 and § 2.4.4.

### 2.3.2 Analysis

The cold gas properties of DG1, DG1LT, and nDG1 are compared directly with those from comparable dwarfs in The HI Nearby Galaxy Survey (THINGS: Tamburro et al. 2009), in addition to the samples of O’Brien et al. (2010) and Stanimirovic et al. (1999). The bulk properties of DG1 (e.g., mass, luminosity, and gas fraction) are consistent with those observed in nature (e.g. Walter et al. 2008; van den Bosch 2001), All of the dwarfs analysed in the following sections sit on the HI-luminosity relation (Fig 2.1), and its present-day star formation rate ( $\sim 0.005 M_{\odot}/\text{yr}$ ) and luminosity ( $M_i \approx -16$ ) are (specifically and directly) comparable to those of the three dwarfs from Tamburro et al. (2009), with Holmberg II (HoII) being perhaps the closest direct analog (and, as such, being the empirical counterpart to which we will refer DG1 most often). As noted earlier, the properties which we derive include the radial extent, the velocity dispersion as a function of galacto-centric radius, and the power spectrum of the ISM.

In this work, unless otherwise stated, the label “cold gas” refers to those SPH particles with temperatures less than  $T_{\text{max}}=15000$  K (after Stinson et al. (2006)). The bulk of the gas in DG1 (nDG1) lies near 7000K (9000K), which at face value would appear to be more appropriate for the warm HI phase of the ISM, rather than the cold, star-forming, gas, to which we have associated star formation within the simulation. However, the cooling, despite the inclusion of metal-line cooling, is limited primarily to hydrogen and helium cooling, which can only cool gas down to these temperatures, and as emphasised in Stinson et al (2006; §5.1.1), we are averaging over scales much larger than individual star forming cores. The effect of varying this maximum temperature threshold ( $T_{\text{max}}$ ) for star formation was examined in detail by Stinson et al. (2006), to which the reader is referred. We can summarise that analysis by stating that provided  $T_{\text{max}}$  is chosen to be not too similar in value

## CHAPTER 2

to that of the mean temperature of the gas particles, its specific value does not critically affect star formation (see also, Shen et al. (2010a)). Efforts are underway to implement molecular hydrogen cooling within GASOLINE, after which a quantitative comparison with our results can be undertaken.

DG1LT, the low density threshold analog to DG1, is analysed in parallel, to provide something of a canonical “control” sample. As described in Governato et al. (2010), the properties of DG1LT (e.g., rotation curve, dark matter density profile, bulge-to-disc ratio) are not well-matched to those observed in nature, due to the traditional limitations that the new suite of simulations were designed to overcome in the first place. As a juxtaposition to DG1 though, it is invaluable. The present day star formation rate ( $0.2 M_{\odot}/\text{yr}$ ) and luminosity ( $M_i = -19.1$ ) are much higher than that of DG1 (and the associated stellar mass is correspondingly a factor of ten higher), driven (as described by Governato et al. (2010)) by its adoption of the lower star formation threshold (see Fig 2.2).

This analysis uses a newly generated variant of DG1 (labelled nDG1), employing both the same initial conditions and the higher star formation threshold ( $100 \text{ cm}^{-3}$ ). As alluded to earlier, where nDG1 differs from its predecessors is in its inclusion of metal-line cooling (following Shen et al. (2010a)) and a more efficient coupling of SN thermal energy to the ISM; qualitatively, we can anticipate this leading to a somewhat more turbulent ISM. On the whole, the star formation rate of nDG1 is suppressed relative to DG1, but extends to lower redshifts (see Fig 2.2, where one can see that the star formation rate from  $8 \lesssim t \lesssim 10$  Gyr is  $\sim 10\times$  higher in nDG1 than in DG1); its luminosity is, not surprisingly, somewhat lower than that of DG1 ( $M_i = -15.8$ , as opposed to  $M_i = -16.5$ ), considering its stellar mass is a factor of two lower ( $M_* \approx 2.1 \times 10^8 M_{\odot}$  vs  $M_* \approx 4.4 \times 10^8 M_{\odot}$ ). Zeroth (density), first (velocity), and second (velocity dispersion) moment maps of the simulated neutral

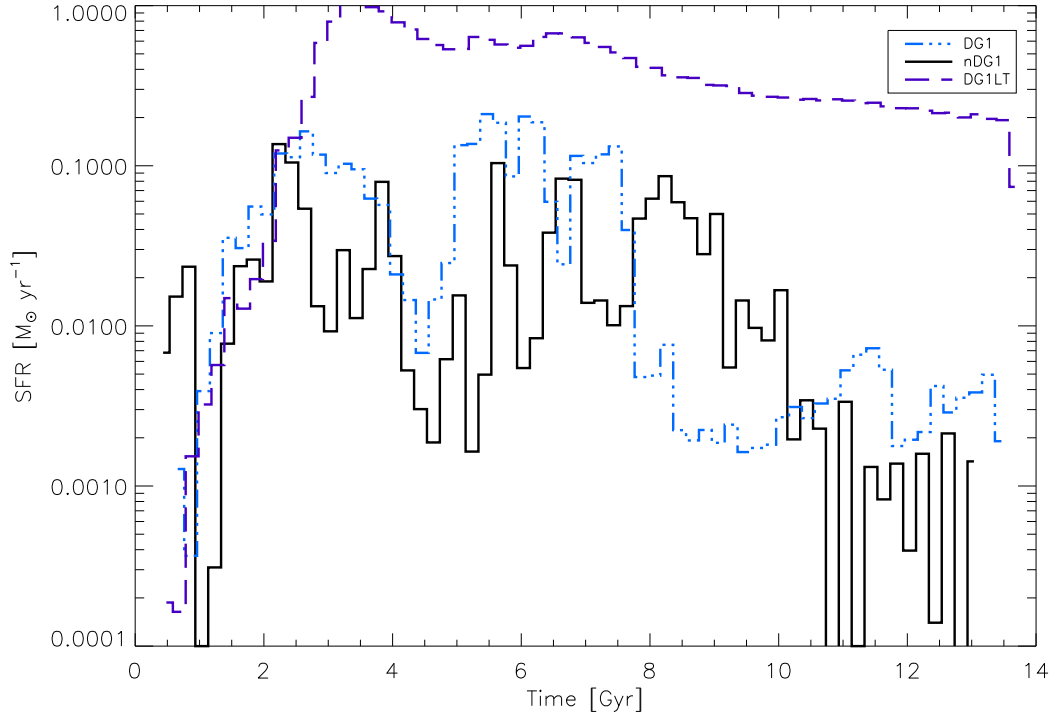


Figure 2.2: The star formation rates of nDG1 (solid line), DG1 (dot-dashed line), and DG1LT (dashed line). Star formation in nDG1 is suppressed overall, relative to DG1, but extends  $\sim 2$  Gyrs beyond the cessation of bulk star formation in DG1 (in the range  $8 \lesssim t \lesssim 10$  Gyrs). There is intermittent star formation in both dwarfs up to the present day, but it has been consistently low for the past  $\sim 3$  Gyrs in nDG1 and  $\sim 5$  Gyrs in DG1. The star formation history of DG1LT is overall considerably higher than its two higher density threshold analogs.

## CHAPTER 2

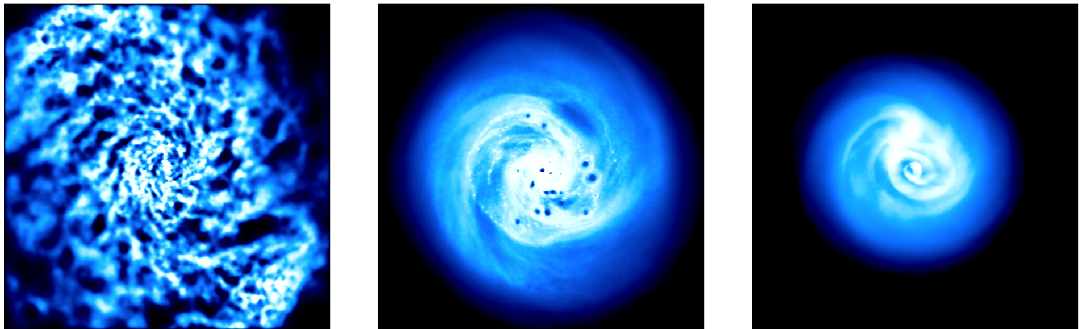


Figure 2.3: Neutral hydrogen (HI) moment zero maps of the three simulations analysed here - from left to right: DG1LT, DG1, and nDG1. Each panel has dimensions  $14 \times 14$  kpc; a lower column density threshold of  $N(\text{HI}) = 1 \times 10^{19} \text{ cm}^{-2}$  was employed for each map.

hydrogen distributions were generated using TIPS<sup>4</sup> (Figure 2.3), after matching the  $\sim 40^\circ$  inclination of the dwarfs from the Tamburro et al. (2009) THINGS sample (which, again, includes HoII, the primary analog against which the simulations will be compared, as noted in § 2). The conversion from “cold gas” to “HI” within GASOLINE suffices for the purposes outlined here; the values derived are close to the values one would predict under the assumption of combined photo- and collisional-ionisation equilibrium. All our results were cross-checked using both cold gas and HI moment maps, in addition to further cross-checks undertaken after eliminating high column density HI gas for which the conversion from cold gas to HI is most insecure. The results described here are robust to these choices, and for expediency are not discussed further.

The velocity dispersion analysis made use of the second HI moment map (i.e., line-of-sight velocity dispersion) produced from viewing the DG1, nDG1, and DG1LT simulations with an inclination angle matching that of HoII. For the analysis of the distribution of structural “power” within the cold ISM of the simulations, again the zeroth HI moment maps and their Fourier Transforms were used, and the inferred

---

<sup>4</sup>[www-hpcc.astro.washington.edu/tools/tipsy/tipsy.html](http://www-hpcc.astro.washington.edu/tools/tipsy/tipsy.html)

power law spectra compared with that derived for the SMC by Stanimirovic et al. (1999).

## 2.4 Results

### 2.4.1 Radial Density Profiles

First, it was confirmed independently that the stellar light associated with DG1 was indeed consistent with a pure exponential of scalelength  $\sim 1$  kpc (i.e. bulgeless) disk (akin to the Type I profiles categorised by, for example, Pohlen & Trujillo (2006)); as shown in the lower panel of Fig 2.4, this was the case. DG1LT also has a radial (stellar) scalelength of  $\sim 1$  kpc, but shows the classical problem of possessing a substantive stellar bulge within the inner kpc ( $B/D \approx 0.2$ ). The stellar disk component of nDG1 is not well-represented by a single pure exponential (cf. DG1); instead, its surface density profile shows a deficit of matter (and light) in the outskirts of the stellar disk (beyond a so-called “break radius” at  $\sim 2-3$  kpc), consistent with the more common Type II profiles observed in nature (e.g. Pohlen & Trujillo 2006; Sánchez-Blázquez et al. 2009); the inner and outer parts of the nDG1 stellar disk show radial scalelengths of  $\sim 2$  kpc and  $\sim 1$  kpc, respectively. The bulge-to-disc ratio of nDG1 matches formally that of DG1, although it is also readily apparent that the surface density (and light) profile of nDG1 shows a high-density stellar “core”, in which  $\sim 10^7 M_{\odot}$  ( $\sim 10\%$  of the nDG1 stellar mass, as a whole) is concentrated within the inner 100 pc. Importantly, this stellar “core” is inconsistent with a bulge. Instead, it consists of a large cluster of stars that was formed in the disk during a merger at high-redshift, and traveled inward with time so that at  $z=0$  it is close to, but not located at, the dynamical center of the galaxy (i.e., it can be seen to rotate about the galaxy center).

## CHAPTER 2

The cold gas of DG1 displays a rapid increase in density within  $\sim 1$  kpc of its centre. Exterior to this is an extended disk with an exponential scalelength  $r_d \sim 6$  kpc; the cold gas disk truncates at  $\sim 1r_d$ , somewhat short of those observed by Tamburro et al. (2009) and O'Brien et al. (2010), where the respective HI disks are traced out to  $\sim 2-6 r_d$ . Bigiel et al. (2008) showed that there is an empirical HI upper limit encountered in nature -  $\Sigma_{HI} \sim \leq 9 M_\odot/\text{pc}^2$ . This upper limit is represented by the horizontal line in the upper panel of Figure 2.4. Because we do not yet resolve the microphysics associated with molecular processes on parsec-scales, one might ascribe some fraction of the cold gas in the simulation (particularly that above the upper limit observed by Bigiel et al. (2008)) to molecular gas. Again using the results from Bigiel et al. (2008) for the fraction of  $\text{H}_2/\text{HI}$  as a function of radius (see their Figure 13), we can verify that the high density gas interior to 1 kpc could be taken as being consistent with being molecular gas. Assuming that as much of this gas within the inner  $\sim 1$  kpc could be ascribed to HI as possible (i.e., the upper limit of  $\Sigma_{HI} = 9 M_\odot/\text{pc}^2$ ), then the results from Bigiel et al. (2008) suggest that  $7.9 M_\odot/\text{pc}^2$  could be tied up in molecular gas within the innermost radius of DG1, dropping to  $7.2 M_\odot/\text{pc}^2$  at 0.8 kpc, and declining rapidly to  $\sim \leq 0.1 \text{H}_2/\text{HI}$  at 2 kpc.<sup>5</sup> That is, while the total amount of gas in DG1 is consistent with empirical bulk scaling relations, and the gas within 1 kpc is not inconsistent with potentially being ascribed to (mostly) molecular, the cold gas surface densities beyond 1 kpc are too high relative to nature.<sup>6</sup>

It is difficult to fully interpret the source of this excess gas; for example, perhaps this is gas that should instead be lost from the galaxy in winds? While it may be tempting to suggest that this gas is overly concentrated, comparison of the cold gas scale lengths for these simulated galaxies (which has been fit beyond  $r_{25}$ ) to

---

<sup>5</sup> $r_{25}$ , the isophotal radius corresponding to 25 mag/arcsec<sup>2</sup>, is 2.0 kpc for DG1.

<sup>6</sup>The additional simulations (DG2 and DG3) from the same suite (Governato et al. 2010) show the same behaviour (§2.4.5).

## CHAPTER 2

the scalelengths beyond  $r_{25}$ , in the sample of Bigiel et al. (2010), suggests that the excess gas in these simulations is actually too extended compared to real galaxies. Alternatively, as discussed below for the case of DG1LT, additional star formation in the outskirts of the simulated galaxy disks could decrease the surface density of gas (as it goes instead into stars). While Brooks et al. (2011) showed that the  $B$ -band scale length of DG1 is comparable to observed dwarf galaxies, a factor of 1.5 to 2 increase in size is still allowable to be fully consistent with nature. In fact, preliminary tests of molecular cooling and star formation in GASOLINE suggest that the star formation is more extended at  $z=0$ . Hence, the addition of  $H_2$  to these simulations may alleviate the problem of this excess gas.

As was the case for the stellar light, the disk of nDG1 is better represented by a “broken”, or two-component exponential, with inner and outer disk scalelengths of  $\sim 2$  kpc and  $\sim 1$  kpc, respectively (with the break occurring near a galactocentric radius of  $\sim 3$  kpc). The arguments of the previous paragraph concerning the excess surface density of cold gas in DG1 applies obviously to nDG1, as well.

Conversely, the cold gas in the disk of DG1LT extends radially to  $\sim 8$  kpc (Fig 2.5) with an essentially flat density profile (formally, with a radial scalelength of  $\sim 18$  kpc – i.e. , the gas disk truncates near  $\sim 0.5r_d$  – again, short of the typical disc in nature, but since the profile is so flat, the formal exponential “scalelength” is somewhat ill-defined). Like DG1, DG1LT also shows a high density cold gas “core” (of mass  $\sim 2 \times 10^6 M_\odot$ ), although it is somewhat more extreme, in the sense of it being concentrated solely within the inner  $\sim 100$  pc (note that this is within twice the force softening length). Being more extended, and the gas fraction being an order-of-magnitude lower (Governato et al. (2010); Tbl 2), it is not surprising that the cold gas surface density profile of DG1LT is consistently a factor of  $\sim 3 \times$  lower than the empirical upper limit derived by (Bigiel et al. 2008). However, this result should not be interpreted to mean that DG1LT is the more realistic version of this galaxy

CHAPTER 2

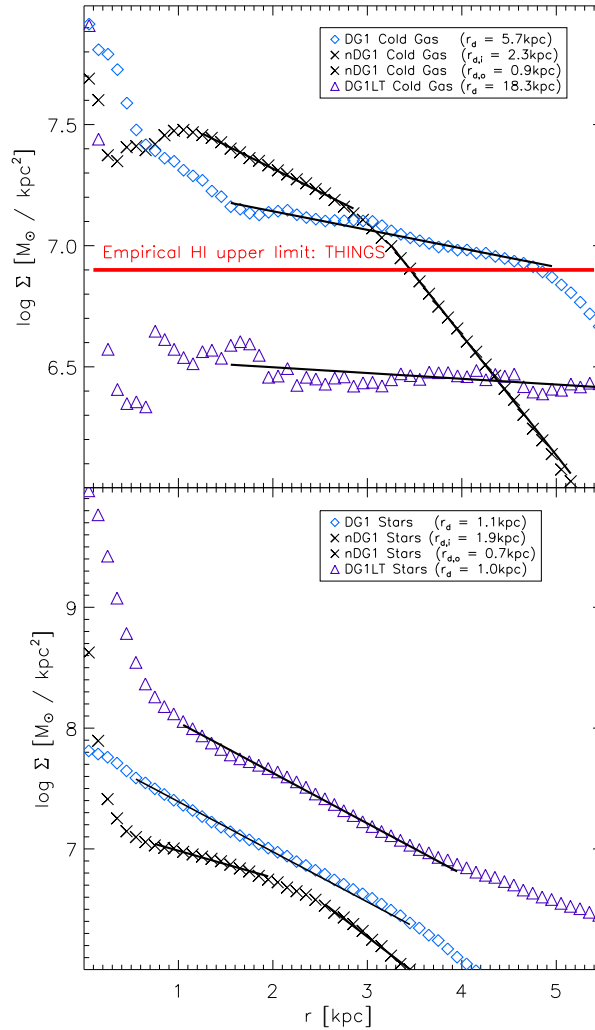


Figure 2.4: Radial gas (top) and stellar (bottom) density profiles for the simulated dwarfs DG1 (diamonds), DG1LT (triangles), and nDG1 (crosses). The thick over-plotted lines show the exponential fits to the distributions, from which the noted scalelengths were derived. The stellar component of DG1 obeys a pure exponential of scalelength  $\sim 1$  kpc, with no evidence for a central bulge, while both nDG1 and DG1LT show central cores. Both the stellar and cold gas components of nDG1 are best represented by double exponentials, with a break between the two near  $\sim 3$  kpc. The cold gas of DG1 is distributed in a more extended exponential disk component of scalelength  $\sim 6$  kpc, while that of DG1LT is  $\sim 18$  kpc. The horizontal line in the upper panel corresponds to the empirical upper limit to HI encountered in nature, from the THINGS work (Bigiel et al. 2008).

## CHAPTER 2

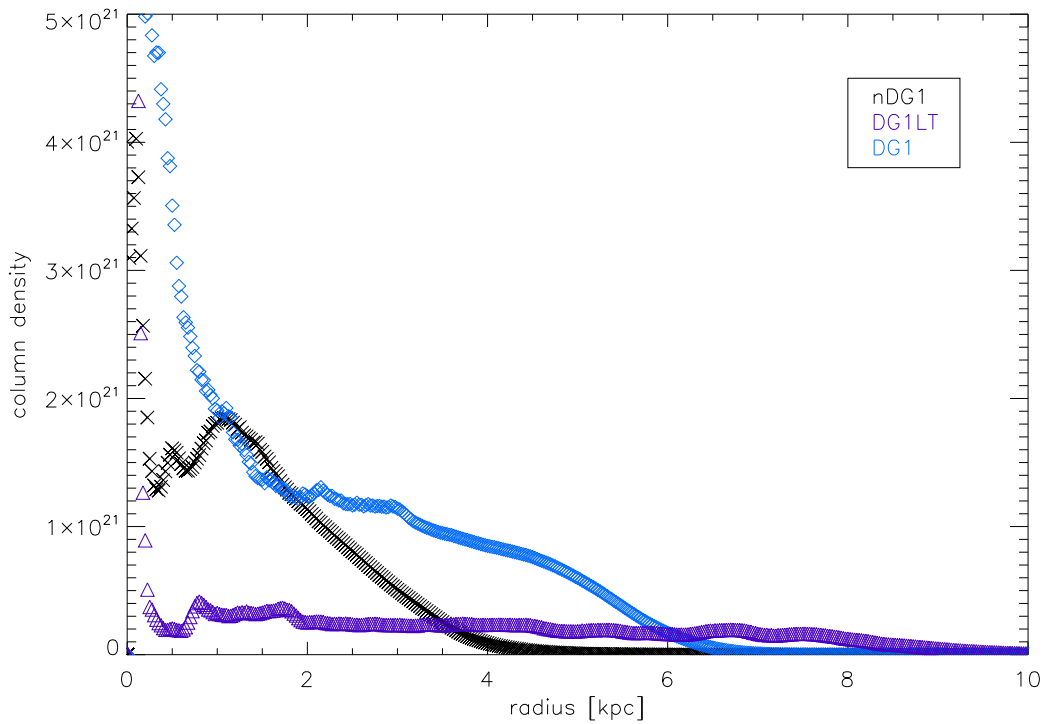


Figure 2.5: The HI column density as a function of radius for DG1, nDG1, and DG1LT - in black is shown the profile for nDG1; blue shows the profile for DG1; purple shows the profile for DG1LT. The HI profiles are consistent with those shown for the ‘cold gas’ (Fig. 2.4).

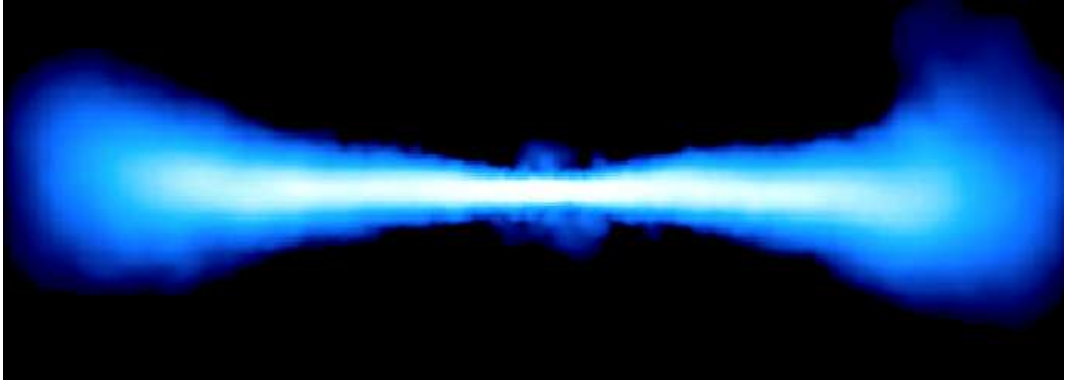


Figure 2.6: Neutral hydrogen column density map ( $14 \text{ kpc} \times 5 \text{ kpc} \times 1 \text{ kpc}$ ) of the simulated dwarf DG1 (Governato et al. 2010), as viewed edge-on with an adopted lower column density limit of  $N(\text{HI})=4 \times 10^{17} \text{ cm}^{-2}$ . An obvious and significant degree of flaring of the HI disk is apparent.

simulation. As Governato et al. (2010) and Oh et al. (2011) have demonstrated, the mass of this galaxy is overly concentrated, with a large bulge and peaked inner rotation curve that are inconsistent with observed galaxies in the same mass range.

### 2.4.2 Flaring

When viewed edge-on, the DG1 column density map shows evidence for significant flaring of the HI disk (Fig 2.6), although the degree of flaring only becomes readily apparent at column densities  $N(\text{HI}) \sim \leq 10^{18} \text{ cm}^{-2}$ . At the same column density limit, nDG1 also shows evidence of flaring (Fig 2.7), but not to same degree as DG1. Typical dwarfs, when viewed comparably, also show flaring, with the FWHM of the vertical density distribution increasing by  $\sim 50\%$  when measured at  $\sim 0.4 r_d$  and  $\sim 1 r_d$ , respectively (O’Brien et al. 2010); the most extreme flare amongst the dwarfs in the O’Brien et al. (2010) sample (ESO 274–G001) doubles in ‘thickness’ over this same radial range.

To quantify the flaring seen visually in Fig 2.6 and 2.7, we show in Fig 2.8 the vertical density profiles of the cold gas in DG1 (bottom) and nDG1 (top) for

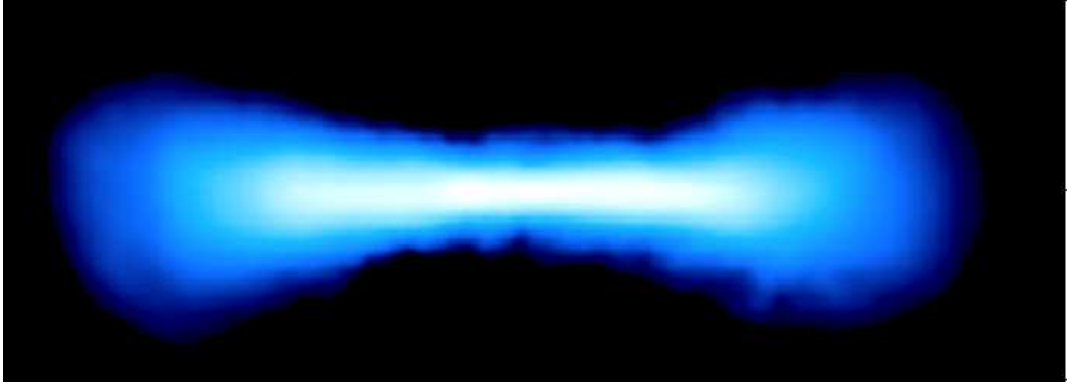


Figure 2.7: Neutral hydrogen column density map ( $14 \text{ kpc} \times 5 \text{ kpc} \times 1 \text{ kpc}$ ) of the newly simulated dwarf nDG1, as viewed edge-on with an adopted lower column density limit of  $N(\text{HI})=4 \times 10^{17} \text{ cm}^{-2}$ . The flaring of the disk of nDG1 is considerably less than that of DG1.

three different annuli. Over the same  $\sim 0.4r_d$  to  $\sim 1.0r_d$  radial range, the vertical scaleheight (and FWHM) of DG1 increases by a factor of  $\sim 4$  - i.e. the cold disk of DG1 flares more dramatically than that observed in the typical dwarf spiral, albeit only by a factor of two more so than ESO 274–G001 (O’Brien et al. 2010) – i.e. while DG1 is somewhat extreme in this sense, it does not stand apart overly from those observed in nature. Indeed, the degree of flaring, in terms of physical units of kpc, is completely compatible with that observed; it is the fractional degree of flaring which stands out as significant, due to the extremely thin and kinematically cold disk in DG1, which causes the simulation to stand out from observations (a point to which we return shortly). In contrast, nDG1 flares only by a factor of  $\sim 1.5$  over the same radial range, consistent with the flaring observed in nearby dwarfs by O’Brien et al. (2010). In the inner disk, at  $\sim 0.1r_d$ , nDG1 is twice as thick as DG1, while in the outer disk, nDG1 is roughly half as thick as DG1. DG1LT does not show the same (fractional) degree of flaring as that seen in DG1, again, a point to which we will return when discussing the velocity dispersion profile of the respective disks.

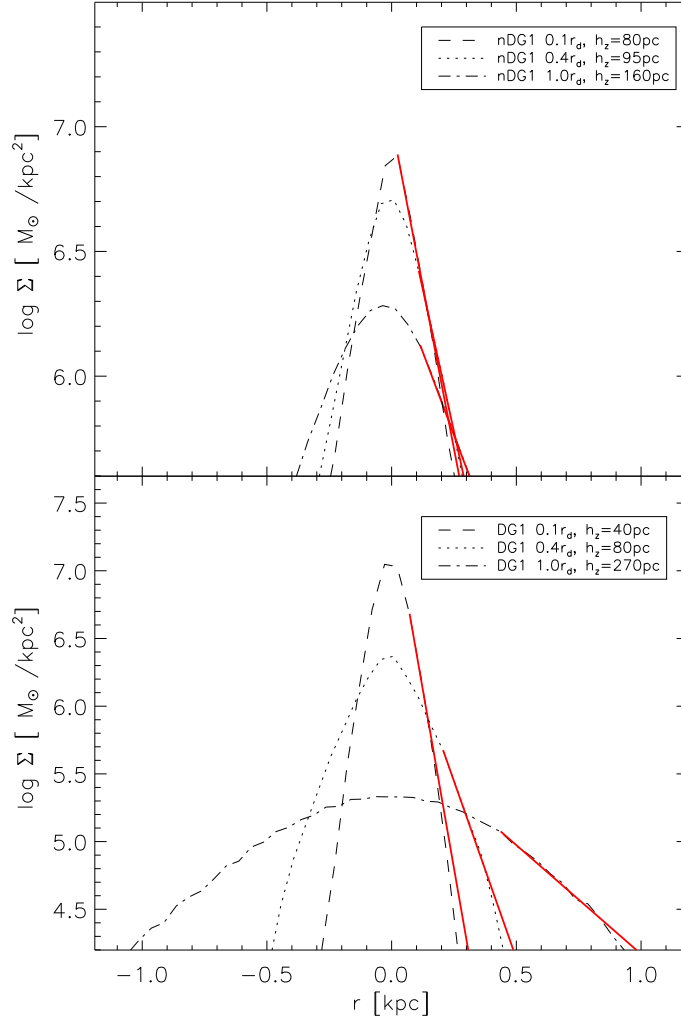


Figure 2.8: Vertical surface density profiles of the cold gas ( $T < 15000$  K) associated with the simulated dwarfs nDG1 (top) and DG1 (bottom). Profiles are shown for three 500 pc wide annuli centred on  $\sim 0.1$ ,  $\sim 0.4$ , and  $\sim 1.0$  HI disk scalelengths. The associated scaleheights were derived from the overlaid exponentials (solid lines). The scaleheights in DG1 increase from  $\sim 40$  pc in the inner disk to  $\sim 300$  pc in the outer disk; in nDG1 the increase is from  $\sim 80$  pc to  $\sim 160$  pc; comparable behaviour is observed when measuring ‘thickness’ as the FWHM of either the cold gas or the neutral hydrogen in the vertical direction.

### 2.4.3 Velocity Dispersion

Here, we examine the velocity dispersion of the HI disks of DG1, nDG1, and DG1LT, and compare with those observed in various samples of dwarfs from the literature (e.g. Crosthwaite et al. 2000, 2001; Tamburro et al. 2009; O’Brien et al. 2010). Observations show that independent of present-day star formation rate, luminosity, or mass, disks possess a characteristic velocity dispersion of  $\sim 8\text{--}10$  km/s, rising to  $\sim 12\text{--}15$  km/s in the inner star-forming regions (i.e. , within  $r_{25}$ , the isophotal radius corresponding to 25 mag/arcsec<sup>2</sup>).<sup>7</sup> A typical radial velocity dispersion distribution is shown in Fig 2.9 for HoII (diamonds), from the THINGS sample (Tamburro et al. 2009).

In addition to the curve for HoII, in Figure 2.9 we also show the corresponding velocity dispersion profiles (line-of-sight, assuming again a  $\sim 40^\circ$  inclination, similar to that of HoII) for DG1 (open squares), nDG1 (crosses), and DG1LT (triangles), derived from the SPH gas particles’ *streaming velocities* (see below, and van den Bosch et al. (2002)), and for DG1 (filled squares) and nDG1 (plus signs), taking into account said particles’ *thermal velocities*. Circular annuli<sup>8</sup> projected on the inclined galaxy were used to set the bins.

For typical Milky Way-scale simulations, the thermal broadening component is often neglected, since the ‘streaming velocity’ of the SPH particle usually dominates over the ‘thermal component’. For our simulated dwarfs, this is inadequate, as the streaming velocity dispersion can be much smaller than the relevant thermal velocity dispersion. To incorporate the latter, we follow the procedure outlined by van den

---

<sup>7</sup>At these resolutions ( $\sim 100$  pc), the velocity dispersions of the molecular and neutral gas are not dramatically different - (Crosthwaite et al. 2000, 2001).

<sup>8</sup>Technically, elliptical annuli should be used, but the results are not sensitive to this choice, at these inclination angles; in addition, the velocity dispersion profile on the raw THINGS data for HoII was re-measured using circular annuli, to ensure self-consistency with the analysis of the simulations.

## CHAPTER 2

Bosch et al. (2002) (§2.3) and note that the velocity of each particle can be written as  $v = u + w$ , where  $u$  is the mean streaming velocity at the location  $x$  and  $w$  is the particle’s random (thermal) velocity. Because SPH only tracks the streaming motions of the particles, we make use of the internal energy of each particle, in order to derive an appropriate random component to apply to each particle. In practice, random velocities for each Cartesian coordinate are drawn from a Gaussian of dispersion  $\sigma = \sqrt{kT/\mu}$  and add those to each of the coordinates of the streaming motion, where  $T$  is the temperature of the gas particle (typically,  $\sim 7000\text{--}9000$  K, for the simulations),  $k$  is Boltzmann’s constant, and  $\mu$  is the mean molecular weight of the gas.

Without the inclusion of thermal broadening, both DG1 and nDG1 show extremely (and unphysically) kinematically cold interstellar media compared to DG1LT and, more importantly, dwarfs in nature (compare the crosses and open squares of Figure 2.9 (simulations) with those of the plus symbols (observations) for a graphic example of the mismatch between unphysical streaming velocity dispersions and those encountered in nature). This is not to imply, however, that DG1LT as presented in Figure 2.9 is ‘physical’. First, and most importantly, as already noted in §2.4.1 and, especially, by Governato et al. (2010) and Oh et al. (2011), the rotation curve and dynamics of DG1LT are problematic, as is the associated significant overproduction of the stellar bulge. As can be seen in Fig 2.2, DG1LT has a star formation rate two orders of magnitude larger than DG1 or nDG1; while this does not impact upon its consistency with the stellar mass-metallicity, luminosity-metallicity, or HI gas fraction-luminosity scaling relations (see §2.6), it does worsen significantly the consistency with the dynamical-to-stellar mass ratio distribution of Blanton et al. (2008). This large star formation rate drives more turbulence, leading to the large streaming velocities for this simulation. We have not included the thermal

## CHAPTER 2

component for DG1LT in Fig 2.9, as doing so would only increase its velocity dispersion from  $\sim 12$  km/s to  $\sim 14$  km/s. The inferred line-of-sight velocity dispersion profile for DG1, after application of the above thermal broadening (which effectively amounts to a  $\sigma \sim 7-9$  km/s broadening of the essentially negligible  $\sim 1$  km/s streaming motions), is represented by the filled squares in Figure 2.9.

The characteristic velocity dispersions of the cold gas within DG1 and nDG1 are comparable to those encountered in nature ( $\sim 8-10$  km/s - Tamburro et al. (2009)) when thermal velocities are considered. The thermally broadened velocity dispersion profile of DG1 shows a few enhanced features (near  $0.5r_{25}$ ). These are due to high temperature gas particles in and around superbubbles blown by SNe feedback (discussed further below and shown in Figure 2.3). By design, including a random thermal component to the velocity dispersion accentuates these features. However, by chance, the particular timestep we examine here for nDG1 does not show any bubbles (though does at previous timesteps), and hence no thermal features are introduced into the profile of this simulation. As can be seen from the streaming-only profiles for these galaxies, both have slightly higher macroscopic velocity dispersions in the inner few hundred parsecs. However, in DG1 this gas is  $\sim 35\%$  hotter than the rest of the disk, while in nDG1 it is cooler by a similar factor. Figure 2.9 shows that, when this is considered in the thermally broadened velocity dispersions, it has the effect of maintaining the higher velocity dispersion structure in the inner region of DG1, while “washing out” the inner structure in nDG1. This result highlights a conundrum in terms of comparing the velocity dispersion profiles of these dwarf galaxy simulations to real dwarfs.

A more subtle effect of imposing the random thermal velocity perturbation to each particle’s streaming motion is that the velocity ellipsoid of the cold gas becomes necessarily isotropic, disguising any anisotropies that might have been present in the streaming motions (i.e., young stars, and the cold gas from which

CHAPTER 2

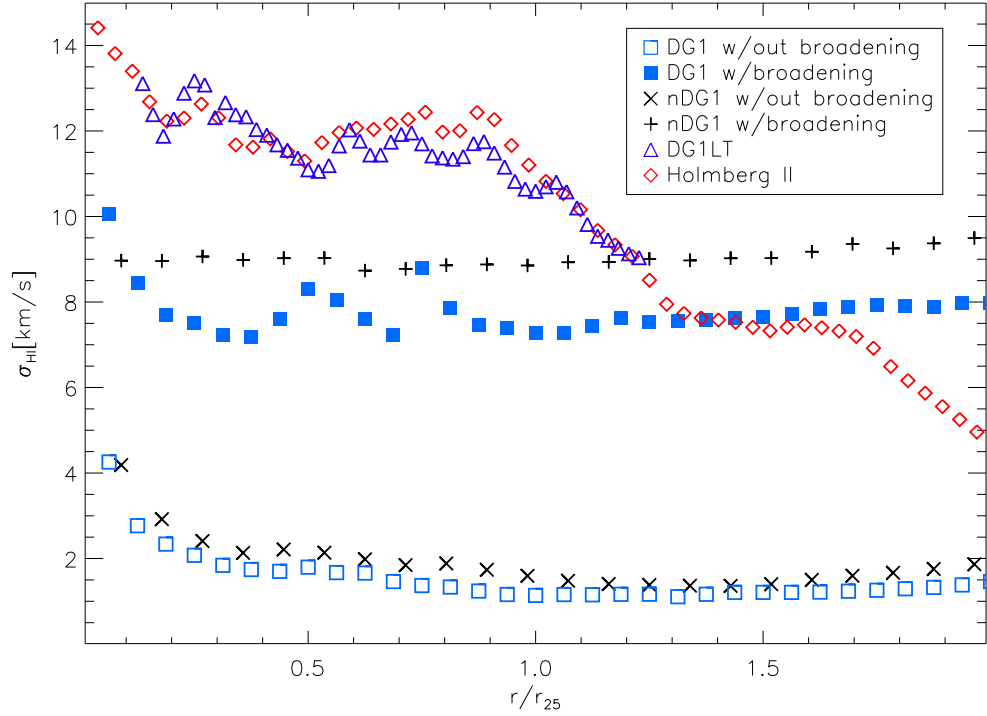


Figure 2.9: Radial behaviour (in units of the B-band  $r_{25}$  - i.e. the isophotal radius corresponding to 25 mag/arcsec<sup>2</sup> or, roughly, to the extent of the star forming disk) of the HI line-of-sight velocity dispersion of the DG1 (open squares), DG1LT (open triangles), and nDG1 (crosses) simulations, derived from the SPH gas particles’ ‘streaming velocities’ (after van den Bosch et al. (2002)), in addition to the true HI line-of-sight velocity dispersion profile for DG1 (filled squares) and nDG1 (plus signs), after correcting the streaming velocities isotropically for their internal thermal energies. Also shown is a representative dwarf spiral from the THINGS (Tamburro et al. 2009) sample (HoII: open diamonds). note:  $r_{25}$  is 2.0 kpc, 5.5 kpc, 1.4 kpc, and 3.3 kpc, respectively, for DG1, DG1LT, nDG1, and HoII.

## CHAPTER 2

they formed, will necessarily have different velocity ellipsoids). For example, for DG1 (nDG1), the radial, azimuthal, and vertical velocity dispersions inferred from the cold gas particles' streaming motions, measured at  $\sim 0.5r_d$ , are  $\sigma_r \approx 4$  km/s ( $\sim 6$  km/s),  $\sigma_\phi \approx 3$  km/s ( $\sim 6$  km/s), and  $\sigma_z \approx 1$  km/s ( $\sim 2$  km/s) – i.e.,  $\sigma_r:\sigma_\phi:\sigma_z \approx 3:3:1$  (anisotropic). After thermal broadening, the derived respective velocity dispersions are  $\sigma_r \approx 8.5$  km/s ( $\sim 10$  km/s),  $\sigma_\phi \approx 8$  km/s ( $\sim 10$  km/s), and  $\sigma_z \approx 7.5$  km/s ( $\sim 8.5$  km/s) – i.e.,  $\sigma_r:\sigma_\phi:\sigma_z \approx 1:1:1$  (isotropic). This is illustrated in figures 2.10, 2.11, 2.12, and 2.13.

What this means is that an unavoidable outcome of our current inability to resolve pc-scale molecular heating and cooling processes within the simulations is the lack of any significant correlation between velocity dispersion and galactocentric radius and/or underlying star formation. Until we can resolve densities (and temperatures) corresponding to the cores of molecular clouds, this apparent mismatch between observations and simulations would appear difficult to avoid.<sup>9</sup>

### 2.4.4 Power Spectrum and Superbubbles

Following Stanimirovic et al. (1999), we generated the Fourier Transform of the HI moment zero maps of DG1, nDG1, and DG1LT – each shown in Figure 2.3 at the same spatial scale ( $14 \times 14$  kpc) with the same limiting HI column density ( $N(\text{HI}) > 1 \times 10^{19} \text{ cm}^{-2}$ ) – after first convolving the maps with a 100 pc Gaussian, to mimic the typical beam-smearing present within THINGS data for HoII (Tamburro et al. 2009). Circular annuli in Fourier space were then employed to derive the

---

<sup>9</sup>It might be tempting to conclude that since the enhanced feedback did not result in a *significantly* higher line-of-sight velocity dispersion, this is consistent with the earlier work of Dib et al. (2006) and Petric & Rupen (2007), who concluded that supernova feedback alone was insufficient to provide turbulent heating to the cold ISM in excess of a few km/s; in light of the fact that we are not resolving the ISM heating and cooling processes at pc and sub-pc scales, we feel it premature to draw such a conclusion from this aspect of our analysis.

CHAPTER 2

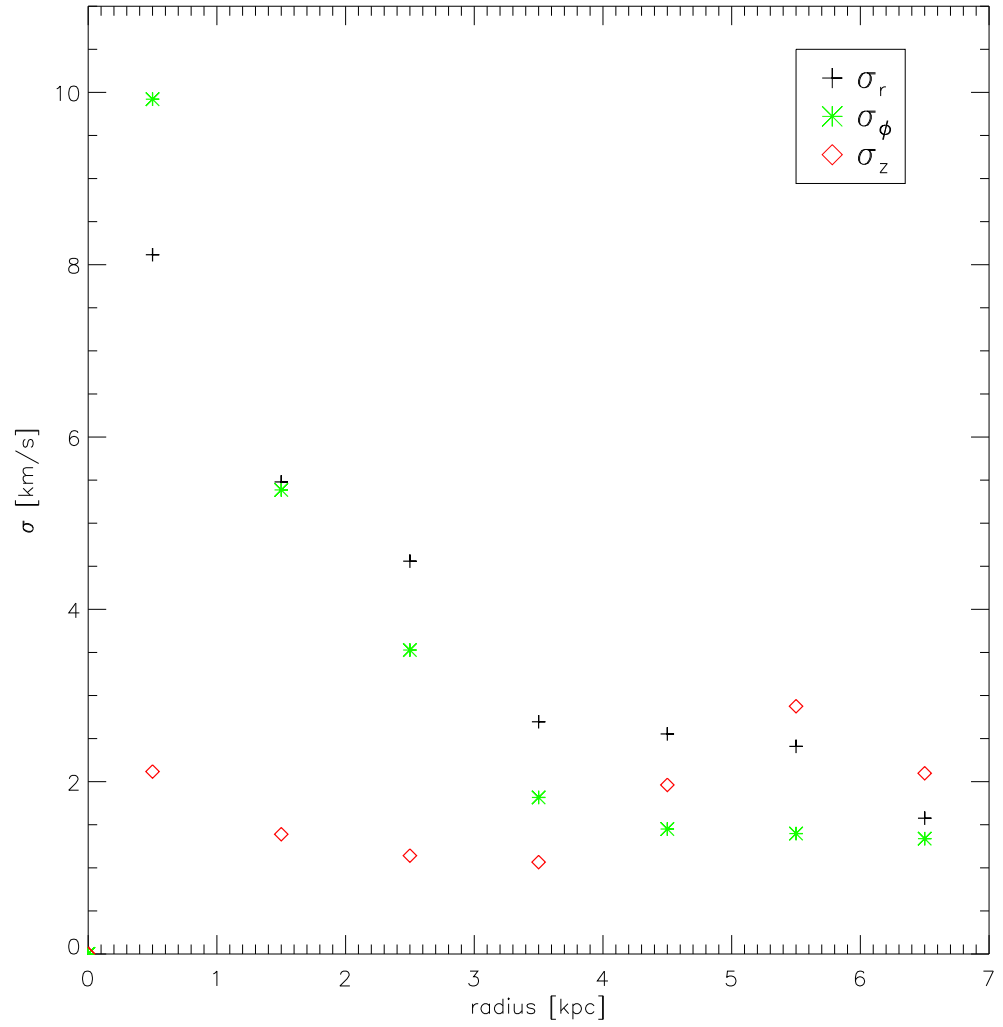


Figure 2.10: Radial (black crosses), azimuthal (green stars), and vertical (red diamonds) velocity dispersions of the simulated HI in DG1 without the inclusion of thermal broadening of the SPH particles.

CHAPTER 2

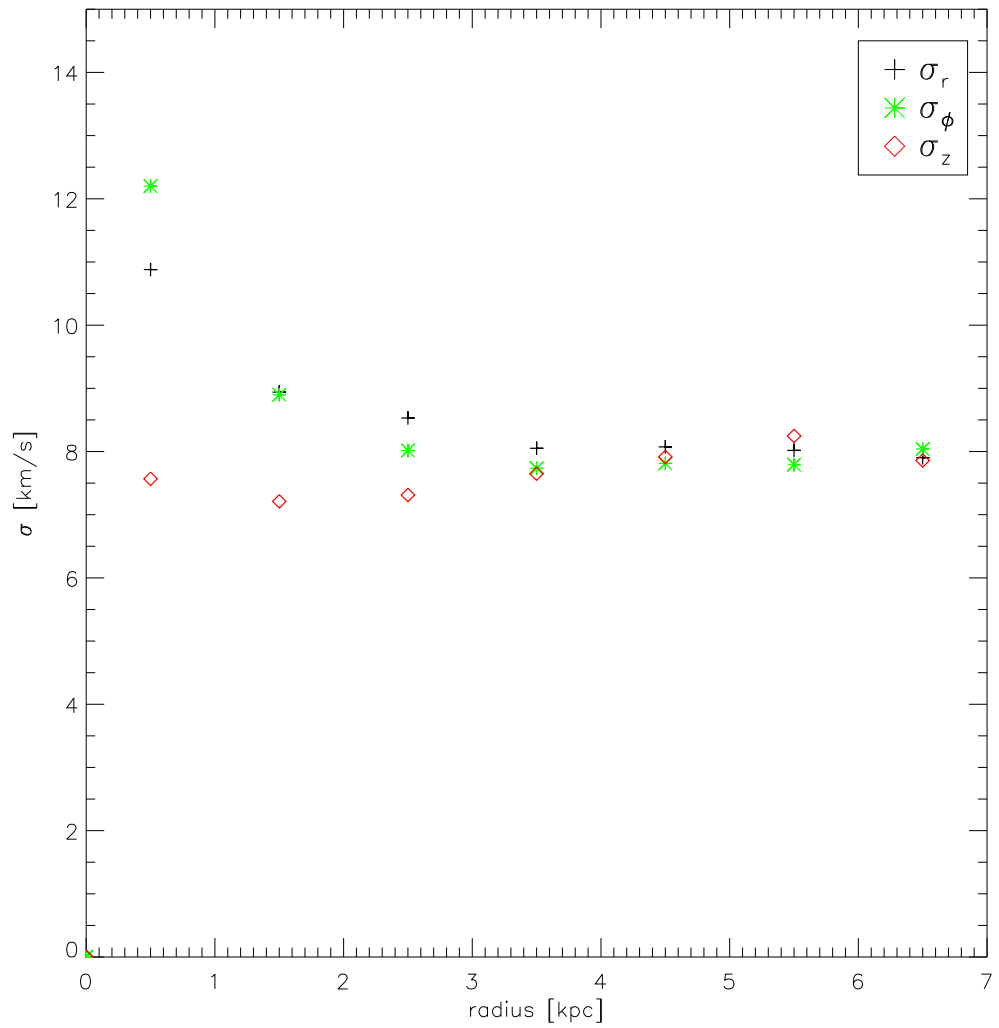


Figure 2.11: Radial (black crosses), azimuthal (green stars), and vertical (red diamonds) velocity dispersions of the simulated HI in DG1 with the inclusion of thermal broadening of the SPH particles.

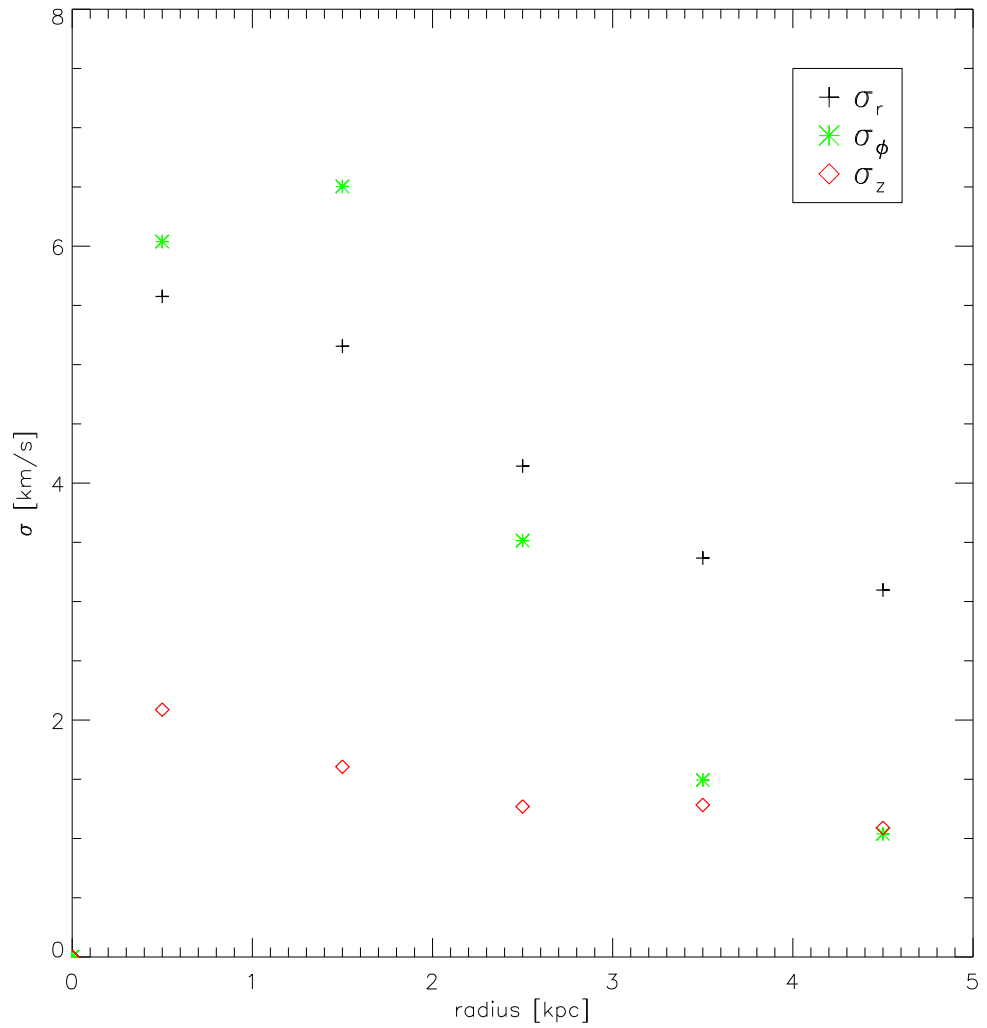


Figure 2.12: Radial (black crosses), azimuthal (green stars), and vertical (red diamonds) velocity dispersions for the simulated HI in nDG1, without the inclusion of thermal broadening of the SPH particles.

## CHAPTER 2

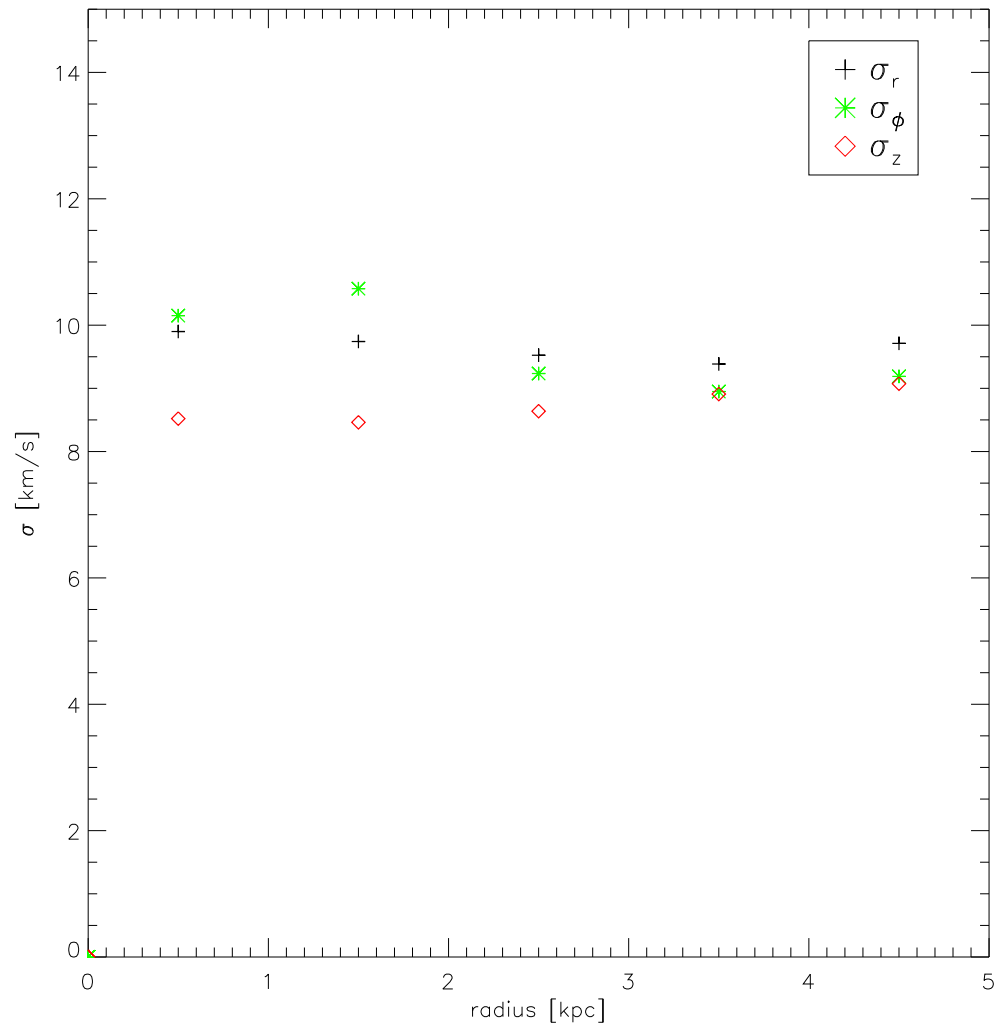


Figure 2.13: Radial (black crosses), azimuthal (green stars), and vertical (red diamonds) velocity dispersions for the simulated HI in nDG1, with the inclusion of thermal broadening of the SPH particles.

## CHAPTER 2

average power in the structure of the ISM on different spatial scales. Figure 2.14 shows the derived power spectra for the simulations DG1, nDG1, and DG1LT, and that for the Small Magellanic Cloud (SMC), re-derived for self-consistency, using the HI datacube of Stanimirovic et al. (1999). Grossly speaking, the distributions can be represented by a power law of the form  $P \propto k^\gamma$ , with  $\gamma = -3.5$  for DG1,  $\gamma = -3.4$  for DG1LT, and  $\gamma = -4.2$  for nDG1, and  $\gamma = -3.2$  for the SMC (consistent with that found originally by Stanimirovic et al. (1999), and consistent with the power spectrum expected when HI density fluctuations dominate the ISM structure, rather than turbulent velocity fluctuations, which dominate the spectrum when isolating ‘thin’ velocity slices).

There are several points to highlight from Fig 2.14: (i) the SMC shows no evidence for departure from a pure power law, and hence there does not appear to be any obvious preferred HI cloud size in nature; (ii) broadly speaking, both DG1 and DG1LT are shallower than nDG1 (i.e., possess more power on smaller scales, rather than larger, relatively speaking); put another way, the enhanced feedback associated with nDG1 shifts power in the simulated ISM from smaller scales to larger scales, just as one might expect; (iii) each of the simulations shows a greater departure from a pure power law, than the SMC does; the most obvious departure from a power law is perhaps seen in the enhanced power on  $\sim 400\text{--}500$  pc scales in nDG1. This enhanced power corresponds to the “radial cadence”, or frequency, of the tightly-wound spiral structure in the inner few kpcs of the simulation (apparent in the right-most panel of Figure 2.3).

Finally, from the present-day moment zero column density map of DG1 (middle panel of Figure 2.3), we identified 13 SNe-driven superbubbles in its cold ISM. While we do not wish to belabour the point when employing such small-number statistics, it is re-assuring to note that upon plotting the superbubble size distribution, the data was consistent with a power law slope between  $-1.5$  and  $-2.0$  (dependent upon

## CHAPTER 2

normalisation). Such slopes are entirely consistent with those observed in nearby dwarfs (Oey & Clarke 1997).

### 2.4.5 DG2 and DG3

#### Simulations

We now increase the sample of dwarf galaxy simulations to include two more, called DG2 and DG3 (Figure 2.15 shows the HI moment zero maps.). Both of these galaxies were run with the same version of the n-body SPH code GASOLINE, as were DG1 and nDG1. These new dwarfs were drawn from same parent cosmological n-body volume as DG1; at  $z=1$ , DG2 and DG3 are separated by  $\sim 770$  pc from one another, a scale comparable to that of, for example, our own Local Group. DG2 was first introduced in Governato et al. (2010), albeit without any significant analysis, while this is the first time DG3 has been discussed.

DG2 and DG3 have a force resolution to match that of DG1 (86 pc), and are both run with a star formation threshold of  $100 \text{ cm}^{-3}$ . The star formation efficiency ( $\epsilon_{\text{SF}}=0.1$ ) and the fraction of supernova (SN) energy coupled to the ISM ( $\epsilon_{\text{SN}}=0.4$ ) are the same values as used for DG1. The luminosity is similar to that of nDG1 and DG1; in the  $r$ -band, DG2 and DG3 have absolute magnitudes of  $-16.1$  and  $-16.7$ , respectively. The present day star formation rates of DG2 and DG3 are  $\sim 0.01 M_{\odot}/\text{yr}$ , roughly twice that of DG1 and nDG1 (Fig 2.16). The star formation history of DG2 is similar to DG1 and nDG1, with most of the star formation occurring in early times followed by long periods with little or no star formation. The majority of the star formation in DG3 occurs at later times. Indeed, little star formation is seen in DG3 before it reaches an age of  $\sim 11$  Gyrs (i.e.,  $z\sim 0.2$ ). At this time, DG3 experiences a strong  $\sim 2$  Gyr burst of star formation.

The stellar masses of the two systems within a 10 kpc sphere are slightly less than those of DG1 and nDG1 ( $4.4 \times 10^8 M_{\odot}$  and  $2.1 \times 10^8 M_{\odot}$ , respectively); DG2

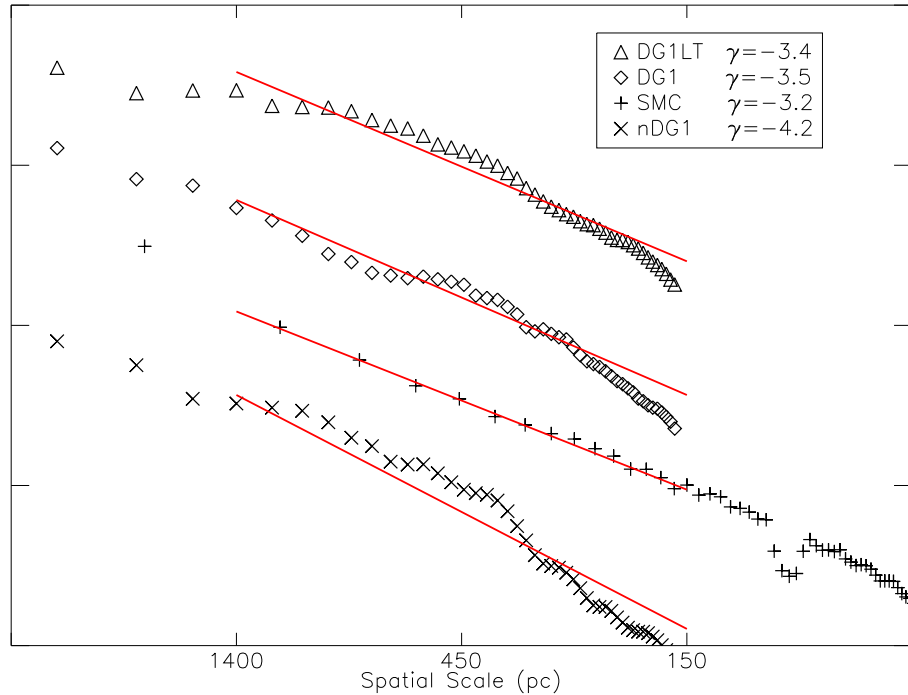


Figure 2.14: Spatial power spectra of the cold ISM of DG1 (diamonds), DG1LT (triangles), nDG1 (crosses), and the SMC (plus signs). Power law slopes of  $-3.5$ ,  $-3.4$ ,  $-4.2$  and  $-3.2$  are overplotted for DG1, DG1LT, nDG1, and the SMC, respectively. The “break” in the SMC power spectrum is due to a missing baseline in the Stanimirovic et al. (1999) ATCA dataset. The power spectra for the three simulations have been truncated at  $\sim 2$  resolution elements ( $2 \times \text{FWHM}$  of the adopted Gaussian beam:  $\sim 200$  pc). Random uncertainties associated with the power at a given spatial scale are smaller than the symbols used, as per the discussion of Stanimirovic et al. (2000). The y axis of the plot shows the relative power, in arbitrary units. The absolute quantities are not important within this work.

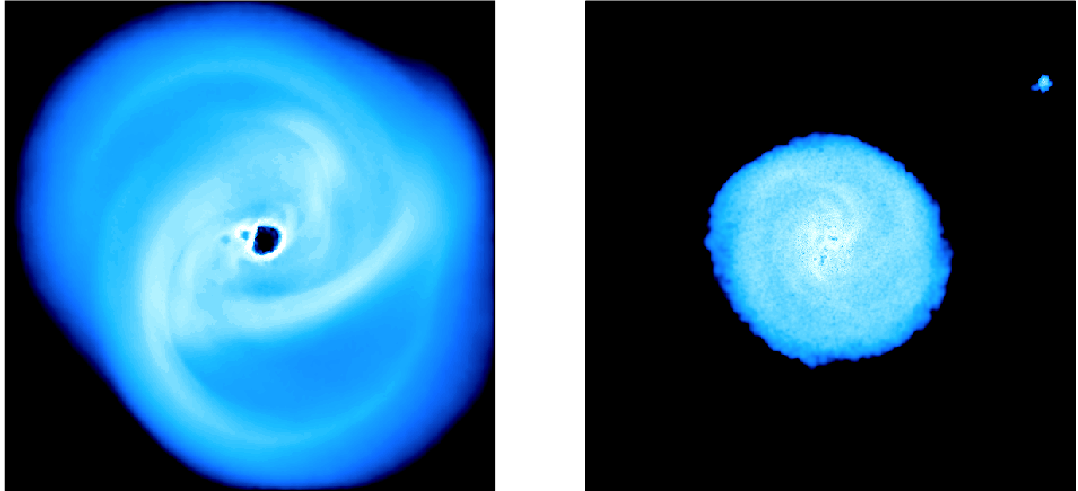


Figure 2.15: The left panel shows the moment zero map for DG2, while the right panel shows that for DG3. Both are viewed face-on and following Fig 2.3, there is a lower column density threshold of  $N(\text{HI})=1\times 10^{19} \text{ cm}^{-2}$  applied to each map. Each panel has dimensions  $14\times 14 \text{ kpc}$ .

has a stellar mass of  $1.85\times 10^8 M_{\odot}$  and DG3 has  $1.83\times 10^8 M_{\odot}$ .

## Results

We first show the stellar and cold gas radial density profiles in Fig 2.17. The fits used to calculate the scale lengths are overplotted in dark purple. DG3 shows a sharp truncation in its cold gas distribution at  $\sim 2.5 \text{ kpc}$ , so its scalelength is reported based upon its fit in the inner 2 kpc. DG2 has a turbulent cold gas disk in its central 2 kpc, as reflected in the structure of the density profile in the inner  $\sim 400 \text{ pc}$ . Recent, multiple, SNe have occurred in the core, causing the gas profile to be modified significantly. Formally, DG2 and DG3 have scalelengths of 2.6 kpc and 1.0 kpc,  $\sim 2\text{--}5\times$  smaller than that found for DG1.

Next, we show the spatial power spectra of DG2 and DG3, compared with data from Stanimirovic et al. (1999) (Fig 2.18). As in Fig 2.14 the simulations shown have been smoothed by a 100pc Gaussian to match the resolution of the observational

## CHAPTER 2

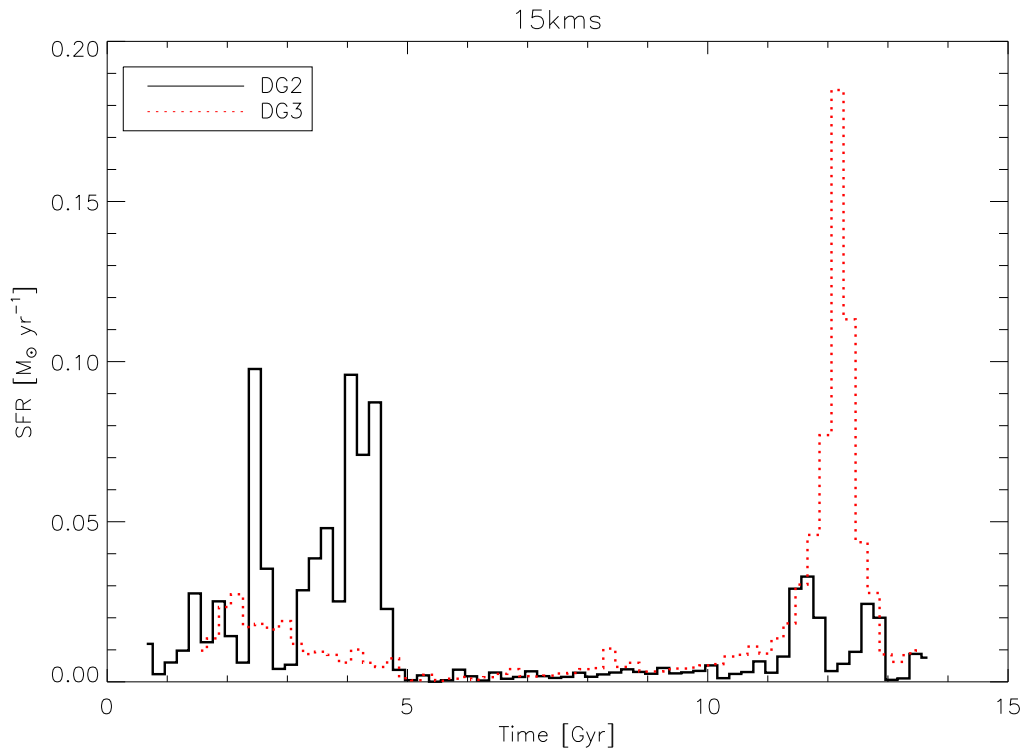


Figure 2.16: The star formation rates of DG2 and DG3 are shown in black (solid) and red (dotted), respectively. Like DG1 and nDG1, the star formation in DG2 is concentrated at early times with the exception of two small bursts occurring near 11 and 12 Gyrs. DG3 shows a very different star formation history than any of the other galaxies, with the majority of the stars formed in a single (recent) burst at  $t \sim 12$  Gyrs.

CHAPTER 2

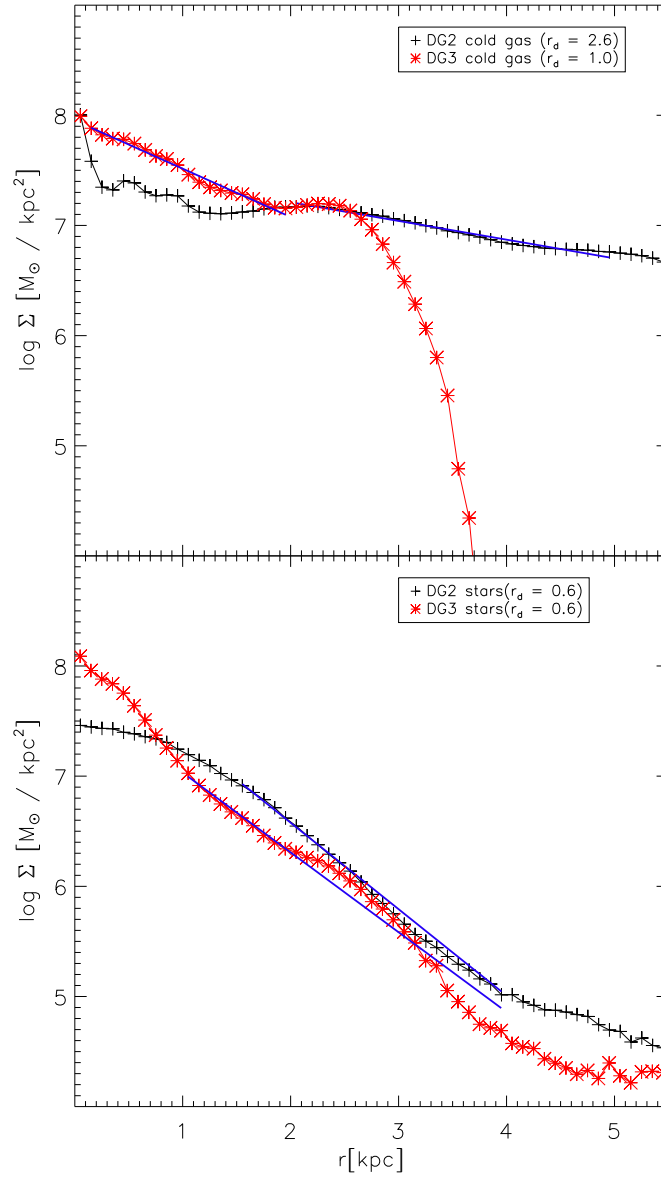


Figure 2.17: Top panel: Cold gas surface density as a function of galactocentric radius for DG2 (black crosses) and DG3 (red asterisks); overplotted in solid purple lines are the lines fitted to derive the scalelength. We find  $r_d \sim 2.6$  kpc and  $\sim 1.0$  kpc for the cold gas scalelengths of DG2 and DG3. Bottom panel: Stellar surface density as a function of galactocentric radius for DG2 (black crosses) and DG3 (red asterisks); overplotted are the fitted regions employed to derive the  $\sim 600$  pc scalelengths quoted in the inset panel.

## CHAPTER 2

data. The method used to produce the power spectra is described in full in §2.4.4. The data is overplotted with a power-law  $P \propto k^\gamma$ , where  $\gamma = -4.1$  and  $\gamma = -3.2$  for DG2 and DG3, respectively. DG3 shows a similar profile to the dwarfs plotted in Fig 2.14 with a similar value of  $\gamma$ ; DG2, however, has a much steeper slope, similar to that seen in nDG1, hence showing more power on large scales. DG2 also shows preferences for ISM scales, as reflected by the more significant deviations from a pure power-law. The number of central SN at this epoch, for DG2, has carved out a significant ‘hole’ at the centre of the galaxy (see Fig 2.15); this has an effect on the power spectrum, as well as on the radial density (Fig 2.17), and the velocity dispersion (Fig 2.19).

Finally, we show the line-of-sight velocity dispersion profiles based on the macroscopic streaming velocities of the SPH particles in Fig 2.19. DG3 shows a profile very similar to that of DG1 and nDG1, with a slight increase in the central regions, but on average the dispersion stays at  $\sim 4$  km/s. DG2, however, shows a very high dispersion in the central regions, out to  $0.5 r_{25}$ . This high dispersion corresponds to the same disruptions shown in the cold gas radial density profile (Fig 2.17). Further away from the central regions of DG2, the velocity dispersion profile decreases slowly at similar values to that found in the other simulations. Following the results of Fig 2.9, it is clear that the inclusion of thermal broadening is necessary to create velocity dispersion profiles of these dwarf galaxies that resemble those seen in nature (at least in their characteristic values, if not their specific radial profile).

## 2.5 Discussion

One immediate concern arising from our analysis relates to the issue of extracting “neutral hydrogen” from the simulations’ “cold gas” (which in some sense consists of both molecular and neutral hydrogen). Because the high-density regions within the simulation have densities more akin to molecular, rather than neutral, clouds,

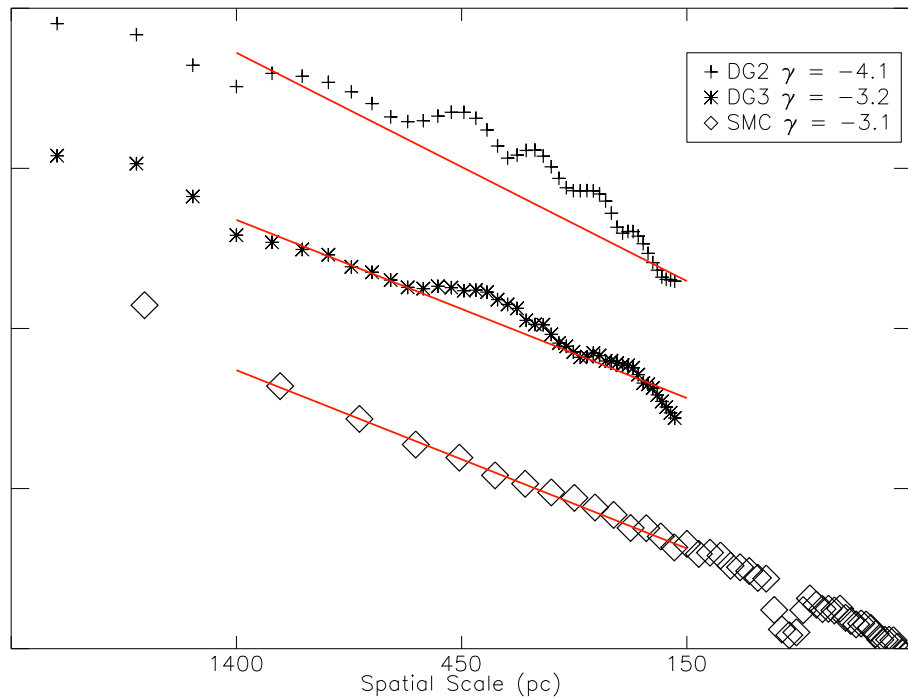


Figure 2.18: Spatial power spectra for the cold IDM of DG2 (crosses), DG3 (asterisks), and the SMC (diamonds). The observational data for the SMC were taken from Stanimirovic et al. (1999); the “break” in their data corresponds to a missing baseline in their observational set-up. Overplotted in red solid lines are the corresponding power laws slopes of  $-3.1$ ,  $-2.2$ , and  $-3.1$ , for DG2, DG3, and the SMC, respectively. The y axis of the plot shows the relative power in arbitrary units. The absolute quantities are not important within this work. The random uncertainties associated with the power at a given spacial scale are much smaller than the symbols used; Stanimirovic et al. (2000) provides a full discussion.

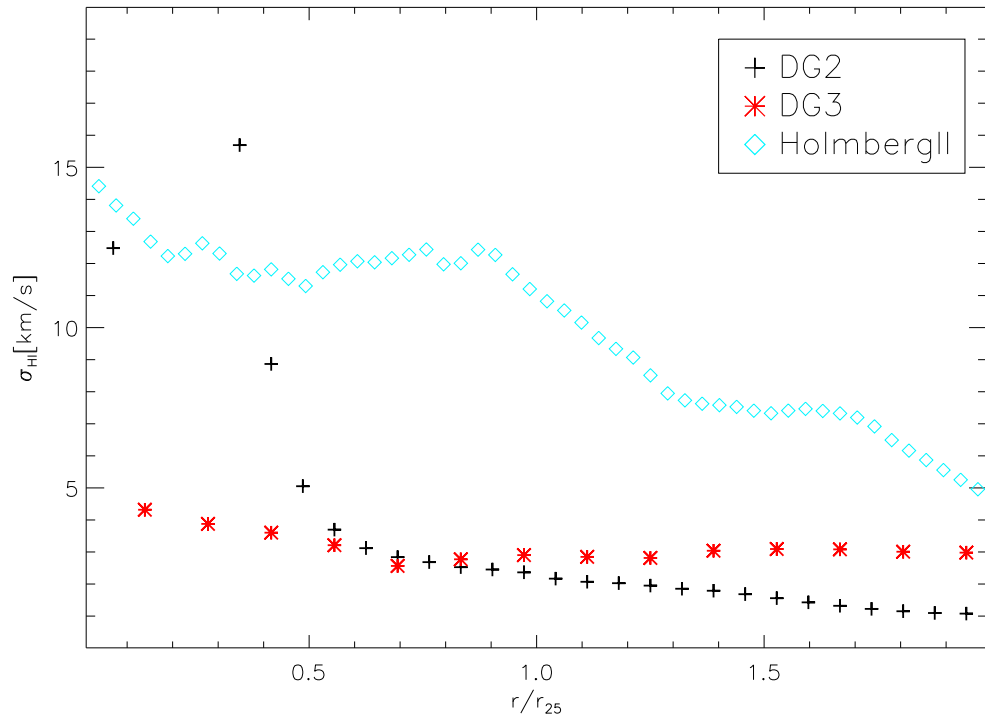


Figure 2.19: Velocity dispersion profiles for DG2 (black crosses), DG3 (red asterix), and Holmberg II (blue diamonds). DG3 shows a very similar profile to that seen in DG1 and nDG1. DG2 shows a large increase in its velocity dispersion near the centre, due to the presence of a large bubble. This profile uses circular annuli to average the velocity dispersion at a given galactocentric radius.  $r_{25}$  is equal to 1.8 kpc and 0.9 kpc in DG2 and DG3, respectively; HoII is as described in Fig 2.9.

## CHAPTER 2

it is important to explore the definition of “neutral” employed here.<sup>10</sup> To do this, we re-generated HI moment maps, but now restricting the gas included to only those particles with densities near the classical value of  $\sim 0.1 \text{ cm}^{-3}$ . As expected, this eliminated the unrealistically high neutral hydrogen column densities in the highest density regions, but at the expense of leading to vertical density profiles that bore little resemblance to the Gaussian profiles observed in nature (O’Brien et al. 2010). Such an extreme “cut” to the definition of neutral hydrogen also led to a radial profile that bore little resemblance to an exponential. We found no density cut which impacted favourably on the observable properties of DG1. For these simulations, because density and temperature are closely correlated in the relevant regime ( $T \leq 30000 \text{ K}$ ;  $\rho \geq 0.001 \text{ cm}^{-3}$ ), the above analysis is degenerate to cuts in volume density or temperature.

It is important to note that the primary process responsible for driving bulk properties in the simulation is the star formation and feedback prescription. Governato et al. (2010) demonstrated that star formation had a larger effect on the rotation curve of our simulated galaxy than resolution (see their Figure 5). The gas properties presented in this chapter are primarily the result of the star formation prescription, and thus it is imperative to use a star formation and feedback prescription that is physically motivated. Until metal-dependent  $\text{H}_2$  creation and cooling is added to the simulations, it is not clear how much HI, as opposed to  $\text{H}_2$ , should be present, how it might be distributed as a function of radius, and what impact it will have on the resulting disk.

After applying the physically-motivated  $\sim 8 \text{ km/s}$  thermal broadening to the Cartesian (velocity) coordinates of the SPH particles’ streaming motion, the inferred *characteristic* velocity dispersions for the cold gas were a reasonable match to those

---

<sup>10</sup>In large part, this was motivated by the fact that in “column density space”, these high-density regions possess column densities close to  $10^{22} \text{ cm}^{-2}$ , higher than those observed in nature; this is a limitation of the conversion employed within GASOLINE.

## CHAPTER 2

observed in nature (albeit, at the unavoidable expense of recovering any correlation between velocity dispersion and galactocentric radius and/or global star formation in the disk, in addition to the imposition of an isotropic velocity ellipsoid to the cold gas, and the young stars which form from this gas). Beyond the aforementioned issue of the lack of a self-consistent treatment of molecular cooling processings on sub-parsec scales, one must also be aware that at the resolutions of these simulations, we are still missing unresolved star forming regions and associated turbulence. The nature of these missing sources is an active area of debate, but magnetorotational instability (MRI) is one of the favoured mechanisms capable of providing a non-negligible amount of turbulence (e.g. Wang & Abel 2009; Piontek & Ostriker 2007; Mac Low 2009)

Enhancing the supernovae energy feedback, as was done for simulation nDG1, at these resolutions, had a marginal impact on the SPH particles' streaming velocities (at the  $\sim 20\%$  level), which in turn meant that its impact on the velocity dispersion profiles was also minimal. This is not surprising, as the increased energy deposition was used in order to offset the effect of the newly included high-temperature metal-line cooling. Without the inclusion of extra SN energy, the additional cooling that comes from metal lines leads to more star formation than in the case of DG1. As shown by Oh et al. (2011), the stellar mass of DG1 is in good agreement with galaxies at similar halo masses, as observed by THINGS. If high-temperature metal-line cooling had been added with  $\epsilon_{\text{SN}}$  held constant, nDG1 would have overproduced stars for galaxies in a comparable halo mass range. However, the enhanced feedback seems to have steepened the spatial power spectrum of the cold ISM of nDG1 relative to DG1, making it less consistent with the power spectrum observed for the SMC. It is unclear, however, how the power spectrum varies with the instantaneous SFR and if this result holds across time. Using the enhanced feedback, did result in significantly reduced flaring showing similar results to observations from O'Brien

## CHAPTER 2

et al. (2010). Capturing all the relevant ISM physics necessary to recover the full spectrum of turbulence sources at pc and sub-pc scales remains an outstanding challenge. Despite these limitations, the simulated dwarf galaxies presented here have been shown to possess bulk characteristics consistent with those observed in nature, including adherence to scaling relations such as the size-luminosity, size-velocity, and luminosity-velocity (Brooks et al. 2011). Additionally, the star formation and feedback prescription used in these simulations has been shown to result in a realistic mass-metallicity relationship (Fig 2.20) as a function of time, and consume gas at a rate that reproduces the incidence rate and metallicities of both QSO-Damped Lyman Alpha (DLA) and GRB-DLA systems (Brooks et al. 2007; Pontzen et al. 2008; Pontzen & Pettini 2009).

In summary, it is clear that the simulations remain extremely successful in recovering many of the *global* optical and dynamical properties of realistic bulgeless dwarfs. That is, although the microphysics of the ISM cannot be fully captured at the force resolutions that must be used currently in cosmological simulations, this does not largely impact the bulk macrophysics such as the rotation curves (stellar and dark matter mass profiles), angular momentum content, etc. On the other hand, we have seen that higher resolutions and adoption of more realistic physics for star formation leads to simulated galaxies that better reproduce the properties of observed galaxies (e.g., Booth et al. 2007; Robertson & Kravtsov 2008; Tasker & Bryan 2008; Saitoh et al. 2008; Ceverino & Klypin 2009; Governato et al. 2010). The work presented here highlights paths for future improvement in the implementation of ISM physics in cosmological simulations, and provides useful tests for reassessment once (for example) metal-dependent  $H_2$  cooling has been added to GASOLINE and other cosmological simulation codes.

## 2.6 Chemistry of Dwarf Galaxies

### 2.6.1 Introduction

Studying the chemical evolution of the Universe and its constituents allows one to associate the elemental abundance patterns we see today with the primordial composition resulting from Big Bang Nucleosynthesis (BBN) convolved with multiple generations of star formation, stellar nucleosynthesis, and stellar death (in the form of massive Type II supernovae, binary Type Ia supernovae, and asymptotic giant branch/planetary nebulae progenitors), as well as the associated gas infall and merger histories of galaxies.

Elemental chemical evolution within hydrodynamical simulations, taking into account the different stellar lifetimes and nuclear burning processes as a function of initial mass, has only been feasible for  $\sim 15$  years, commencing with the work of Raiteri et al. (1996b). Their study included, for the first time, oxygen and iron (i.e., SNeII and SNeIa), and their pollution of the ISM on different timescales. With the advent of large, high-resolution, spectroscopic surveys of Local Group dwarfs (e.g., DART), over the past five years, we now finally have a wealth of empirical chemical (and kinematic) stellar data against which to compare such chemodynamical models.

Local Group dwarfs have been subject to many investigations to determine their chemical abundances. One of the earliest attempts from Canterna (1975), using photometric abundance determinations of four stars in the Draco dSph, found  $[\text{Fe}/\text{H}]$  values to range from  $\sim -2.1$  to  $\sim -3.2$  dex. Shetrone et al. (1998) found  $[\text{Fe}/\text{H}]$  values to range from  $\sim -1.5$  to  $\sim -3.0$  using high dispersion spectra of four giants. Of the four stars, Shetrone et al. (1998) found one to have abundances of the  $\alpha$ -elements<sup>11</sup> different to those found in the Galactic halo. Due to the small sample of stars, no firm (statistical) conclusions could be drawn. Subsequent to this, Shetrone et al.

---

<sup>11</sup>The generic term used to identify elements which result from nuclear fusion involving  $\alpha$ -particles - i.e., helium nuclei.

## CHAPTER 2

(2001), working with a larger sample of stars spanning three Local Group dwarfs, found the  $[\alpha/\text{Fe}]$  to be  $\sim 0.2$  dex *lower* in the dwarf galaxies.

The two (claimed) chemical differences between the Galactic halo and the Local Group dwarfs studied in the most depth are: (i) in the mean, a lower  $[\alpha/\text{Fe}]$  in dSphs relative to the halo, at the same  $[\text{Fe}/\text{H}]$ , and (ii) the presence of stars with  $[\text{Fe}/\text{H}] < -3$  in the Galactic halo (Ryan & Norris 1991), but not (apparently) in dSphs (Helmi et al. 2006). These two points appear to be supported by many observations (e.g. Tolstoy et al. 2003; Venn et al. 2004; Aoki et al. 2009), although it is also the case that a range of  $[\alpha/\text{Fe}]$  is encountered in any given dwarf galaxy, such that there is some overlap in the patterns seen in the Galactic halo and (some stars in) dwarfs (McWilliam et al. 1995; Cohen & Huang 2009, 2010). What the observations do imply though is the fact that the Galactic halo could not have formed simply from mergers of galaxies like the present-day Local Group dSphs, as originally thought (e.g. Searle & Zinn 1978; White & Rees 1978). The galaxy halo must have formed from dwarf building blocks, but presumably ones which possessed different abundance patterns to those seen in dwarfs today.

Both classical analytical models representative of chemical evolution in a “closed-box” and full chemodynamical simulations have suffered from an overproduction of metal-poor stars relative to those observed in nature - a manifestation of the so-called “G-dwarf problem”. Recently though, Frebel et al. (2010) discovered an extremely metal-poor star in the Sculptor dSph. It was found to have  $[\text{Fe}/\text{H}] = -3.81$  and element ratios similar to those found in the Galactic halo, consistent with the metal-poor stars found in several of the Milky Way’s ultra-faint dSphs ( $M_B < -8$ ). The discovery of these metal poor stars does not solve the G-dwarf problem, but do suggest that we have not fully characterised the distribution of extremely metal-poor stars in Local Group dwarfs.

Ultra-faint dSphs seem to possess metallicity distribution functions unlike the

## CHAPTER 2

classic dwarfs but similar to that of the Galactic halo (Kirby et al. 2008), leading to the conclusion that they were perhaps the missing piece of the puzzle, and ultimately responsible for the shape and population of the metal-poor tail of the Galactic halo's distribution function.

The simulations analysed in the following work track oxygen, iron, and a proxy for total metallicity ( $Z$ , where  $Z=O+Fe$ , here). The oxygen (the representative, and dominant,  $\alpha$ -element) and iron tracked comes from SNeII and SNeIa explosions. For SNeIa, the Thielemann et al. (1986) tables are followed with  $0.63 M_{\odot}$  ( $0.13 M_{\odot}$ ) of iron (oxygen) ejected per SNIa event. The oxygen and iron yields from SNeII are taken from the  $Z=Z_{\odot}$  grid of models from Woosley & Weaver (1995), as parametrised by Raiteri et al. (1996b). The implementation of metals within GASOLINE is discussed further in chapters 4 and 3.

### 2.6.2 The Mass-Metallicity relation

Lequeux et al. (1979) found that with increasing mass in irregular galaxies, the metallicity also increased, concluding that the higher star formation rate of the more massive galaxies resulted in more significant chemical enrichment. This formed the basis of what is now known as the luminosity-metallicity relation. As observational data has grown, the relation has only become more apparent (e.g. Zahid et al. 2011), and been extended to include more morphological types (Pilyugin & Ferrini 2000; Lee et al. 2006).

Stellar mass and metallicity are important factors in understanding the chemical evolution of a galaxy. Stellar winds and supernovae, along with inflows and outflows of gas, all affect the overall gas phase metallicity. Understanding why dwarf galaxies have a lower metallicity than more massive galaxies is a debated point. There are three main physical processes at present used to describe the differences observed: first, it was concluded in Tremonti et al. (2004) that low mass galaxies have lower

## CHAPTER 2

metallicities due to the shallow potential wells, making large outflows of metal enriched gas more common. This is in contrast to higher mass galaxies where the gas is retained and re-used to enrich the ISM. Outflows of gas have been predicted since Mathews & Baker (1971) used them to explain the lack of gas in elliptical galaxies. They were later used to explain the mass-metallicity relation by Larson (1974). Gas outflows have now been confirmed by many observational studies (e.g. Heckman et al. 2000; Martin et al. 2002).

Second, lower mass galaxies may be more metal poor because they are inefficient at converting gas into stars and are as a consequence less evolved. This has been suggested to account for the scatter seen in the mass-metallicity relation in lower mass galaxies (Lee et al. 2006), which was not readily explained simply by gas outflows. Brooks et al. (2007) found with cosmological N-body + SPH simulations that the lower oxygen abundances in the low mass galaxies were due mainly to the star formation efficiency, rather than a direct consequence of gas outflows; similar conclusions were drawn by de Rossi et al. (2007).

Thirdly, Köppen et al. (2007) concluded that lower mass galaxies may need a different initial mass function to describe their observed stellar populations. Varying the IMF in order to suppress the relative proportion of massive-to-lower mass stars reduced the SNeII rate, and consequently the oxygen abundance. By doing so, they found good agreement with the mass-metallicity relation in dwarf galaxies, and were able to explain the scatter associated with the Lee et al. (2006) sample.

We now show where the Governato et al. (2010) dwarfs (nDG1, DG1, DG1LT, DG2 and DG3) lie on the mass-metallicity and luminosity metallicity relations (Figs. 2.20 and 2.21). Table 2.1 lists the relevant data for the simulations. The properties of all the simulations are given in §2.3.1 and §2.4.5.

The simulations are consistent with the mass-metallicity trend, in the sense of

CHAPTER 2

Galaxy	$M_g$	Radius (kpc)	$\log(M/M_\odot)$	$12+\log(O/H)$
nDG1	-15.42	2.3	8.15	7.50
DG1	-16.04	2.2	8.42	7.64
DG1LT	-18.62	1.6	9.40	8.35
DG2	-15.68	1.2	8.08	7.42
DG3	-16.32	1.6	8.09	7.83

Table 2.1: Relevant integrated data for the Governato et al. (2010) simulated dwarfs employed here. Column one lists the absolute SDSS  $g$ -band magnitude; column two the radius encapsulating two thirds of the stellar mass; column three the stellar mass; and column four, the gas phase oxygen abundance.

the metallicities being lower for the low stellar mass dwarfs. The observational data from Fig 2.20 is taken from Tremonti et al. (2004). This includes  $\sim 53000$  star forming SDSS galaxies, all at low redshift. Figure 2.20 shows the median of the SDSS sample, accompanied by two “flanking” contours encapsulating 68% and 95% of the data points, respectively. The method used by Tremonti et al. (2004) for determining oxygen abundances is known to be an overestimate of the true value. This was noted by Erb et al. (2006) and Brooks et al. (2007), and in order to be consistent with these latter studies, we shift the SDSS data downwards by 0.26 dex.

Following Brooks et al. (2007), the stellar mass used is two thirds that of the total stellar mass and the oxygen abundances are derived from “cool” gas ( $T < 40000$  K) situated within the radius encompassing two thirds of the stellar mass. The luminosity of the simulations in any given bandpass was calculated using SUNRISE (Jonsson et al. 2010), a dusty radiative transfer code used to produce simulated observations from SPH codes. Simulated SDSS filters are used to give results that can be compared directly with observations. GASOLINE does not track total hydrogen or helium, directly, so their abundances are inferred using the relations  $Y = Y_p + (\Delta Y / \Delta Z)Z$  and  $X = 1 - Y - Z$ , where, following Jimenez et al. (2003),  $\Delta Y / \Delta Z = 2.1$  and the primordial

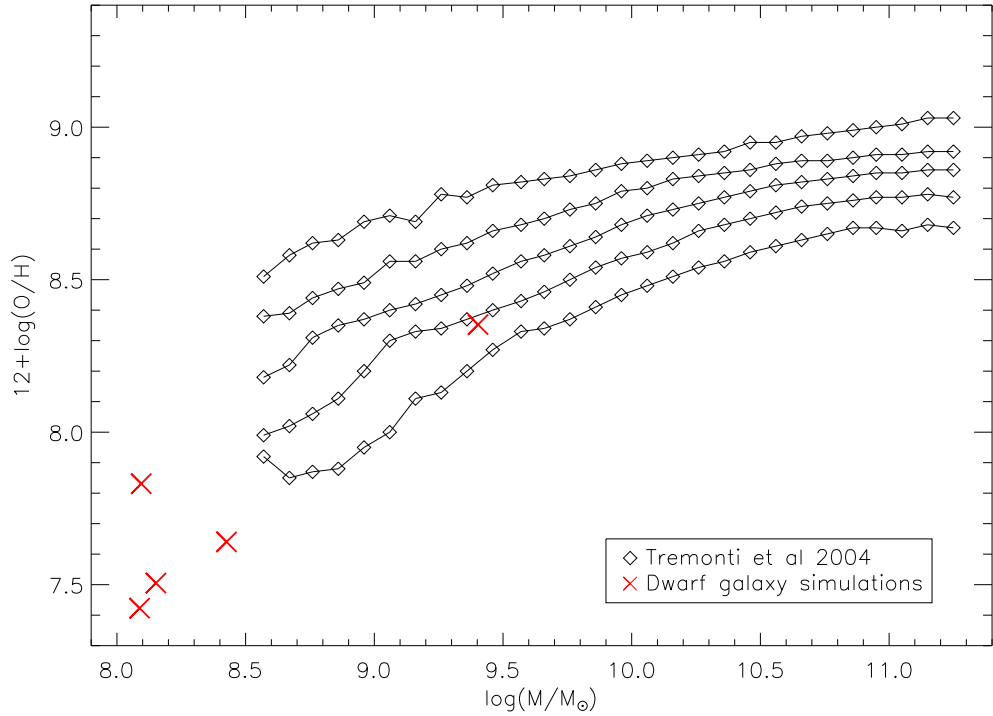


Figure 2.20: The present-day mass-metallicity relation. Plotted is the stellar mass against the gas phase oxygen abundance. Observational data is taken from Tremonti et al. (2004). The central contour corresponds to the median of the SDSS data, while the flanking contours correspond to the encapsulation of 68% and 95% of the data, respectively. Overplotted in red are our five dwarf galaxy simulations. After Erb et al. (2006), the observational data has been reduced in metallicity by 0.26 dex.

helium abundance  $Y_p$  is 0.236.

Due to the difficulties of observationally inferring a galaxy's stellar mass, luminosity is often used as a proxy (Skillman et al. 1989). Observational data is widely available for the resulting luminosity-metallicity relation; here in Fig 2.21, observational data is taken from Guseva et al. (2009), combining a number of relevant sources (each of which are referenced with inset to Fig 2.21). Included are  $\sim 9000$  galaxies spanning a 8 mags in luminosity in the SDSS  $g$ -band and a factor of  $\sim 100$  in oxygen abundance ( $\sim 2$  dex).

## CHAPTER 2

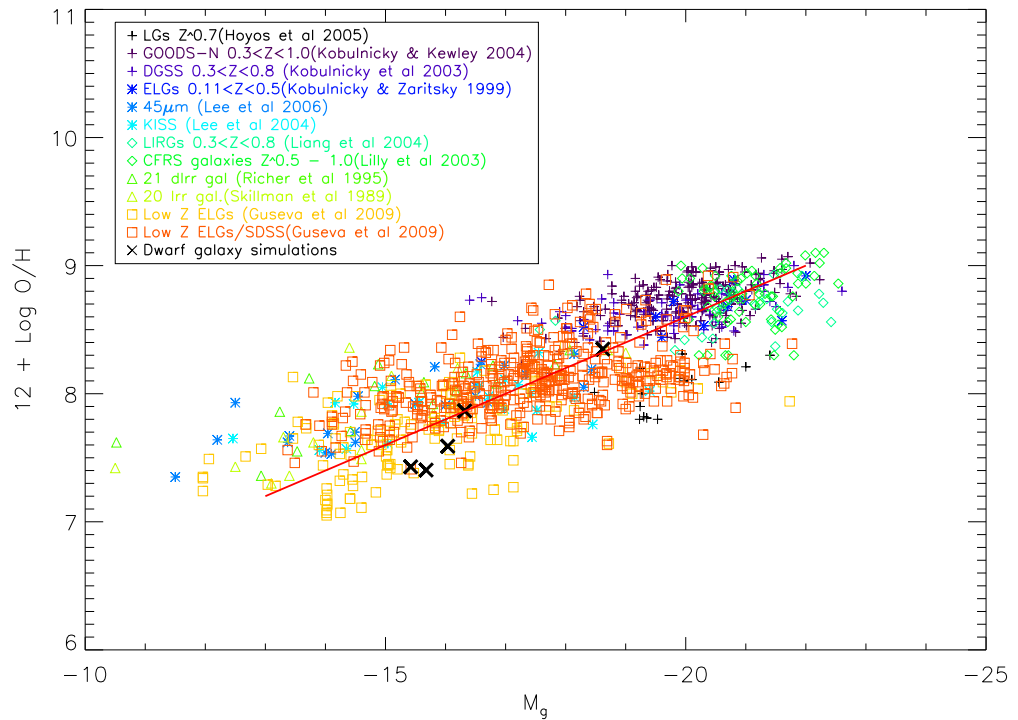


Figure 2.21: The luminosity-metallicity relation. Shown is the gas-phase oxygen abundance versus the integrated absolute magnitude in the SDSS  $g$ -band; data has been extracted from the compilation of Guseva et al. (2009). Overplotted in larger black crosses are our five dwarf galaxy simulations. The solid red line shows the least squares fit to all of the observational data.

## CHAPTER 2

We find the simulations lie on the luminosity-metallicity relation. DG2 sits the furthest away from the least squares fit but is still well within the scatter. For their stellar mass though, the simulations sit somewhat low on the extrapolation of the mass-metallicity relation, although any conclusion based upon such an extrapolation should be viewed with caution. Increasing the supernova feedback, as was done for nDG1, resulted in a lowering of the overall stellar mass and gas phase oxygen abundance.

More recent observational data from Zahid et al. (2011) shows a sample of 1348 galaxies, from which the redshift  $z\sim 0.8$  mass-metallicity and luminosity-metallicity relations have been derived. At a given stellar mass (or luminosity), the galaxies at  $z\sim 0.8$  are on average,  $\sim 0.2$  dex lower in gas-phase oxygen abundance, relative to their  $z\sim 0.1$  counterparts (Tremonti et al. 2004). It would be useful to examine the location of our five cosmological dwarfs on the mass-metallicity and luminosity-metallicity relations at  $z\sim 0.8$ , in order to compare with the new (Zahid et al. 2011) dataset, to confirm if the time evolution of the oxygen abundances match that observed.

### 2.6.3 MDFs

We now look at the metallicity distribution function (MDF) for each of the simulations. In particular, Figure 2.22 shows each of the derived  $[\text{Fe}/\text{H}]$  MDFs, making use of all the stars present in a 5 kpc sphere centred on the galaxy. Discrete ‘peaks’ in each MDF are apparent, where an enhancement in the number of stars in a specific metallicity ‘bin’ has occurred. nDG1 is perhaps the least susceptible to the appearance of such ‘binning’. Such peaks are not readily apparent in observational datasets, but in the latter cases, the uncertainty in the  $[\text{Fe}/\text{H}]$  determinations is of the order 0.1–0.2 dex, and so the simulated MDFs should be post-processed by convolving their intrinsic profile with a Gaussian of dispersion 0.1–0.2 dex; this is

## CHAPTER 2

examined in detail in Chapter 3.

The peaks seen in the simulations' MDFs (Fig 2.22) can be related back to the underlying age-metallicity relations (Fig 2.26). For example, take DG3; this MDF shows two very clear peaks, one centered near  $[\text{Fe}/\text{H}]\approx-0.75$  and the other centered near  $\sim-1.5$ . Looking at the age-metallicity relation of DG3, one can see immediately that for most of its evolution, stars are produced with metallicities near  $-0.75$ , which corresponds to the largest peak. However, near time  $t\sim 11$  Gyr, there is a significant infall of lower metallicity gas, resulting in the formation of the secondary peak in the MDF (as shown in Fig 2.26), but at a *lower* metallicity of  $[\text{Fe}/\text{H}]\approx-1.5$ . This surprising result (lower metallicities occurring at *later* times) will also be discussed in detail in Chapter 3.

Using the MDFs shown in Figure 2.22 we now show the cumulative MDFs (Fig 2.23), in this case, isolating the extreme metal-poor tail ( $-4.5 < [\text{Fe}/\text{H}] < -2.0$ ). Each of the MDFs has been normalised to unity at  $[\text{Fe}/\text{H}]=-2.3$ , to match the observational data for the Galactic halo and Local Group dSphs (symbols, as noted in the inset to the figure).

The observational data in Fig 2.23 are taken from Schörck et al. (2009); the data represents the Galactic halo and a sample from the DART dataset. We can see immediately that *all* of the simulations possess significantly larger fractions of extremely metal-poor stars than observed in comparable systems in nature. It is interesting to note that DG1LT, despite its inherent problems elsewhere, predicts (approximately) an order of magnitude fewer metal poor stars than the other simulations. The main (numerical) parameter controlling the production of metal-poor stars within these simulations is the diffusion coefficient. We return to this 'metal-poor star overproduction' issue specifically in Chapter 3.

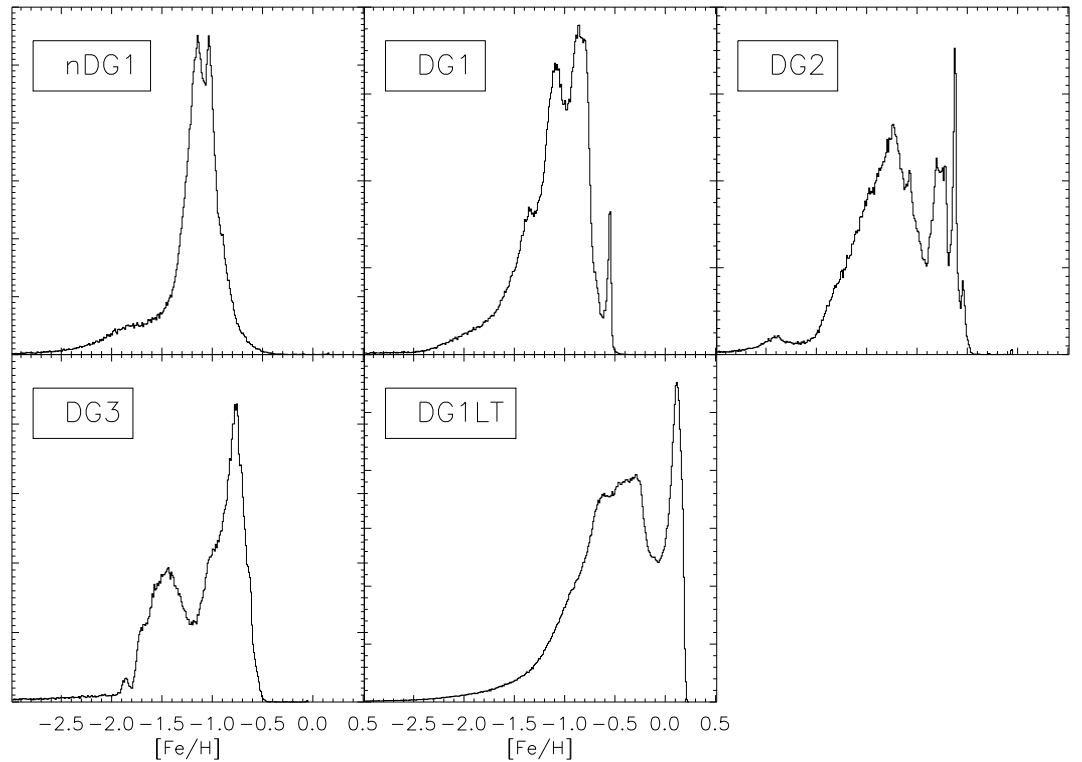


Figure 2.22: The metallicity distribution functions (MDFs) for the Governato et al. (2010) simulated dwarf galaxies. All stars within a 5 kpc sphere centred on the galaxy are plotted. The MDFs show ‘preferred’ peaks in the number of stars at specific values of  $[\text{Fe}/\text{H}]$  which, in some cases, appears to be physical (eg. driven by a flat age-metallicity relation) and in others, appears to be numerical (eg. a density-metallicity relation appears at late-times within the gas phases of some of the simulations).

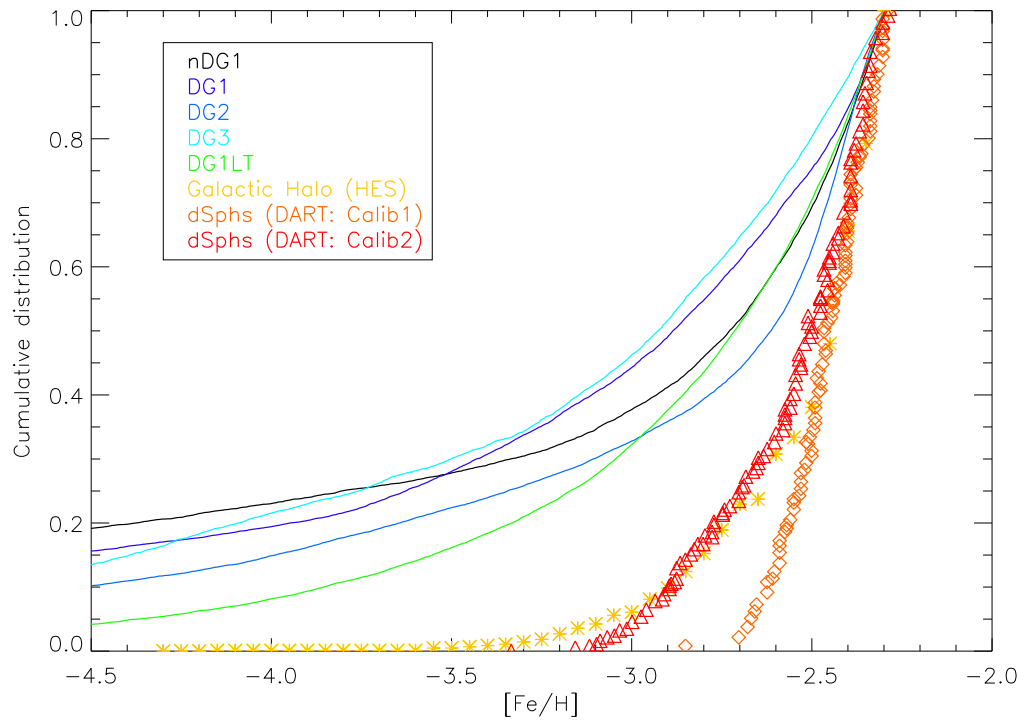


Figure 2.23: Cumulative MDFs (for  $[\text{Fe}/\text{H}]$ ) isolating the metal-poor tail. Observational data is taken from Schörck et al. (2009) (their Fig 18). The DART data (red triangles and orange diamonds) is a combined cumulative MDF for Carina, Sextans, and Sculptor: Calib 2 (red triangles) adopts the Ca-to-Fe calibration described in Winnick (2003). HES (Hamburg/ESO survey) data for the metal poor stars present in the Galactic halo are shown by yellow asterisk. These observational results are compared to nDG1, DG1, DG2, DG3, and DG1LT.

## CHAPTER 2

### Abundance Ratios

We next show the abundance ratios for the dwarf simulations, specifically the ratio of  $[\text{O}/\text{Fe}]$  vs  $[\text{Fe}/\text{H}]$  trend at  $z=0$  for each of the five cosmological dwarfs. Observationally, such abundance ratios are used to infer the star formation histories of a system, as oxygen is tied to short-lived SNeII while the lower-mass stars in binary SNeIa progenitors are longer-lived, thereby providing something of a clock for star formation timescales. What this means is that in early times, the SNeII will dominate and the ratio of  $[\text{O}/\text{Fe}]$  should be high and then show a decrease with increasing  $[\text{Fe}/\text{H}]$  as more and more SNeIa affect the iron abundance. This trend was first explained in Tinsley (1979) and since then has been employed repeatedly throughout the Milky Way and in external systems. We see such trends, broadly speaking, in the simulations, although the point at which the decline from the higher  $[\text{O}/\text{Fe}]$  ‘plateau’ does not always occur at the same  $[\text{Fe}/\text{H}]$ ; that said, these dwarfs are not expected to show the same absolute trend as the Milky Way, but should better reflect the behaviour seen in, for example, the DART data.

First, Figure 2.24 shows the behaviour of  $[\text{O}/\text{Fe}]$  as a function of  $[\text{Fe}/\text{H}]$ , again for the stars which lie within the central 4 kpc of the galaxy. Overplotted, again not because it is supposed to be a true analog of nDG1 but because it provides a useful benchmark, are the  $[\alpha/\text{Fe}]$ -  $[\text{Fe}/\text{H}]$  data (plus signs) for the Local Group dwarfs, Sculptor, Carina, Fornax, and Sagittarius. The distribution of the residuals in  $[\text{O}/\text{Fe}]$  about the best-fit lines through the Sculptor and nDG1 datasets are both consistent with intrinsic scatters of  $\sim 0.13$  dex. For nDG1, this scatter varies somewhat with metallicity, with the scatter in the  $[\text{O}/\text{Fe}]$  residuals for stars near  $[\text{Fe}/\text{H}] \approx -1$  being  $\sim 0.1$  dex, while those with  $[\text{Fe}/\text{H}] < -1.5$  show a scatter closer to  $\sim 0.2$  dex. To first order though, it would suggest that the adopted magnitude of metal diffusion employed was reasonable. Again, the issues surrounding diffusion will be discussed in Chapter 3

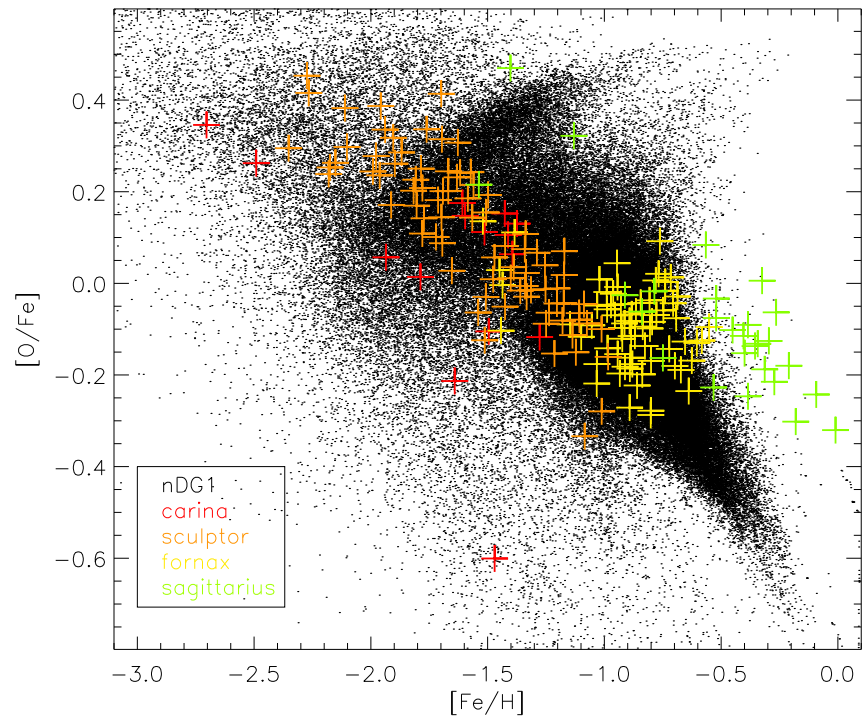


Figure 2.24: The abundance ratio  $[O/Fe]$  of nDG1 stars, compared with observational data from Carina (red), Fornax (orange), Sculptor (yellow) and Sagittarius (green), taken from Tolstoy et al. (2009).

## CHAPTER 2

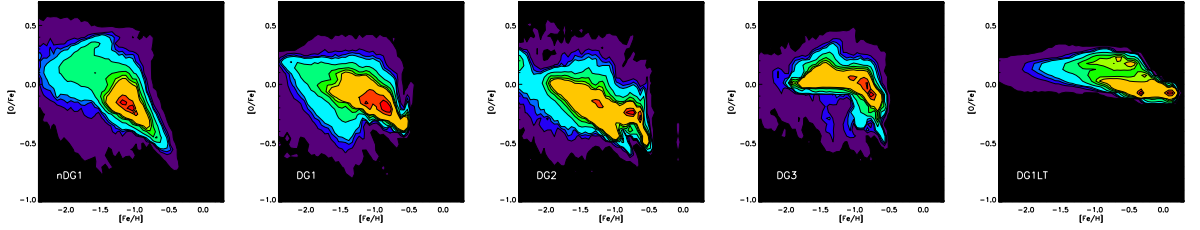


Figure 2.25: The abundance ratio  $[O/Fe]$  versus  $[Fe/H]$  for all the stars within a 5 kpc sphere centred on each dwarf. Shown from left to right are nDG1, DG1, DG2, DG3, and DG1LT. Contours show the regions with the highest density of stars in red, and lowest in purple.

Figure 2.25 shows  $[O/Fe]$  against  $[Fe/H]$  for the stars associated with the five simulated dwarfs. The redder contours indicate the regions with the highest stellar density. nDG1, DG1, and DG2 show a clear decline in  $[O/Fe]$  immediately (starting at  $[Fe/H] \approx -2$ ), whereas DG3 shows a flat profile until  $[Fe/H]$  reaches  $\sim -1.0$ , and DG1LT shows an almost constant value of  $[O/Fe]$  for all metallicities. For DG1LT, it is noticeable that there is much less spread in  $[O/Fe]$ . The dispersion in  $[O/Fe]$  at a given  $[Fe/H]$  should provide an important constraint on the magnitude of metal diffusion within chemodynamical simulations (whether they be ours described here, or any others in the literature).

We next show the age-metallicity plots for the simulations (Fig 2.26); again, the contours corresponding to the most populated regions are shown in red, and the least populated regions in blue. Each of the simulations shows a similar early evolution in metallicity, from ‘low’ to ‘high’  $[Fe/H]$  values in the first  $\sim 2$  Gyrs. At present the only observational age-metallicity relations (particularly for dwarf galaxies) are very poorly populated (e.g., bottom right panel of Fig 3.4), making it difficult to compare with extant data (although this will certainly change in the future). This issue will be addressed in more detail in Chapter 3.

## CHAPTER 2

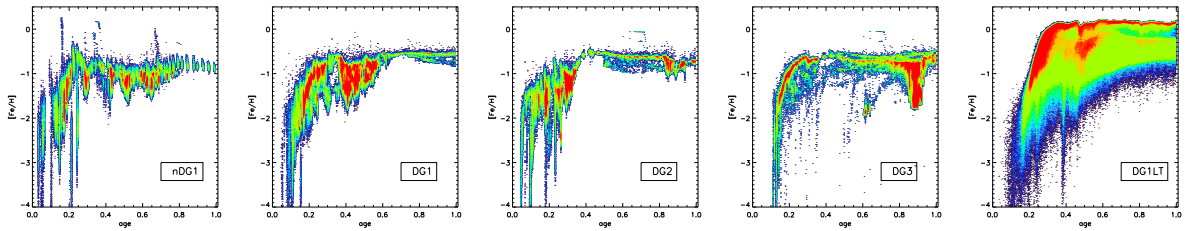


Figure 2.26: Age-metallicity relations for the dwarf simulations employed here. Age is plotted along the abscissa, normalised to unity (which itself corresponds to 13.7 Gyrs in cosmic time). Contours correspond to the number density of stars present in each bin, with the redder regions associated with the most populated regions of age-metallicity space. From left to right, the plot shows the simulations nDG1, DG1, DG2, DG3, and DG1LT.

## 2.7 Summary

Section 2.6 has looked into the chemical properties of the Governato et al. (2010) dwarfs to complement the analysis of their cold gas. These simulations have been shown to agree well with the mass-metallicity relation (Fig 2.20) and the luminosity-metallicity relation (Fig 2.21) but this does not necessarily mean they are correct. The MDFs of each of the simulations agree well with observations (e.g. Kirby et al. 2011a) apart from the (apparent) peaks they show; smoothing the theoretical MDFs with typical empirical uncertainties will ameliorate this issue (a point to which we return later). In this chapter, we have not smoothed with the relevant empirical uncertainty, in order to better associate the MDF peaks with their relevant origin in the corresponding age-metallicity relation.

All of the simulations show an overproduction of metal poor stars compared to data from Schörck et al. (2009); this might lead one to believe that diffusion is too low within the simulations (i.e., how easily metals are spread from one SPH particle to its neighbours). This is one of the tests we will undertake in Chapter 3. The abundance ratios agree well with data from Tolstoy et al. (2009). As always, more

## CHAPTER 2

observational points would be of benefit to this work so the scatter could correctly be constrained.

This section transitions naturally into a more detailed study of the issues outlined here, where a relevant parameter study will be undertaken, in order to quantify the impact of sub-grid physics on the resulting chemistry of the simulated galaxies.

# Chapter 3

## The Distribution of Metals in Cosmological Simulations of Dwarf Disc Galaxies

### 3.1 Abstract

Here, we examine the chemical properties of five cosmological hydrodynamical simulations of an M33-like disc galaxy which have been shown previously (Brook et al. 2012b) to be consistent with the morphological characteristics and bulk scaling relations expected of late-type spirals. These simulations are part of the Making Galaxies In a Cosmological Context (MaGICC) Project, in which stellar feedback is tuned to match the stellar mass – halo mass relationship. Each realisation employed identical initial conditions and assembly histories, but differed from one another in their underlying baryonic physics prescriptions, including (a) the efficiency with which each supernova energy couples to the surrounding interstellar medium, (b) the impact of feedback associated with massive star radiation pressure, (c) the role of the minimum shut-off time for radiative cooling of Type II supernovae remnants,

## CHAPTER 3

(d) the treatment of metal diffusion, and (e) varying the initial mass function. Our analysis focusses on the resulting stellar metallicity distribution functions (MDFs) in each simulated (analogous) ‘solar neighbourhood’ (2–3 disc scalelengths from the galactic centre) and central ‘bulge’ region. We compare and contrast the simulated MDFs’ skewness, kurtosis, and dispersion (inter-quartile, inter-decile, inter-centile, and inter-tenth-percentile regions) with that of the empirical solar neighbourhood MDF and Local Group dwarf galaxies. We find that the MDFs of the simulated discs are more negatively skewed, with higher kurtosis, than those observed locally in the Milky Way and local group dwarfs. We can trace this difference to the simulations’ very tight and correlated age-metallicity relations (compared with that of the Milky Way’s solar neighbourhood), suggesting that these relations within ‘dwarf’ discs might be steeper than in  $L_*$  discs (consistent with the simulations’ star formation histories and extant empirical data) and/or the degree of stellar orbital re-distribution and migration inferred locally has not been captured in their entirety, at the resolution of our simulations. The important role of metal diffusion in ameliorating the over-production of extremely metal-poor stars is highlighted.

### 3.2 Introduction

The relative number of stars of a given metallicity in a given environment, whether it be the local stellar disc, central spheroid/bulge, and or baryonic halo – the so-called metallicity distribution function (MDF) – has embedded within it, the time evolution of a system’s star formation, assembly/infall, and outflow history, all convolved with the initial mass function (IMF) (Tinsley 1980). Seminal reviews of the diagnostic power of the MDF include those of Haywood (2001) and Caimmi (2008).

Well in advance of our now empirical appreciation of (a) the hierarchical assembly of galaxies from sub-galactic units, (b) the ongoing infall of fresh material from halos to discs (e.g. High-Velocity Clouds: Gibson et al. (2001)), and (c) the

## CHAPTER 3

ongoing outflow of enriched material from discs via stellar- and supernovae-driven winds/fountains (e.g. McClure-Griffiths et al. 2006), it was recognised that the local MDF provided crucial evidence that the Milky Way (and presumably galaxies as a whole) did not behave as a ‘closed-box’, in an evolutionary sense (Pagel & Patchett 1975).

This latter recognition was perhaps best manifest in what became known as the ‘G-dwarf Problem’ (Hartwick 1976); specifically, a simple model in which gas was not allowed to infall or outflow from the system would necessarily lead to a significant population of long-lived, low metallicity, stars in the solar neighbourhood, with  $\sim 20\%$  of the stars locally predicted to possess metallicities below  $[\text{Fe}/\text{H}] \approx -1$  (Tinsley 1980). In nature, such a population is not observed, with the empirical fraction of local low-metallicity stars being  $\sim 2$  orders of magnitude smaller than the aforementioned closed-box predictions (e.g. Kotoneva et al. 2002; Casagrande et al. 2011).

Since this recognition of its fundamental importance, the MDF has acted as one of the primary constraints / boundary conditions against which all analytical (e.g. Schörck et al. 2009; Kirby et al. 2011a), semi-numerical (e.g. Chiappini et al. 2001; Fenner & Gibson 2003), and chemo-dynamical (e.g. Roškar et al. 2008; Sánchez-Blázquez et al. 2009; Tissera et al. 2012; Calura et al. 2012) models are compared.

From a chemo-dynamical perspective, recent work has focused on the sensitivity of global metal re-distribution to different physical prescriptions, within the context of the OWLS project (Wiersma et al. 2011); at higher redshift, a similar, equally comprehensive, study was undertaken by Sommer-Larsen & Fynbo (2008). In both cases, the emphasis was placed on the whereabouts of the ‘missing metals’ – i.e., metals thought to reside in the Warm-Hot Intergalactic Medium (WHIM) and/or halos of massive galaxies, but have thus far proven challenging to detect directly.<sup>1</sup>

---

<sup>1</sup>Tumlinson et al. (2011) is an example of recent efforts, though, to characterise the properties of these difficult-to-observe baryon reservoirs.

## CHAPTER 3

While not fully cosmological, the reader is also referred to the chemo-dynamical work of Kobayashi & Nakasato (2011), for a complementary analysis of a simulated Milky Way-like system.

Each of the above chemo-dynamical studies examines cursory aspects of the MDF ‘constraint’, but the focus for each was never meant to be a comprehensive analysis of the dispersion and higher-order moments of the shape characteristics,<sup>2</sup> nor their link to the associated age-metallicity relations, star formation histories, and putative G-dwarf problem; such higher-order moments include the MDF skewness, kurtosis, and inter-quartile, inter-decile, inter-centile, and inter-tenth-percentile regions.

The skewness of an MDF can be a reflection of both the classical G-dwarf problem and the slope of the age-metallicity relation (AMR); kurtosis is often thought of as being a measure of the ‘peakedness’ of the MDF (e.g., by how much the peak is ‘flatter’ or ‘peakier’ than a Gaussian), while in practice it is often more sensitive to the presence of ‘heavy’ tails, rather than the shape of the peak; the inter-quartile, -decile, etc., regions probe both the effects of star formation histories and AMRs and, in the case of the inter-centile and (especially) the inter-tenth-percentile regions, the impact of metal diffusion on the extreme metal-poor tail of the distribution. In the context of cosmological chemo-dynamical disc simulations, to our knowledge, *our’s is the first quantitative discussion of these higher-order moments of the MDF.*

Further, from an observational perspective, the recent re-calibrations of the original Geneva-Copenhagen Survey (GCS: Nordström et al. (2004)) by Holmberg et al. (2009) and Casagrande et al. (2011) has made for a timely investigation of the predicted characteristics of the MDFs of simulated disc galaxies. Parallel developments slightly further afield<sup>3</sup> include targeted MDF studies of the thin–thick disc transition region and the thick disk proper (Schlesinger et al. 2012), the stellar halo

---

<sup>2</sup>cf. Kirby et al. (2011a), though, for a study of the higher-order moments of the MDFs of Local Group dwarf spheroidals which is similar in spirit to our work here on disc galaxies.

<sup>3</sup>Spatially speaking, in relation to that of the solar neighbourhood region probed by the GCS.

## CHAPTER 3

(Schörck et al. 2009), and the Galactic bulge (Bensby et al. 2011; Hill et al. 2011).

This chapter fills an important gap in the literature, by making use of a new suite of fully cosmological chemo-dynamical simulations whose properties have been shown to be in remarkable agreement with the basic scaling laws to which late-type disc galaxies adhere in nature (Brook et al. 2012b; Macciò et al. 2012). The simulations themselves are outlined briefly in §3.3, alongside a description of the adopted analogous ‘solar neighbourhood’ regions. The associated age-metallicity relations (AMRs) are presented in §3.4; the need for this will become apparent when analysing the higher-order moments of the MDFs within these regions and, in particular, their metal-poor tails (§3.5). Our results will then be summarised in §3.6.

### 3.3 Simulations

In what follows, we analyse five cosmological zoom variants of the ‘scaled-down’ M33-like disc galaxy simulation (`g15784`) described by Brook et al. (2012a). The initial conditions are identical for each realisation, and taken from the eponymous `g15784` of Stinson et al. (2010) after re-scaling (e.g. Kannan et al. 2012) the mass (length) scales by a factor of eight (two). Differences in the underlying power spectrum that result from this re-scaling are minor (e.g. Springel et al. 2008; Macciò et al. 2012; Kannan et al. 2012; Vera-Ciro et al. 2012), and do not affect our results. The virial mass of the scaled `g15784` is  $2 \times 10^{11} M_{\odot}$ , with  $\sim 10^7$  particles within the virial radius at  $z=0$ , with a mean stellar particle mass of  $\sim 6400 M_{\odot}$ . A gravitational softening of  $\varepsilon=165$  pc was used; to ensure that gas resolves the Jeans mass, rather than undergoing artificial fragmentation, pressure is added to the gas, after Robertson & Kravtsov (2008). Further, a maximum density limit is imposed by setting the

## CHAPTER 3

minimum SPH smoothing length to be 1/4 that of the softening length.<sup>4</sup>

Each of the five simulations was evolved using the gravitational N-body + smoothed particle hydrodynamics (SPH) code GASOLINE (Wadsley et al. 2004). Metal-dependent cooling of the gas, under the assumption of ionisation equilibrium, is applied, after Shen et al. (2010a), coupled to a uniform, evolving, Haardt & Madau (1996) ionising ultraviolet background. Our reference/fiducial simulation (11mKroupa) was introduced by Brook et al. (2012a), in the context of its outflow and angular momentum characteristics. The structural and kinematic properties (e.g., rotation curves, bulge-to-disc decomposition, ratio of rotational-to-anisotropic support, etc.) of the simulations presented here are indistinguishable from those presented in Brook et al. (2012a), to which the reader is referred for supplementary details.

When gas reaches a sufficiently cool temperature –  $T < 10,000 - 15,000$  K – and resides within a sufficiently dense environment –  $n_{\text{th}} > 9.3 \text{ cm}^{-3}$  –<sup>5</sup> it becomes eligible to form stars according to  $\frac{dM_{\star}}{dt} = c_{\star} \frac{M_{\text{gas}}}{t_{\text{dyn}}}$ , where  $c_{\star}$  is the star formation efficiency,<sup>6</sup>  $\Delta t$  is the timestep between star formation events (0.8 Myrs, here),  $M_{\text{gas}}$  is the SPH particle mass,  $t_{\text{dyn}}$  is the SPH particle’s dynamical time, and  $\Delta M_{\star}$  is the mass of the star particle formed.

We have extended the chemical ‘network’ of GASOLINE from oxygen and iron, to now also track the evolution of carbon, nitrogen, neon, magnesium, and silicon. After Raiteri et al. (1996b), power law fits to the Woosley & Weaver (1995)  $Z=0.02$

---

<sup>4</sup>In comparison, the original Stinson et al. (2010) simulations used a minimum SPH smoothing length of  $\epsilon/100$ , resulting a dramatic increase in computational time, but with only minimal impact on the simulation itself.

<sup>5</sup>The star formation density threshold  $n_{\text{th}}$  corresponds to the maximum density gas can reach using gravity – i.e.,  $n_{\text{th}} = 32M_{\text{gas}}/\epsilon^3$ .

<sup>6</sup>The star formation efficiency  $c_{\star}$  was taken to be 10% for all the runs, except for 11mChab, for a value of 7.5% was adopted.

## CHAPTER 3

SNeII yields were generated for the dominant isotopes for each of these seven elements; a further extension was implemented, in order to include the van den Hoek & Groenewegen (1997) metallicity-dependent carbon, nitrogen, and oxygen yields from asymptotic giant branch (AGB) stars. By expanding upon the chemical species being tracked, the earlier concern regarding the underprediction of the global metallicity by a factor of  $\sim 2$  (and the consequent underestimate to the SPH cooling and star formation rates) is naturally alleviated (Pilkington et al. 2012a). We note in passing that all abundances (and ratios) presented here are relative to the solar scale defined by Asplund et al. (2009).

Feedback from supernovae (SNe) follows the blastwave formalism of Stinson et al. (2006), with 100% of the energy ( $10^{51}$  erg/SN) thermally coupled to the surrounding ISM. Cooling is disabled for particles within the blast region (corresponding to the radius of the remnant when the interior pressure has been reduced to that of the pressure of the ambient ISM) for a timescale corresponding to that required to cool the hot interior gas to  $T \sim 10^4$  K.<sup>7</sup> Bearing in mind the 0.8 Myr timesteps of our runs, we impose a minimum cooling ‘shut-off time’ which matches this value.<sup>8</sup>

We employ the “MaGICC” (Making Galaxies In a Cosmological Context) feedback model described by Brook et al. (2012a) and Stinson et al. (2012), taking into account the effect of energy feedback from massive stars into the ISM<sup>9</sup> (cf. Hopkins et al. (2011)). While a typical massive star might emit  $\sim 10^{53}$  erg of radiation energy during its pre-SN lifetime, these photons do not couple efficiently to the surrounding ISM; as such, we only inject 10% of this energy in the form of thermal energy into the surrounding gas, and cooling is not disabled for this form of energy input. Of this injected energy typically 90-100% is radiated away within a single dynamical

---

<sup>7</sup>To use the terminology of Gibson (1994), the relevant radius and timescale correspond to  $R_{\text{merge}}$  and  $t_{\text{cool}}$ , respectively.

<sup>8</sup>Save, for the one run for which this restriction was relaxed (`11mNoMinShut`).

<sup>9</sup>Except for the one run included here without radiation energy (`11mNoRad`).

## CHAPTER 3

time.

The default initial mass function (IMF) is that of Kroupa et al. (1993); the `11mChab` run incorporates the more contemporary (and currently favoured) Chabrier (2003) functional form; per stellar generation, the latter possesses a factor of  $\sim 4\times$  the number of SNeII as that of the former. Finally, the treatment of metal diffusion within GASOLINE is detailed by Shen et al. (2010a); a diffusion coefficient  $C=0.05$  has been adopted for our runs, except for one simulation for which diffusion was prohibited (`11mNoDiff`).<sup>10</sup> The primary numerical characteristics of the five simulations employed here are listed in Table 3.1, and the plots used to derive the radial and vertical gradients are shown in Figures 3.2 and 3.1.

For our MDF and AMR analyses, for each simulation we identify an analogous region to that of the Milky Way’s ‘solar neighbourhood’, defined to be a radial range from 3.0 to 3.5 disc scalelengths (see Table 3.1) and to lie within 500 pc of the galactic mid-plane. The fraction of accreted stars in these high-feedback runs is negligible; as such their contamination in the ‘solar neighbourhood’ is equally negligible. Consequently, there was no need to undertake the sort of kinematic decomposition of the orbital circularity  $\epsilon_J \equiv J_z/J_{circ}(E)$  distribution<sup>11</sup> that was needed to isolate disc/in-situ stars from spheroid/accreted stars in our parallel analysis of the MDFs of the more massive (and accretion-contaminated) Stinson et al. (2010) simulations (Calura et al. 2012).<sup>12</sup>

---

<sup>10</sup>Our ‘no diffusion’ run possesses MDF and chemical ‘characteristics’ similar to those of `DG1` (Governato et al. 2010), the latter for which a brief chemical analysis was shown in Pilkington et al. (2012c). This similarity can be traced to the less efficient metal diffusion adopted for the `DG1` runs (i.e.,  $C=0.01$  vs the  $C=0.05$  now employed for our GASOLINE runs, after Shen et al. (2010a)).

<sup>11</sup>Where  $J_z$  is the  $z$ -component of the specific angular momentum and  $J_{circ}(E)$  is the angular momentum of a circular orbit at a given specific binding energy.

<sup>12</sup>Note, this was confirmed by undertaking a kinematic decomposition of `11mKroupa` using the modified technique introduced by Abadi et al. (2003b), and employed by Calura et al. (2012);

## CHAPTER 3

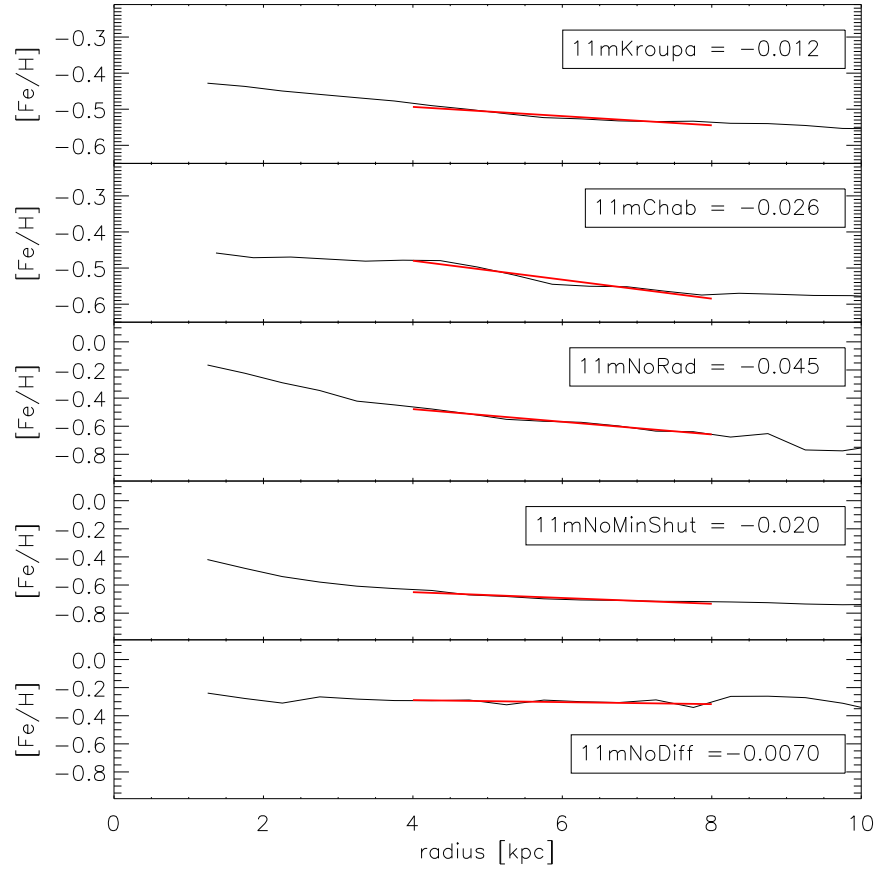


Figure 3.1: Radial metallicity gradients of the five 11m simulations; from the upper to lower panels: 11mKroupa, 11mChab, 11mNoRad, 11mNoMinShut, and 11mNoDiff, respectively. The gradients were inferred from the ‘young’ stellar population (defined here as the stars born within the past 100 Myrs). The (bold) red line indicates the region over which the gradient was measured (4 to 8 kpc). Each of the gradients has been weighted by the mass of the stellar particle.

## CHAPTER 3

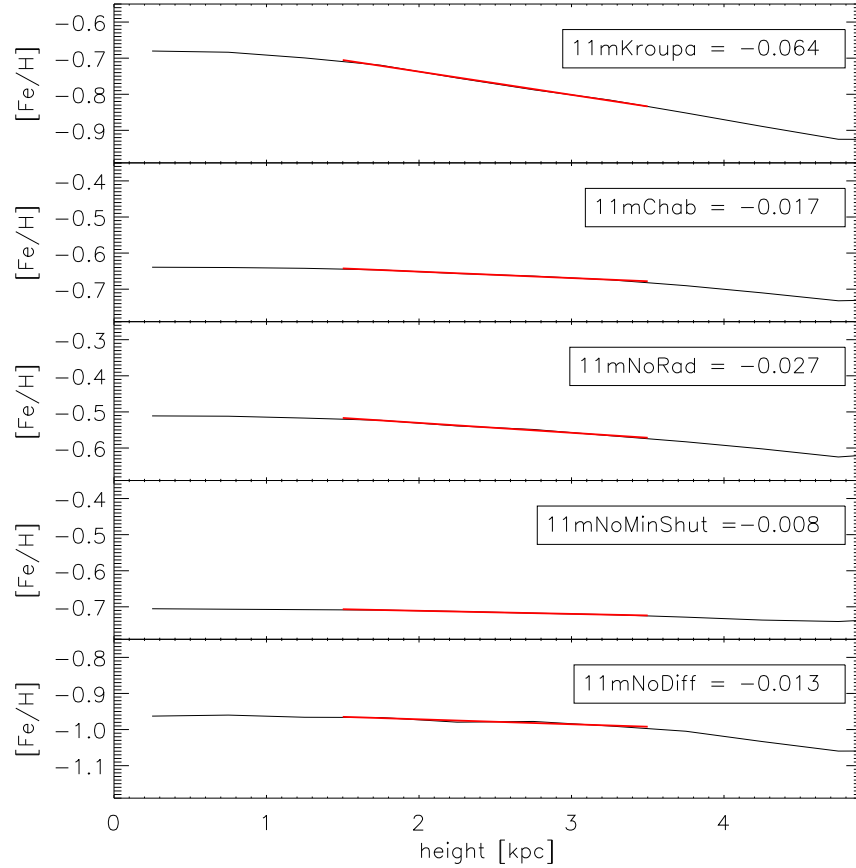


Figure 3.2: Vertical metallicity gradients of the five 11m simulations; from the upper to lower panels: 11mKroupa, 11mChab, 11mNoRad, 11mNoMinShut, and 11mNoDiff, respectively. Each gradient was derived using the local stellar particles and, as previously, was weighted by particle mass. The gradients were measured at the corresponding ‘solar neighbourhood’ (between 3 and 3.5 disk scalelengths from the galactic centre). The (bold) red line indicates the region over which the gradient was measured.

Galaxy	IMF	$c_*$	$\epsilon$ SN	SR	$T_{max}$	Stellar Mass	Scale Length	Vertical Gradient	Radial Gradient
11mKroupa	Kroupa	0.1	100%	10%	15000	$7.1 \times 10^9$	2.34	-0.064	-0.012
11mChab	Chabrier	0.075	100%	10%	10000	$1.3 \times 10^9$	2.78	-0.017	-0.026
11mNoRad	Kroupa	0.1	100%	0%	15000	$9.1 \times 10^9$	1.58	-0.027	-0.045
11mNoMinShut	Kroupa	0.1	100%	10%	15000	$14.0 \times 10^9$	1.71	-0.008	-0.020
11mNoDiff	Kroupa	0.1	100%	10%	10000	$2.1 \times 10^9$	1.43	-0.013	-0.007

Table 3.1: Primary parameters employed for the five simulations analysed in this work. Column (1): simulation/galaxy name; Column (2): adopted IMF (Kroupa $\equiv$ Kroupa et al. (1993); Chabrier $\equiv$ Chabrier (2003); Column (3): star formation efficiency; Column (4): thermalised SN energy fraction coupled to the ISM; Column (5): thermalised massive star radiation energy fraction coupled to the ISM; Column (6): maximum allowable gas temperature for star formation; Column (7): present-day stellar mass (in solar masses) within the virial radius; Column (8): stellar disc exponential scalelength (in kpc); Column (9): vertical [Fe/H] gradient (in dex/kpc); Column (10): radial [Fe/H] gradient (in dex/kpc).

## CHAPTER 3

We first show the inferred star formation histories (SFHs) of the solar neighbourhoods associated with each of the five simulations (Fig 3.3). Several important points should be made, before analysing the AMRs and MDFs. Qualitatively speaking, the SFHs of these regions within `11mKroupa`, `11mNoMinShut`, and `11mNoRad` are similar to those seen in gas-rich dwarfs like NGC 6822, Sextans A, WLM, and to some extent, the LMC (Dolphin et al. 2005). In that sense, they are (not surprisingly) different from the typical exponentially-decaying SFH (timescales of  $\sim 5\text{--}7$  Gyrs) inferred for the Milky Way’s solar neighbourhood (e.g. Renda et al. 2005), and so we should not expect *identical* trends in the ancillary AMRs and MDFs, as those observed locally. Indeed, we will show this to be case momentarily, but our interest here is more in identifying trends, rather than *exact* star-by-star comparisons.

The one simulation which shows an exponentially-declining SFH at later times is that of `11mNoDiff`; the lack of diffusion here acts to minimise the ‘spread’ of metals to a degree that star formation is restricted (preferentially) to much less enriched SPH particles (in part, because the cooling then becomes less efficient for a greater number of SPH particles, which has a greater impact at later times where there are fewer efficiently cooling metal-enriched SPH particles out of which to potentially form stars. We will return to the special case of the ‘no diffusion’ model shortly.

The SFH of `11mChab` also shows a distinct behaviour relative to the `11mKroupa` fiducial. Specifically, it is significantly lower, and relatively constant, at all times; in spirit, this is similar to the inferred SFH of the LMC (e.g. Holtzman et al. 1999). This is reflected in the stellar mass at  $z=0$  being significantly lower than `11mKroupa`,  

---

specifically, none of our conclusions were contingent upon the need for a kinematic decomposition. More quantitatively, only  $\sim 3\%$  of the stars in our simulated ‘solar neighbourhoods’ would be kinematically classified as ‘bulge/spheroid’ stars, impacting on the various MDF metrics to be discussed later at the  $<3\%$  level (smaller than the uncertainty associated with the treatment of extreme ( $>5\sigma$ ) outliers - see §3.5). In light of this negligible impact, we have avoided imposing any personal preferred kinematic decomposition scheme into the analysis.

## CHAPTER 3

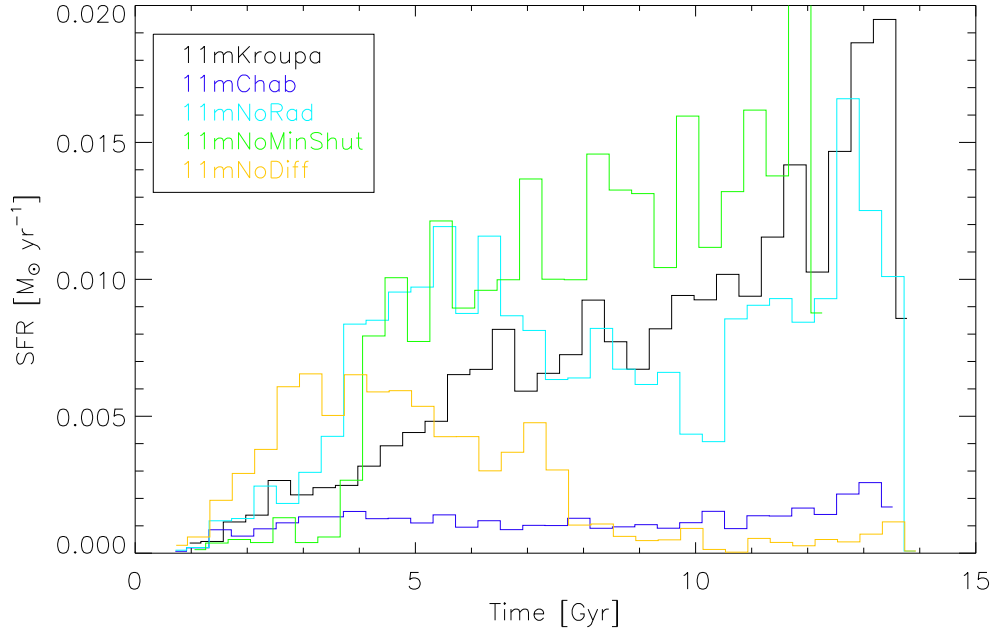


Figure 3.3: Star formation histories of the solar neighbourhoods associated with the five simulations; colour-coding is as noted in the inset to the panel.

which in turn aids considerably in bringing its properties into close agreement with essentially all traditional scaling relations Brook et al. (2012b). This behaviour is driven by (a) the factor of four increase in the SNe per stellar generation (via the more massive star-biased IMF), and (b) the reduced maximum temperature for star formation (as noted earlier).

The subtle effect of allowing the minimum shut-off time for radiative cooling of SN remnants to become prohibitively small in high-density regions (in practice what this means is that the shut-off time becomes smaller than the timestep of 0.8 Myrs) can be seen in the `11mNoMinShut` curve of Fig 3.3. Specifically, SPH particles affected by this effectively cool ‘instantly’ within the same timestep, without any delay. Hence, the particles in question become ‘available’ for star formation much sooner than they might otherwise; this has the effect of ‘boosting’ the star formation relative to that of the fiducial `11mKroupa`.

### 3.4 Age-Metallicity Relations

As noted earlier, the MDF bears the imprint of a region’s star formation history (SFH), convolved with its age-metallicity relation (AMR). Having introduced the ‘solar neighbourhood’ SFHs in §3.3, we now present their associated AMRs in Fig 3.4. The time evolution of the  $[\text{Fe}/\text{H}]$  abundances is shown for each of the five simulations listed in Table 3.1. Colour-coding within each panel corresponds to stellar age, ranging from old (black/blue) to young (red).

To provide a representative empirical dataset against which to compare, we make use of the recent re-calibration of the Geneva-Copenhagen Survey (GCS) presented by Holmberg et al. (2009). The base GCS provides invaluable spectral parameters for  $\sim 17,000$  F- and G- stars in the solar neighbourhood. Following Holmberg et al. (2007), we define a ‘cleaned’ sub-sample by eliminating (i) binary stars, (ii) stars for which the uncertainty in age is  $>25\%$ , (iii) stars for which the uncertainty in trigonometric parallax is  $>13\%$ , and (iv) stars for which a ‘null’ entry was provided for any of the parallax, age, metallicity, or their associated uncertainties. The AMR for this ‘cleaned’ sub-sampled of  $\sim 4,000$  stars is shown in the lower-right panel of Fig 3.4. A fifth criterion is applied for the determination of the higher-order moments of the MDF shape; specifically, following Holmberg et al. (2007) and constructing an unbiased volume-limited sub-sample from the stars lying within 40 pc of the Sun. Doing so yields a smaller sample of only  $\sim 500$  stars. While this does not impact on the shape characteristics of §3.5 or the behaviour of the AMR, for clarity, we show the AMR inferred from the aforementioned sub-sample of  $\sim 4,000$  stars in Fig 3.4.<sup>13</sup>

It is worth re-emphasising that we are using the Holmberg et al. (2009) variant of the GCS solely as a useful ‘comparator’ against which to contrast our various MDF

---

<sup>13</sup>The ‘upturn’ towards high-metallicities at young ages in the GCS sample is likely traced to the very young Fm/Fp stars which are difficult to characterise with Stromgren photometry alone (Holmberg et al. 2009).

## CHAPTER 3

metrics / higher-order moments. It should not be interpreted as an endorsement of one solar neighbourhood MDF over another; there is a rich literature describing the various pros and cons of any number of potential selection biases within this (or any other) re-calibration of the GCS (e.g. Schönrich & Binney 2009; Casagrande et al. 2011) and we are not equipped to enter into that particular debate. The GCS remains the standard-bearer for MDF analysis, reflecting the nature of (fairly) volume-limited and (fairly) complete nature, making it ideal for probing the active star forming component of the thin disc; other exquisite MDFs, including those of the aforementioned (predominantly) thick disc (Schlesinger et al. 2012) and halo (Schörck et al. 2009) studies, are more suited for simulations targeting regions further from the mid-plane than we are doing here. Ideally, of course, we would like to replace the solar neighbourhood ‘comparator’ used here (the GCS) with an empirical sample more representative of star formation histories associated with massive dwarf spiral/irregulars (e.g. Skillman et al. 2003; Dolphin et al. 2003; Kirby et al. 2011a), but until the statistics, completeness, and accuracy of the age and metallicity determinations for such distance dwarfs reaches that of the solar neighbourhood, we are reluctant to compare (in detail) the predictions of the simulations with those of the observations. Having said that, we will comment on, in a qualitative sense, the AMR and MDF trends seen in our simulations and how they compare with said dwarfs.

Several key points can be inferred from Fig 3.4. First, not surprisingly, the metallicities of the stars in the Milky Way’s solar neighbourhood (GCS) are typically a factor of  $\sim 5\text{--}100\times$  higher at a given age compared with the five simulations. This reflects the discussion of §3.3 in relation to the fact that the simulations in question are more similar to lower-luminosity disc galaxies (in terms of both mass and SFHs), rather than being Milky Way ‘clones’. The simulations are consistent with the various scaling relations to which galaxies adhere (Brook et al. 2012b); as

## CHAPTER 3

such, for their mass, their mean metallicities are a factor of  $\sim 3\text{--}5\times$  lower than that of the Milky Way.<sup>14</sup>

More important for our purposes here, there are two additional characteristics which are readily apparent in Fig 3.4. First, the AMR of the solar neighbourhood is essentially non-existent, save for a trace of old, metal-poor, stars. In contrast, the corresponding regions of the simulations show *extremely* correlated AMRs (especially those of the fiducial simulations, `11mKroupa` and `11mChab`). This is partly traced to the differences in the aforementioned SFHs, although the correlation persists (admittedly with larger scatter at a given age) even in `11mNoDiff`, the simulation whose SFH bears the closest resemblance to that of the Milky Way. The impact of these tightly-correlated AMRs manifest themselves significantly within the inferred MDFs, a point to which we will return in §3.5. Qualitatively speaking, these tightly-correlated AMRs resemble those predicted by semi-numerical galactic chemical evolution models (e.g. Chiappini et al. 2001; Fenner & Gibson 2003; Renda et al. 2005; Mollá & Díaz 2005).

In the bottom right panel of Fig 3.4, we also overplot the AMRs inferred from the colour-magnitude diagram-derived star formation histories of the dwarf irregulars Sextans A (Dolphin et al. 2003) and IC 1613 (Skillman et al. 2003); like the Milky Way, neither are meant to be one-to-one matches to the `11m` series of simulations, but in some sense they do provide a useful complementary constraint, in the sense that their respective star formation histories are not dissimilar to those shown in Fig 3.3 (in particular, those of `11mKroupa`, `11mNoMinShut`, and `11mNoRad`). Their

---

<sup>14</sup>The MDFs and AMRs of systems more directly comparable to the Milky Way proper – i.e., the more massive ‘parent’ simulations to those employed here (Stinson et al. 2010) – are described by Calura et al. (2012) and Gibson et al. (2013, in prep), respectively. The significant contamination from accreted stars in these more massive simulations tends to impact upon both the scatter of the AMR and skewness/dispersion of the IMF, in a negative sense, relative to the high-feedback models here, for which the accreted fraction is negligible.

## CHAPTER 3

associated AMRs, while lacking the statistics, completeness, and accuracy of the GCS dataset necessary to make detailed quantitative comparisons, do show evidence of possessing somewhat stronger correlations. Again, the statistics of these dwarf systems' MDFs and AMRs make it difficult to say anything more regarding the degree of 'agreement' between the 11m series and that encountered in nature, but it is suggestive and certainly merits revisiting once data comparable to that of the GCS becomes available for dwarf irregulars/spirals.

Second, the scatter in  $[\text{Fe}/\text{H}]$  at a given stellar age is significantly smaller (compared with that of the Milky Way) in the three simulations where the injection of thermalised massive star radiation energy to the surrounding ISM is included (i.e., 11mKroupa, 11mChab, and 11mNoMinShut). Neglecting this feedback term, within the context of these cosmological hydrodynamical disc simulations, acts to increase the scatter in  $[\text{Fe}/\text{H}]$ , at a given in time, to a level comparable to that seen in Milky Way's solar neighbourhood.<sup>15</sup> Not surprisingly, the one simulation for which metal diffusion was suppressed (11mNoDiff) possesses the largest scatter in  $[\text{Fe}/\text{H}]$  at a given age, particularly at early times/low metallicities, where the neglect of diffusion is most problematic (again, a point to which we return in §3.5).

### 3.5 Metallicity Distribution Functions

Having been informed by the empirical and simulated solar neighbourhoods' SFHs and AMRs (§3.3 and §3.4), we now present the  $[\text{Fe}/\text{H}]$  metallicity distribution functions (MDFs) for the same regions.<sup>16</sup> Fig 3.5 shows the MDFs (black histograms)

---

<sup>15</sup>A secondary byproduct is also a mildly steeper radial abundance gradient, although the effect is minor - recall, Table 3.1.

<sup>16</sup>We confirmed that our conclusions are robust to the specific definition of the 'solar neighbourhood', by increasing its vertical range from  $\pm 0.5$  kpc to  $\pm 2$  kpc. Similarly, varying the radial range from  $3.50 \pm 0.25$  disc scalelengths, by  $\pm 1$  scalelength has negligible impact (recall from Table 3.1 that the metallicity gradients here are shallow).

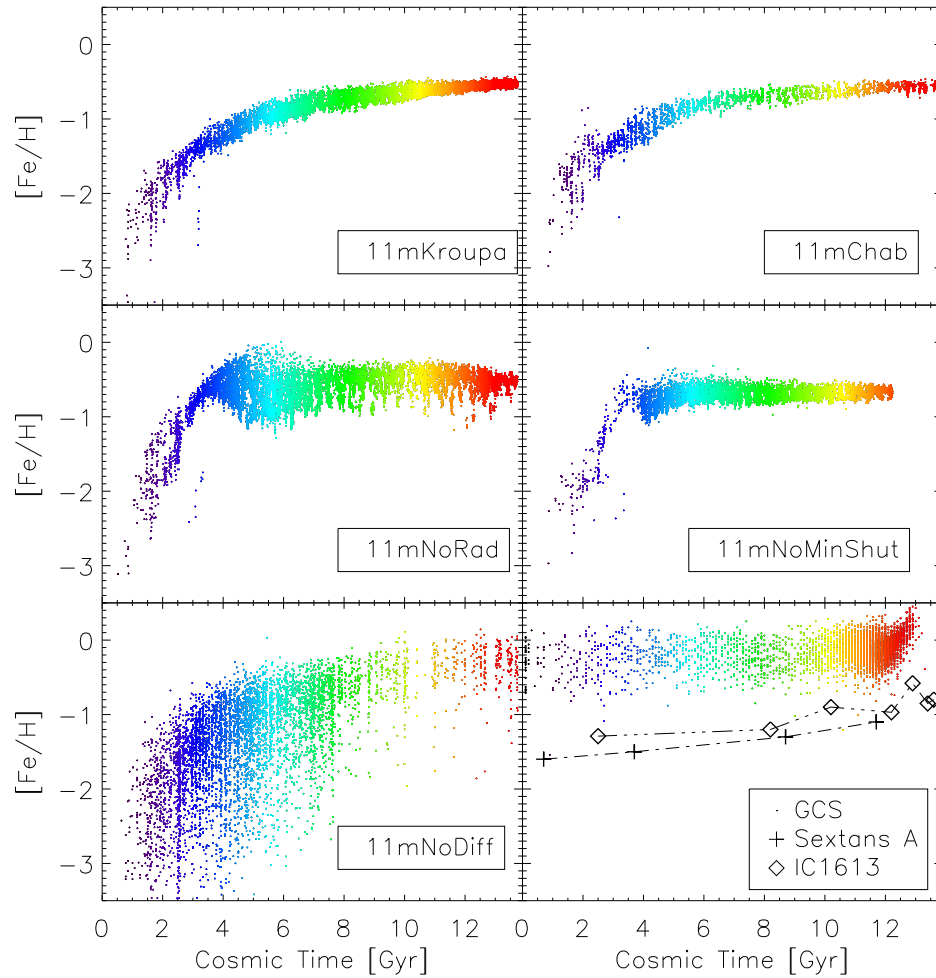


Figure 3.4: Age-metallicity relations (where metallicity  $\equiv [Fe/H]$ ) in the analogous solar neighbourhoods of the five simulations employed here, in addition to the reference relationship found in the solar neighbourhood of the Milky Way and the dwarf irregulars Sextans A (Dolphin et al. 2003) and IC 1613 (Skillman et al. 2003). Colour-coding in each panel is by stellar age, ranging from black/blue (oldest) to red (youngest).

## CHAPTER 3

for the five simulations, the Milky Way (GCS: lower right panel) and the Local Group dwarf Fornax (also, lower right panel, from Kirby et al. (2011a)). The two sub-samples of the GCS are shown; in black, the aforementioned (§3.4) sub-sample of  $\sim 4,000$  stars (matching those shown in Fig 3.4 – i.e., the ‘cleaned’ sub-sample, but without any distance constraint applied, labeled ‘GCS’ in the lower-right panel), and in blue, the volume-limited sample (i.e., those lying within 40 pc of the Sun, labeled ‘GCScut’). As stressed earlier, the shape characteristics of the GCS MDF are not contingent upon this latter cut; the labels ‘GCS’ and ‘GCScut’ will be employed to differentiate between the two, where relevant. Overlaid in each panel is simple ‘best-fit’ (single) Gaussian to the respective distributions (and their associated full-width at half-maximum (FWHM) values). For the Fornax dwarf, we use the full sample of 675 stars taken from Kirby et al. (2011a), in order to show an MDF for a representative local dwarf. Three caveats should be noted, in relation to the latter: (i) the sample size is 1-2 orders of magnitude smaller than the GCS, not surprisingly, considering the challenging nature of this observational work; (ii) no analogous ‘solar neighbourhood’ can be identified within this dataset (it is simply all the stars in the sample covering a range of fields in Fornax); and (iii) the uncertainty in  $[\text{Fe}/\text{H}]$  for a given individual star in Fornax is  $\sim 0.5$  dex, compared with the  $\sim 0.1$  dex associated with individual stars in the GCS. Fornax is neither better nor worse than the GCS, as a comparator, so it is useful to at least show both, as they represent the state-of-the-art, observationally-speaking.

Even before undertaking any quantitative analysis of the MDFs, it is readily apparent that the simulations (particularly, **11mKroupa**, and **11mChab**) possess an excess of stars to the left (i.e., to the negative side) of the peak of the MDF, relative to the right, when compared with that of the GCS and Fornax (i.e., the simulated MDFs are more negatively skewed). This ‘excess’ of lower-metallicity stars is formed *in situ* during the first  $\sim 4$  Gyrs of the simulations. The exception to this trend is

## CHAPTER 3

11mNoMinShut, for which the lack of significant star formation at early epochs (recall, Fig 3.3) and the extremely flat AMR at late times (Fig 3.4) conspires to present the narrow and symmetric MDF shown in Fig 3.5. As noted in §3.4, for both 11mNoRad and 11mNoDiff, the larger scatter in  $[\text{Fe}/\text{H}]$  at a given age manifests itself in the broader MDFs seen in Fig 3.5.

It is worth delving deeper into the source of the broader MDF seen in, for example, 11mNoRad, relative to the fiducial 11mKroupa. Here, it is at high-redshift that the radiation energy has an impact on the regulation of star formation. 11mNoRad has higher star formation at early times (Fig 3.3), but not at later times, primarily because it exhausts its available gas, whereas with the radiation energy, star formation is regulated during that crucial period when gas accretion is at its most active; this gas remains available at later times to form stars, resulting in the MDF of 11mNoRad being broader relative to the fiducial. Ultimately, the length of time that gas spends in the disk before it forms stars shapes the MDF ‘width’ here. With radiation energy included, this gas is in the disk for a longer period of time, meaning more metal mixing occurs. Linking back to the star formation histories of Fig 3.3, we note that most of the gas is accreted during the first  $\sim 6$  Gyr, and one can see that the star formation rate shows an early peak in the case of 11mNoRad (and 11mNoDiff), but not in the cases which include radiation energy - i.e., gas that forms stars (relatively) rapidly after accretion does not mix as much, and hence the broader MDF.

We next undertook a quantitative analysis of the MDFs shown in Fig 3.5, including a determination of the skewness, kurtosis, and widths at a range of inter-percentiles of the distributions. These determinations are listed in Tables 3.2 and 3.3, and plots showing the calculations of the inter-percentiles are shown in Figures 3.6, 3.7, 3.8, 3.9, and 3.10. As both skewness and kurtosis are highly sensitive to the presence of outliers, we imposed a fairly standard  $5\sigma$  clipping to the distributions. To mimic the observational uncertainties associated with the determination

## CHAPTER 3

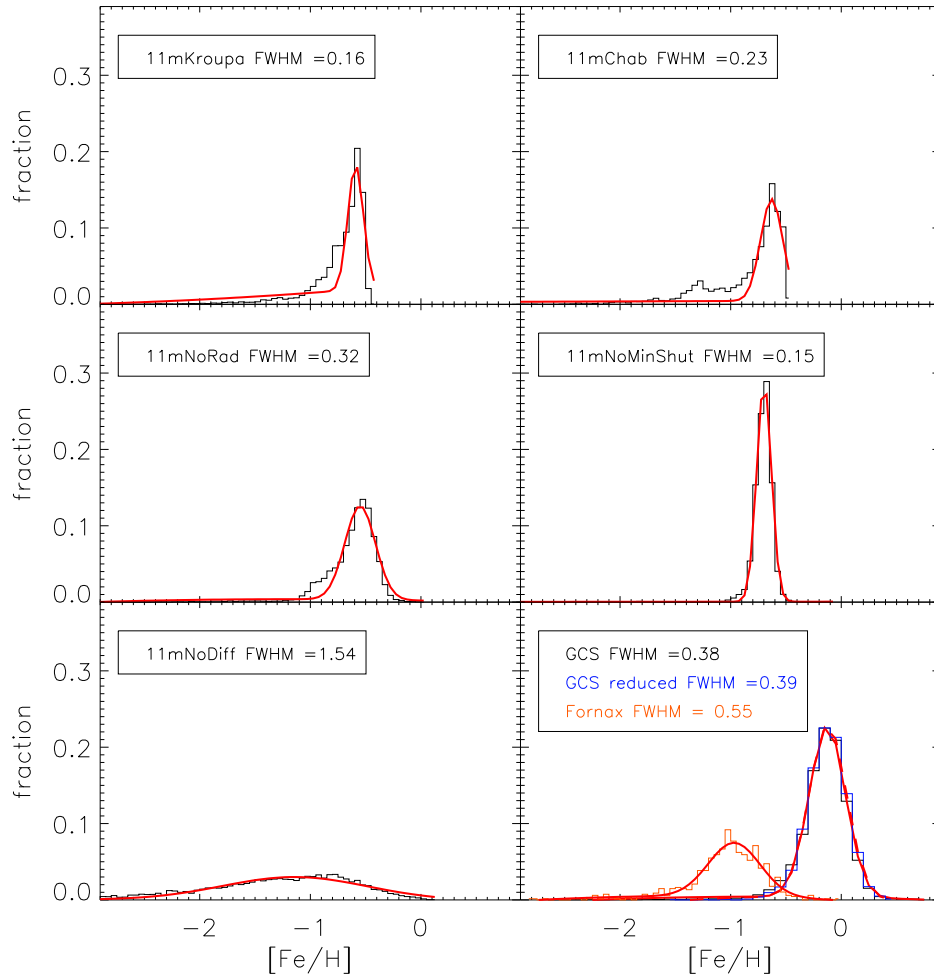


Figure 3.5: The  $[\text{Fe}/\text{H}]$  metallicity distribution functions in the solar neighbourhoods of the five simulations employed here. The bottom-right panel shows the MDF of the Milky Way’s solar neighbourhood, based upon two sub-samples of stars selected from Holmberg et al. (2009), as well as that for Local Group dwarf Fornax, from Kirby et al. (2011a) (see text for details). In each panel, the overlaid curve is the best-fit single component Gaussian to the aforementioned MDF; the associated FWHM of said Gaussian is listed in the inset to each panel.

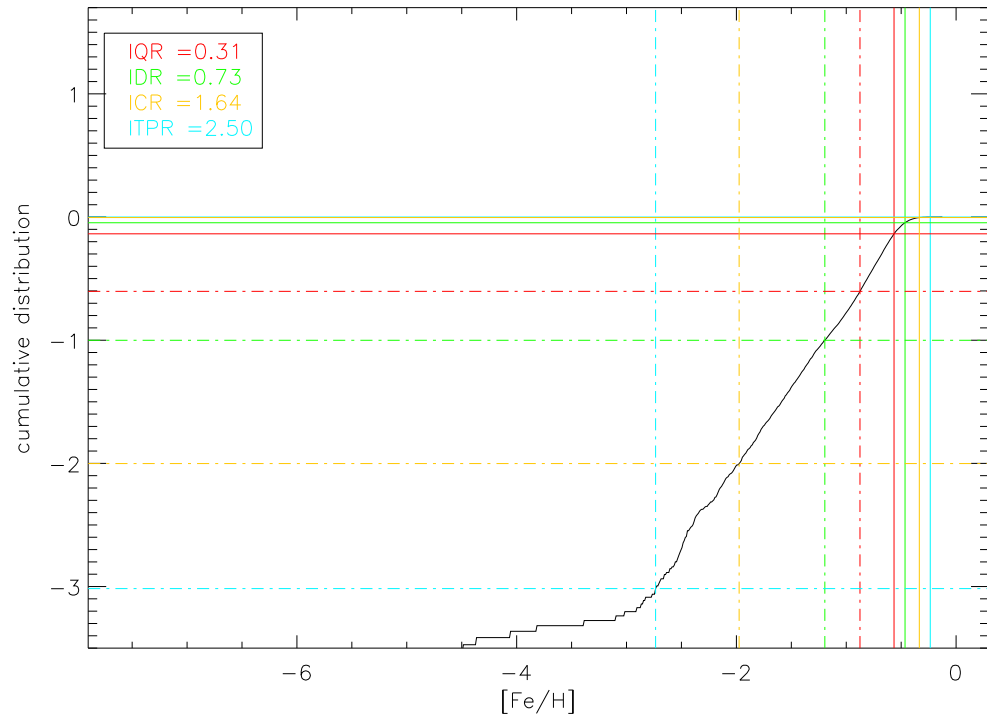


Figure 3.6: Cumulative MDF of the solar neighbourhood of 11mKroupa (black line); coloured lines show the inter-quartile range (red), inter-decile range (green), inter-centile range (yellow) and the inter tenth percentile range (blue). Solid lines show the upper limit of each of the ranges and the lower limit is the dot-dashed line. As in Table 3.3, the MDF has been convolved with a 0.1 dex Gaussian. Note that the difference in the numbers between the legend and Table 3.3 arises from using a random number generator when convolving with the MDF.

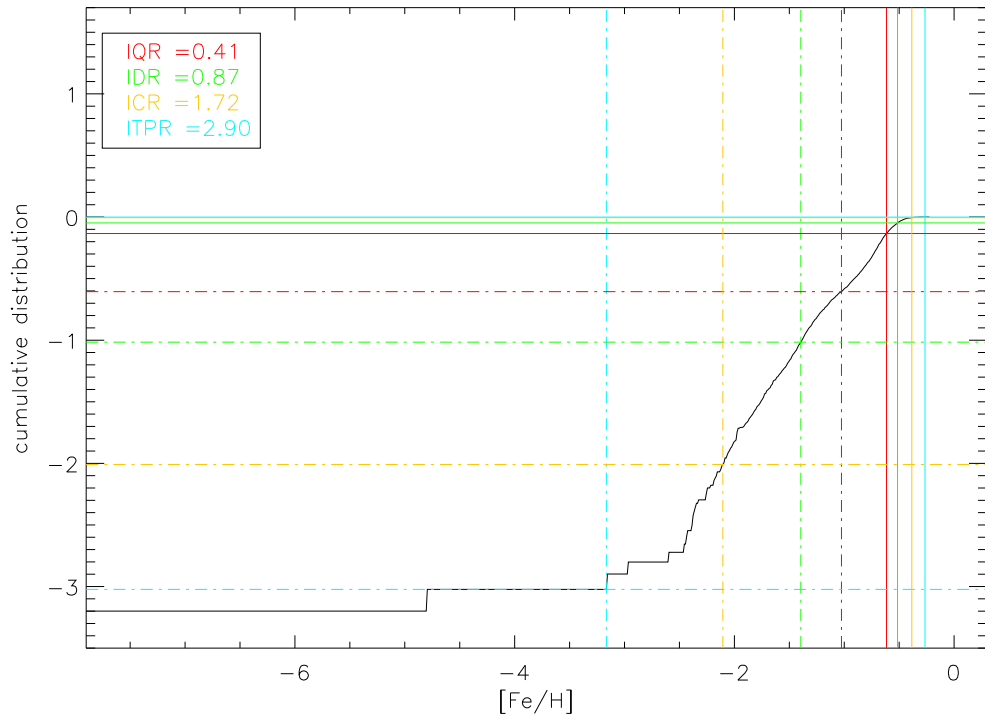


Figure 3.7: Cumulative MDF of the solar neighbourhood of 11mChab (black line); coloured lines show the inter-quartile range (red), inter-decile range (green), inter-centile range (yellow) and the inter tenth percentile range (blue). Solid lines show the upper limit of each of the ranges and the lower limit is the dot-dashed line. As in Table 3.3, the MDF has been convolved with a 0.1 dex Gaussian. Note that the difference in the numbers between the legend and Table 3.3 arises from using a random number generator when convolving with the MDF.

## CHAPTER 3

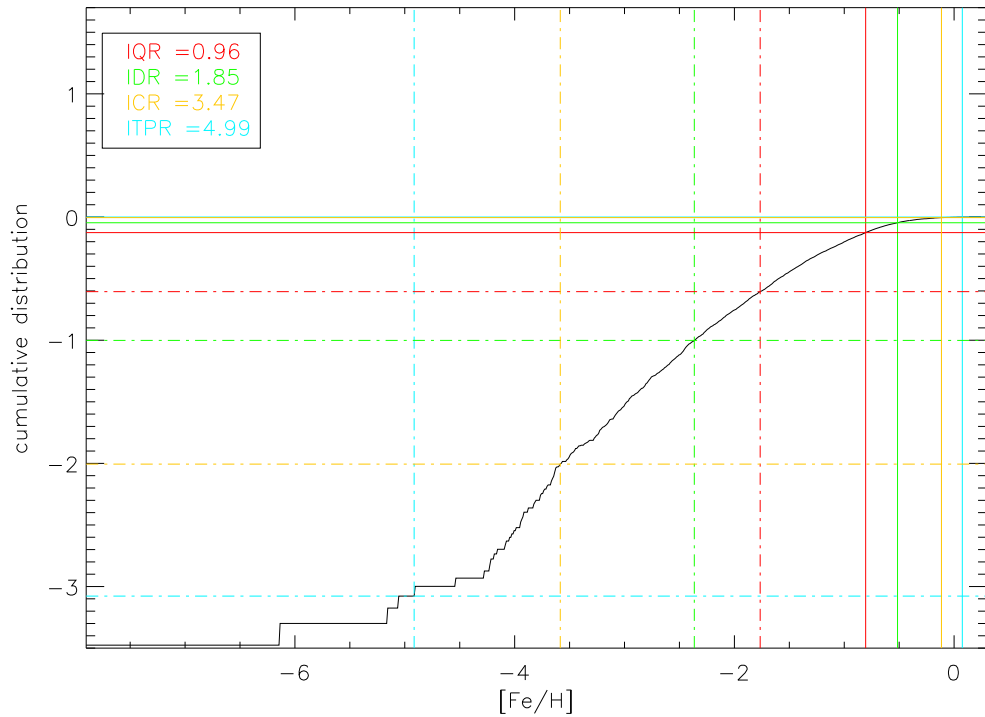


Figure 3.8: Cumulative MDF of the solar neighbourhood of 11mNoDiff (black line); coloured lines show the inter-quartile range (red), inter-decile range (green), inter-centile range (yellow), and the inter tenth percentile range (blue). Solid lines show the upper limit of each of the ranges and the lower limit is the dot-dashed line. As in Table 3.3, the MDF has been convolved with a 0.1 dex Gaussian. Note that the difference in the numbers between the legend and Table 3.3 arises from using a random number generator when convolving with the MDF.

## CHAPTER 3

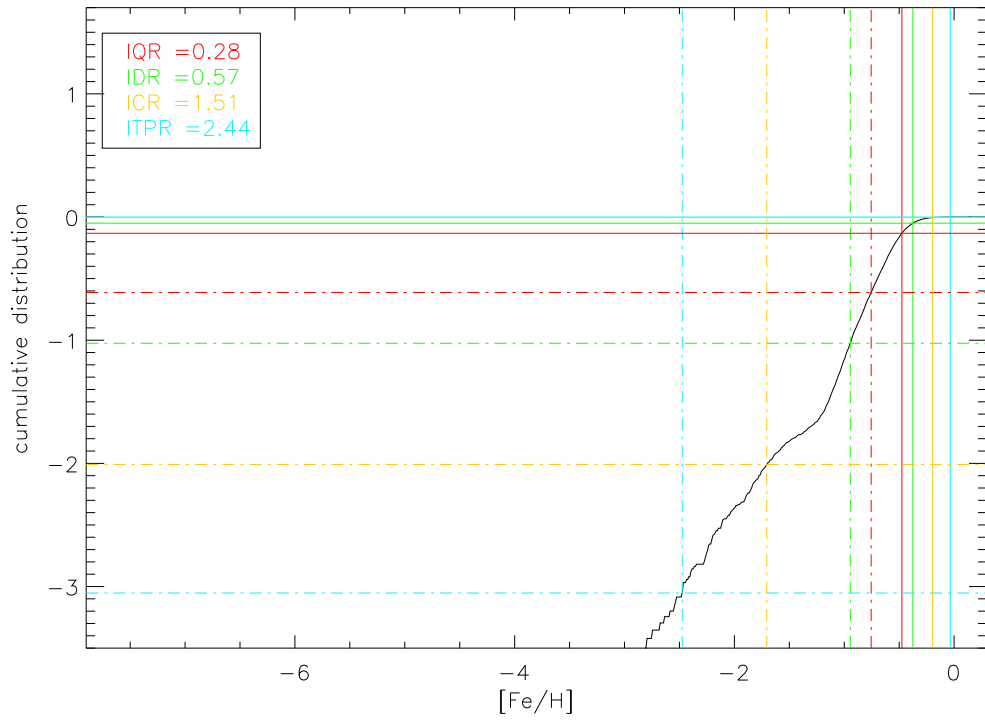


Figure 3.9: Cumulative MDF of the solar neighbourhood of 11mNoRad (black line); coloured lines show the inter-quartile range (red), inter-decile range (green), inter-centile range (yellow) and the inter tenth percentile range (blue). Solid lines show the upper limit of each of the ranges and the lower limit is the dot-dashed line. As in Table 3.3, the MDF has been convolved with a 0.1 dex Gaussian. Note that the difference in the numbers between the legend and Table 3.3 arises from using a random number generator when convolving with the MDF.

## CHAPTER 3

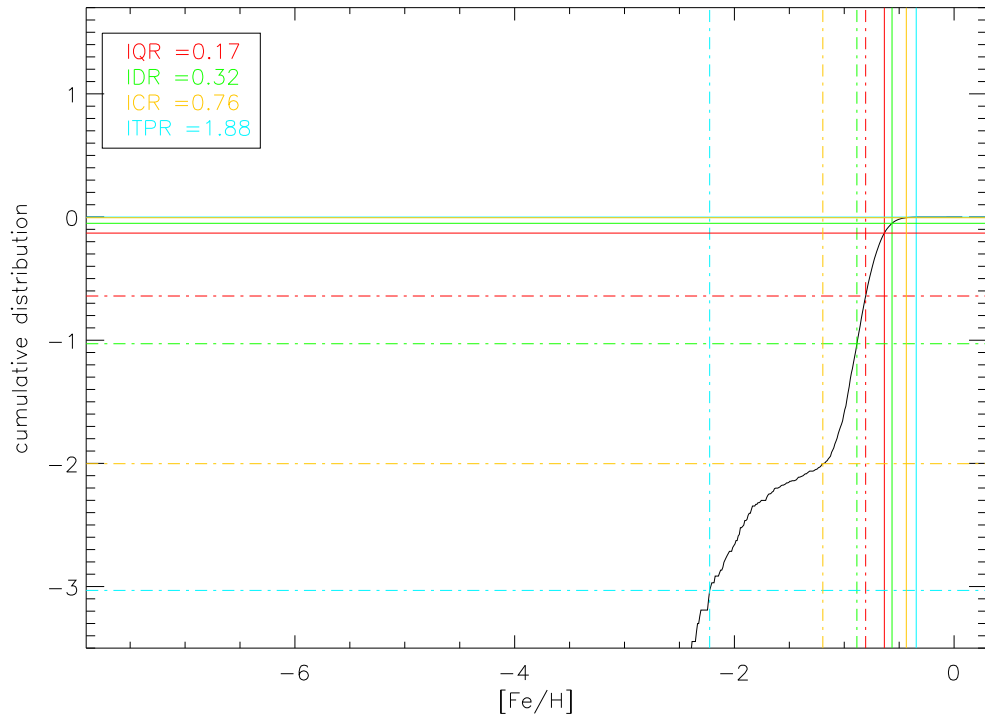


Figure 3.10: Cumulative MDF of the solar neighbourhood of 11mNoMinShut (black line); coloured lines show the inter-quartile range (red), inter-decile range (green), inter-centile range (yellow), and the inter tenth percentile range (blue). Solid lines show the upper limit of each of the ranges and the lower limit is the dot-dashed line. As in Table 3.3, the MDF has been convolved with a 0.1 dex Gaussian. Note that the difference in the numbers between the legend and Table 3.3 arises from using a random number generator when convolving with the MDF.

CHAPTER 3

Simulation	Skewness	Kurtosis	IQR	IDR	ICR	ITPR
11mKroupa	-1.87	3.81	0.30	0.68	1.50	2.26
11mChab	-1.59	2.36	0.40	0.81	1.56	2.50
11mNoRad	-1.10	2.15	0.24	0.50	1.42	2.32
11mNoMinShut	-0.62	2.05	0.09	0.17	0.62	1.78
11mNoDiff	-0.85	0.73	0.95	1.82	3.45	4.85

Table 3.2: The raw MDF data for the five 11m galaxies. Column (1): the name of the simulation or empirical dataset; Column (2): the skewness of the MDF ( $5\sigma$  clipping of outliers was imposed, to minimise their impact on the determination); Column (3): the kurtosis of the MDF, again with the adoption of  $5\sigma$  clipping; Columns (4) – (7): the interquartile (IQR), interdecile (IDR), intercentile (ICR), and inter-tenth-percentile (ITPR) for each MDF.

of individual stellar [Fe/H] abundances, after Fenner & Gibson (2003), the ‘theoretical’ MDFs shown in Fig 3.5 were convolved first with either a 0.1 dex Gaussian (to mimic the GCS uncertainties - Holmberg et al. (2009)) or a 0.5 dex Gaussian (to mimic the uncertainties with the Fornax data - Kirby et al. (2011a)). In Table 3.3, each column has two numbers; the first is the relevant metric, as measured on the MDF convolved with a 0.1 dex Gaussian, while the second (in brackets) is that measured on the MDF convolved with a 0.5 dex Gaussian. As the simulated MDFs are typically much broader than the GCS uncertainties, the impact of the 0.1 dex smoothing is minimal.

As inferred from the above qualitative discussions of the MDF and the AMR (§3.4), MDFs of the simulated solar neighbourhoods are all (save for **11mNoMinShut**, whose exceedingly flat AMR results in the elimination of essentially all tails, positive or negative of the MDF’s peak) more negatively skewed than that of the Milky Way’s solar neighbourhood (from both the volume-limited **GCS**cut sample of stars, and

Simulation/Dataset	Skewness	Kurtosis	IQR	IDR	ICR	ITPR
11mKroupa	-1.63(-0.30)	3.26(0.36)	0.33(0.78)	0.72(1.49)	1.65(2.84)	2.46(4.07)
11mChab	-1.40(-0.32)	1.92(0.27)	0.41(0.80)	0.88(1.54)	1.73(2.92)	2.62(4.22)
11mNoRad	-0.98(-0.21)	2.26(0.34)	0.28(0.72)	0.56(1.41)	1.50(2.61)	2.44(3.69)
11mNoMinShut	-0.24(-0.11)	0.75(0.22)	0.17(0.69)	0.32(1.32)	0.76(2.43)	1.97(3.45)
11mNoDiff	-0.83(-0.51)	0.70(0.31)	0.96(1.20)	1.84(2.24)	3.46(4.12)	4.77(5.82)
GCS	-0.61	2.04	0.23	0.48	1.26	2.63
GCScut	-0.37	0.78	0.24	0.45	0.94	1.43
Fornax	(-1.33)	(3.58)	(0.38)	(2.25)	(2.75)	(2.85)

Table 3.3: Primary MDF shape characteristics for the solar neighbourhoods of the five simulations described here, the two sub-samples based upon the Holmberg et al. (2009) **GCS** empirical dataset are as described in the text and data for the Fornax dwarf galaxy taken from Kirby et al. (2011a). After Fenner & Gibson (2003), the simulated MDFs were convolved with either a 0.1 dex Gaussian (left-most entry within each column) or a 0.5 dex Gaussian (right-most / bracketed entry within each column), to mimic the typical uncertainties associated with the  $[\text{Fe}/\text{H}]$  determinations in nature (the GCS in the case of the former, and Fornax in the case of the latter). Column (1): the name of the simulation or empirical dataset; Column (2): the skewness of the MDF ( $5\sigma$  clipping of outliers was imposed, to minimise their impact on the determination); Column (3): the kurtosis of the MDF, again with the adoption of  $5\sigma$  clipping; Columns (4) – (7): the interquartile (IQR), interdecile (IDR), intercentile (ICR), and inter-tenth-percentile (ITPR) for each MDF.

## CHAPTER 3

the unrestricted GCS sample) and the sample from Fornax. It must be emphasised though that the typical 0.5 dex uncertainty associated with the determination of  $[\text{Fe}/\text{H}]$  for individual stars in Fornax means that broadening the simulated MDFs, with their typical dispersions of  $\sim 0.1$  dex, by 0.5 dex, ‘washes out’ much of our ability to compare and contrast the higher-order MDF metrics, and hence the analysis which follows emphasises the differences between the simulated MDFs and that of the GCS. The ‘tail’ of stars to the negative side of the peak should not be associated immediately with the traditional ‘G-dwarf problem’, since these fully cosmological simulations relax the ‘closed-box’ framework which is the hallmark of this problem. Instead, as noted earlier, it is the tightly-correlated AMRs which are driving the large negative skewness values; these AMRs do not resemble that of the Milky Way’s solar neighbourhood. The different SFHs are certainly part of the difference, but as noted earlier, both the fiducial `11mChab` and `11mNoDiff` show SFHs not dissimilar to the exponentially-declining one of the Milky Way, and the coordinated AMRs remain responsible for the larger negative skewness in both cases. An analysis of the kurtosis values for each distribution are consistent with this picture. Specifically, the simulations’ kurtosis values are all larger than those of `GCScut`, and as noted in §3.3, large kurtosis values are driven in part by the presence of a ‘peaky’ MDF, but more importantly, the impact of extended, ‘heavy’, tails. These tails (positive or negative) are driven by the coordinated AMRs and are reflected in the generally large values of kurtosis relative to the Milky Way’s distribution.

Alongside the skewness and kurtosis determinations, we present four measures of the shape of the MDF, through its dispersion, or width, at different amplitudes. This is done via the width of the inter-quartile range (IQR), inter-decile range (IDR), inter-centile range (ICR), and the inter-tenth-percentile range (ITPR).<sup>17</sup>

---

<sup>17</sup>The IQR corresponds to the difference in metallicity between the 25% lowest metallicity stars and the 25% higher metallicity stars; similarly, the IDR corresponds to the difference between the 10% lowest and 10% highest metallicity stars; etc.

## CHAPTER 3

The metrics associated with these width measures require some comment in relation to the information provided by Fig 3.5. Specifically, the best-fit single Gaussian fits overlaid in each panel show that grossly speaking, the Milky Way’s and Fornax’s MDF are broader than those associated with the simulations.<sup>18</sup> At first glance, the IQR, ITR, etc, measures listed in Table 3.3 appear counter to this result (which are all, essentially, larger than the values found for `GCScut`, for example). It is important to remember though that, much like the case for skewness and kurtosis, these measures of the breadth of the MDF are sensitive to the impact of outliers in the tails of the distribution.

It is particularly useful to note the quantitative impact of the role of metal diffusion in setting the width of the MDF in tails of the distribution. For example, in the solar neighbourhood of the Milky Way, the range in metallicity between the bottom and top 0.1% of the stars is  $\sim 2$  dex. For our simulation in which metal diffusion was neglected (`11mNoDiff`), the corresponding width is  $\sim 5$  dex – i.e., a factor of  $\sim 1000\times$  greater than the other simulations with diffusion and that encountered in the Milky Way, similar to what we found for other low diffusion runs (Pilkington et al. 2012c).

After Casagrande et al. (2011), we show in Fig 3.11 the MDF for the solar neighbourhood of one of our fiducial simulations (`11mKroupa`), but now binned more finely in metallicity and colour-coded by age. Here, young stars correspond to those formed in the last 1 Gyr at redshift  $z=0$ ; intermediate-age stars are those with ages between 5 and 7 Gyrs; old corresponds to stars with ages greater than 9 Gyrs. Using the `GCS`, Casagrande et al. (2011) conclude that the younger stars have a narrower MDF than the older stars, consistent with our results (and to be expected, given its AMR). Casagrande et al. (2011) also found though that the locations of the peaks associated with these old and young stars were at the same metallicity,

---

<sup>18</sup>Save for `11mNoDiff`, as noted in §3.4.

## CHAPTER 3

which is not consistent with our simulations. Again, this is to be expected given the tightly-correlated AMRs of the simulations, relative to that of the Milky Way.

While it may be the case that we are not capturing all of the relevant stellar migration physics within these simulations (e.g., bars, spiral arms, resonances, etc.), there *is* radial migration occurring. That said, the radial gradients are shallow for these fiducial dwarfs ( $-0.01 \rightarrow -0.02$  dex/kpc, recalling Table 3.1<sup>19</sup>) and, as such, over the few kpcs of ‘disc’ associated with each simulated dwarf, systematic migration of metal-rich inner-disc stars outwards (and vice versa) has little impact on the position of the MDF ‘sub-structure’ (in which the young, intermediate, and old ‘peaks’ are offset by  $\sim 0.3-0.5$  dex from one another). Again, this is entirely consistent with the expected behaviour, based upon the AMR.

The central regions of our simulations show similar characteristics to those seen in the simulated solar neighbourhoods. Specifically, the  $[\text{Fe}/\text{H}]$  MDF of the ‘bulge’ (inner 2 kpc) shows a peak near  $[\text{Fe}/\text{H}] \sim -0.5$ , with a number of sub-components at lower metallicity which correspond to progressively older and metal-poor populations (see Fig 3.12). In spirit, such behaviour has been seen in the MDF of the bulge of the Milky Way, where Bensby et al. (2011) finds two populations, also separated comparably in age and metallicity, to which they associate separate formation scenarios. This result is updated in Bensby et al. (2013) where there are not two distinct populations but multiple components of a complex structure. Similarly, Hill et al. (2011) finds bulge sub-components within the MDF which they also separate into separate age, metallicity, and kinematic sub-structures, concluding the metal-poor component can be associated with an old spheroid, and the more metal-rich component can be associated with a longer timescale event (perhaps the evolution of the bar / psuedo-bulge).

---

<sup>19</sup>Flatter than the gradients seen in our work on the massive galactic analogues to these dwarfs (Chapter 4), consistent with the empirical work on gradients in dwarfs (e.g. Carrera et al. 2008).

## CHAPTER 3

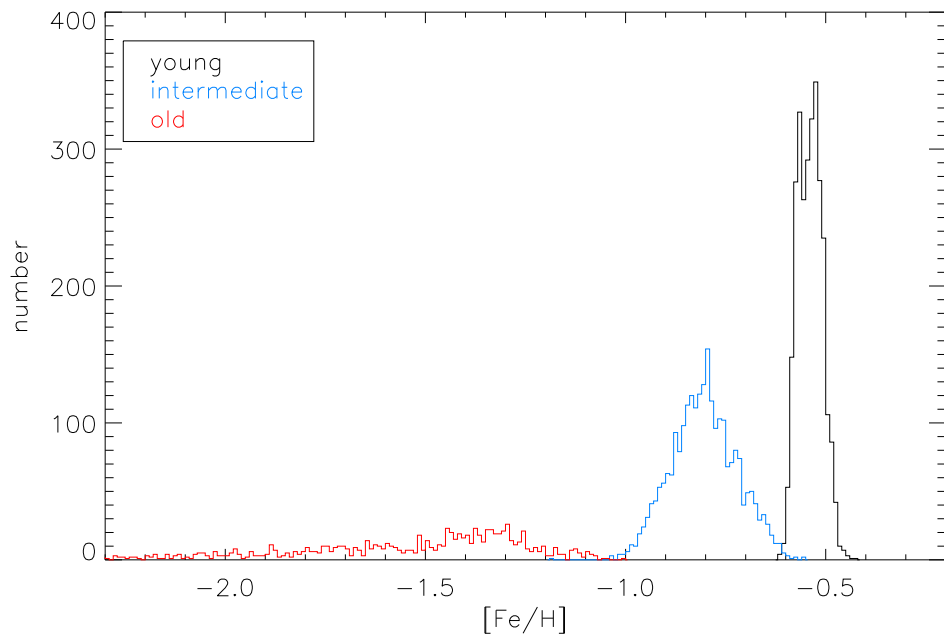


Figure 3.11: The  $[\text{Fe}/\text{H}]$  MDF in the ‘solar neighbourhood’ of 11mKroupa, split into three age intervals: young (black) defined as any star particle in the solar neighbourhood at redshift  $z=0$  with an age less than 1 Gyr; intermediate (blue) defined as any star with an age between 5 and 7 Gyr; old (red) defined as any star with an age greater than 9 Gyr.

## CHAPTER 3

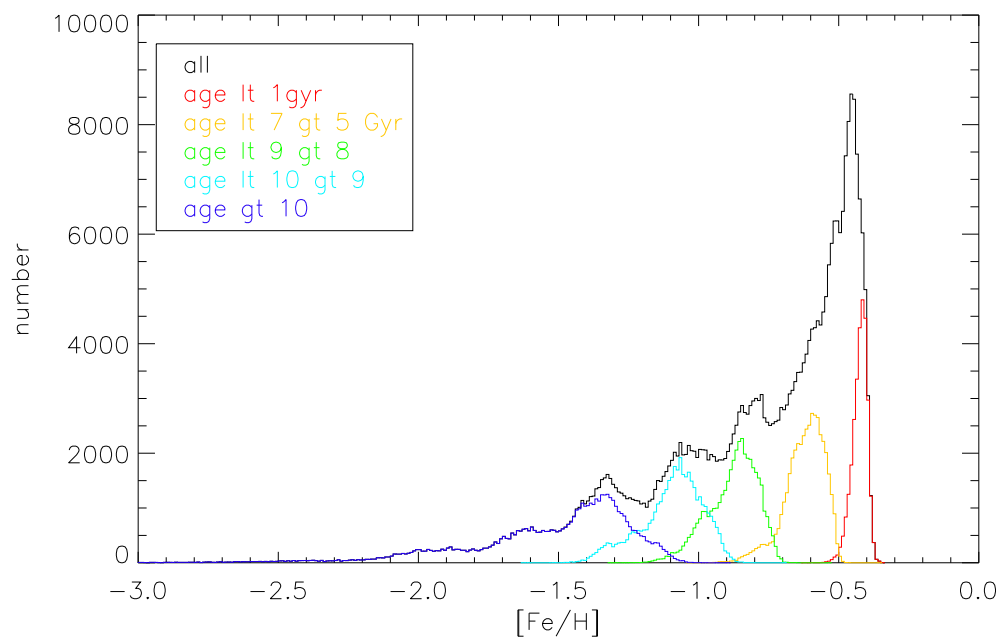


Figure 3.12: The  $[\text{Fe}/\text{H}]$  MDF of the ‘bulge’ of 11mKroupa; here, the bulge is simply defined as those stars located within 2 kpc of the galactic centre at  $z=0$ . Alongside the full MDF (black line), sub-components based upon the age intervals noted in the inset are overdrawn.

## CHAPTER 3

In our simulations, we see systematic trends in age and kinematics for each metallicity sub-component of Fig 3.4, in the sense of the more metal-poor components being older and progressively less rotationally-supported, in exactly the manner one might predict from the AMR (§3.4). It should be emphasised though that within the simulations, the behaviour of these age, metallicity, and kinematic ‘sub-structure’ in the bulge MDF is continuous, rather than showing any discrete transition from rotational support to anisotropic velocity support.

Finally, we now examine in slightly more detail the behaviour of the extreme metal-poor tails of the simulated MDFs (see Figs 3.13 and 3.14). In Fig 3.13, we show all stars beyond the inner 3 kpc (and within 10 kpc), in order to minimise the effect of the ‘spheroid’ stars in the analysis. We experimented, as before, with the impact of using a full kinematic decomposition between disc and spheroid stars, but again, for these dwarfs, the spatial cut alone is indistinguishable from the decomposed galaxy. In Fig 3.14, we only show those star particles lying within the previously defined ‘solar neighbourhoods’ of each simulation.

One additional curve is included in both figures (labeled 109CH), that of the disc generated with the adaptive mesh refinement code RAMSES and described by Few et al. (2012a), in which diffusion is handled ‘naturally’. As noted previously, each of the 11m series of simulations employ the Shen et al. (2010a) metal diffusion framework with a diffusion coefficient  $C=0.05$ , except for (obviously) 11mNoDiff which assumes  $C=0.0$ .

Each of the cumulative MDFs (Figs 3.13 and 3.14) are normalised. In both cases, the normalisation occurs at the  $[\text{Fe}/\text{H}]$  corresponding to the metallicity of the lowest 1% of the stars (in terms of  $[\text{Fe}/\text{H}]$ ). For plotting purposes, these are then aligned arbitrarily at  $[\text{Fe}/\text{H}]\equiv+0.0$ , to show the relative distributions of extremely low-metallicity stars within each simulation and the empirical datasets. One could take a different approach and, say, normalise at (i) the same metallicity, (ii) the same

## CHAPTER 3

amplitude, or (iii) the same number of stars. For example, in our analysis of the Governato et al. (2010) bulgeless dwarf galaxy simulations (Pilkington et al. 2012c), we adopted (i), normalising all MDFs at  $[\text{Fe}/\text{H}]=-2.3$ . This was similar in spirit to Schörck et al. (2009), who fixed the normalisations of the Milky Way halo and Local Group dwarf spheroidal MDFs to be unity at the metallicity corresponding to the lowest (in terms of  $[\text{Fe}/\text{H}]$ )  $\sim 100$  stars in each. For distributions which peak at (potentially) very different metallicities, such normalisations can result in significant outliers which are not necessarily driven by any MDF ‘tail’.<sup>20</sup> For our work here, while small quantitative differences exist depending upon the adopted normalisation, the qualitative results are robust regardless of the choice.

What is immediately clear from even a cursory examination of Fig 3.13 is that the relative distribution of extremely metal-poor stars within all the simulations in which metal diffusion acts - i.e., all but `11mNoDiff` - are consistent with each other. This reflects graphically what we have commented upon earlier in relation to the tabulated ICR and ITPR values for the various MDFs (Table 3.3). Specifically, the lack of metal diffusion within `11mNoDiff` drives its discrepant ICR and ITPR values (Table 3.3), and its outlier status in Fig 3.13. When compared with Fig 5 of Pilkington et al. (2012c), one can see that the overly ‘heavy’ metal-poor tail to the MDF of `11mNoDiff` matches that encountered in, for example, the low metal-diffusion simulations of Governato et al. (2010).<sup>21</sup> One fairly robust conclusion that can be drawn from Fig 3.13 is that the *relative* distribution of *extremely* metal-poor stars is robust against the choice of feedback scheme; instead, diffusion plays a more important role in *shaping* this distribution.

---

<sup>20</sup>In the case of the analysis of Schörck et al. (2009), the similarity of the positions of the peaks of the Milky Way halo and Local Group dSph MDFs meant that their analysis was robust against the choice of normalisation.

<sup>21</sup>Demonstrating the quantitative power of the MDF to constrain the magnitude of diffusion within SPH simulations of galaxy formation.

## CHAPTER 3

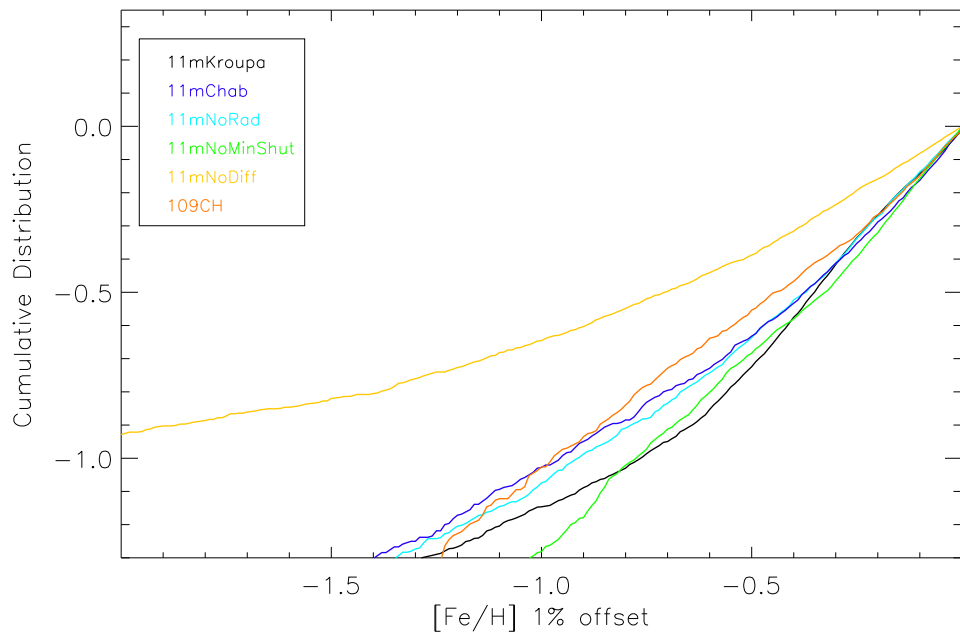


Figure 3.13: The cumulative MDFs of the five 11m simulations: 11mKroupa (black), 11mNoRad (cyan), 11mChab (blue), 11mNoMinShut (green), and 11mNoDiff (gold), in addition to that of 109CH (orange: Few et al. (2012a)). For these six simulations, all stars lying within 3 and 10 kpc of their respective galactic centres are included in the analysis. The normalisation in each case is at the metallicity corresponding to that of the lowest 1% (in terms of  $[\text{Fe}/\text{H}]$ ) of the stars in each case.

## CHAPTER 3

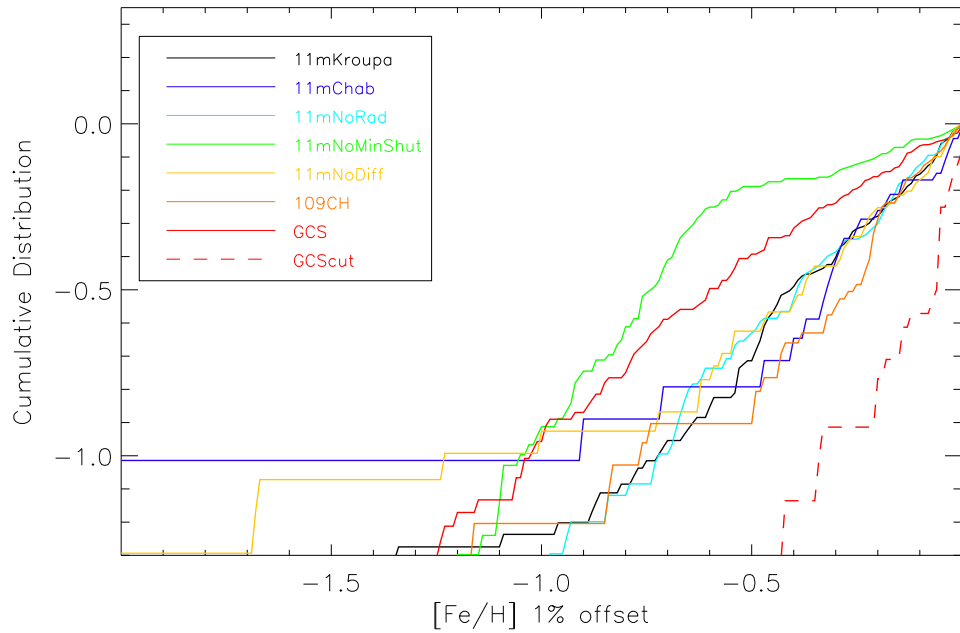


Figure 3.14: The cumulative MDFs of the analogous solar neighbourhoods associated with the five 11m simulations: **11mKroupa** (black), **11mNoRad** (purple), **11mChab** (blue), **11mNoMinShut** (green), and **11mNoDiff** (gold), in addition to that of **109CH** (orange: Few et al. (2012a)). For these six simulations, the solar neighbourhood is defined spatially to include stars lying between 3 and 3.5 disc scale-lengths from their respective galactic centres, and within 0.5 kpc of the mid-plane. The **GCS** and **GCScut** sub-samples described in §3.3 are shown in red. The normalisation for each curve is as described for Fig 3.13.

## CHAPTER 3

In some sense, the better ‘statistics’ afforded by Fig 3.13 provides a ‘cleaner’ picture than that seen when restricting the analysis to just the ‘solar neighbourhoods’.<sup>22</sup> For completeness though, in Fig 3.14 we also show the cumulative MDFs of the metal-poor tails for each dataset, normalised as in Fig 3.13. We should emphasise though that the small number of star particles in the ‘bottom’ 1% (in terms of metallicity) of the `11mNoDiff`, `11mChab`, and `GCScut` samples ( $\sim 30$  in each) make any interpretation susceptible to small-number statistics (and stochastic point-to-point ‘fluctuations’ which are ‘averaged’ over when employed the full disc, as in Fig 3.13).

### 3.6 Summary

Employing a suite of five simulations of an M33-scale late-type disc galaxy, each with the same assembly history, but with different prescriptions for stellar and supernovae feedback, initial mass functions, metal diffusion, and supernova remnant cooling ‘shut-off’ period, we have analysed the resulting chemistry of the stellar populations, with a particular focus on the metallicity distribution functions and the characteristics of the extreme metal-poor tail of said distributions.

In the context of the distribution of metals (in the sense of the higher-order moments of the resulting MDFs) within these discs, the impact of feedback and the IMF is more subtle than that of, for example, metal diffusion. Employing a Chabrier (2003) IMF, rather than the Kroupa et al. (1993) form adopted in our earlier work, does impact significantly on the resulting star formation history (and associated, reduced, stellar mass fraction, resulting in remarkably close adherence to a wide range of empirical scaling relations - Brook et al. (2012b)).

The star formation histories of the ‘solar’ neighbourhoods associated with each

---

<sup>22</sup>And given the lack of any substantial gradient in the stellar populations for these dwarfs, the comparison is not invalid.

## CHAPTER 3

simulation show exceedingly tight age-metallicity relations. In shape, these relations are akin to those predicted by classical galactic chemical evolution models (e.g. Chiappini et al. 2001; Fenner & Gibson 2003), but bear somewhat less resemblance to that seen, for example, in the Milky Way’s solar neighbourhood (Holmberg et al. 2009). These correlated age-metallicity relations result inexorably in (negatively) skewed MDFs with large kurtosis values, when compared with the Milky Way. Star formation histories of dwarf irregulars, which qualitatively speaking are a better match to those of the `11m` series of simulations presented here, suggest though that somewhat steeper age-metallicity relations might eventuate in nature in these environments (e.g. Dolphin et al. 2003; Skillman et al. 2003). MDFs and AMRs of a comparable quality to that of the GCS (Holmberg et al. 2009) will be required to substantively progress the field.

An excess ‘tail’ of extremely metal-poor stars (amongst the bottom 0.1–1% of the most metal-poor stars) –  $\sim 2\text{--}3$  dex below the peak of the MDF – exists in all of the simulations, as reflected in their inter-centile (ICR) and inter-tenth-of-a-percentile (ITPR) region measures. This tail is particularly problematic in simulations without metal diffusion (`11mNoDiff`) and those for which the diffusion coefficient was set relatively low (e.g. Governato et al. 2010; Pilkington et al. 2012c). As demonstrated, the ICR and ITPR, in the absence of metal diffusion, can be  $\sim 30\text{--}3000\times$  larger than that encountered in the Milky Way.

We end with a re-statement of our initial caveat. The simulations presented here (particularly the fiducials, `11mKroupa` and `11mChab`) have been shown to be remarkably consistent with a wide range of scaling relations (Brook et al. 2012b). That said, their star formation histories are more akin to those of NGC 6822, Sextans A, WLM, and to some extent, the LMC (at least in the case of `11mChab`) – i.e., these systems are not ‘clones’ of the Milky Way. We have used the wonderful Geneva-Copenhagen Survey’s wealth of data to generate empirical age-metallicity

## CHAPTER 3

relations and metallicity distribution functions against which to compare, but exact one-to-one matches are not to be expected. That said, they do provide useful, hopefully generic, relations against which to compare. In the future, we hope to extend our analysis to equally comprehensive datasets for the LMC, making use of, for example, the data provided by the Vista Magellanic Cloud Survey (Cioni et al. 2011).

### 3.7 Satellite Galaxies

Of the galaxies in the previous section, three (`11mKroupa`, `11mChab` and `11mNoRad`) have a satellite galaxy within close range of the host. Each satellite lies just over 100 kpc from its host and (at the resolution employed here), there is just the one well-resolved satellite present for each host. The satellites of `11mKroupa`, `11mChab`, and `11mNoRad` have stellar masses of  $2.5 \times 10^6 M_{\odot}$ ,  $1.2 \times 10^6 M_{\odot}$ , and  $6.3 \times 10^6 M_{\odot}$ , respectively; the satellites of `11mKroupa` and `11mChab` have no cold gas particles in their vicinity. The satellite of `11mNoRad` does have (apparent) cold gas particles associated with it, but in fact, they are entirely consistent with being associated with the background particles in the corona of the host - i.e., there is no obvious cold gas associated with this satellite, either.

This lack of cold gas and small distance to the host galaxy makes these satellites seem like good candidates to compare to the Milky Way's dwarf spheroidal (dSph) satellites which are also lacking in any obvious associated cold gas. In hydrodynamical simulations, dSphs (as opposed to, say,  $L^{\star}$  discs) are relatively understudied; Revaz et al. (2009) presented a suite of isolated dSph realisations and found similarities to many of the Local Group dSphs, however they could not reproduce the observed low gas fractions. Comparable non-cosmological and fully cosmological work has also been undertaken (e.g. Stinson et al. 2007; Pilkington et al. 2011; Sawala et al. 2010). There is now a wealth of observational data for Local Group

## CHAPTER 3

dSphs (e.g. Shetrone et al. 1998, 2001; Tolstoy et al. 2003; Venn et al. 2004; Helmi et al. 2006; Aoki et al. 2009; Tolstoy et al. 2009; Venn et al. 2012, and references therein) making them ideal test-beds for pursuit with hydrodynamical simulations. Here, we compare the dSphs present in the three different 11m simulations to various observational constraints, in order to see if the simulations are able to produce something akin to a Local Group dSphs.

Figures 3.15, 3.16, and 3.17 show the star formation history of the satellites. Each shows very low star formation rates throughout their history with the majority of stars being formed at early times ( $t < 5$  Gyr), again similar to the inferred for Local Group dSphs (e.g. van den Bergh 1994; Dolphin et al. 2005). This is most clearly seen in the dwarf associated with 11mKroupa (Fig 3.15) which shows one early burst of star formation followed by very low, intermittent, star formation. The dwarfs associated with 11mChab and 11mNoRad (Figs 3.16 and 3.17) also show a significant early burst of star formation but both present additional, significant, bursts throughout their evolution. For both of the dwarfs, the star formation rate as a function of time is essentially exponentially declining.

Dolphin et al. (2005) categorise the Local Group dwarfs into either irregulars (dIrr) or spheroidals (dSph), depending on their star formation over the past  $\sim 1$  Gyr. They found that none of the local dSphs showed any evidence for significant star formation in the past  $\sim 100$  Myr. The simulated dSphs shown here similarly show no star formation over the past  $\sim 1$  Gyr, in agreement with Dolphin et al. (2005).

Next, we show the MDF of each of the satellites (Figs 3.18, 3.19, and 3.20). Kirby et al. (2011a) showed the MDF of many of the Local Group dSphs, as well as the predictions from analytical chemical evolution models (the data we employed for the Fornax dwarf in Fig 3.5 was taken from Kirby et al.). The MDFs for the three dwarfs are typical of those in the local group dSphs Kirby et al. (2011a) they all show a mean metallicity around  $\sim 1.5$  dex similar to Leo I, Leo II and Sculptor. The MDFs

## CHAPTER 3

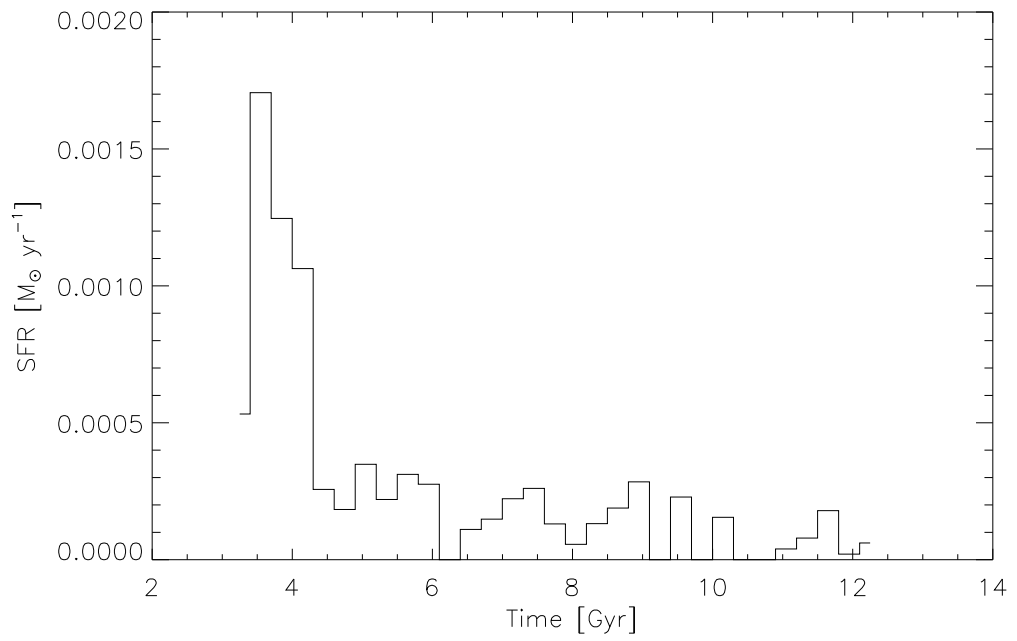


Figure 3.15: Star formation rate as a function of time for the satellite associated with 11mKroupa.

## CHAPTER 3

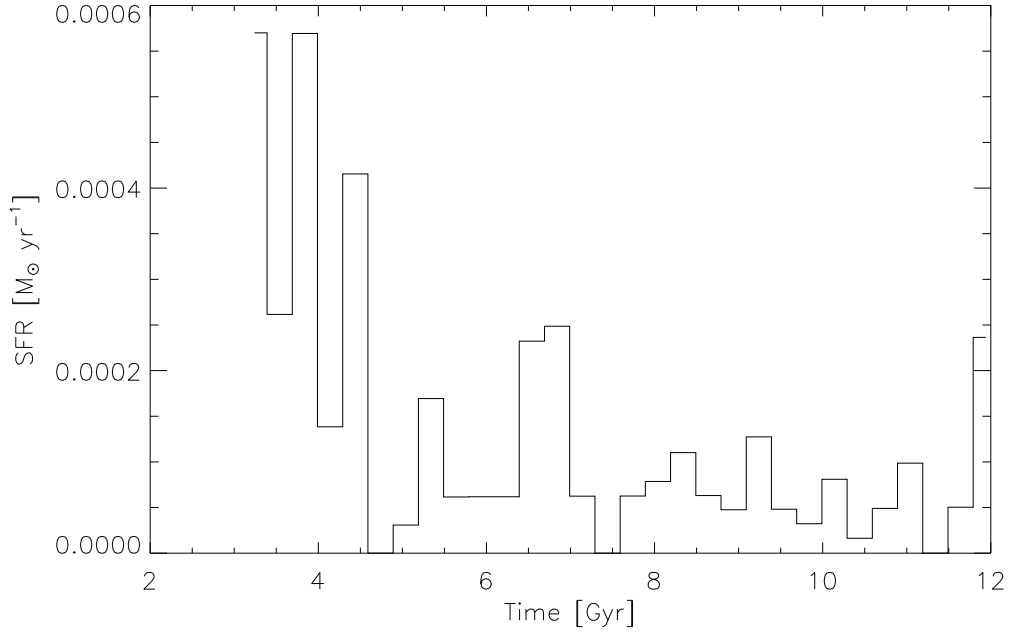


Figure 3.16: Star formation rate as a function of time for the satellite associated with 11mChab.

here have not been convolved with a Gaussian corresponding to the typical empirical uncertainties, as in Figure 3.5; they are, instead, the raw MDFs, as in Figures 3.11 and 3.12. Because of the limited number of stellar particles associated with each of the satellites (Kroupa: 456; Chab: 255; NoRad: 1109), such convolution tended to result in an overly aggressive ‘blurring’ of the results; hence, we have avoided doing so, at least for these (marginally resolved) satellites.

Now, we show the age-metallicity relation for the same three satellites (Figs 3.21, 3.22, and 3.23). Figure 3.4 shows the age-metallicity relation observed in two Local Group dwarf irregulars, Sextans A Dolphin et al. (2003) and IC 1613 Skillman et al. (2003). While not dSphs, they provide useful comparators for the simulated age-metallicity relations. The observed relations show a steady increase from  $[\text{Fe}/\text{H}] \sim -1.5$  to  $[\text{Fe}/\text{H}] \sim -0.8$  which is much flatter than that seen in the simulated dwarfs; observationally, the systems do not show evidence for the presence of many

### CHAPTER 3

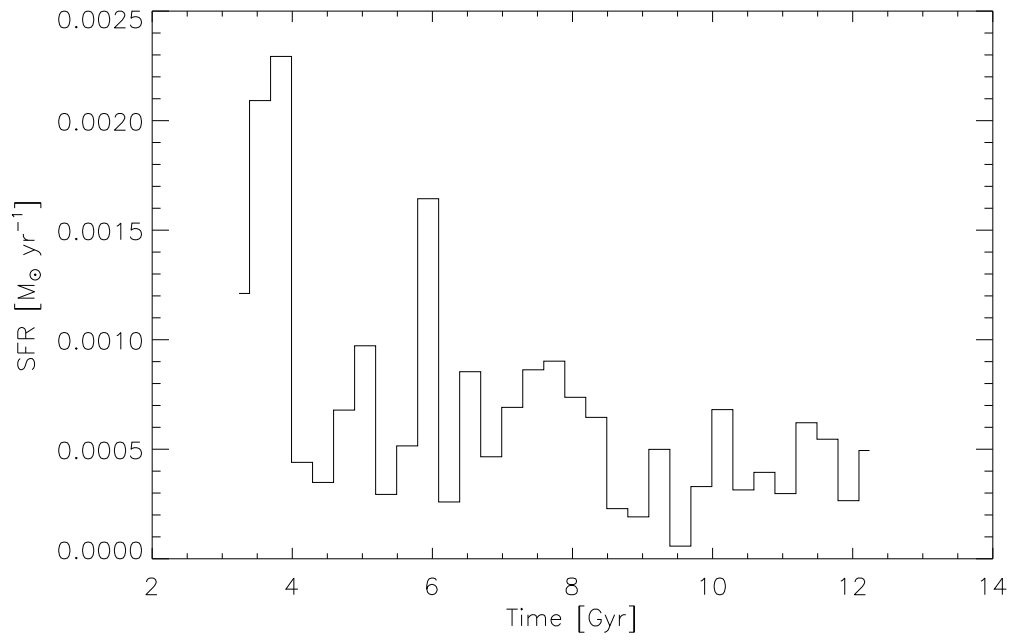


Figure 3.17: Star formation rate as a function of time for the satellite associated with 11mNoRad.

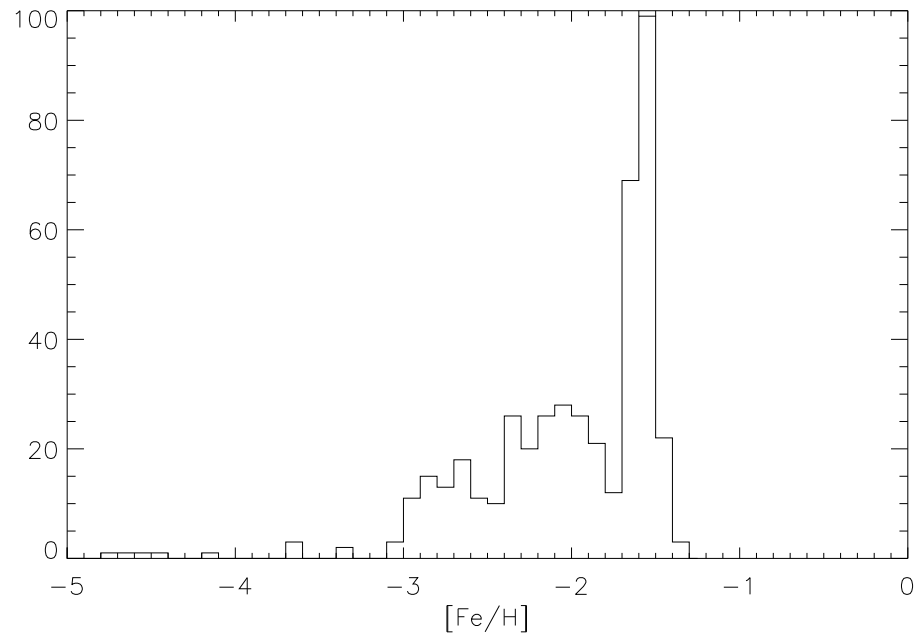


Figure 3.18: Raw MDF of the satellite associated with 11mKroupa.

## CHAPTER 3

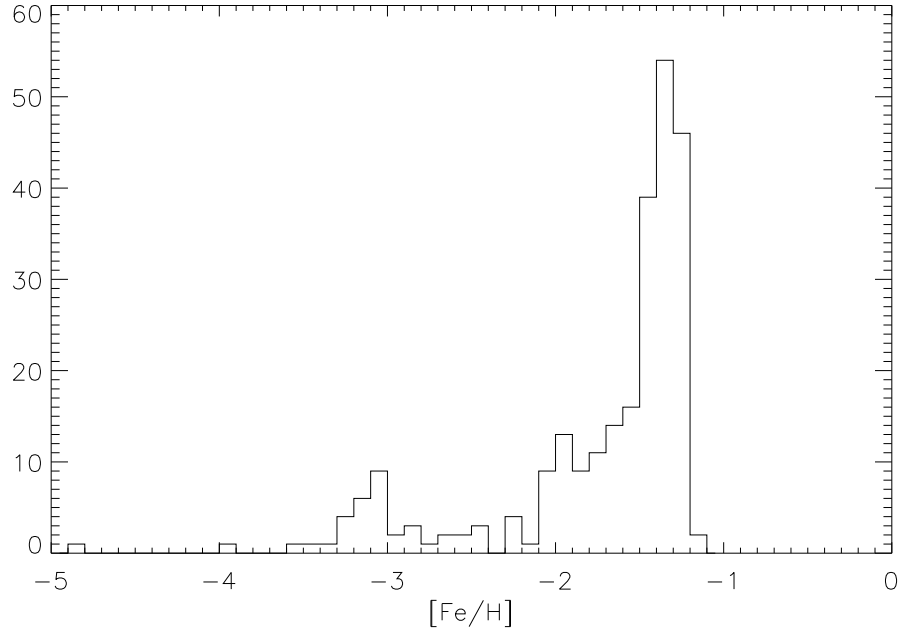


Figure 3.19: Metallicity distribution function of the satellite associated with 11mChab.

(very) low metallicity stars, contrary to that encountered in the simulations. Each of the simulated age-metallicity relations shows an initial rapid increase in metallicity (for the first  $\sim 5$  Gyr) followed by relatively flat behaviour. Tolstoy et al. (2003) shows the age-metallicity relation for several elements in the dSphs Sculptor, Fornax, Carina, and Leo I, finding a significant spread in metallicity for a given age. The three simulated satellites show a large spread in metallicity at earlier epochs but are much more tightly correlated at later times. Without much larger observational datasets against which to compare our work, it is difficult to draw any deeper conclusions.

Finally, we show the abundance ratios for stars associated with each of the three (satellite) dSphs (Figs 3.24, 3.25, and 3.26). In the version of GASOLINE used to run these simulations, oxygen, iron, carbon, nitrogen, and neon are tracked, as well as the overall metallicity (§3.3). In the following plots, we focus on oxygen and iron

## CHAPTER 3

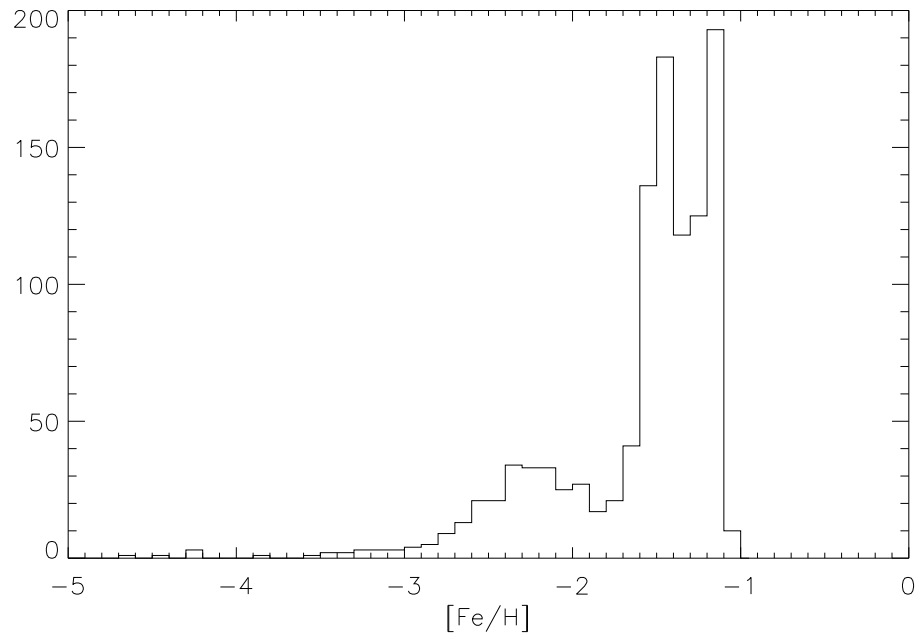


Figure 3.20: Metallicity distribution function of the satellite associated with 11mNoRad.

and leave carbon, nitrogen, and neon for future work.

The alpha-elements as a function of  $[\text{Fe}/\text{H}]$  are a well-studied relation in systems such as the Local Group dwarfs, with the ratios being a powerful probe of star formation / supernova enrichment timescales. Within the Milky Way itself, we observe a fairly ‘flat’ evolution in  $[\text{O}/\text{Fe}]$  as a function of  $[\text{Fe}/\text{H}]$  until a certain (critical) metallicity is reached (around  $[\text{Fe}/\text{H}] \cong -1$ ; see Venn et al. (2004)); beyond this so-called ‘knee’, there is seen a decrease in  $[\text{O}/\text{Fe}]$  as the contribution from Type Ia supernovae begins to impact upon the iron content substantially (e.g. Tinsley 1979).

This ‘knee’ seen in the Milky Way’s abundance patterns is also seen in dwarf galaxies. Venn & Hill (2008) shows the  $[\text{O}/\text{Fe}]$  abundance ratio for Sagittarius, Fornax, Carina, and the Large Magellanic Cloud (LMC). Venn & Hill find that each dSph has a different position for the ‘knee’, tied to the specific chemical evolution for each

## CHAPTER 3

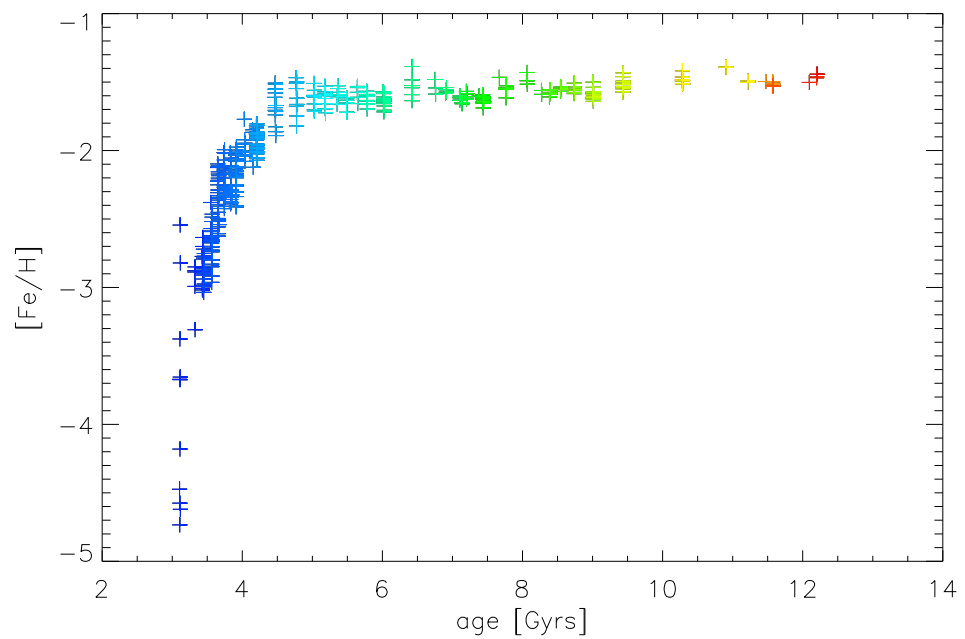


Figure 3.21: Age-metallicity relation of the satellite associated with 11mKroupa. Colour-coding is according to age, with bluer colours showing the older star particles and redder colours showing the younger particles.

## CHAPTER 3

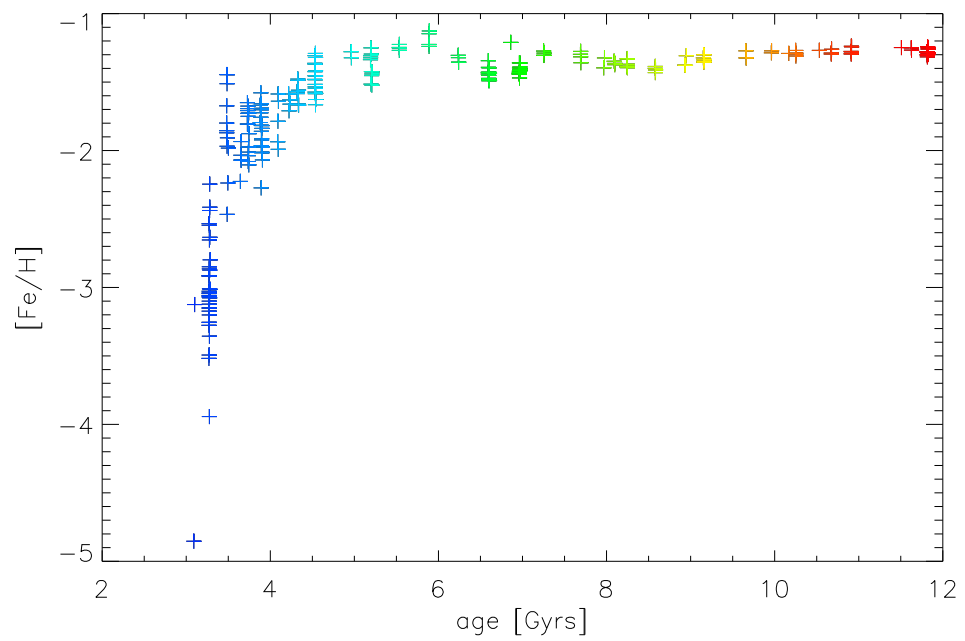


Figure 3.22: Age-metallicity relation of the satellite associated with 11mChab. Colour-coding according to age, with the oldest stars having bluer colours and the youngest stars having redder colours.

## CHAPTER 3

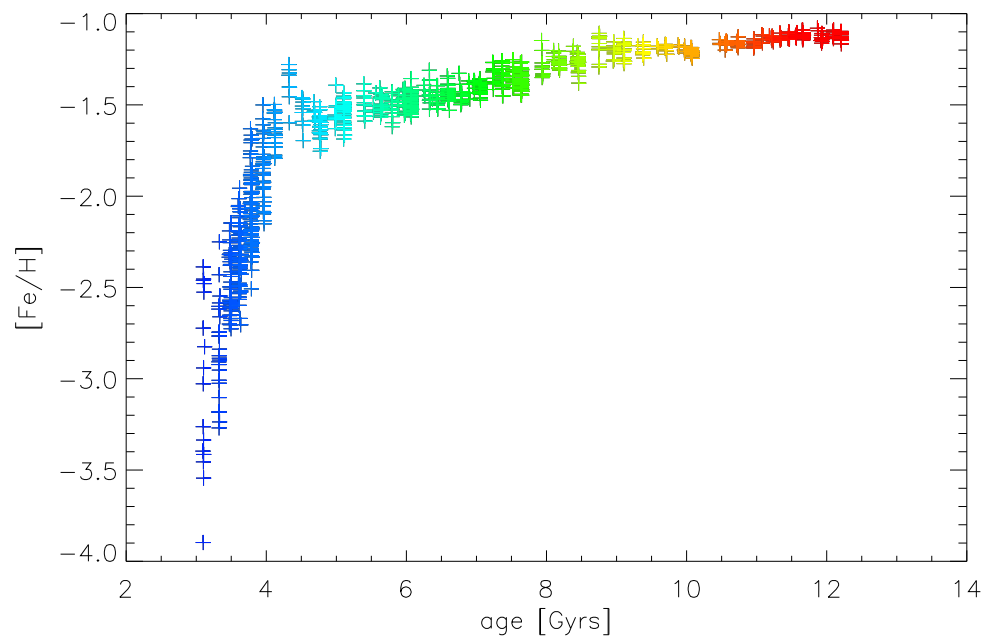


Figure 3.23: Age-metallicity relation for the satellite associated with 11mNoRad. The star particles are colour-coded by age with older stars progressively bluer and younger stars progressively redder.

## CHAPTER 3

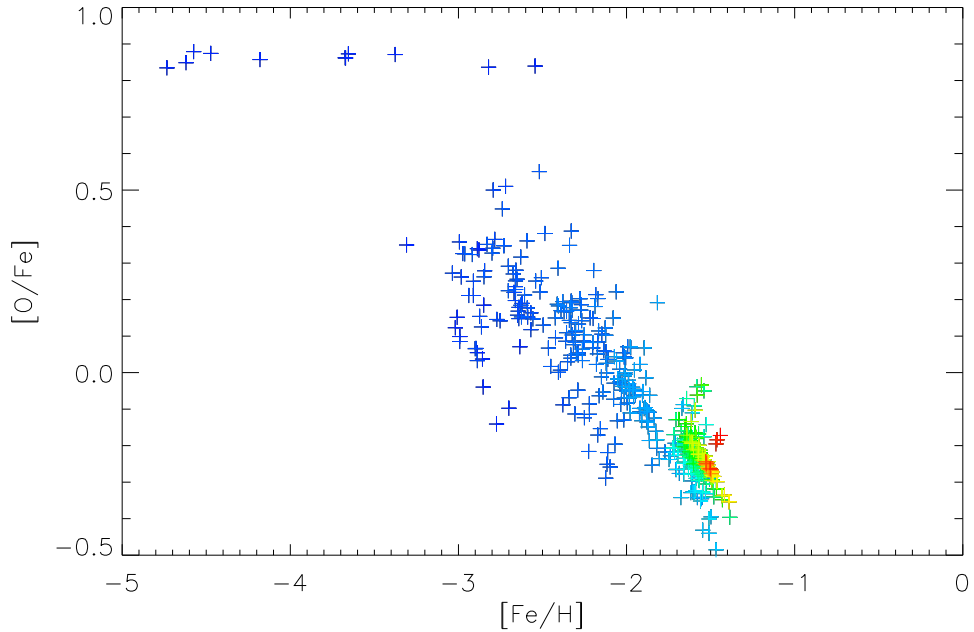


Figure 3.24:  $[O/Fe]$  as a function of  $[Fe/H]$  for the satellite associated with 11mKroupa. The star particles are coloured as in Figure 3.21, with the oldest star particles in blue and the youngest in red.

system. Sculptor was the only dSph for which the knee’s position could be derived precisely, due simply to statistics; they found the knee to be near  $[Fe/H] \sim -1.8$  (cf.  $-1$  for the Milky Way).

In the simulations for each of the satellite, a large spread in  $[O/Fe]$  is seen ( $\sim 0.5$  dex larger than observed) but there is no distinct ‘knee’ present in any of the relevant distributions. Each show a smooth decreasing trend of  $[O/Fe]$ , albeit at what appears to be somewhat steeper than that seen in the Local Group dSphs (Venn & Hill 2008).

### 3.7.1 Conclusions

This section provides a brief examination of the (dSph-like) satellites associated with the 11m suite of M33-like simulations. Here, we re-iterate that the satellites

## CHAPTER 3

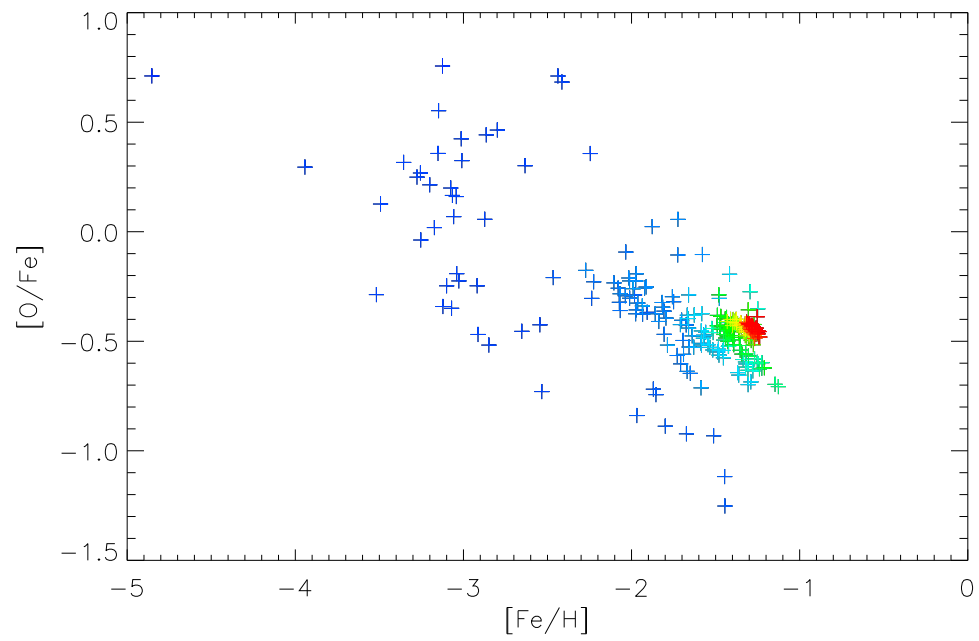


Figure 3.25:  $[O/Fe]$  as a function of  $[Fe/H]$  for the satellite associated with 11mChab. The star particles are coloured according to age with the bluer (redder) colours representing older (younger) ages (as in Figure 3.22).

## CHAPTER 3

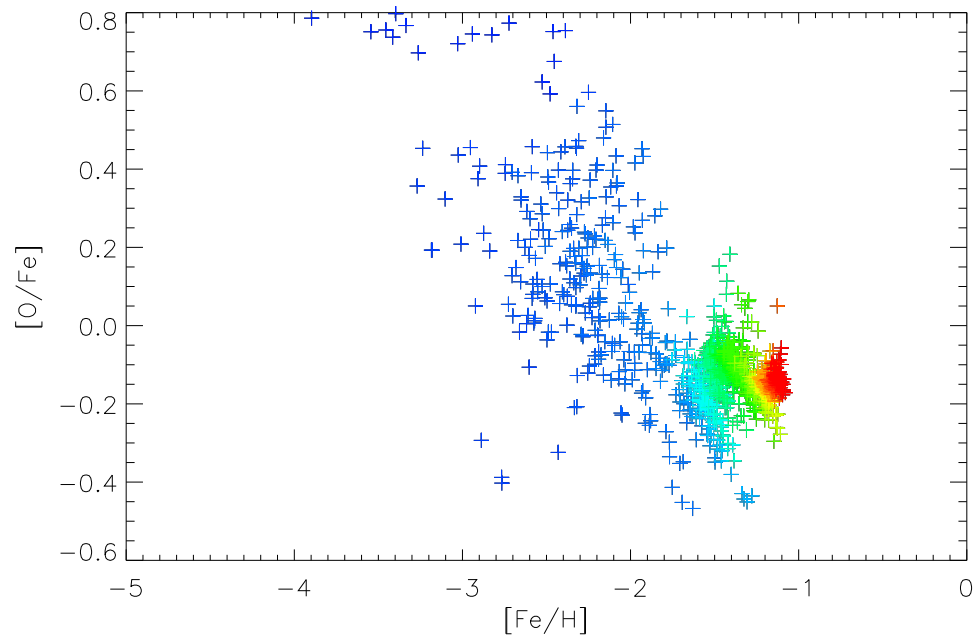


Figure 3.26:  $[O/Fe]$  as a function of  $[Fe/H]$  for the satellite associated with 11mNoRad. The star particles are coloured according to age, as in Figure 3.23, with older (younger) stars in blue (red).

## CHAPTER 3

are drawn from `11mKroupa`, `11mChab`, and `11mNoRad` (one from each); the subtle differences in the employed sub-grid physics are listed in Table 3.1.

Each of the star formation histories is similar to that expected from Local Group dSphs (e.g. Dolphin et al. 2003), resulting in MDFs which are also in good agreement with observation (e.g. Kirby et al. 2011a). There are very few observational constraints on the age-metallicity relations for Local Group dwarfs (e.g. Tolstoy et al. 2003; Dolphin et al. 2005, and references therein), and the limited existing data possess such large uncertainties as to make it difficult to infer the direction and magnitude of any underlying trend(s). As in the `11m` simulations described in the previous section, it appears that the age-metallicity relations in these satellites are overly ‘correlated’ (see §3.4). Finally, the  $[\text{O}/\text{Fe}]-[\text{Fe}/\text{H}]$  abundance ratio distribution shows a steeper behaviour than that observed (e.g. Venn & Hill 2008), in addition to greater scatter in  $[\text{O}/\text{Fe}]$  at a given  $[\text{Fe}/\text{H}]$ .

The initial (and admittedly, cursory) analysis of these (satellite) dSphs really calls for further study of additional cosmological dSphs embedded within the halo of massive hosts (something which has *not* been attempted before this work); regardless, we summarise our conclusions here, in order to point the way forward, if nothing else:

1. Examine earlier timesteps, to better quantify their orbital histories, in order to better make direct comparisons with the orbital patterns of the Local Group dSphs (e.g. Pasetto et al. 2011).
2. Examine the interactions (if any) with the host galaxy; this will enable us to see if any stripping of the cold gas has occurred and if there has been any loss (or gain) of stars due to tidal interactions (e.g. Nichols & Bland-Hawthorn 2011, and references therein).
3. Examine the birth place of every star formed throughout the simulation volume, to assess whether any stars are now ‘missing’ from the present-day dSph

## CHAPTER 3

and, if so, where said ‘stripped’ stars now reside.

4. Compare in a more systematic manner the abundance patterns of stars in the simulated dSphs with those in the halo stars of the associated host (11m) galaxies (e.g. Venn et al. 2004, and references therein).

# Chapter 4

## Metallicity Gradients in Disk Galaxies

### 4.1 Abstract

We examine radial and vertical metallicity gradients using a suite of disk galaxy hydrodynamical simulations, supplemented with two classic chemical evolution approaches. We determine the rate of change of gradient slope and reconcile the differences existing between extant models and observations within the canonical “inside-out” disk growth paradigm. A suite of 25 cosmological disks is used to examine the evolution of metallicity gradients; this consists of 19 galaxies selected from the RaDES (Ramses Disk Environment Study) sample (Few et al. 2012b), realised with the adaptive mesh refinement code RAMSES, including nine drawn from the ‘field’ and ten from ‘loose group’ environments. Four disks are selected from the MUGS (McMaster Unbiased Galaxy Simulations) sample (Stinson et al. 2010), generated with the smoothed particle hydrodynamics (SPH) code GASOLINE, alongside disks from Rahimi et al. (2011) (GCD+) and Kobayashi & Nakasato (2011) (GRAPE-SPH). Two chemical evolution models of inside-out disk growth Chiappini

## CHAPTER 4

et al. (2001); Mollá & Díaz (2005) were employed to contrast the temporal evolution of their radial gradients with those of the simulations. We first show that generically flatter gradients are observed at redshift zero when comparing older stars with those forming today, consistent with expectations of kinematically hot simulations, but counter to that observed in the Milky Way. The vertical abundance gradients at  $\sim 1-3$  disk scalelengths are comparable to those observed in the thick disk of the Milky Way, but significantly shallower than those seen in the thin disk. Most importantly, we find that systematic differences exist between the predicted evolution of radial abundance gradients in the RaDES and chemical evolution models, compared with the MUGS sample; specifically, the MUGS simulations are systematically steeper at high-redshift, and present much more rapid evolution in their gradients. We find that the majority of the models predict radial gradients today which are consistent with those observed in late-type disks, but they evolve to this self-similarity in different fashions, despite each adhering to classical ‘inside-out’ growth. We find that radial dependence of the efficiency with which stars form as a function of time drives the differences seen in the gradients; systematic differences in the sub-grid physics between the various codes are responsible for setting these gradients. Recent, albeit limited, data at redshift  $z \sim 1.5$  are consistent with the steeper gradients seen in our SPH sample, suggesting a modest revision of the classical chemical evolution models may be required.

### 4.2 Introduction

The recognition that metals are not distributed homogeneously throughout the disk of the Milky Way (Shaver et al. 1983) has proven to be fundamental in our efforts to understand the role of interactions, mergers, accretion, migration, and gas flows, in shaping the formation and evolution of galaxies. A rich literature now exists which confirms these radial abundance trends in both spirals (e.g. Simpson et al. 1995;

## CHAPTER 4

Afflerbach et al. 1997; Mollá et al. 1999; Carrera et al. 2008; Kewley et al. 2010; Sánchez-Blázquez et al. 2011) and ellipticals (e.g. Kormendy & Djorgovski 1989; Franx & Illingworth 1990; Peletier et al. 1990). Vertical trends have been studied somewhat less frequently (e.g. Marsakov & Borkova 2005, 2006; Soubiran et al. 2008; Navarro et al. 2011), but provide unique insights into the discrete nature (or lack thereof) of the thin disk – thick disk interface (and associated kinematical heating processes).

Observations of nearby spiral galaxies show that the inner disks have higher metallicities than their associated outer disk regions; at the present day, typical gradients of  $\sim -0.05$  dex/kpc are encountered. These somewhat shallow gradients have provided *critical* constraints on models of galaxy formation and evolution, and are fundamental to the predictions of the classical “inside-out” paradigm for disk growth. Predictions have been made of the time evolution of metallicity gradients in chemical evolution models (e.g. Mollá et al. 1997; Fu et al. 2009) and observationally from planetary nebulae (e.g. Maciel et al. 2003), although until recently, we have had essentially no *direct* observational constraints on what the magnitude of the time evolution of the gradients should be. This has changed with the work of Cresci et al. (2010), Jones et al. (2010), Queyrel et al. (2011), and Yuan et al. (2011), who have, for the first time, extended radial abundance gradient work to high redshifts. Yuan et al. (2011) show that for at least one “Grand Design” disk at redshift  $z \sim 1.5$ , the metallicity gradient is significantly steeper ( $-0.16$  dex/kpc) than the typical gradient encountered today.<sup>1</sup> Constraining the metallicity gradients of

---

<sup>1</sup>At even higher redshifts ( $z \sim 3.3$ ), Cresci et al. (2010) and Troncoso et al. (2013, in prep), as part of the AMAZE/LSD surveys, suggest that *both* inverted gradients (higher abundances in the outskirts, relative to the inner disk) *and* standard declining gradients are seen. From the latter surveys, inverted gradients (ranging from  $+0.0$  to  $+0.1$  dex/kpc) appear associated with very massive stellar disks at these high-redshifts ( $M_* > 3 \times 10^9 M_\odot$ ), while declining gradients (ranging from  $-0.0$  to  $-0.2$  dex/kpc) appear associated with lower mass stellar disks ( $M_* < 3 \times 10^9 M_\odot$ ). Cresci et al. (2010) suggest that the inverted gradients are due perhaps to recent infall of pristine

## CHAPTER 4

galaxies beyond the local Universe remains a challenge for the future.

Using SPH simulations of disk galaxy mergers, Rupke et al. (2010a) show strong correlations of metallicity with environment and merger history, focussing on the effects of gas inflows and star formation rate. Observations by Cooper et al. (2008) show that higher metallicity galaxies are more abundant in group environments and Kewley et al. (2006) showed that interacting pairs of galaxies have systematically lower metallicities ( $\sim 0.2$  dex lower) than field galaxies or more loosely associated pairs. Radial gradients have been shown to flatten for galaxies that have experienced recent mergers (Kewley et al. 2010); these also result in higher velocity dispersions and redistribution of the cold gas. In agreement with this, Michel-Dansac et al. (2008) studied the mass-metallicity relation for merging galaxies and concluded that the infall of metal poor gas during merger events lowers the gas phase metallicity. However, the timescale over which redistributed gas develops into a gradient like those we see in spiral galaxies today is unknown.

There have been several studies of chemistry within cosmological hydrodynamical simulations (e.g. Raiteri et al. 1996b; Kawata & Gibson 2003; Okamoto et al. 2008; Scannapieco et al. 2008; Zolotov et al. 2010; Rahimi et al. 2010; Wiersma et al. 2011; Kobayashi & Nakasato 2011), each modelling certain observational properties with varying degrees of success. Some studies have examined the radial and/or vertical gradients using hydrodynamical codes (e.g. Rupke et al. 2010a; Rahimi et al. 2011), but the numerical study of radial gradients has predominantly been in the context of classical galactic chemical evolution codes (e.g. Prantzos & Boissier 2000; Chiappini et al. 2001; Mollá & Díaz 2005). In this chapter, we use 25 simulations realised with four different cosmological hydrodynamical codes: GASOLINE (Wadsley et al. 2004), material into the inner disk. These Lyman Break Galaxies, with their  $\sim 1-2$  orders of magnitude greater star formation rates (relative to the typical Milky Way progenitor at that redshift), are more likely associated with massive spheroids in clusters/groups today (e.g. Nagamine 2002), as opposed to the Milky Way, and so are not directly comparable with the simulations described here.

## CHAPTER 4

GRAPE-SPH (Kobayashi & Nakasato 2011) and GCD+ (Kawata & Gibson 2003), all gravitational N-Body + Smoothed Particle Hydrodynamic (SPH) (Monaghan 1992) codes, and RAMSES (Teyssier 2002), an Adaptive Mesh Refinement (AMR) code. Alongside these, we use the results from the chemical evolution models of Chiappini et al. (2001) and Mollá & Díaz (2005).

Our work aims to fill an important gap in the field, by complementing orbital parameter studies (e.g. Rupke et al. 2010a; Perez et al. 2011), systematic sub-grid physics parameter studies (e.g. Wiersma et al. 2011), and detailed dissections of individual systems (e.g. Rahimi et al. 2011; Zolotov et al. 2010; Kobayashi & Nakasato 2011), with a statistical sample of Milky Way-like analogs. Our approach is different, but complementary, to the careful and compelling parameter study of Wiersma et al. (2011); their, the goal was to vary the input physics and examine the outcome, regardless of whether or not the simulated end-products might be classified still as Milky Way-like. Instead, we have sampled a range of codes, sub-grid physics, and initial conditions, each of which has been ‘calibrated’, in some sense, by their respective authors, to resemble a classical Milky Way-like system. With that calibrated sample, our unique contribution is to examine the ‘path’ by which the gradients evolve, search for both random and systematic trends/differences between the samples, and compare with new empirical data at high-redshift.<sup>2</sup> *This is the first time such a comparison of the temporal evolution of metallicity gradients has been undertaken with a statistical sample of simulated disk galaxies.*

The outline of the chapter is as follows. The main differences between the codes are described in §4.3, where we concentrate primarily upon the relevant mechanisms associated with the treatment of star formation and feedback (both energetic and

---

<sup>2</sup>In spirit, this is exactly the approach taken in the seminal Galactic Chemical Evolution Comparison Project (Tosi 1996), which examined the time evolution of classic chemical evolution models *calibrated* to the solar neighbourhood, in order to see where they differed ‘away’ from this calibrated boundary condition.

chemical). The metallicity gradients inferred today for stellar populations of different ages are presented in §4.4. This is expanded upon in §4.5 where the radial metallicity gradients of the young stellar population as a function of redshift are considered. Finally, we summarise our findings in §4.7.

## 4.3 Simulations

The simulations used in this paper are fully described in Stinson et al. (2010: MUGS), Rahimi et al. (2011: Gal1), Kobayashi & Nakasato (2011: KN11) and Few et al. (2012b: RaDES); the main characteristics of the simulations and their parent codes are described here and itemised in Table 4.1. The chemical evolution models are fully described in Chiappini et al. (2001) and Mollá & Díaz (2005), but again we describe the main aspects in the following section.

### 4.3.1 MUGS

The MUGS galaxies were run using the gravitational N-body + SPH code GASOLINE which was introduced and described in Wadsley et al. (2004). Below, we emphasise the the main points concerning the star formation and feedback sub-grid physics used to generate this suite of simulations, but first remind the reader of the background framework in which they were evolved, in addition to their basic characteristics.

The MUGS sample (Stinson et al. 2010) consists of 16 galaxies randomly drawn from a cosmological volume  $50h^{-1}$  Mpc on a side, evolved in a Wilkinson Microwave Anisotropy Probe Three (WMAP3)  $\Lambda$ CDM cosmology with  $H_0 = 73 \text{ km s}^{-1} \text{ Mpc}^{-1}$ ,  $\Omega_m = 0.24$ ,  $\Omega_\Lambda = 0.76$ ,  $\Omega_b = 0.04$ , and  $\sigma_8 = 0.76$ . Each galaxy is resimulated at high resolution by using the volume renormalisation technique (Klypin et al. 2001), with a gravitational softening length of 310 pc. The galaxies range in mass from  $5 \times 10^{11} M_\odot$  to  $2 \times 10^{12} M_\odot$ . The four galaxies with the most prominent disks<sup>3</sup> were

---

<sup>3</sup>By ‘prominent’, we mean the inclusion of those for which there was unequivocal identification

CHAPTER 4

Suite	Galaxy	$M_{\text{Tot}}$	$M_{*,\text{disk}}$	$r_{\text{disk}}$	Environment	$d[Z_{*,\text{all}}]/dh$	$d[Z_{*,\text{young}}]/dR$
	Galaxy	( $10^{11}M_{\odot}$ )	( $10^{10}M_{\odot}$ )	(kpc)		(dex/kpc)	(dex/kpc)
MUGS	g15784	14.0	5.9	3.2	Field	-0.05	-0.04
	g422	9.1	2.0	2.8	Field	-0.06	-0.08
	g1536	7.0	3.3	2.5	Field	-0.07	-0.05
	g24334	7.7	2.7	1.0	Field	-0.03	-0.19
GCD+	Gal1	8.8	4.1	2.7	Field	-0.04	-0.01
Grape-SPH	KN11	11.0	2.0	4.7	Field	-0.03	-0.04
RaDES	Castor	10.5	7.2	4.0	Loose Group	-0.17	-0.03
	Pollux	4.2	3.4	3.0	Loose Group	-0.06	-0.05
	Tyndareus	3.3	1.3	1.3	Loose Group	-0.02	-0.05
	Zeus	2.3	1.0	1.7	Loose Group	-0.07	-0.04
	Apollo	8.9	6.3	3.0	Loose Group	-0.04	-0.06
	Artemis	7.5	3.2	1.9	Loose Group	-0.08	-0.05
	Daphne	3.1	2.1	2.7	Loose Group	-0.03	-0.06
	Leto	2.5	1.2	1.8	Loose Group	-0.04	-0.05
	Luke	11.3	6.6	5.4	Loose Group	-0.01	-0.03
	Leia	3.9	3.0	4.1	Loose Group	-0.05	-0.02
	Tethys	7.2	5.1	2.8	Field	-0.08	-0.05
	Krios	5.7	4.0	2.5	Field	-0.10	-0.05
	Atlas	6.5	4.4	2.8	Field	-0.06	-0.04
	Hyperion	10.0	7.7	3.6	Field	-0.07	-0.04
	Eos	4.6	2.5	2.0	Field	-0.19	-0.07
	Helios	10.5	6.6	1.6	Field	-0.11	-0.04
	Selene	6.1	5.2	3.5	Field	-0.05	-0.06
Oceanus	11.0	10.0	6.6	Field	-0.03	-0.03	
Ben	7.7	4.2	3.9	Field	-0.04	-0.03	

Table 4.1: Basic present-day ( $z=0$ ) characteristics of the 25 simulated disks. Column (1): simulation suite to which the the code used to simulate the galaxy (Column (2)) belongs; Column (3): total (dynamical) mass within the virial radius; Column (4): mass of the stellar disk, after application of the kinematic and spatial cuts described in § 4.4; Column (5): exponential scalelength of the stellar disk; Column (6): local environment of the galaxy; Column (7): mass-weighted vertical stellar abundance gradient, averaged over the radial range  $1.5 < r_{\text{disk}} < 2.5$ ; Column (8): mass-weighted radial *young* (stars born within the past 100 Myrs) stellar abundance gradient, after application of the kinematic and spatial cuts described in § 4.4.

## CHAPTER 4

selected: g422<sup>4</sup>, g1536, g24334, and g15784, the latter of which is the closest to a Milky Way analog in the sample.

Star formation and supernovae feedback uses the blastwave model (Stinson et al. 2006) whereby gas particles can form stars when they are sufficiently dense ( $>1 \text{ cm}^{-3}$ ) and cool ( $<15000 \text{ K}$ ). Gas particles which satisfy these criteria can form stars according to the equation  $\frac{dM_{\star}}{dt} = c^{\star} \frac{M_{gas}}{t_{dyn}}$ , where  $c^{\star}$  is the star formation efficiency and is fixed to be 0.05.  $M_{gas}$  is the mass of the gas particle forming the star particle of mass  $M_{\star}$  and  $t_{dyn}$  is the dynamical time of the gas. Heating from a uniform ultraviolet ionising background radiation field (Haardt & Madau 1996) is employed, and cooling is derived from the contributions of both primordial gas and metals; the metal cooling grid is derived using CLOUDY (v.07.02: Ferland et al. (1998)), under the assumption of ionisation of equilibrium, as detailed by Shen et al. (2010b).

The chemical evolution model used in GASOLINE is fully described in Raiteri et al. (1996a); here, we only discuss the main points. All stars with masses above  $8 M_{\odot}$  explode as Type II supernova (SNeII). An efficiency factor couples 40% of a given supernova’s energy ( $10^{51} \text{ erg}$ ) to the surrounding interstellar medium (ISM). The metals that are tracked in this version of GASOLINE (O and Fe) all come from supernovae and are allowed to diffuse between neighbouring SPH particles, after Shen et al. (2010b). The Type Ia supernovae (SNeIa) eject iron and oxygen; for every SNIa,  $0.76 M_{\odot}$  of ‘metals’ is ejected, divided between iron ( $0.63 M_{\odot}$ ) and oxygen ( $0.13 M_{\odot}$ ). Our binary model for Type Ia supernovae is based upon the 

---

of the disk (from angular momentum arguments constructed from the gas and young star distributions, as discussed in §3.1. In a secondary sense, this eliminated extreme values of bulge-to-total, but formally, we only included those disks for which alignment based upon the gas/young stars was obvious.

<sup>4</sup>g422 was not described in the original MUGS paper (Stinson et al. 2010); it was produced identically to the MUGS suite and will be described fully in an upcoming paper.

## CHAPTER 4

single-degenerate progenitor formalism of Greggio & Renzini (1983), with secondaries spanning in mass from 1.5 to 8.0  $M_{\odot}$ .<sup>5</sup> Enrichment from SNeII is based upon power law fits in stellar mass to the nucleosynthesis yield tables of Woosley & Weaver (1995), convolved with a Kroupa (Kroupa et al. 1993) initial mass function (IMF), in order to determine the mass fraction of metals ejected. The total metallicity in this version of the code is tracked by assuming  $Z \equiv O + Fe$ .<sup>6</sup> For these runs, only the  $Z = Z_{\odot}$  yields were used, and long-lived SNeIa progenitors (those with secondaries with mass  $m < 1.5 M_{\odot}$ ) were neglected.

### 4.3.2 Gal1

Gal1 is a higher-resolution re-simulation of galaxy D1 from Kawata et al. (2004) using the SPH code GCD+ (Kawata & Gibson 2003); while its characteristics have been discussed previously by Bailin et al. (2005), Rahimi et al. (2010), and Rahimi et al. (2011), an overview is provided here for completeness. Employing a comparable volume renormalisation / ‘zoom-style’ technique to that described in § 4.3.1 (with a gravitational softening of 570 pc in the highest resolution region), Gal1 was realised within a  $\Lambda$ CDM cosmological framework with  $H_0 = 70 \text{ km s}^{-1} \text{ Mpc}^{-1}$ ,  $\Omega_m = 0.3$ ,  $\Omega_{\Lambda} = 0.7$ ,  $\Omega_b = 0.04$ , and  $\sigma_8 = 0.9$ , resulting in a Milky Way analog of virial mass  $8.8 \times 10^{11} M_{\odot}$ . The effect of the ultraviolet background radiation field was neglected, while metal-dependent radiative cooling (adopted from MAPPINGS-III (Sutherland & Dopita 1993)) was included.

The star formation prescription employed requires (i) the gas density to be above

---

<sup>5</sup>We have excluded secondaries in the 0.8 - 1.5  $M_{\odot}$  range; doing so, regardless of IMF, only impacts on the SNeIa rate at the  $\sim 20\%$  level.

<sup>6</sup>By assuming  $Z = O + Fe$ , we admittedly underestimate the global metal production rate by nearly a factor of two; our next generation runs with GASOLINE employ a more detailed chemical evolution model, incorporating the nucleosynthetic byproducts of asymptotic giant branch evolution and thereby ameliorating this effect.

## CHAPTER 4

a threshold of  $0.1 \text{ cm}^{-3}$ , (ii) a convergent gas flow to exist, and (iii) the gas to be locally Jeans unstable. A standard Salpeter initial mass function (IMF) was assumed, along with pure thermal feedback from both SNeII and SNeIa ( $10^{50} \text{ erg/SN}$ ) being coupled to the surrounding SPH particles.

The chemical evolution implementation within GCD+ takes into account the metal-dependent nucleosynthetic byproducts of SNeII (Woosley & Weaver 1995), SNeIa (Iwamoto et al. 1999), and low- and intermediate-mass AGB stars (van den Hoek & Groenewegen 1997). Relaxing the instantaneous recycling approximation, GCD+ tracks the temporal evolution of the nine dominant isotopes of H, He, C, N, O, Ne, Mg, Si, and Fe. The SNeIa progenitor formalism of Kobayashi et al. (2000) is adopted.

### 4.3.3 KN11

KN11 corresponds to the so-called ‘Wider Region’ model described by Kobayashi & Nakasato (2011), realized using a hybrid GRAPE-SPH code. This model was drawn from the five Milky Way-analogs which eventuated from a larger suite of 150 semi-cosmological<sup>7</sup> simulations. The cosmological parameters employed match those of §4.3.2, and led to a Milky Way analog of mass  $1.1 \times 10^{12} M_{\odot}$ . The effect of the ultraviolet background radiation field was included, as was metal-dependent radiative cooling (adopted from MAPPINGS-III (Sutherland & Dopita 1993)).

The star formation prescription employed requires (i) the gas density to be cooling, (ii) a convergent gas flow to exist, and (iii) the gas to be locally Jeans unstable. The star formation timescale is chosen to be proportional to the dynamical timescale

---

<sup>7</sup>By ‘semi-cosmological’, we mean that the simulated field was not large enough to sample the longest waves (and, as such, underestimate the degree of gravitational tidal torque which would otherwise be present in a fully cosmological framework), and so the initial system is provided with an initial angular momentum via the application of rigid rotation with a constant spin parameter  $\lambda=1$ .

## CHAPTER 4

( $t_{\text{sf}} \equiv t_{\text{dyn}}/c$ ), where the star formation efficiency is chosen to be  $c=0.1$ . A standard Salpeter initial mass function (IMF) was assumed (with lower and upper mass limits of 0.07 and 120  $M_{\odot}$ , respectively), along with pure thermal feedback from both SNeII<sup>8</sup> and SNeIa ( $\sim 10^{51}$  erg/SN) being distributed to the surrounding SPH particles within 1 kpc (weighted by the SPH kernel).

The chemical evolution implementation within GRAPE-SPH takes into account the metal-dependent nucleosynthetic byproducts of SNeII (Kobayashi et al. 2006), SNeIa (Nomoto et al. 1997), and low- and intermediate-mass AGB stars (Karakas 2010).

### 4.3.4 RaDES

The third galaxy sample (RaDES: Ramses Disk Environment Study - Few et al. (2012b)) was simulated using the adaptive mesh refinement (AMR) code RAMSES (Teyssier 2002). The motivation behind these simulations was to determine the systematic differences between simulated galaxies with neighbouring dark matter haloes similar to the Local Group and those in the field. The RAMSES simulations include gravity, radiative cooling, and heating from a uniform ionising UV background radiation (Haardt & Madau 1996). Hydrodynamic behaviour of the gas phase and gravitational potential is calculated on a spatially adaptive grid. A full description of the star formation model used in RAMSES is given by Dubois & Teyssier (2008); here we give just a brief account of its implementation.

Gas cells with density greater than a given threshold allow stars to form at a rate proportional to the density,  $\dot{\rho} = -\rho/t_{\star}$ , where  $t_{\star}$  is the star formation timescale, which itself is proportional to the dynamical time ( $t_0(\rho/\rho_0)^{-1/2}$ ), as first described by Rasera & Teyssier (2006). After Dubois & Teyssier (2008), we use a threshold of  $\rho_0$

---

<sup>8</sup>50% of the massive stars are assumed to end their lives as SNeII, while the remaining 50% are assumed to end their lives as  $10\times$  more energetic hypernovae.

## CHAPTER 4

$= 0.1 \text{ cm}^{-3}$  and  $t_0 = 8 \text{ Gyr}$ . In combination, these choices correspond to an adopted star formation efficiency of 2%. Feedback from SNeII<sup>9</sup> occurs instantaneously and the mass carried away is parameterised as  $(\eta_{SN} + \eta_W)$ , where  $\eta_{SN}$  is the fraction of a stellar particle’s mass that is ejected by SNeII and  $\eta_W$  is the fraction that is swept up in the SNII wind. In the RaDES simulations,  $\eta_{SN} = 0.1$  and  $\eta_W = 0$ , which for these runs, led to less strongly peaked rotation curves. Energy is injected into the gas phase in the form of thermal and kinetic energy, distributed across a superbubble of radius  $r_{\text{bubble}}$  according to a Sedov blastwave formalism. The metallicity of SN ejecta is determined by converting a fixed fraction,  $f_Z$ , of the non-metal content of new stars into metals; all galaxies in the RaDES sample used  $f_Z=0.1$ .

RaDES is comprised of two subsamples allowing for a statistical intercomparison of field galaxies and those in environments similar to those of loose groups; the full details are presented in (Few et al. 2012b). These simulations take place in either  $20h^{-1} \text{ Mpc}$  (grid resolution of 440 pc) or  $24h^{-1} \text{ Mpc}$  (grid resolution of 520 pc) volumes with  $512^3$  dark matter particles in the central region. The cosmology of these boxes is  $H_0=70 \text{ km s}^{-1}\text{Mpc}^{-1}$ ,  $\Omega_\Lambda=0.72$ ,  $\Omega_m=0.28$ ,  $\Omega_b=0.045$ , and  $\sigma_8=0.8$ .

The sample employed here consists of nine isolated (field) galaxies and ten situated within loose groups. The latter are defined as being those for which two  $L_*$  halos of comparable mass reside within 1.5 Mpc of one another, and neither are located within 5 Mpc of a halo with mass in excess of  $5 \times 10^{12} M_\odot$ . The latter criterion avoids the proximity to rich clusters. In a statistical sense, these ‘loose groups’ can be thought of as Local Group analogs, at least in terms of dynamical mass, proximity to companion galaxies, and the avoidance of rich clusters. The field sample contains those halos that are even more isolated from neighbouring massive halos: specifically, no  $M_{\text{halo}} > 3 \times 10^{11} M_\odot$  within 3 Mpc). The virial mass range of the

---

<sup>9</sup>SNIa are not accounted for in RaDES, although we have recently completed a chemical evolution upgrade to RAMSES which parallels that implemented within GCD+ (§ 4.3.2); this work is described elsewhere by Few et al. (2012a).

## CHAPTER 4

RaDES sample spans  $2.5 \times 10^{11}$  to  $1.6 \times 10^{12} M_{\odot}$ .

### 4.3.5 Chemical Evolution Models

In this work, we compare our results from the hydrodynamical simulations described in § 4.3.1–4.3.4 to two chemical evolution models both designed to reproduce the main features of our Galaxy. The models are described by Chiappini et al. (2001) and Mollá & Díaz (2005), and we refer the reader to these papers for full details.

In the model by Chiappini et al. (2001), the Milky Way forms by means of two main infall episodes, both represented by exponential infall rates. The first infall episode, characterised by the rate  $\dot{\sigma}_H \propto A e^{-t/\tau_{inf,H}}$ , is associated with the formation of the halo and thick disk, with an  $e$ -folding timescale ( $\tau_{inf,H}$ ) of  $\sim 1$  Gyr. The constant  $A$  is determined by requiring that the present-day mass surface density of the halo is reproduced.

The second infall phase is represented as  $\dot{\sigma}_D \propto B(R) e^{-t/\tau_{inf,D}}$ , and is associated with the formation of the thin disk. The thin disk is represented by independent annuli, each 2 kpc wide, with no exchange of matter between them (i.e., no radial gas flows). The  $e$ -folding timescale ( $\tau_{inf,D}$ ) of the second infall is assumed to be a linear function with increasing galactocentric radius (i.e.,  $\tau_{inf,D}(R) \propto R$ ) - enforcing the so-called “inside-out” paradigm for disk growth, with the gas accumulating faster in the inner regions of the disk, relative to the outer disk. The timescales here vary from  $\sim 2$  Gyr in the inner disk, to  $\sim 7$  Gyr in the solar neighbourhood, and up to  $\sim 20$  Gyr in the outermost parts of the disk. The constant  $B(R)$  is fixed in order to reproduce the present-day total surface mass density (stars + gas) in the solar neighbourhood. The star formation rate  $\dot{\sigma}_*$  is expressed by the common Schmidt-Kennicutt law,  $\dot{\sigma}_* \propto \nu \sigma_{gas}^k(R, t)$ , where  $\sigma_{gas}(R, t)$  represents the gas density at the radius  $R$  and at the time  $t$ , and  $k = 1.5$ . The star formation efficiency  $\nu$  is set to  $1 \text{ Gyr}^{-1}$ , and becomes zero when the gas surface density drops below a certain critical threshold,

## CHAPTER 4

adopted here to be  $\sigma_{th}=7 M_{\odot} pc^{-2}$ . The nucleosynthesis prescriptions for AGB stars and SNeIa+SNeII are drawn from the same sources listed in § 4.3.2.

The chemical evolution model of Mollá & Díaz (2005) differs from that of Chiappini et al. (2001) in several aspects, in that it is multiphase, treating the ISM as a mixture of hot diffuse gas and cold molecular clouds. Each galaxy is assumed to be a two-zone system, comprised of a halo formed in an early gas-rich phase and a disk. The gas of the disk is acquired from the halo through an imposed infall prescription characterised by the inverse of the collapse time, which itself depends upon the total mass of the galaxy. The mass profile is imposed to adhere to the Persic et al. (1996) universal rotation curve. Similar to Chiappini et al. (2001), each galaxy is divided into concentric cylindrical zones 1 kpc wide. The collapse timescale depends on radius via an exponential function  $\tau(R) \propto e^R$ , rather than the linear dependence upon  $R$  employed by Chiappini et al. (2001). Another important difference concerns the treatment of star formation: in the Mollá & Díaz (2005) model, stars form in two stages: first, molecular clouds condense with some efficiency out of the diffuse gas reservoir, and second, stars form with a second efficiency factor based upon cloud-cloud collision timescales. In spirit, this mimics the effect of the threshold effect in the Chiappini et al. (2001) model: specifically, stars may form only in dense regions. The relation between the star formation rate and the gas density can be approximated by a power law with  $n > 1$ , again, in qualitative agreement with the law employed by Chiappini et al. (2001). In the halo, star formation follows a common Schmidt-Kennicutt law with exponent  $n = 1.5$ . Extensive testing and tuning of the main parameters resulted in a grid of 440 models spanning 44 different masses (from dwarfs to giants, with 10 different star formation efficiencies per mass model). The chemical prescriptions for SNeIa and SNeII are again similar to those listed in § 4.3.2.

## 4.4 Present-Day Gradients

### 4.4.1 Radial Gradients

In this section, the present-day radial abundance gradients of the MUGS and RaDES simulations are presented. We focus here on one MUGS (g15784) and one RaDES galaxy (Apollo), which have been chosen as fiducial representatives of these two suites of simulations. Observational constraints on the abundance gradient of  $z=0$  late-type galaxies may be found in, for example, Zaritsky et al. (1994) who measured a mean gradient of  $-0.058$  dex/kpc for local spiral galaxies and van Zee et al. (1998), who found a comparable mean gradient from their sample ( $-0.053$  dex/kpc). In Kewley et al. (2010) close galaxy pairs were found to have systematically shallower gradients (typically,  $-0.021$  dex/kpc). In each of these cases, the gradients are inferred from gas-phase nebular emission, which provides a “snapshot” of the present-day gradient, similar to that inferred from, for example, B-stars (i.e., stars with ages  $<100$  Myrs).<sup>10</sup>

We employed a strict kinematic decomposition of spheroid and disk stars for each of the 25 simulations<sup>11</sup>, following the Abadi et al. (2003b) formalism. Additional (conservative) spatial cuts were employed to eliminate any satellite interlopers that

---

<sup>10</sup>Loose group galaxies in the RaDES suite exhibit the same qualitative flattening of metallicity gradients when compared with their ‘field’ equivalents, however the order of this difference is significantly smaller ( $<0.005$  dex/kpc) than the systematic differences found between the RaDES and MUGS galaxies ( $\sim 0.05$ – $0.2$  dex/kpc). A comprehensive analysis of the (subtle) systematic differences between the field and loose group galaxies within RaDES can be found in Few et al. (2012b), but is not pursued here, simply because this difference is negligible to the scope of the present analysis.

<sup>11</sup>The kinematic decomposition employed for the MUGS galaxies differs from that used in the original Stinson et al. (2010) analysis, in that  $J_z/J_{circ}$  for each star was derived self-consistently taking into account the shape of the potential, rather than assuming spherical symmetry and using the enclosed mass at a given star particle’s position.

## CHAPTER 4

might pass the initial kinematic decomposition. We define three age bins: young (stars born in the last 100 Myrs, to correspond roughly with B-stars), intermediate (stars formed 6–7 Gyr ago), and old (stars older than 10 Gyr).

Observational studies of radial gradients typically show higher metallicities in the inner disk relative to the outer disk (e.g. Rupke et al. 2010b). As noted above, observations of external systems typically make use of gas-phase oxygen abundances, as measured from HII regions, but consistency exists between that tracer and others known to provide a “snapshot” of the gradient (e.g., planetary nebulae and short-lived main sequence B-stars). Our gas-phase and young (B-star) gradients are identical in amplitude and gradient, and hence in what follows, we employ “young stars” (those formed in the previous 100 Myr period) to determine the abundance gradients.

The current RaDES sample only tracks global metallicity  $Z$ , but as oxygen consistently accounts for  $\sim 50\%$  of  $Z$ , we use  $Z$  as a first-order proxy for oxygen, when making comparisons with observations.<sup>12</sup> The version of GASOLINE employed for these MUGS runs track both O and Fe (from SNeII and SNeIa), and assume  $Z \equiv O + Fe$ ; as noted earlier, this latter assumption leads to an  $\sim 0.2$  dex underestimate of the global metallicity in the MUGS sample. This does not impact upon our gradient analysis, but does serve to explain why the RaDES and MUGS galaxies are offset by  $\sim 0.2$  dex from one another in  $[Z]$  in the figures presented here.

Figure 4.1 shows the mass-weighted radial gradients at  $z=0$  in  $[Z]$  for one MUGS galaxy (g15784, top panel) and one RaDES galaxy (Apollo, lower panel). The radial gradients are calculated using linear fits over the noted disk regions (overdrawn in black). These are chosen to exclude the central region, avoiding any residual co-rotating bulge stars that escaped the kinematic decomposition. The outer edge of the disk is taken as the point at which the surface brightness profile of the young

---

<sup>12</sup>We have recently completed the implementation of full chemical evolution, including SNeII, SNeIa, and AGB stars, within RAMSES - Few et al. (2012a).

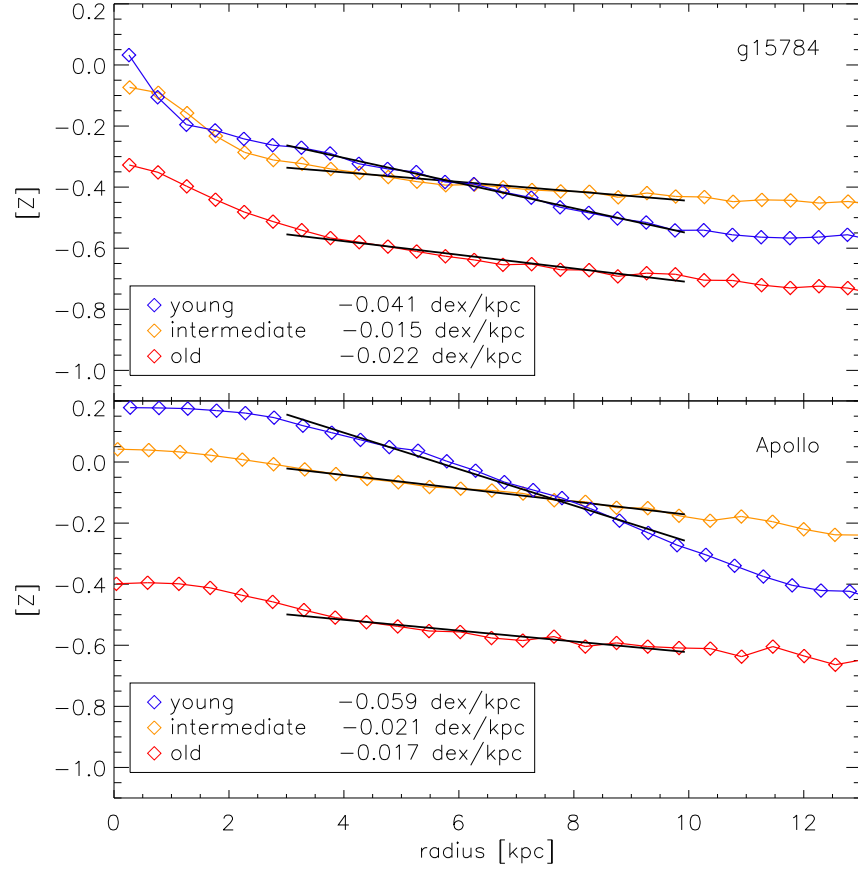


Figure 4.1: Stellar radial  $[Z]$  gradients, for disk stars in three different stellar populations: young (blue) is defined as stars formed in the last 100 Myrs, intermediate (yellow) is defined as stars formed 6 to 7 Gyr ago, and old (red) is defined as stars older than 10 Gyr. Fits to the disk are overdrawn in black; the length of the black line corresponds to the region of the disk used in the fitting (see text for details). For clarity, only two galaxies are shown, one from MUGS (g15784, upper panel) and one from RaDES (Apollo, lower panel).

# CHAPTER 4

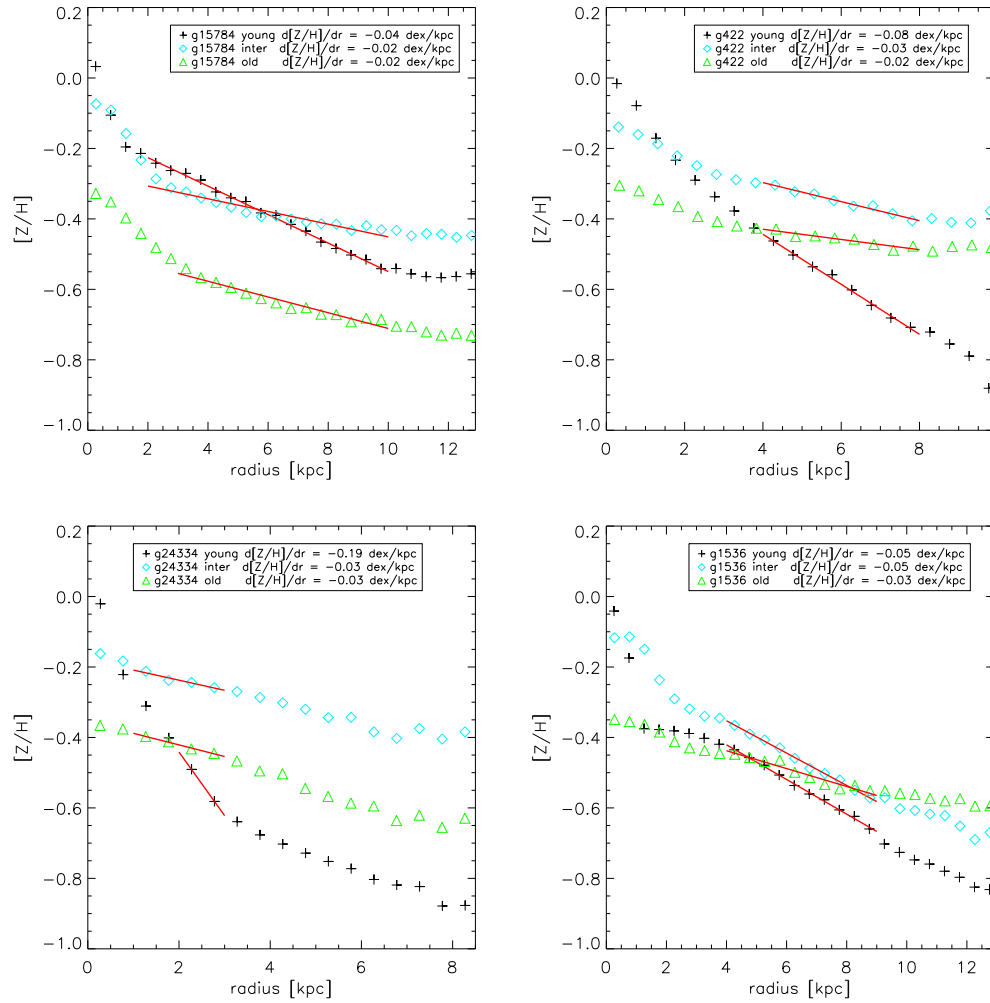


Figure 4.2: Same as figure 4.1 but for all four of the MUGS galaxies Black shows the young stars, blue the intermediate population and green the old.

## CHAPTER 4

stars (effectively, the cold gas) deviates from an exponential. To ensure that an appropriate region is considered here, we have been conservative in choosing the “disk region”. The gradient is robust to the choice of outer radius; reducing the choice of inner radius from 5 kpc to 2 kpc has only a  $\pm 0.007$  dex/kpc impact on the inferred formal gradient - i.e., the differences in gradients between young, intermediate, and old populations are not significantly affected. Throughout this paper we use the Asplund et al. (2009) values for the solar metallicity.

As one considers progressively older stellar populations (at the present-day), Figure 4.1 shows that the measured radial metallicity gradient becomes progressively flatter. Such behaviour is not unexpected in cosmological simulations which include gas infall, radial flows, high velocity dispersion gas, kinematically hot disks, and dynamical mixing/radial migration which is more pronounced for older stars (e.g. Sánchez-Blázquez et al. 2009; Rahimi et al. 2011; Pilkington et al. 2012d). The timescale of the mixing that flattens the gradients in the MUGS and RaDES simulations is shorter than the difference between intermediate and old populations of stars, as evidenced by radial gradients for the two populations, regardless of simulation suite, being quite similar. The degree of flattening of the *stellar* abundance gradients is such that by the present day, *within the simulations*, the older stellar tracers show a flatter abundance gradient than the younger tracers (recall Fig 4.1 and Fig 4.2, re-iterating results shown by Sánchez-Blázquez et al. (2009), Rahimi et al. (2011), and Pilkington et al. (2012d)). This is counter to what is observed in the Milky Way when inferring gradients using younger planetary nebulae versus older planetary nebulae (e.g. Maciel et al. 2003), but again, this is fully expected given the degree of kinematic (stellar) heating within these cosmological simulations, and does *not* impact on the use of gas-phase and young-star probes of the gradients (both possess the expected steeper abundance gradients at early-times). Indeed, future work in this area can, and should, make use of this powerful constraint on

## CHAPTER 4

migration/heating: specifically, the fact that (empirically) older stellar probes today have a steeper abundance gradients than younger stellar probes, while extant, kinematically hot, simulations, show the opposite trend.

For completeness, in Table 4.1 we list the present-day mass-weighted stellar radial metallicity gradients ( $d[Z]/dR$ , in units of dex/kpc) for each of the 25 simulations employed here (column 8). The similarity of the gradients is readily apparent, save for the MUGS galaxy g24334, which was included in the sample despite its stellar fraction being dominated by accreted stars, rather than *in situ* star formation (discussed further in § 4.5). Its relatively small disk scalelength (1.0 kpc) also made fitting its gradient more challenging than the other MUGS disks.

Following Sánchez-Blázquez et al. (2011), we examined the effect of applying a different weighting scheme in determining the mean metallicities. When examining just the young stars or the gas, the weighting employed has no effect upon the inferred gradient. However, when deriving a composite gradient making use of *all* stars in the disk, the weighting can become important, as Sánchez-Blázquez et al. (2011) suggested. We explored the impact of using, for example, luminosity-weighting (and log-weighting), by deriving the absolute magnitude of each simulated star particle, making use of its age, metallicity, and initial mass function, alongside the Marigo et al. (2008) isochrones.<sup>13</sup> As expected from the Sánchez-Blázquez et al. (2011) analysis, the mean abundance shifted by  $\sim 0.1$  dex depending upon the weighting employed, but the inferred gradient was not affected.

The abundance gradient of young stars (or equivalently, the ISM) is shaped by the time evolution of the radial star formation rate. To illustrate this we show the normalised star formation rate per unit surface area as a function of galactocentric radius in Figure 4.3. To match the chemical evolution models of Chiappini et al. (2001) for the Milky Way (with the understanding that our simulations are not

---

<sup>13</sup>[http://stev.oapd.inaf.it/cgi-bin/cmd\\_2.1](http://stev.oapd.inaf.it/cgi-bin/cmd_2.1)

CHAPTER 4

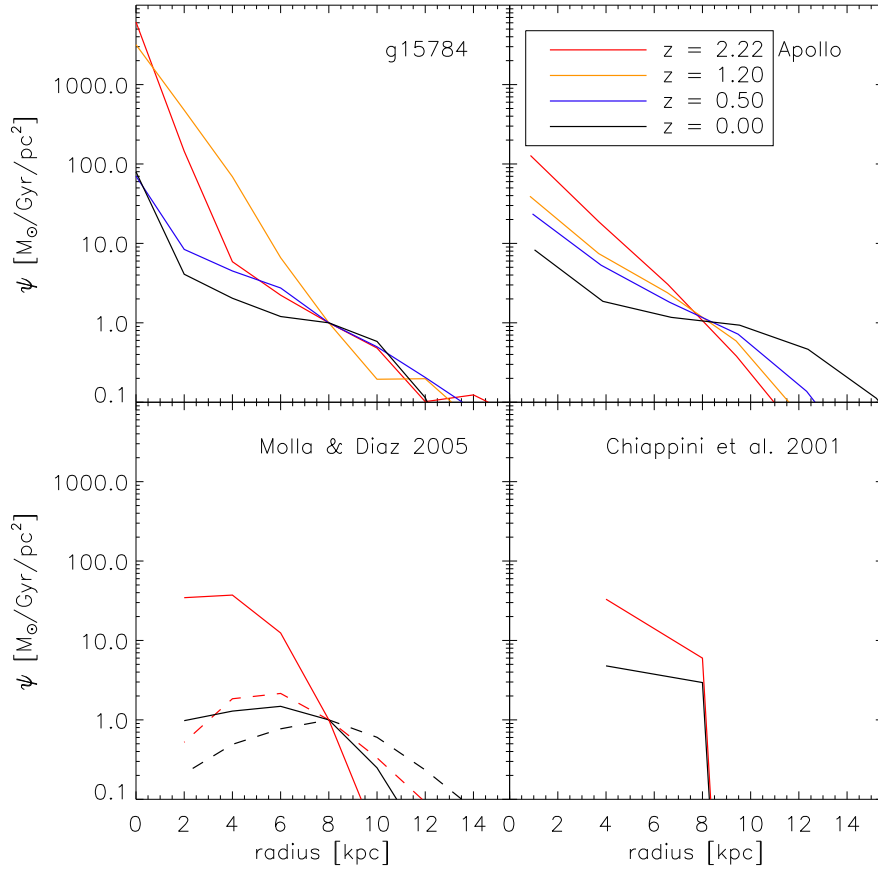


Figure 4.3: Star formation rate per unit surface area as a function of radius for the MUGS galaxy g15784 (upper-left panel) and the RaDES galaxy Apollo (upper-right panel). We show the simulations at four different redshifts:  $z=0.0$ ,  $0.5$ ,  $1.2$ , and  $2.2$ , as noted in the inset to the upper-right panel. 1 kpc annuli are used along with a height cut of  $\pm 5$  kpc above and below the disk. The mass of stars formed in the last 100 Myrs is calculated for each annulus out to a radius of 15 kpc. The curves have been normalised to  $1 \text{ M}_\odot/\text{Gyr}/\text{pc}^2$  at galactocentric radius 8 kpc. The bottom panels show the corresponding predicted behaviour of the Chiappini et al. (2001) (right) and Mollá & Díaz (2005) (left) models. Only redshifts 0.0 and 2.2 are shown, other redshifts are excluded as these models evolve smoothly from  $z=2.2$  to  $z=0.0$ . Two of the Mollá & Díaz (2005) models are shown, one with high star formation efficiency (dashed lines) and one with low star formation efficiency (solid lines) .

## CHAPTER 4

constructed *a priori* to be perfect replicas of the Milky Way), we normalise the star formation rate to have a value of  $1 \text{ M}_\odot/\text{Gyr}/\text{pc}^2$  at a galactocentric radius of 8 kpc.<sup>14</sup>

Each of the star formation rate profiles behave qualitatively like the classic inside-out chemical evolution models of Chiappini et al. (2001) and Mollá & Díaz (2005), in the sense of decreasing outwards from the inner to outer disks. An important systematic difference between these representative simulations is apparent though, at least at higher redshifts ( $1 < z < 2$ ). Specifically, the gradient in the star formation rate per unit area is steeper at higher redshifts for the MUGS galaxies; it is not clear if this is symptomatic of a single difference between the MUGS and RaDES galaxies, or (more likely) a combination of factors including the star formation threshold, star formation efficiency, feedback schemes, and resolution of the respective simulations. Regardless, it is clear that *star formation is more centrally-concentrated in the MUGS sample at early stages in the formation of the disk which unsurprisingly leads to steeper abundance gradients in the early disk* (a point to which we return shortly).

### 4.4.2 Vertical Gradients

For completeness, as in Figs. 4.1 and 4.3, for g15784 (MUGS) and Apollo (RaDES), the mass-weighted vertical stellar abundance gradients in the simulations are presented in Figure 4.5. A ‘solar neighbourhood’ is defined for each simulation as being a 2 kpc annulus situated at a galactocentric radius of  $\sim 2.5$  disk scalelengths (column 5 of Table 4.1). These radial scalelengths were derived from exponential fits to the

---

<sup>14</sup>For context, the ‘normalised’ and ‘pre-normalised’ star formation rate surface densities (at 8 kpc), for each of the simulations, are not dissimilar; the latter lie in the range  $\sim 1\text{--}2 \text{ M}_\odot/\text{Gyr}/\text{pc}^2$ , save for the (known) discrepant MUGS galaxy g24334 (which, pre-normalised, lies at  $\sim 0.2 \text{ M}_\odot/\text{Gyr}/\text{pc}^2$ , reflective of the fact that its stellar content is more dominated by its accreted component, rather than in situ star formation).

## CHAPTER 4

stellar surface density profiles.

Classic work from, for example, Marsakov & Borkova (2005, 2006) and Soubiran et al. (2008), and soon-to-be-released work using SDSS-SEGUE and RAVE datasets, show that vertical metallicity profiles can provide extremely effective tools for separating the thin disk from the thick disk. With  $\sim 300\text{--}500$  pc softening/grid cells, we do not resolve the thin-thick disk transition. Figure 4.5, shows the vertical gradient for the MUGS galaxy g15784 (orange) and the RaDES galaxy Apollo (purple), along with observational data for the Milky Way from Marsakov & Borkova (2005) and Marsakov & Borkova (2006). The two vertical lines show the respective resolutions of the MUGS and RaDES simulations.

The vertical metallicity gradients (in their respective ‘solar neighbourhoods’) for the 25 simulations analysed here are listed in column 7 of Table 4.1. We find little variation between the simulations in question, with the typical vertical gradient lying in the  $-0.05\pm 0.03$  dex/kpc range. Only Eos, Castor, and Krios lie outside this range, possessing somewhat steeper vertical abundance gradients. These three undergo the most extended late-time period of ‘quiescent’ evolution, as noted by Few et al. (2012b).

At face value, the vertical gradients in  $[\alpha/\text{H}]$ <sup>15</sup> and  $[\text{Fe}/\text{H}]$  inferred from the simulations are consistent with the observed values seen in the thick disk of the Milky Way ( $\sim -0.05 - \sim -0.08$  dex/kpc). The vertical gradients in the Milky Way’s thin disk, though, are consistently much steeper (where many authors find the thin disk gradient to be between  $\sim -0.25 - \sim -0.35$  dex/kpc (e.g. Soubiran et al. 2008; Marsakov & Borkova 2006; Bartašiūtė et al. 2003; Chen et al. 2003)) than the results we obtain from our simulations. Our spatial ‘resolutions’ range from  $\sim 300\text{--}500$  pc,

---

<sup>15</sup>Here, total metallicity is used as a proxy for  $\alpha$  in the RaDES suite, while oxygen is used for the MUGS and GCD+ suites; magnesium is used in the observational datasets described by Marsakov & Borkova (2005, 2006).

## CHAPTER 4

and the results appear compromised on vertical scales up to  $\sim 2-3$  resolution ‘elements’ - i.e., any putative ‘thin’ disk would be (not surprisingly) unresolved. In a chemical sense, these disks are too ‘hot’, in much the same way that their ISM and stellar populations are also kinematically hot (e.g. House et al. 2011).

On this issue of ‘resolution’, the global star formation rates reported are comparatively well converged as a function of resolution (Stinson et al. 2006, §5.2.4) The most notable change with increasing resolution is the addition of higher redshift populations, containing comparatively little mass, as earlier generations of halos are resolved. This is at least partially a result of star formation models largely being constrained to reproduce observed star formation rates.

The dependence of gradients on resolution though is far less predictable. At our current resolution we resolve sufficient substructure and disc dynamics to capture the salient physical mechanisms involved in migration. However, increasing resolution does resolve the physics behind migration processes better, but it also makes the diffusion model more localized. Equally importantly, it is not clear to what extent the numerous processes involved in migration will interact with one another as resolution is increased. Taking the alternative approach of lowering resolution makes processes less likely to be captured (particularly substructure-induced migration), so it is not clear that convergence happens in a simple fashion. Ultimately, a definitive answer on the impact of resolution on migration requires far higher resolution than we are currently able to achieve and future work is required to address this issue.

### 4.5 Evolution of the Radial Gradients

While there exist a handful of studies of radial abundance gradients at high redshift (Jones et al. 2010; Cresci et al. 2010; Yuan et al. 2011), the difficulties in obtaining high resolution data for likely Milky Way-like progenitors has meant that theoreticians have had very few constraints on their models; as noted earlier, inside-out

CHAPTER 4

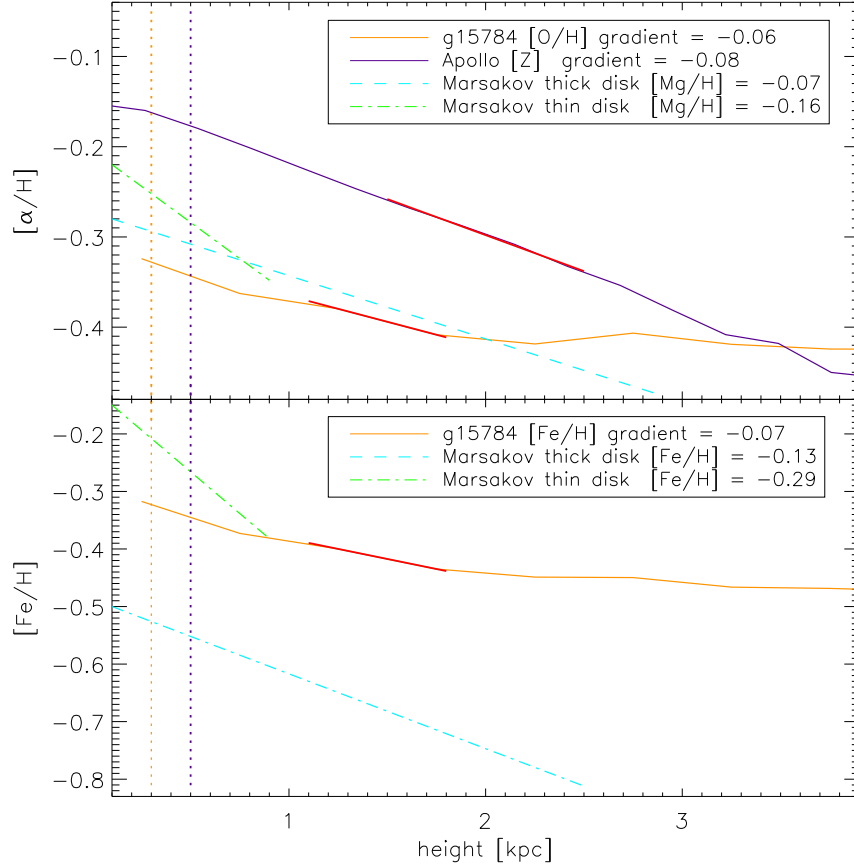


Figure 4.4: The vertical gradients of disk stars in the simulations. The top panel shows the [Z] vertical gradient of Apollo (purple, grad =  $-0.08$ ) with the [O/H] gradient of g15784 (orange, grad =  $-0.06$ ) and observational data from Marsakov & Borkova (2005, 2006) of [Mg/H] gradients in the thin (blue, grad =  $-0.16$ ) and thick (green, grad =  $-0.07$ ) disk of the Milky Way. The lower panel shows the [Fe/H] gradients of the Marsakov & Borkova (2005, 2006) thin (grad =  $-0.29$ ) and thick (grad =  $-0.13$ ) disk data along with the g15784 (grad =  $-0.07$ ) [Fe/H] gradient. Overplotted vertically are the softening length of the MUGS (orange) and the minimum grid size of the RaDES (purple) simulations. The bold red lines show the region used to calculate the gradient.

## CHAPTER 4

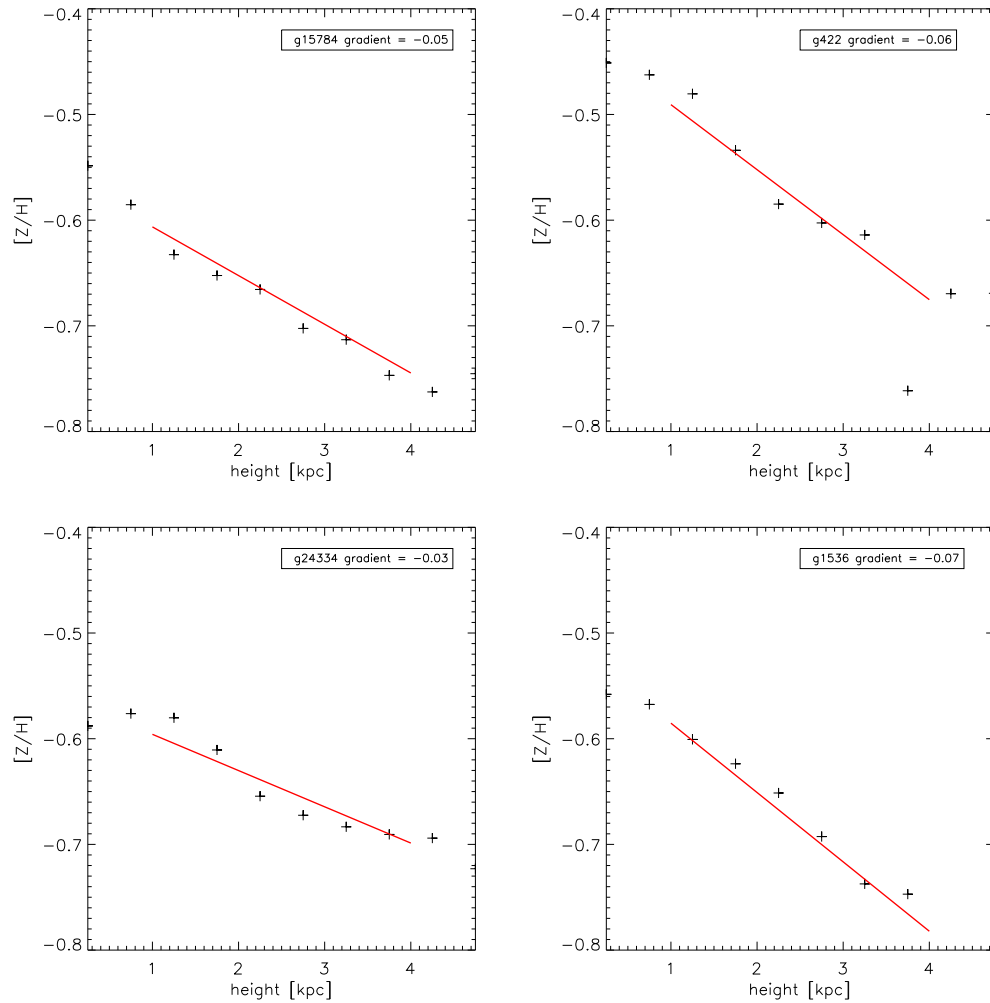


Figure 4.5: The vertical gradients of disk stars in the 4 MUGS simulations. The metallicity shown is the overall metallicity  $Z$ , the red lines show the linear fits to the gradients.

## CHAPTER 4

galactic chemical evolution models can be constructed which recover the present-day gradients seen in the Milky Way, but they can take very different paths to get there. Some such models predict a steepening with time starting from initially inverted or flat gradients (e.g., Chiappini et al. (2001)), while others predict an initially negative gradient that flattens (e.g. Mollá & Díaz (2005)).

To make progress in this area, we now analyse the time evolution of the gradients within our 25 simulations, supplemented with two classical chemical evolution models, making fits radially at each timestep for which a clear disk could be identified. As the disk is continually growing and evolving, we examined each timestep visually, identifying the outer ‘edge’ using the cold gas and young stars as a demarcation point. It should be noted here that the kinematic decomposition used to identify ‘disk stars’ in § 4.3.1 and § 4.3.2 was not used for this component of our analysis. By working only with very young stars at 2–3 disk scalelengths, when fitting gradients at each timestep, kinematic decomposition of disk vs spheroid stars becomes unnecessary. Radial gradients were then derived by fitting typically from the outer edge of the disk to the inner part of the disk, where the inner point corresponds to the point at which the surface density profile deviates from an exponential. Again, as we are only using the stars formed in the previous 100 Myrs (B-stars) at a given timestep, the relevant disk (rather than star-forming bulge) regime is not difficult to identify.

In Figure 4.6, we show the time evolution of the radial gradient for our two ‘fiducial’ simulations: MUGS (g15784, upper panel) and RaDES (Apollo, lower panel). The gradients measured at each timestep are noted in the inset to each panel. Much steeper abundance gradients at high-redshift ( $z > 1$ ) are seen within the MUGS galaxy. Further, the offset in mean metallicity between the two, as already alluded to, can be traced to the manner in which chemistry was included in the version of GASOLINE employed (i.e., the assumption that  $Z \equiv O + Fe$ , which affects

## CHAPTER 4

the mean metallicity, but not the gradient).

In Figure 4.7, we show the time evolution of the  $[Z]$  gradients for the 4 MUGS galaxies, the GCD+ galaxy (Gal1), the GRAPE-SPH galaxy (KN11), and the 19 RaDES galaxies. Importantly, we have also derived the time evolution of the predicted gradients for the chemical evolution models of Chiappini et al. (2001) and two of the Milky Way-like models of Mollá & Díaz (2005); with the Mollá & Díaz (2005) data, the fits to determine the gradient at each timestep evolved as they did in the hydrodynamical simulations. As the disk grew, the fits were made at larger radii, to exclude the central region. From the earliest timestep to the latest the fitted region shifts  $\sim 3$  kpc in radius (reflecting the growth of the disk over the timescales under consideration). The Chiappini et al. (2001) data were fit over the radial range 4 to 8 kpc at each timestep, reflecting the fewer relevant annuli available over which to make the fit. Chiappini et al. (2001) fit their gradients to the same chemical evolution models over a broader radial range (4–14 kpc), but our interests here are restricted to the inner disks of these models, where the star formation density threshold is less important in shaping the metallicity gradient.

For the Mollá & Díaz (2005) models, we show a low-efficiency (28,8) and high-efficiency (28,2) example, (where model 28 corresponds to a circular velocity of  $\sim 200$  km/s and the efficiency factors correspond to the combined efficiency of molecular cloud formation and cloud-cloud collisions). The Chiappini et al. (2001) and, to a lesser extent, the high efficiency Mollá & Díaz (2005) models (at least since

## CHAPTER 4

$z \sim 1$ ) steepen with time.<sup>16</sup> Conversely, the RaDES sample (represented by the purple hatched region, which encompasses  $1\sigma$  of the gradient values at a given redshift) shows a mild flattening with time, more in keeping with full time evolution of the high efficiency Mollá & Díaz (2005) model. The MUGS sample shows not only steeper gradients as a whole at  $z > 1$  (except for g24334, to which we return below), but also three of the four show the more significant degree of flattening alluded to in relation to Fig 4.6; this degree of flattening is more dramatic than that seen in any of the RaDES galaxies or the chemical evolution models (except for the low efficiency models of Mollá & Díaz (2005)).<sup>17</sup>

Shown also in Fig 4.7 are the typical gradients encountered in nearby isolated (Zaritsky et al. (1994); blue asterisk) and interacting (Kewley et al. (2010); red asterisk) disk galaxies (offset at  $z=0$ , for clarity, in Fig 4.7). The black asterisk at redshift  $z \sim 1.5$  corresponds to the recent determination of a steep metallicity gradient in a high-redshift grand design spiral by Yuan et al. (2011). While intriguing, it is

---

<sup>16</sup>The Chiappini et al. (2001) models have gradients which are mildly inverted at high-redshift ( $\sim +0.02$  dex/kpc at redshift  $z \sim 2$ ); this works in the same direction as the inverted gradients observed by Cresci et al. (2010) at  $z \sim 3$ , albeit the gradients claimed by the latter are significantly more inverted (i.e.,  $\sim +0.1$  dex/kpc) than encountered in any of the simulations or chemical evolution models. It is important to remember though that the AMAZE/LSD samples at  $z \sim 3.3$  are (a) primarily Lyman-Break Galaxies with star formation rates ( $\sim 100\text{--}300 M_{\odot}/\text{yr}$ ) well in excess of that expected for Milky Way-like progenitors, and are not likely ideal progenitors against which to compare these simulations or chemical evolution models, and (b) in none of the current simulations are we able to unequivocally identify stable rotationally-supported disks, like those compiled by AMAZE/LSD. We require targeted simulations with much higher resolution at high-redshift than we have access to here, and tuned to be more representative of high-redshift Lyman-break galaxies, before commenting further on this potentially interesting constraint.

<sup>17</sup>It is worth noting that no obvious trend is seen when comparing the field and group galaxies in the RaDES sample. This is perhaps attributable to our selection criteria; by removing strongly interacting galaxies (at or near a pericentre passage), the sort of systematic differences seen in the work of Rupke et al. (2010a,b); Perez et al. (2011), for example, would not be encountered here.

## CHAPTER 4

important to bear in mind that one should not necessarily make a causal link between these disparate data points; until a statistical sample of high-redshift gradients has been constructed, linking the Yuan et al. (2011) point with those at low-redshift should be done with caution. This is a point we will return to in chapter 6.

For this latter reason, we have also included one MUGS galaxy (g24334) in our analysis (red curve: Fig 4.7) that does not have a present-day gradient consistent with the typical late-type spiral. We chose to include it, in order for the reader to see one example of a disk which possesses a steep gas-phase abundance gradient at high-redshift, comparable in slope to the Yuan et al. (2011) observation, but one which does not evolve in time to resemble the shallower slopes seen in nature today. g24334 differs from the other MUGS galaxies, in the sense that the fraction of its stellar population born ‘in situ’, as opposed to ‘accreted’, is significantly lower. Further, its disk is less extended than the other Milky Way-analogs and its abundance gradient was derived at  $\sim 0.5 \times$  disc scalelengths, where the gradient is more robust to interaction-induced flattening (e.g. Perez et al. 2011).

These differences are ultimately traced to the underlying treatment of star formation and feedback within the simulations; for example, the MUGS galaxies have a higher star formation threshold than the RaDES suite ( $1 \text{ cm}^{-3}$  vs  $0.1 \text{ cm}^{-3}$ ). As such, both the MUGS sample and the low efficiency models of Mollá & Díaz (2005) preferentially form stars in the inner disk where the densities are higher; the RaDES galaxies and the remaining chemical evolution models, with the lower threshold, have star formation occurring more uniformly throughout the early disk. Further, both MUGS and RaDES employ a standard blast-wave formalism for energy deposition into the ISM (Stinson et al. 2006), but the latter imposes a minimum blast wave radius of 2 grid cells, which means that ejecta is in some sense more “localised” in the MUGS simulations (for the same SN energy, the RaDES blast waves are  $\sim 2-3 \times$  larger); distributing energy (and metals) on larger radial scales can result in a more

## CHAPTER 4

uniform (i.e., flattened) metallicity distribution. The trend of Gal1 lies somewhat between the extremes of MUGS and RaDES, which can be traced to the fact that Gal1 uses a lower star formation threshold density ( $0.1 \text{ cm}^{-3}$ ), and almost negligible feedback, resulting in more localised metal enrichment. KN11 also lies very close to the MUGS fiducial (g15784) in terms of the temporal evolution of its abundance gradient; both employ high SNe feedback efficiencies, albeit on different spatial scales (a density-dependent blast wave radius in the case of g15784 and a fixed 1 kpc radius in the case of KN11) and with different star formation prescriptions (a  $1 \text{ cm}^{-3}$  star formation density threshold in the case of g15784 and an absence of a threshold for KN11). Note that although these hydrodynamical simulations experience different merger histories, the metallicity gradients are more affected by the recipe of sub-grid physics. This is highlighted by our large samples of simulations generated with different codes. Our updated work (figure 4.8) shows the effect of feedback on the temporal evolution of the abundance gradients. New high redshift data of metallicity gradients is critical for this work in constraining the efficiency with which this energy couples with the ISM.

As detailed in § 2.5, Chiappini et al. (2001) use a two infall model; at early times the infall of primordial gas is rapid and independent of galactocentric radius, while at later times, gas is assumed to fall preferentially on the outer regions of the disk, causing a steepening of the gradient with time. The radial dependence of this disk infall timescale is fairly gentle (linear with increasing radius); on the other hand, Mollá & Díaz (2005) calculate the overall infall rate as a function of the mass distribution and rotation of the galaxy, and assume a much stronger radial dependence for the infall timescale. Specifically, the inner disk's infall timescale is much more rapid than that of Chiappini et al. (2001), while the outer disk's infall timescale is much longer. In combination, the gradient tends to flatten with time (particularly for their low efficiency models).

CHAPTER 4

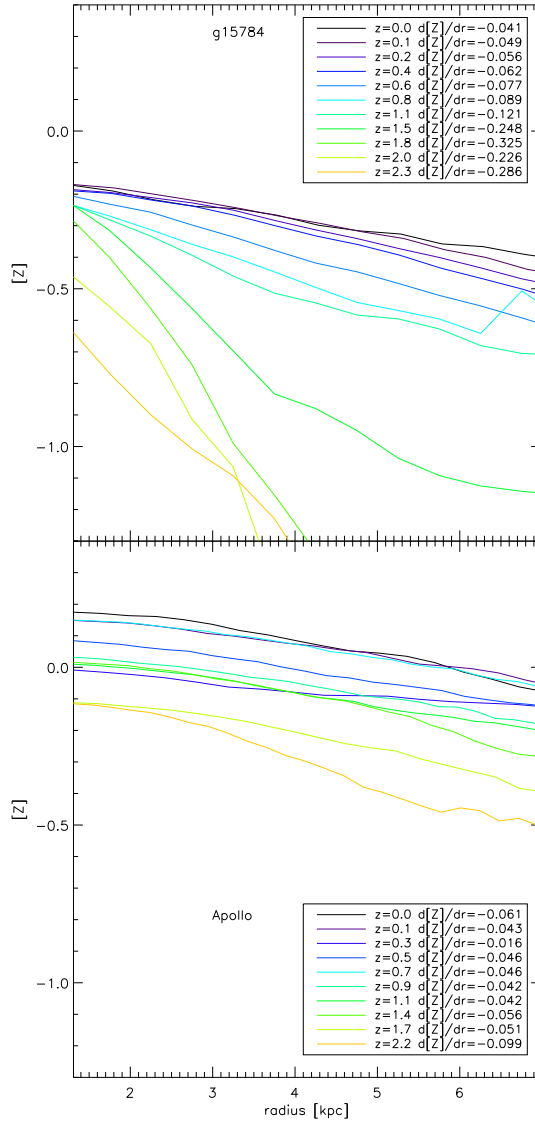


Figure 4.6: The radial  $[Z]$  gradients of young stars in g15784 (top panel) and Apollo (bottom panel). The different colors correspond to different redshifts running from  $z=0$  (black) to  $z=2.2$  (orange), illustrating the time evolution of the abundance gradients in both simulations. Note the more dramatic flattening of the MUGS (g15784) relative to that of RaDES (Apollo). The fitted gradients were not done in an ‘automated’ fashion; we examined each timestep’s surface density, kinematic, and abundance profiles, to take into account the growth of the disk and identify the ‘cleanest’ disk region within which to determine the gradient.

CHAPTER 4

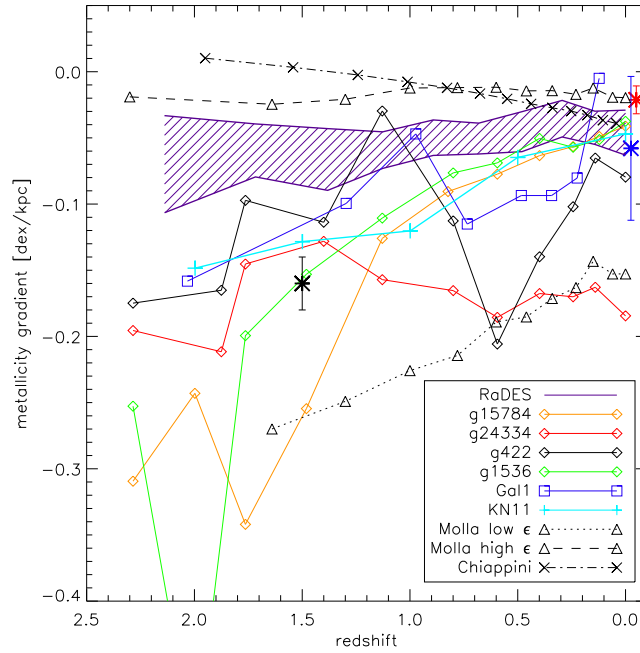


Figure 4.7: The derived radial  $[Z]$  gradient as a function of redshift. Here, we have used 11 different redshifts and measured the radial gradient of the young stars (stars formed in the last 100 Myrs at each step) in the disk at that time. We examined the disks at each redshift, to determine the appropriate galactocentric radius over which to measure the gradients (see text for details). Four MUGS galaxies (g15784 (orange diamonds); g24334 (red diamonds); g422 (black diamonds); g1536 (green diamonds)) are shown, along with Gal1 (blue squares) from Rahimi et al. (2011), KN11 (cyan plus symbols) from Kobayashi & Nakasato (2011), and the 19 RaDES galaxies (denoted by the purple hatched area showing the region encapsulating  $1\sigma$  of the gradients measured at a given redshift). The two chemical evolution models are overlaid for completeness: Chiappini (black dot dashed crosses), and Mollá high efficiency (black dashed triangles) and low efficiency (black dotted triangles). The black asterisk corresponds to the result from one lensed grand design spiral at  $z \sim 1.5$  (Yuan et al. 2011), the blue asterisk to the typical gradient inferred in nearby spirals (Zaritsky et al. 1994), and the the red asterisk to the typical gradient seen in interacting disks (Kewley et al. 2010); these latter local points are offset slightly at  $z=0$ , for clarity.

## CHAPTER 4

We find clear evidence of inside-out formation in the star formation profiles at different redshifts. Starting from an initially concentrated distribution, this flattens with time to the present-day, where star formation is more extended (and close to constant) over a large fraction of the disk (Fig 4.3). The radial dependence of star formation rate to infall rate sets the magnitude of the abundance gradient (Chiappini et al. 2001); a stronger radial dependence resulting in a steeper gradient. Such a configuration appears to come about naturally in the MUGS simulations, due in part to their higher star formation rate density threshold and perhaps the higher star formation efficiency and more localised chemical/energetic feedback. This contributes to the steeper gradients seen at early times in these simulations, relative to the other models. The RaDES galaxies behave more like the high efficiency model of Mollá & Díaz (2005). It should be noted however that despite the significant differences seen in the early stages of these galaxies' evolution, the star formation distribution in the majority of these simulations is very similar at the present day.

### 4.6 Effects of Feedback on the Evolution of Metallicity Gradients

To quantify the effects of feedback on the evolution of the metallicity gradients we now examine 2 of the MUGS galaxies from the previous section (g15784 and g1536) and compare them with two galaxies from the MaGICC suite (Some of which were discussed in chapter 3). The MaGICC galaxies analysed here are variants of the MUGS galaxies g15784 and g1536. This allows us to compare the same simulations, with the same initial conditions, varying solely the intensity of feedback between MUGS (conservative) and MaGICC (enhanced).

The differences between the implementation of feedback is discussed here, it has previously been discussed in Gibson et al. (2013) and Stinson et al. (2013) but

## CHAPTER 4

we will highlight the main differences for completeness. MUGS-g1536 and MUGS-g15784 use thermal feedback in which  $0.4 \times 10^{51}$  ergs of energy is used to heat up the surrounding ISM. MaGICC-g1536 and MaGICC-g15784 use the same feedback scheme but with  $10^{51}$  erg/SN made available to heat the surrounding ISM. The MUGS simulations use a Kroupa et al. (1993) IMF and the MaGICC simulations use the Chabrier (2003) IMF. In the MaGICC simulations, radiation feedback from massive stars is included (the implementation of this is discussed in chapter 3 section 3.3 and further in Stinson et al. (2013)), this was not included in the MUGS simulations. Star formation within MUGS and MaGICC can happen when a gas particle is sufficiently cool (MUGS  $< 15000\text{K}$ , MaGICC  $< 10000\text{K}$ ) and dense (MUGS  $> 1\text{cm}^{-3}$ , MaGICC  $> 9\text{cm}^{-3}$ ).

In Fig 4.8, we show graphically the impact of strong (MaGICC), as opposed to conventional (MUGS) feedback; specifically, the strong feedback associated with the MaGICC realisations results in flatter metallicity gradients at high-redshift which do not evolve significantly with time (in contradistinction to the MUGS runs). The importance of feedback in driving the temporal evolution of metallicity gradients, and the critical role that more and better observations can and will play in constraining the uncertain efficiency with which energy couples to ISM, makes this critical work for the future (e.g. Spitoni et al. 2013).

## 4.7 Summary

This work provides evidence in support of the *imposed* inside-out disk growth paradigm adopted within chemical evolution models; this growth is a natural outcome of both Eulerian and Lagrangian hydrodynamical simulations of disk galaxy formation within a cosmological context. We have examined how this inside-out growth impacts on the magnitude and evolution of abundance gradients in these galaxies, using a suite of simulations and models which were calibrated to recover

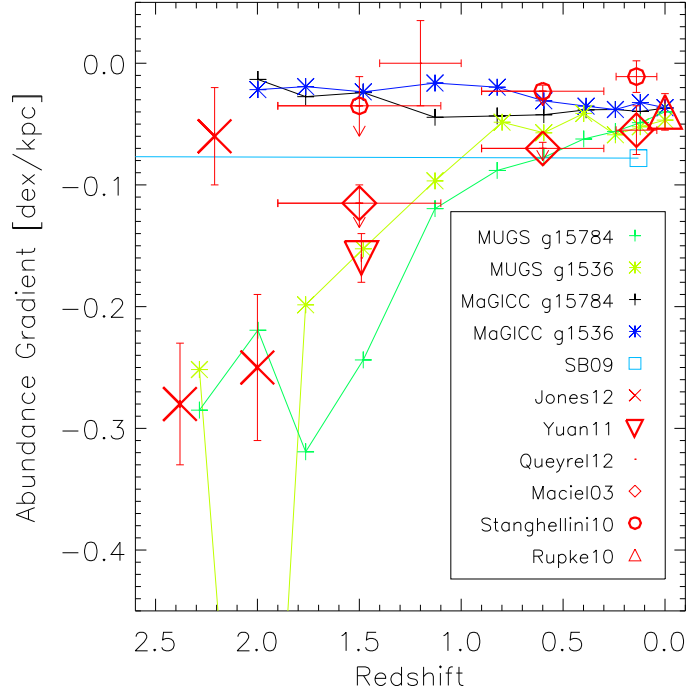


Figure 4.8: Comparison of the role of feedback in shaping the temporal evolution of metallicity gradients. Shown are two MUGS simulations from Figure 4.7: MUGS-g15784 and MUGS-g1536 (dark green and light green lines). In addition, we show two versions of the same runs, but now using the much more efficient MaGICC feedback scheme (Brook et al. (2012b) ; Stinson et al. (2012)): MaGICC-g15784 and MaGICC-g1536 (black and dark blue lines). Characteristics of the MaGICC feedback scheme are discussed in Chapter 3 and are used here just as a comparison. The cyan curve corresponds to the analytical model of Schönrich & Binney (2009). The red points show the observational constraints, as of January 2013. Crosses from Jones et al. (2010), upside down triangles from Yuan et al. (2011), dots from Queyrel et al. (2011), diamonds from Maciel et al. (2003), circles from Stanghellini & Haywood (2010) and triangles from Rupke et al. (2010a).

## CHAPTER 4

the present-day shallow gradients observed in late-type spirals. This is not meant to be a comprehensive, systematic, examination of sub-grid physics, in the vein of Wiersma et al. (2011), for example; instead, we have taken (in some sense) the ‘best’ Milky Way-like simulations from several groups, using different codes, different initial conditions, and different assembly histories, and conducted a ‘blind’ experiment on the outputs, to quantify *how* the gradients evolved to the imposed boundary condition of a shallow present-day gradient. Our findings include the following:

1. All galaxy models and simulations described in this work exhibit inside-out formation of the disk with varying degrees of centrally-concentrated star formation at early times (Figure 4.3). The evolving radial star formation rate dependence directly influences the resulting metallicity gradient; put another way, the signature of the star formation profile is embedded within the gradient of the young stars at each timestep. This signature though is diluted on the timescale of a few Gyrs. This is reflected in the differing gradients at the present-day between old and young stars (Figure 4.1); young stars at high-redshift within the MUGS sample (and observationally, it would appear, tentatively) form with a steep metallicity gradient, while those same stars today (now, old) have a fairly flat metallicity gradient (see Pilkington et al. (2012d) and Pilkington & Gibson (2012b))
2. Within the suite of 25 cosmological hydrodynamical simulations the derived vertical abundance gradients are comparable to those observed locally in the Milky Way’s thick disk. The resolution is, however, not sufficient to discriminate between thin and thick disks.
3. The evolution of simulated metallicity gradients depends strongly on the choice of sub-grid physics employed and as such the magnitude and direction of

## CHAPTER 4

its evolution depends critically upon the specific details of the recipes implemented. While it is difficult to disentangle the behaviour of the star formation profile *a priori*, it is clear that simulated galaxies with more centrally-concentrated star formation have initially steeper abundance gradients. These are more consistent with the (albeit limited) observation of high redshift normal Grand Design spiral galaxies (Yuan et al. 2011). Again highlighted in chapter 6 is the critical role that observations can and will play in constraining the uncertain nature of feedback within hydrodynamical simulations.

4. All the models and simulations tend to similar present-day abundance gradients, despite the diversity at earlier times, save for g24334 (which was chosen specifically in violation of the imposed shallow present-day gradient boundary condition, for illustrative purposes). In almost every case this requires the gradient to flatten with time, the exception being the chemical evolution model of Chiappini et al. (2001). This model starts with an initially positive gradient that is independent of its halo phase. The gradient then inverts to become negative, with a gradient similar to other chemical evolution models.
5. The diversity of the evolution of metallicity gradients is for the first time highlighted by our large sample of both hydrodynamical simulations and chemical evolution models. Our results indicate that observations of the metallicity gradient for disk galaxies at different redshifts and that for the different age populations in the Galaxy are key to reveal the formation processes of disk galaxies and better constrain the sub-grid physics implemented with all the codes sampled.
6. Finally our work comparing the MUGS feedback scheme with the MaGICC feedback scheme in the context of the evolution of the metallicity gradients shows how big of an effect the feedback scheme implemented within simulations

## CHAPTER 4

can have on the high redshift radial metallicity gradients. New observations of gradients at high redshift will allow us to better constrain the feedback within our models.

Future work in this area will see us employ a finer temporal cadence, in order to better track the precise influence of merger events on the abundance gradients (both the magnitude of the effect and the timescale for re-establishing a stable abundance gradient). This study will also yield a deeper understanding of how the non-linear processes of star formation and feedback influence systematic differences between the various simulations presented here. We are near completion of a major upgrade to RAMSES which will allow us to re-simulate the RaDES suite with a broad spectrum of chemical elements, including those from SNeII, SNeIa, and AGB stars Few et al. (2012a). With ongoing and future large scale spectroscopic surveys and missions such as RAVE, APOGEE, SEGUE, HERMES, LAMOST, and Gaia, providing detailed information on the phase and chemical space signatures of the Milky Way and beyond, such a chemodynamical exploration will be both timely and critical for understanding the origin and evolution of abundances in galaxies, and their link to the underlying physics of galaxy formation.

## 4.8 Azimuthal Variations

### 4.8.1 Overview and Results

While radial and, to some extent, vertical abundance gradients have been the primary thrust of this aspect of our work, it is worth examining, at least in a cursory manner (for completeness, if nothing else), aspects of the *azimuthal* abundance variations of our fiducial MUGS simulation, g15784. Said realisation shows the most prominent spiral arms at redshift  $z=0$ , another reason for employing this fiducial for this analysis.

## CHAPTER 4

Empirically, Lépine et al. (2011) has suggested the existence of an azimuthal metallicity gradient in the Milky Way, via the use of a carefully-selected sample of Cepheids. Restricting their analysis to those Cepheids in a Galactocentric radius range of 7 to 11 kpc, spanning an  $\sim 60^\circ$  wedge in azimuth, they found a gradient of  $\sim 0.05$  dex/kpc in  $[\text{Fe}/\text{H}]$ . Lépine et al. (2011) attribute the azimuthal variations to the underlying spiral structure of the Galaxy. Here, we employ **g15784**, to see if comparable azimuthal variations can be seen within our simulations.

Figure 4.9 shows the young stellar population ( $< 300$  Myr) of **g15784**. This sample is then sub-divided into 100 Myr bins, with blue showing the youngest, green the intermediate, and red the oldest. We find that for the most prominent spiral arm (panel 2 of Figure 4.9), the youngest stars tend to lie along the ‘inner’ / ‘trailing’ side of the arm, while the older stars lie along the ‘outer’ / ‘leading’ side. This is in agreement with recent work from Dobbs & Pringle (2010), at least in the sense of the trend expected. However, much finer time resolution would be needed within our galaxies to achieve a dataset that could be compared more directly with that of Dobbs & Pringle (2010) or Sánchez-Gil et al. (2011); we simply do not have the resolution at this stage to undertake a comparison with (say) 1 Myr binning (Figure 4.10). That said, as Calzetti et al. (2005) have shown, these sorts of gross trends in orthogonal gradients do appear to extend to  $\sim 100$  Myr old stellar populations, and so perhaps the result highlighted here is not obviated entirely by the use of the larger age bins.

We next show how the density distribution of young stars (born since  $t=13$  Gyr) and cold gas ( $T < 15000$  K) changes as a function of the azimuthal angle. Figure 4.12 shows this, when restricting the radii to that between 10 and 11 kpc (a choice motivated by identifying the maximum impact over the spiral arms). Figures 4.9 and 4.11 show one clear predominant arm in **g15784** and three others which are noticeable, but significantly weaker. Figures 4.12 and 4.11 also demonstrate that

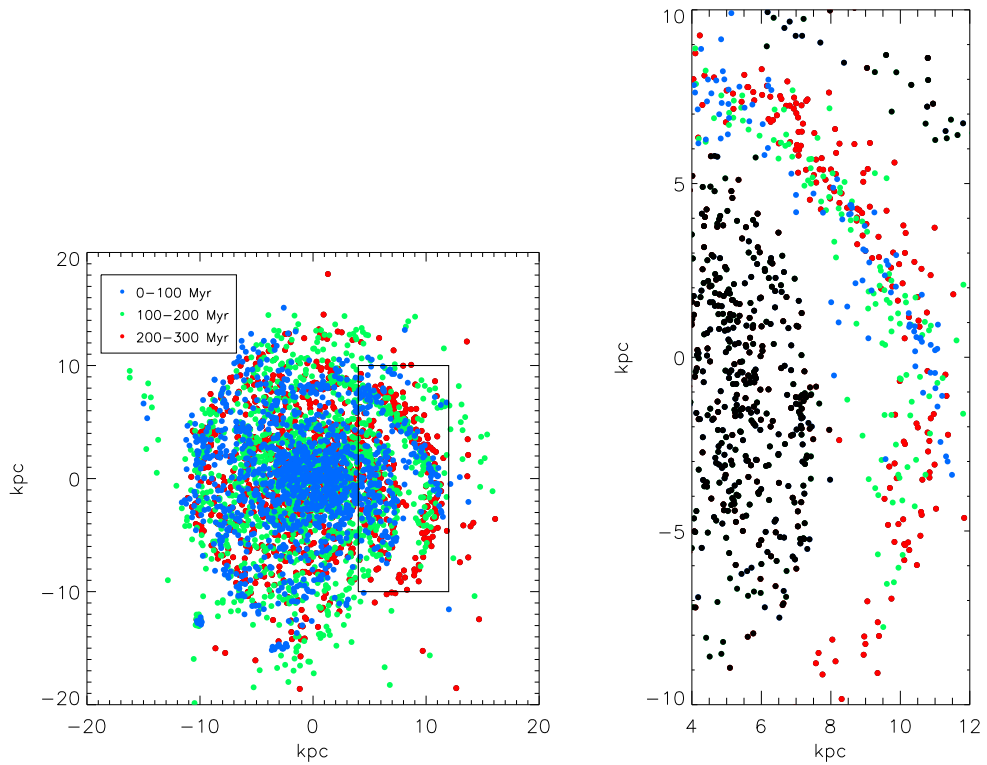


Figure 4.9: Shown as the stellar particles born in the last 300 Myr of the g15784 simulation. Particles have been sub-divided into three age bins: young (0–100 Myr; blue), intermediate (100–200 Myr; green), and old (200–300 Myr; red). The black box shows the location of the expanded region isolated in the second panel. The black points in the second panel show the location of the stars born within the past 300 Myrs which are not part of the isolated spiral arm.

## CHAPTER 4

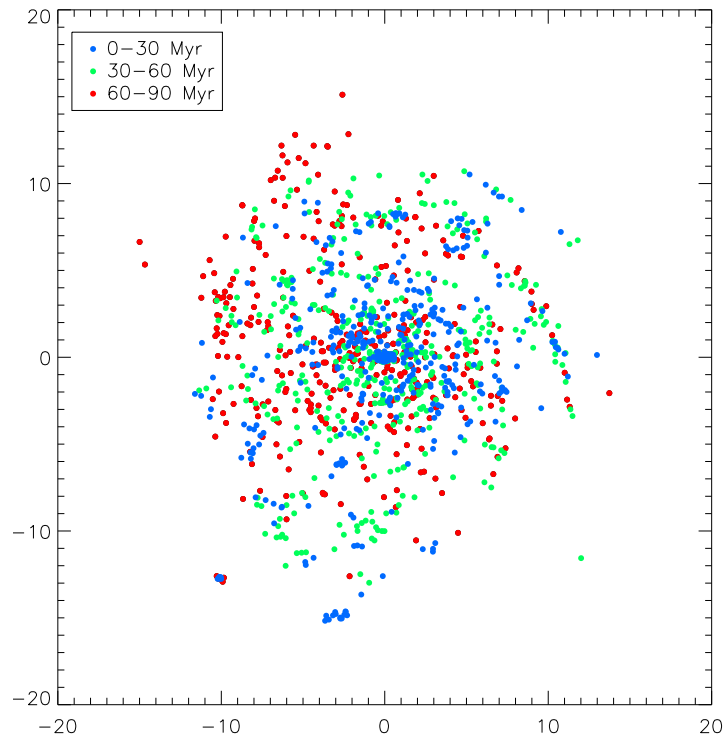


Figure 4.10: Similar to that of Figure 4.9, save for the use of a finer temporal subdivision. Now, star particles born in the last 90 Myrs are shown: young (0–30 Myrs; blue), intermediate (30–60 Myrs; green), and red (60–90 Myrs; red). The bins were chosen to match those used by Sánchez-Gil et al. (2011), in their empirical study. The problem alluded to within the text - i.e., our simulation resolution not being sufficient to probe overly fine temporal bins - is becoming apparent.

## CHAPTER 4

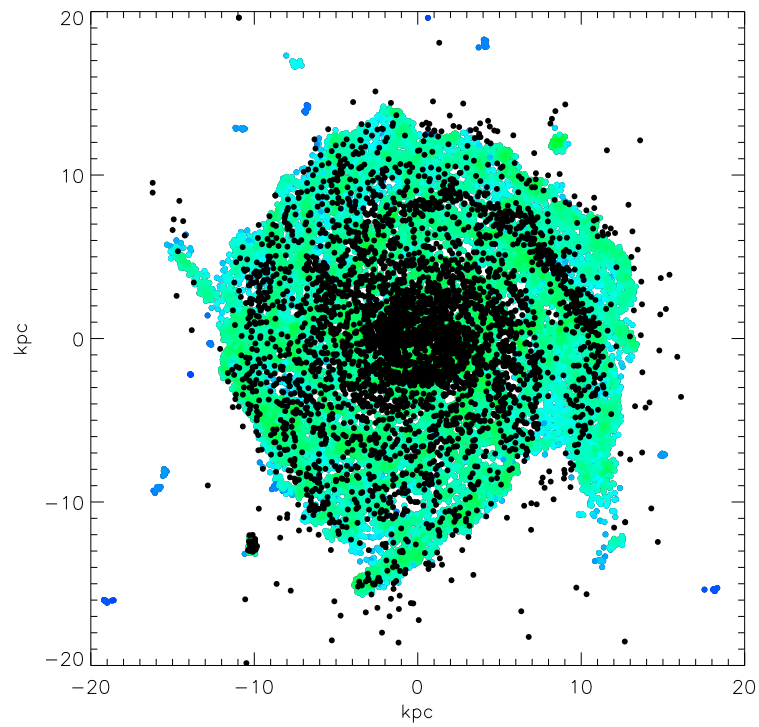


Figure 4.11: In colour, shown is the cold gas ( $T < 15000$  K) density distribution, where higher (lower) density is plotted in yellow (blue). Overplotted in black is the young stellar distribution. As in Figure 4.9, the stars shown are those born in the last 300 Myr.

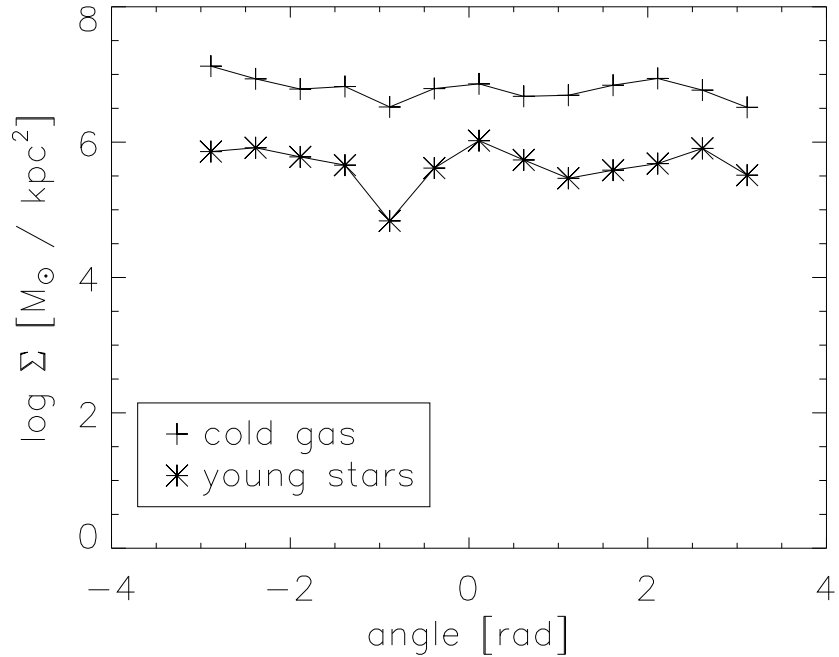


Figure 4.12: Azimuthal density distribution of g15784, restricted to galactocentric radii between 10 and 11 kpc. Here, young stars (star symbols) are those born after  $t=13$  Gyr, and cold gas (plus symbols) is that colder than  $T=15000$  K.

the spiral features of g15784 are more discernible in ‘young stars’ than they are in ‘cold gas’.

Finally, in Figure 4.13, we show the mass-weighted metallicity as a function of the azimuthal angle. The same binning as Figure 4.12 is used (every 0.5 radians). The change in metallicity is very small (less than 0.1 dex); the shape of the distribution is also different from that of the azimuthal density distribution - i.e., the lowest metallicity region does not correlate with the lowest density region, being offset by  $\sim 0.5$  radians (although, again, the peak-to-peak metallicity variation is very small, and likely difficult to discern, had we applied typical observational uncertainties).

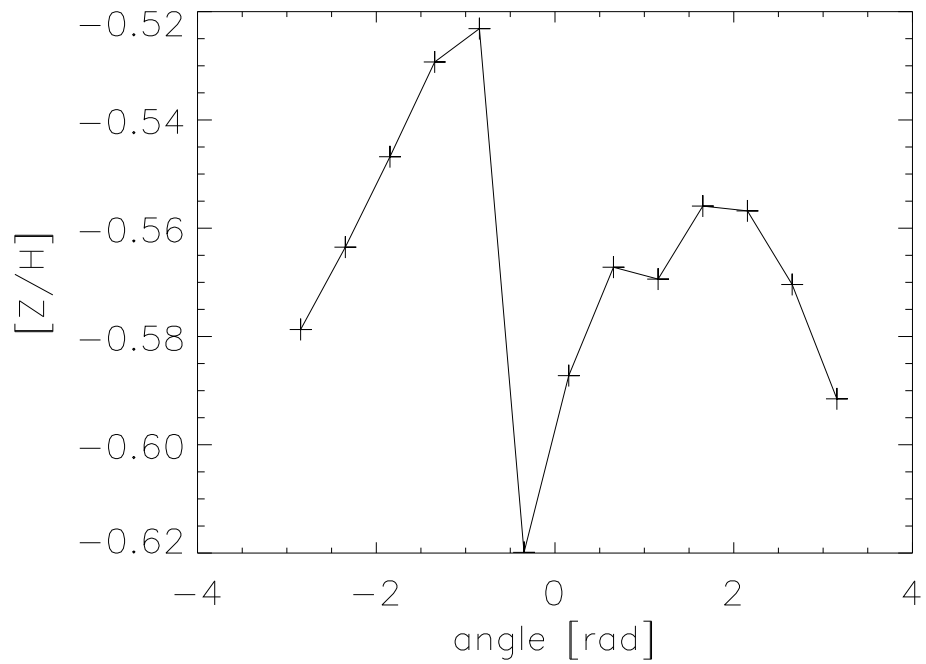


Figure 4.13: The mass weighted metallicity of young stars in g15784 as a function of azimuthal angle. Note the change in metallicity is less than 0.1 dex but the shape of the distribution is unlike the azimuthal density distribution in Figure 4.12. As before, a galactocentric radius range between 10 and 11 kpc was used, and young stars are those born after  $t=13$  Gyrs.

### 4.8.2 Conclusions

This section has focused on the most prominent arm in the fiducial MUGS galaxy g15784. We have shown how the density and metallicity of the cold gas and young stars change as a function of the azimuthal angle. We found the shape of azimuthal mass-weighted metallicity distribution did not correlate with the azimuthal density distribution, being offset from one another by  $\sim 0.5$  radians. Azimuthal gradients have been relatively understudied in spirals galaxies; at face value, the work of L epine et al. (2011) suggests that at least near the solar neighbourhood, significant gradient structure is seen in metallicity when ‘crossing’ a spiral arm. At our current resolution though, we simply cannot relate any putative metallicity structure with that of the underlying spiral arms.

Beyond this attempt of quantifying azimuthal metallicity variations within the simulation, we undertook a cursory azimuthal age variation analysis. Here, we found that on average, the youngest stars tend to populate the trailing parts of predominant spirals arms, while the older stars tend to populate the leading parts. Such a conclusion is in agreement with empirical observations from S anchez-Gil et al. (2011) and consistent with the predictions of classical density wave theory (Dobbs & Pringle 2010), although the reader is referred to Grand et al. (2012) for an alternative conclusion.

# Chapter 5

## Chemical Evolution of the Local Group Dwarf Spheroidals

### 5.1 Abstract

Local Group dwarf galaxies play a critical role in underpinning our understanding of the evolution of galaxies throughout the entire Universe, in large part because they are the only systems for which the otherwise highly uncertain (and essentially unconstrained) star formation history is *not* a variable. Using our `GETool` package, coupled with colour-magnitude diagram (CMD) inferred star formation histories, we present models for several ‘resolved’ Local Group dwarfs. We highlight the impact of the remaining uncertainties in the modeling - specifically, gas inflows and outflows, and ram pressure stripping due to the local intra-group and circum-galactic media - by attempting to match our models with the wealth of recent, spatially-resolved data for these systems.

We find that our models provide satisfactory matches to the bulk of the observed abundance patterns and metallicity distribution functions (MDFs). However, the neutron capture elemental predictions show clear deficiencies associated with the

## CHAPTER 5

underlying nucleosynthesis prescriptions adopted. Our best results occur when using supernova-driven outflows (i.e., super-winds), with partial re-accretion of gas. Without ram pressure stripping, our predicted gas fractions in dwarf spheroidals are up to an order of magnitude too high (similar to that found by comparable models in the literature); stripping ameliorates this apparent mismatch, although at the price of worsening the predicted abundance pattern distributions. Our adopted framework, while useful in a gross sense, should be improved with a more sophisticated treatment of ram pressure stripping.

### 5.2 Introduction

A wealth of spatially-resolved kinematic and chemical information now exists for many, if not most, of the Local Group's dwarfs. Recent observations of the Milky Way's satellites include Venn et al. (2012): Carina, de Boer et al. (2012b): Fornax, de Boer et al. (2012a): Sculptor, Cohen & Huang (2010): Ursa Minor, Koch et al. (2012): Hercules and Lai et al. (2011): Boötes. Dwarf satellite galaxies of other hosts, such as M31, have also been the subject of recent study (e.g. Tollerud et al. 2012), the latter proving invaluable as a comparator to the Milky Way's system (e.g. McConnachie & Irwin 2006).

Dwarf galaxies are not as simple as once thought, with multiple stellar populations seen in many (e.g. Amorisco & Evans 2012, :Fornax), evidence seen for significant amounts of inflowing and outflowing material (e.g. Kirby et al. 2011b; Qian & Wasserburg 2012), and even metallicity gradients seemingly present in some dwarfs (e.g. Monelli et al. 2012, :Tucana). The impact of these new data on the chemical evolution of Local Group dwarfs has only been explored in a cursory sense, to date. Subsets of many these, and other, empirical constraints have been the focus of previous work, although a fully holistic approach remains a challenge; examples

## CHAPTER 5

of previous work in the field include those pertaining to the satellites' photometric properties (Calura et al. 2008), the evolution of neutron capture abundances (Lanfranchi et al. 2008), metallicity distribution functions (Lanfranchi & Matteucci 2010), and galactic super-winds (Lanfranchi & Matteucci 2007). Less work has been done on 'constrained' modelling of Local Group dwarfs with coupled hydrodynamical and N-body codes (e.g. Revaz & Jablonka 2012; Pasetto et al. 2011), but it is clearly a fruitful avenue for future research.

In this chapter, we present chemical evolution models for three Local Group dwarf spheroidals (dSphs): Carina, Fornax, and Sculptor. With their fixed, CMD-inferred, star formation histories (e.g. Fenner et al. 2006) as input to our `GEtool` chemical evolution code, we demonstrate the important role of gas inflow and outflow on the predicted elemental abundance patterns.

### 5.3 The Code

The work presented here makes use of the chemical evolution code `GEtool` (e.g. Fenner et al. 2006; Fenner & Gibson 2003; Fenner et al. 2004); the main components of the code will be reviewed here, although a more comprehensive discussion can be found in the aforementioned works.

`GEtool` traces the gas-phase temporal evolution of 107 isotopes of 45 different elements, in a given volume of space, including treatments of both r- and s-process neutron capture nucleosynthesis, as described by Fenner et al. (2006). This work focuses on seven elements in particular (C, O, Mg, Na, Fe, Ba and Eu), to link specifically to extant observations of Local Group dwarfs (e.g. Venn et al. 2012, and reference therein). Within this volume, the impact of inflows and outflows can also be traced, through their shaping of the volume's gas surface density, via:

CHAPTER 5

$$\begin{aligned}
 \frac{d}{dt}\sigma_i(t) &= E_{i,LIMS}(t) + E_{i,SNII}(t) + E_{i,SN Ia}(t) \\
 &\quad - W_{i,ISM}(t) - W_{i,SNII}(t) - W_{i,SN Ia}(t) \\
 &\quad + \frac{d}{dt}\sigma_i(t)_{infall} - X_i(t)\psi(t)
 \end{aligned}
 \tag{5.1}$$

where  $\sigma_i(t)$  is the gas mass surface density of isotope (or element)  $i$  at time  $t$ . The first three terms on the right-hand side,  $E_{i,LIMS}(t)$ ,  $E_{i,SNII}(t)$ , and  $E_{i,SN Ia}(t)$  are the mass surface density of  $i$  ejected at time  $t$  from Low and Intermediate Mass Stars (LIMS), SNeII, and SNeIa, respectively. The next three terms,  $W_{i,ISM}(t)$ ,  $W_{i,SNII}(t)$ , and  $W_{i,SN Ia}(t)$  are the surface density of species  $i$  lost from the system in superwinds at time  $t$ : ISM represents that associated with the neutral Interstellar Medium (ISM), and SNII and SNIa are associated with the material ejected directly from the SNe that is lost in the superwinds.

The term  $\frac{d}{dt}\sigma_i(t)_{infall}$  is the infall rate of gas into the system, and proves to be of critical importance within our framework (and is determined *a posteriori* in a rather unique manner, relative to other approaches in the literature). Specifically, the infall rate is taken to be the quantity of gas that is required to ensure that the total surface density gas during phases of star formation adhere to the Kennicutt star formation law:

$$\psi(t) = \nu \sigma(t)^n
 \tag{5.2}$$

As our star formation rate is fixed from observations (Dolphin et al. 2005; de Boer et al. 2012b,a) the amount of infalling gas required can be determined with the above equation, where  $\psi(t)$  is the star formation rate at time  $t$ ,  $\sigma(t)$  is the gas surface density at time  $t$ , and  $\nu$  is the star formation efficiency. In the following, we use  $n=1.4$  and  $\nu=0.05$ . As discussed in Fenner et al. (2006) and Lanfranchi et al. (2006), low efficiencies of this level result in models more consistent with empirical

## CHAPTER 5

evidence presented by dSphs. The final term in equation 5.1 ( $X_i(t)\psi(t)$ ) corresponds to the depletion of species  $i$  from the ISM into newly-formed stars, where  $\psi(t)$  is the star formation rate at time  $t$  and  $X_i(t)$  is the mass fraction of  $i$  at time  $t$ .

We adopt here a three-component power law initial mass function (IMF), after Kroupa, Tout & Gilmore (1993), with lower and upper stellar mass limits of  $m_{low} = 0.08 M_\odot$  and  $m_{up} = 60 M_\odot$ , respectively. For Type Ia SNe, we assume a fairly conservative singly-degenerate progenitor model, the formalism for which is described by Matteucci & Greggio (1986); we assume that 4% of the mass tied up in binaries (which are assumed to have a total mass (split between primary and secondary) between  $3 M_\odot$  and  $16 M_\odot$ ) end up as SNIa.

Our wind formalism calculates the mass surface density of SNIa and SNII ejecta lost at each timestep as a function of their respective underlying SN rates. As noted above, cold ISM gas is also lost along with the SN ejecta. The functional forms for each are as follows:

$$W_{i,SNIa}(t) = E_{i,SNIa}(t) \min(0.9, \frac{\epsilon_{SNIa}}{m_{tot}} R_{SNIa}) \quad (5.3)$$

$$W_{i,SNII}(t) = E_{i,SNII}(t) \min(0.9, \frac{\epsilon_{SNII}}{m_{tot}} R_{SNII}) \quad (5.4)$$

$$W_{i,ISM}(t) = X_i(t) ML [W_{gas,SNIa}(t) + W_{gas,SNII}(t)] \quad (5.5)$$

where  $E_{i,SNIa}(t)$  and  $E_{i,SNII}(t)$  refer to the ejected material from the SNIa and the SNII at time  $t$ , as in equation 5.1.  $m_{tot}$  is the total galaxy mass taken from Mateo (1998), while  $R_{SNIa}$  and  $R_{SNII}$  are the SNIa and SNII rates. The wind efficiency factors are given by  $\epsilon_{SNIa}$  and  $\epsilon_{SNII}$ . After Hensler et al. (2004), we do not allow more than 90% of the SN ejecta to escape.  $W_{gas,SNIa}$  and  $W_{gas,SNII}$  gives the total amount of stellar ejecta lost in the winds at time  $t$ .  $ML$  is the mass-loading factor, a key parameter in determining the metallicity of the galactic winds; it refers to the mass of the ISM carried away relative to the mass of the stellar ejecta in the winds.

## CHAPTER 5

We adopt  $ML=15$ , a value not dissimilar to that of Silk (2003) ( $ML=10$ ) or Martin et al. (2002) ( $ML=9$ ), despite the very different modelling frameworks employed.

We assume that both SNeIa and SNeII have the same explosion energy ( $10^{51}$  ergs), while the feedback efficiency from SNIa is taken to be  $5\times$  higher than that of the SNeII. The latter was based upon the work of Recchi et al. (2004) and Recchi et al. (2006) who showed that SNeII were less effective at expelling their ejecta as they have had to heat the molecular clouds from which they formed. SNIa progenitors have much longer lifetimes than SNeII allowing more time for migration into less dense regions where their ejecta can spread more readily/efficiently.

From observations, Heckman et al. (2000) suggest that outflow rates in starburst galaxies are comparable to their underlying star formation rates. Such a result has strong theoretical support (e.g. Silk 2003); in our work, we adopt wind efficiencies which ensure the outflow rates are roughly half that of the star formation rate. In addition, we assume the wind efficiency is inversely proportional to the mass of the galaxy after Fenner et al. (2006).

### 5.3.1 Stellar Yields

For low- and intermediate-mass stars (LIMS), we adopt the yields of Karakas (2010). These yields apply for elements up to the iron peak for stellar masses in the range between  $1 M_{\odot}$  and  $6 M_{\odot}$ . We then extrapolate these AGB yields to  $8 M_{\odot}$  with full knowledge of the uncertainties in doing so; unfortunately, the debate over the dominant stellar physics acting in the transition region from massive AGB stars to super-AGB stars to low mass SNeII remains unresolved (e.g. Doherty & Lattanzio 2006). As such, until full and self-consistent grids in this mass range become available, we have been forced to adopt this conservative approach.

As the Karakas (2010) models do not incorporate s-process neutron capture processes (unlike her next-generation of models (e.g. Karakas et al. 2012)), we have

## CHAPTER 5

adopted the post-processed s-process yields of Travaglio et al. (2004), as described by Fenner et al. (2006).

For the Type Ia supernovae (SNeIa), we adopt the yields of Iwamoto et al. (1999). As noted previously, we assume 4% of the mass tied up in the binary mass range 3–16  $M_{\odot}$  result in SNeIa, after Alibés et al. (2001) and Fenner & Gibson (2003)

For massive stars ( $>8M_{\odot}$ ), we adopt the yields of Woosley & Weaver (1995), which span the 11  $M_{\odot}$  to 40  $M_{\odot}$  range; for the 40  $M_{\odot}$  to 60  $M_{\odot}$  (our upper mass limit to the IMF) range, we extrapolate the tabulated yields. For the 8  $M_{\odot}$  to 11  $M_{\odot}$  range, we assume no new material is synthesised, and that the stars eject the same chemical patterns as the gas from which they were born (i.e., purely unprocessed material); again, this assumption will be rectified once comprehensive grids of yields for super-AGB stars become available.

The r-process yields used in our work here are as described by Travaglio et al. (1999) and Fenner et al. (2006); specifically, the yields were inferred from the difference between the solar abundance values and those resulting from the adopted s-process prescription. We assume (admittedly with little guidance from theory or observation) that this r-process component can be associated with SNeII of mass  $<40 M_{\odot}$ .

The total ejected mass (newly synthesised + unprocessed/pre-existing), as a function of progenitor mass, for 6 of the 47 elements traced by `GETool` is shown in Figure 5.1.

### 5.4 Carina

Carina, a dwarf spheroidal (dSph) satellite of the Milky Way, is located  $\sim 100$  kpc from the Galaxy, with a mass of  $\sim 13 \times 10^6 M_{\odot}$  (Mateo 1998). Its episodic star formation history has attracted a wealth of observational study (e.g. Venn et al. 2012; Bono et al. 2010; Koch et al. 2006, and references therein). It has been known since

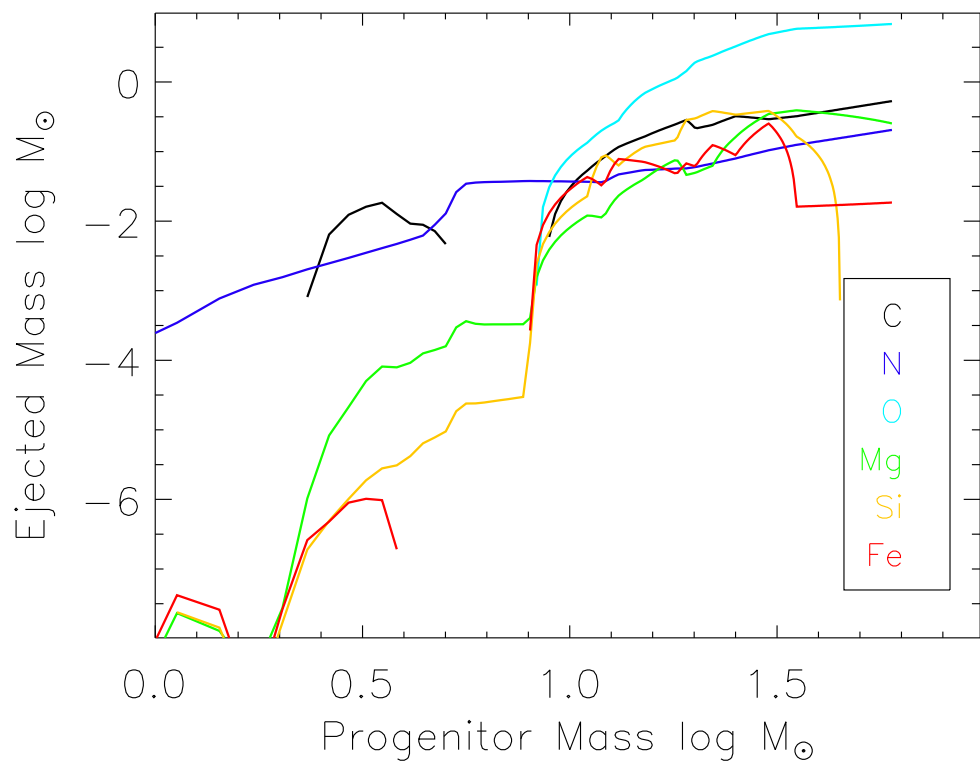


Figure 5.1: The ejected mass for six representative elements (Carbon: black; Nitrogen: purple; Oxygen: blue; Magnesium: green; Silicon: yellow; Iron: red), as a function of progenitor mass.

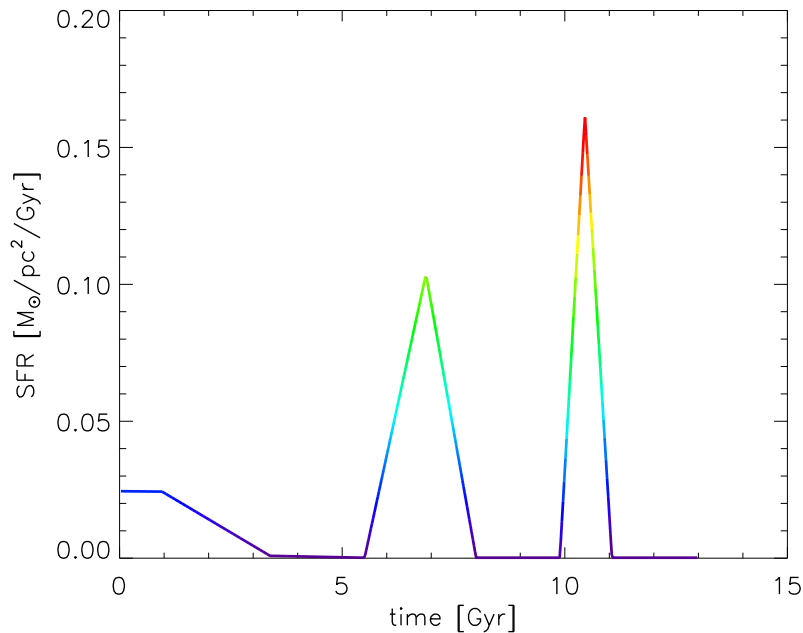


Figure 5.2: Empirically-derived star formation history of the Carina dwarf spheroidal (Dolphin et al. 2005), employed as a ‘fixed’ input to the chemical evolution model, colour-coded by star formation rate (see equation 5.2, where red corresponds to times of high star formation, and purple to times of low star formation).

Mould & Aaronson (1983) that the majority of stars in Carina have intermediate ages (Fig 5.2), and later it was shown there are three distinct bursts of star formation (Smecker-Hane et al. 1996), which are easy to appreciate via the three clear main sequence turnoffs in the associated colour-magnitude diagram (CMD) (e.g. Dolphin et al. 2005). Using the star formation history inferred by Dolphin et al. (2005) from this CMD, we present chemical evolution models for the Carina dSph.

#### 5.4.1 Inflows and Outflows

We first show the inferred temporal evolution of the total gas surface density (see equation 5.1) of Carina (inset panel within Fig. 5.3). We can sub-divide this ‘total’ into five primary sub-components; gas resulting from stellar ejecta (red), that

## CHAPTER 5

taking part in a galactic wind/outflow (blue), that associated with fresh infall of star formation ‘fuel’ (cyan), that associated with material being reaccrued back onto the system (purple), and that being ‘lost’ to star formation at any given time (yellow). The dominant role of gas infall (cyan) is readily apparent; in some sense, the primary novel aspect of our modeling is that said infall is parameterised (or ‘controlled’) to ensure the model adheres strictly to a Kennicutt star formation law (see equation 5.2).

In the absence of exceedingly efficient SNeIa-driven outflows and/or ram pressure stripping, the predicted final gas fraction of the model is  $\sim 90\%$  - i.e., roughly two orders of magnitude higher than observed. Parameterised ram pressure stripping (e.g. Pasetto et al. 2011) should allow us to better recover the low gas fractions seen in dSphs in the vicinity of massive hosts, like the Milky Way. In the interim, simply stripping the most recently infallen fuel (least tightly bound) provides a suitable final fraction.

We next show the three contributors to the SN-driven winds (Fig 5.4), as described by equations 5.5, 5.4, and 5.3; the winds here are dominated by the contribution from the interstellar medium (ISM), while that associated with material expelled directly from SNeIa and SNeII is a much smaller fraction, in comparison.

### 5.4.2 Abundance Patterns

In this section, we highlight several predictions for the abundance ratios of Carina compared to recent observational data from Venn et al. (2012). The latter obtained high-resolution spectra for nine red giant branch (RGB) stars with detailed abundances of 23 chemical elements. They combined their observations with the work of Koch et al. (2008) (10 RGB stars) and Shetrone et al. (2003) (5 RGB stars) to enhance the sample size over a wider range in metallicity. We show the predictions for three  $\alpha$ -elements: magnesium, oxygen, and calcium, two neutron capture elements:

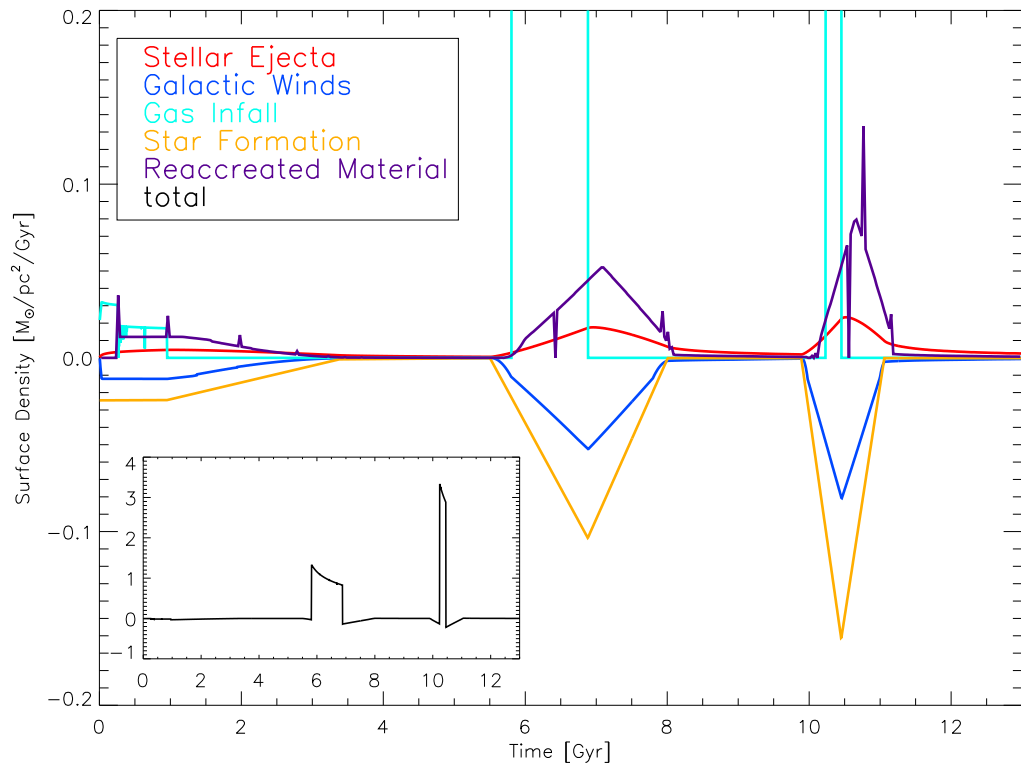


Figure 5.3: The evolution of the gas surface density of gas for the Carina chemical evolution model. In red is shown the material returned to the system from dying stars, as a function of time; dark blue shows the amount of gas removed by the galactic winds; yellow shows the amount of gas used up in star formation; cyan shows the gas infalling to the system and purple shows the amount of gas that is recreated back onto the galaxy. The inset to the panel shows the sum of the four sources of gas - clearly, infalling material dominates over the other sources (10:1 relative to, for example, outflowing wind material).

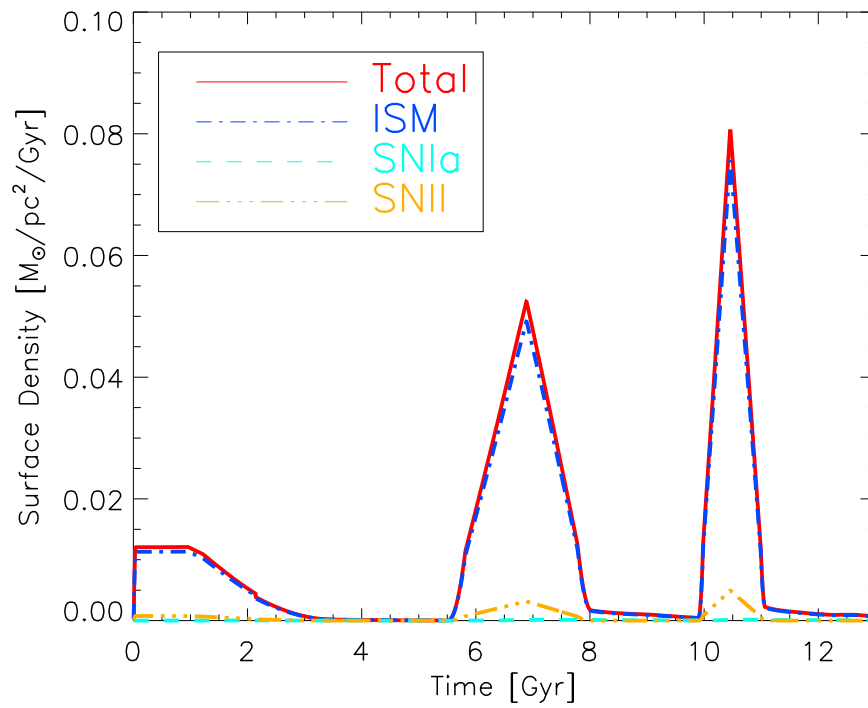


Figure 5.4: The components that make up the stellar winds associated with the Carina dSphs model (i.e., sub-dividing the dark blue line from Figure 5.3): here, the red line shows the total wind component; the dark blue, dash-dotted, line shows the amount of the ISM driven away with the SN winds (equation 5.5); the cyan dashed line show the SNeIa ejecta (equation 5.3) lost; the orange dashed - triple-dotted line shows the SNeII ejecta lost (equation 5.4).

## CHAPTER 5

barium and europium, as well as sodium.

To better mimic the typical observational uncertainties, we convolve the models (both in the abscissa and ordinate, when plotting  $[\text{el}/\text{Fe}]$  vs  $[\text{Fe}/\text{H}]$ , for example) with a  $\sigma=0.1$  dex Gaussian. For plotting purposes, we replace each ‘point’ in the chemical evolution model plane (which corresponds to a single timestep) with  $100 \times \psi(t)/\psi_{\text{max}}$  points (an arbitrary selection, admittedly) drawn at random from the associated 0.1 dex bi-Gaussian distribution.

### Alpha Elements

In Fig 5.5, we show the abundance patterns of three  $\alpha$ -elements: magnesium, oxygen, and calcium. The  $\alpha$ -elements are associated mainly with massive stars and their SNeII ejecta, (recall Figure 5.1). From a chemical evolution perspective, the  $\alpha$ -elements have always been of great interest, in the sense that they provide something of a ‘clock’ for the timescale for star formation in a region - with higher  $\alpha/\text{Fe}$  ratios indicative of more rapid timescales of enrichment. Conversely, on longer timescales,  $\alpha/\text{Fe}$  begins to ‘see’ the impact of the appearance of (longer-lived) SNeIa progenitors, resulting in something of a “knee” in the  $\alpha/\text{Fe}$  vs  $\text{Fe}/\text{H}$  distribution. In the solar neighbourhood, this knee appears near  $[\text{Fe}/\text{H}]=-1$ , and has provided invaluable constraints upon models of the Milky Way and the progenitors of SNeIa. Such a knee is not so well-constrained for Carina (e.g. Lemasle et al. 2012), but is expected to occur earlier than that seen in the solar neighbourhood (i.e., at  $[\text{Fe}/\text{H}]\ll -1$ ). Indeed, it has been suggested (e.g. Gilmore & Wyse 1991) (and some would say expected: e.g., Few et al. (2012a)) that the bursty nature of Carina’s star formation history should result in the presence of multiple such ‘knees’.

From Fig 5.5, we see reasonable agreement with the observational data, particularly for oxygen and calcium. Our predictions for magnesium are less ideal,

## CHAPTER 5

admittedly; in large part, we feel that this represents the well-known issue concerning the underproduction of Mg from the SNeII models of Woosley & Weaver (1995). From the model predictions, we do not see a clear ‘knee’ in the  $\alpha/\text{Fe}$ – $\text{Fe}/\text{H}$  plane. There is a slight downturn in the oxygen and the magnesium when the metallicity reaches  $[\text{Fe}/\text{H}] \sim -2.7$ , but it is not particularly significant.

Here, we have allowed for re-accretion of outflowing wind material; not doing so, within the context of our framework, leads to an underproduction of the global stellar metallicity. We also examined using gas stripping within the models, as this was the only way to recover a reasonable final gas fraction for Carina (consistent with that found by others, it must be stressed, within the context of different assumptions regarding star formation and feedback, for example). Parameterised ram pressure stripping, within the context of our model, works similarly to that described above for the infalling gas. Specifically, the amount of gas needed to satisfy the Kennicutt star formation law is calculated (recall equation 5.2), and that gas is then accommodated (metaphorically, ‘flows’) into the system. If, at any point time, there is an excess of gas relative to equation 5.2, then that gas is made available for ‘stripping’ (e.g., during quiescent periods of star formation where the gas surface density can grow unheeded). That said, for our Carina models, parameterised stripping of this nature was too ‘extreme’, leading to predicted abundance ratios which were significantly lower than those observed.

The earlier generation of our models (Fenner et al. 2006) suffered from a significant overproduction of sodium, but as shown clearly in Fig 5.5, this problem has been rectified naturally via the use of the newer AGB models of Karakas (2010), as opposed to their immediate antecedent (Karakas & Lattanzio 2007).<sup>1</sup>

---

<sup>1</sup>A dramatic change in the relevant reaction rate was responsible for this significant change in the predicted sodium nucleosynthesis.

### Neutron Capture Elements: r- and s-process

Also in Fig 5.5, we show the predicted distributions of the heavy s-process element barium and the r-process element europium. At low metallicities, we capture the behaviour of the neutron capture elements well, but it is equally clear that we grossly underestimate the dynamic range in both the s- and r-process elemental patterns at higher metallicities. It has been suggested that the evolution of barium is actually dominated by the r-process at low metallicities, with the s-process progressively taking over at higher metallicities and, ultimately, being responsible for the larger spread observed in  $[\text{Ba}/\text{Fe}]$  at a given  $[\text{Fe}/\text{H}]$  (e.g. Shetrone et al. 2001). The reasonable agreement between the model  $[\text{Ba}/\text{Fe}]$  and observations, suggests that our inferred r-process component for Ba at low metallicities may not be incorrect; one could also argue that some component of the at low  $[\text{Fe}/\text{H}]$  might be due to a weak-s process contribution from massive stars, rather than an r-process contribution. As both act on comparable (rapid) timescales (being due to high mass progenitors), the argument between them is somewhat academic. Regardless, the quantity of barium at low  $[\text{Fe}/\text{H}]$  in these models appears a reasonable match to the observational data.

### 5.4.3 Metallicity Distribution Function

In Fig 5.6, we show the predicted metallicity distribution function (MDF) of our fiducial Carina model (black histogram), alongside the observed MDF from Koch et al. (2006) (derived using two different metallicity calibrations: Carretta & Gratton (1997), in cyan, and Zinn & West (1984) in orange). From a sample of 437 red giant stars, Koch et al. (2006) showed the mean metallicity of Carina to be  $[\text{Fe}/\text{H}] \sim -1.7$ , with the range of metallicities spanning  $\sim 3$  dex. The model MDF has been convolved with a  $\sigma=0.28$  dex Gaussian, to reflect the quoted observational uncertainties by Koch et al. (2006). One can see that the peak of our MDF matches well with the observed peak (cyan), although the current fiducial model admittedly suffers from

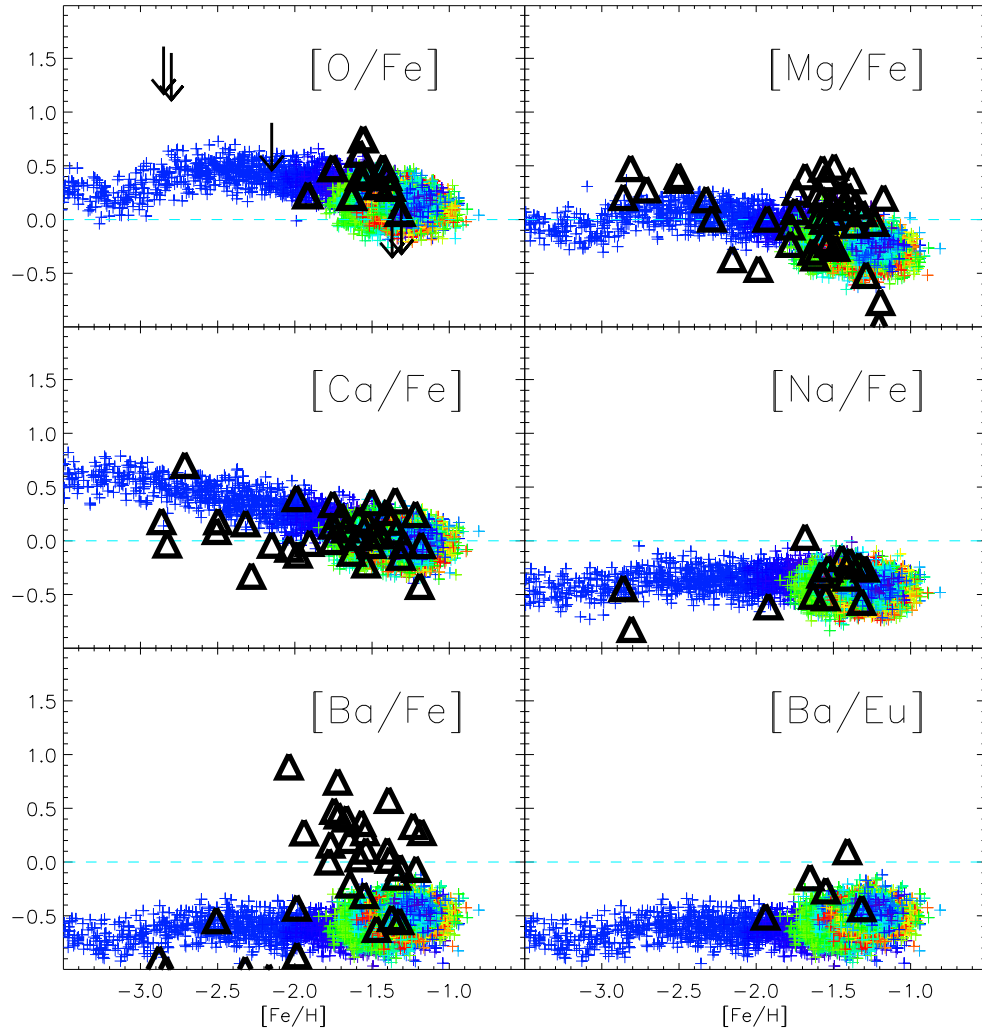


Figure 5.5: Predicted abundance patterns for the chemical evolution model of the Carina dSph (plus symbols), colour-coded by star formation rate coloured according to the star formation rate (recall Fig 5.2), where red and green symbols correspond to periods of higher star formation, while blue and purple correspond to periods of lower star formation. The black triangles correspond to the observational data of Venn et al. (2012); downward facing arrows are also from Venn et al. (2012), but represent data for which only upper limits exist.

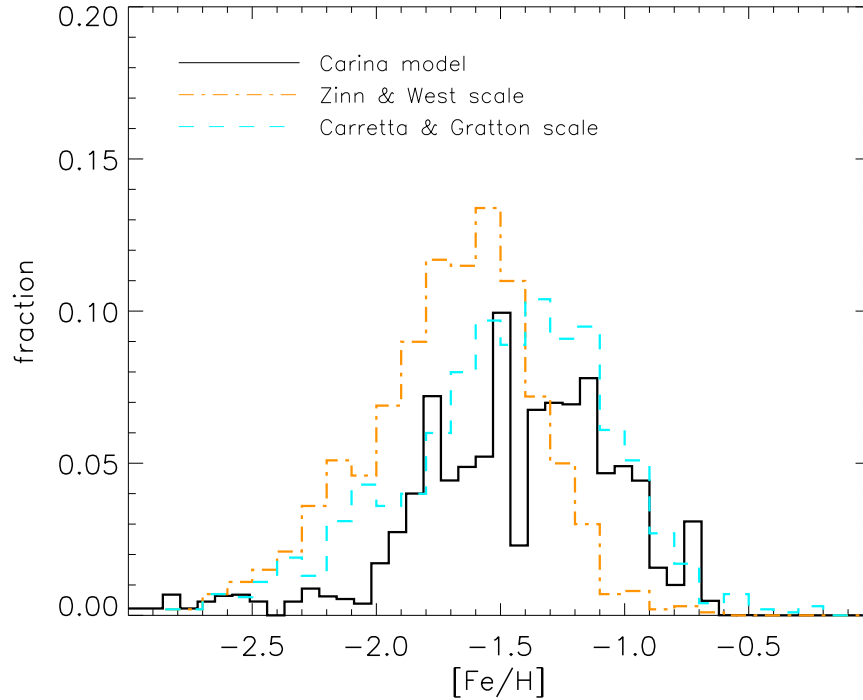


Figure 5.6: The predicted metallicity distribution function of the Carina dSph (black) compared with the observed MDF of Koch et al. (2006) (calibrated with two different metallicity calibrations: Carretta & Gratton (1997) in cyan, and Zinn & West (1984) in orange). Our model has been convolved with a  $\sigma=0.28$  dex Gaussian to mimic the uncertainties associated with observational data.

a dearth of lower metallicity stars in the tail of the MDF.

Lemasle et al. (2012) also find a peak in the MDF of Carina near  $[\text{Fe}/\text{H}] \sim -1.5$ , and quote a mean metallicity of  $\sim -1.7$  (the same as Koch et al. (2006)) for a sample of 35 RGB stars, although they also find more metal-poor stars than our model has predicted. The study in Lemasle et al. (2012) is biased towards higher metallicity stars, meaning there could be even more lower metallicity stars yet to be discovered.

The MDF has been selected to include only  $0.85$  to  $1.25 M_{\odot}$  stars (i.e. G and K stars), still alive today. Had we included M dwarfs in our MDF sample, some of the metal poor tail would begin to fill out.

#### 5.4.4 Choice of Yields

We now discuss the impact of the choice of stellar yields within the chemical evolution modeling. As has been shown previously (e.g. Gibson et al. 1997; Romano et al. 2010), due to the range of underlying stellar physics employed in the various yield compilations, such a choice can have a dramatic effect on the predicted chemical evolution models. Complications arise in that while there are many compilations available in the literature, there are none which span all masses and metallicities with a homogeneous treatment of stellar physics. For different masses and metallicities, the choice available to the end-user is varied, both for low- and intermediate-mass stars (LIMS) (e.g. van den Hoek & Groenewegen 1997; Marigo et al. 2008; Marigo 2001; Karakas & Lattanzio 2007; Karakas 2010) and massive stars (e.g. Woosley & Weaver 1995; Kobayashi et al. 2006; Hirschi et al. 2005; Ekström et al. 2008).

Here, we examine the effect of changing only the massive star yields. Instead of using the standard choice of yields, presented in the previous section (AGB: Karakas (2010); SNIa: Iwamoto et al. (1999); SNII: Woosley & Weaver (1995)), we now employ those of Kobayashi et al. (2006), for the massive stars. In other aspects though, the model matches that of the previous section, in terms of its star formation history, gas infall, outflow, and re-accretion parameterisations.

Graphically, the revised stellar yields for this model can be seen in Figure 5.7, while the impact of this choice on the predicted abundance patterns and MDF can be found in Figures 5.8 and 5.9, respectively.

The yields from Kobayashi et al. (2006) do not show the same underproduction of magnesium which plagues the models of Woosley & Weaver (1995). In Figure 5.8, one can see that the Kobayashi et al. magnesium predictions are on average  $\sim 0.6$  dex greater than those of Woosley & Weaver. The oxygen, calcium, and sodium have also increased, but not as dramatically as seen for magnesium.

The  $[\text{Ba}/\text{Fe}]$  has also increased under the adoption of the Kobayashi et al. (2006)

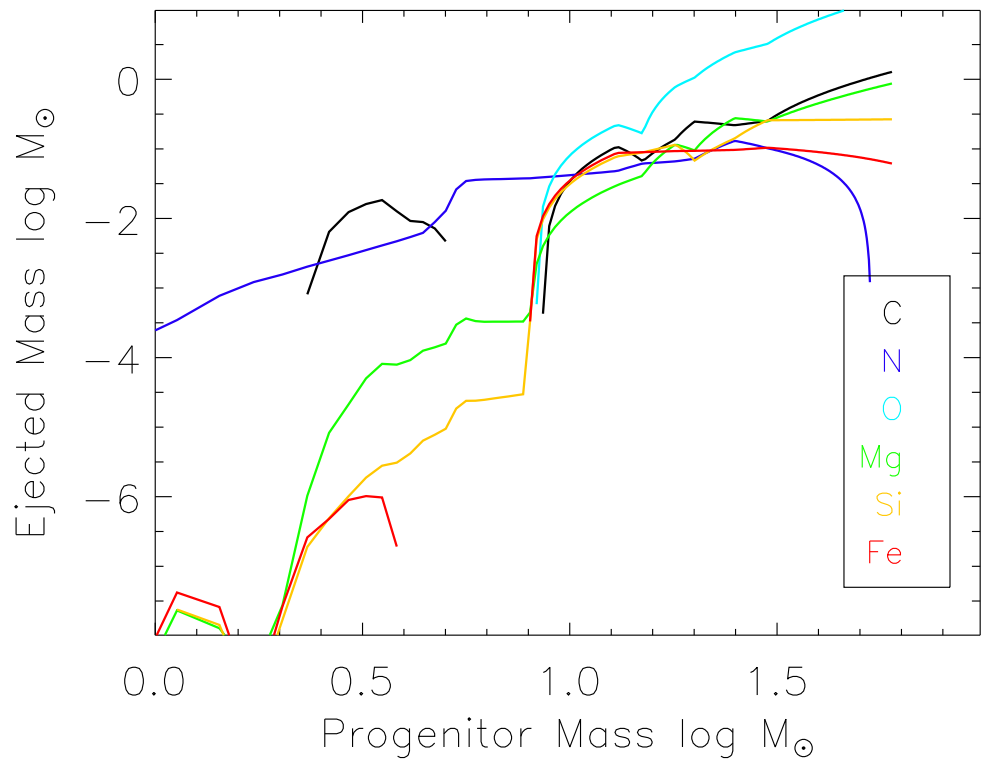


Figure 5.7: The ejected mass for six representative elements (Carbon: black; Nitrogen: purple; Oxygen: blue; Magnesium: green; Silicon: yellow; Iron: red), as a function of progenitor mass. AGB yields from Karakas (2010); SNeII yields from Kobayashi et al. (2006).

## CHAPTER 5

yields, although in this case it is being driven by the changes in iron, rather than barium. Regardless, the dynamic range in  $[\text{Ba}/\text{Fe}]$  seen in the observations is still not recovered. From the bottom-right panel, we find excellent agreement with the empirical trends in  $[\text{Ba}/\text{Eu}]$  with metallicity. However, in this case, ‘two wrongs have made a right’. We know our predictions for barium are incorrect (bottom-left panel of Fig 5.8), as are  $[\text{Eu}/\text{Fe}]$ , but in consort,  $[\text{Ba}/\text{Eu}]$  appears ‘correct’. Clearly though, this is an artifact, and an improved implementation of neutron capture nucleosynthesis is required within `GEtool`.

Finally, we show the predicted MDF using the massive stellar yields from Kobayashi et al. (2006). The observational data plotted in orange and cyan are the same as Figure 5.6, taken from Koch et al. (2006) As with Figure 5.6, the model has been convolved with a  $\sigma=0.28$  dex Gaussian to match the observational uncertainties. We find, as with the predictions using the Woosley & Weaver (1995) yields, the model best matches the Carretta & Gratton (1997) metallicity calibration scale. The tail of low-metallicity stars is even more under-populated when using the Kobayashi et al. SNeII yields.

Broadly speaking, simply changing the SNeII yields from Woosley & Weaver (1995) to those of Kobayashi et al. (2006), does not impact dramatically upon the predicted chemical evolution model of Carina. The most noticeable effect pertains to the aforementioned behaviour for magnesium; indeed, without changing any other aspect of the model, simply replacing the SNeII yields, as such, shifts the predicted  $[\text{Mg}/\text{Fe}]$  distribution to values higher than observed by Venn et al. (2012). We are loathe to modify the stellar yields in an *a posteriori* attempt to better match observations; instead we prefer to show the predicted chemical evolution ‘as is’, allowing us to better identify the elements which require more work in the future.

Weighing up all the various stellar yield uncertainties, Romano et al. (2010) suggest that the optimal yield selection for their chemical evolution code would be:

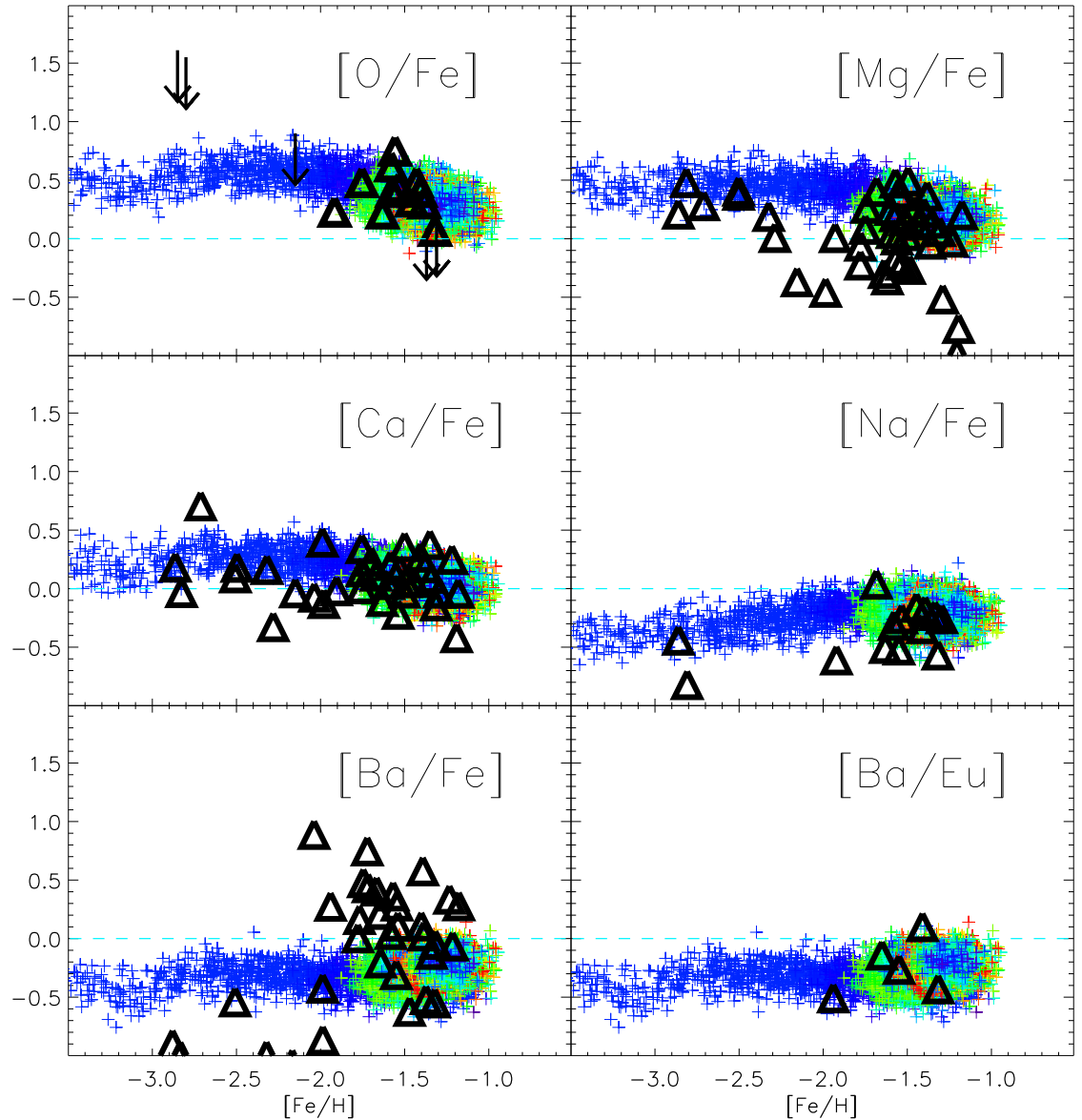


Figure 5.8: Same as Figure 5.5, but using the Kobayashi et al. (2006) SNeII yields, rather than those of Woosley & Weaver (1995). Model predictions from the Carina model are shown as small plus symbols, colour-coded by the star formation rate (recall Fig 5.2). Observational data (Venn et al. 2012) are represented by black triangles and black arrows (upper limits).

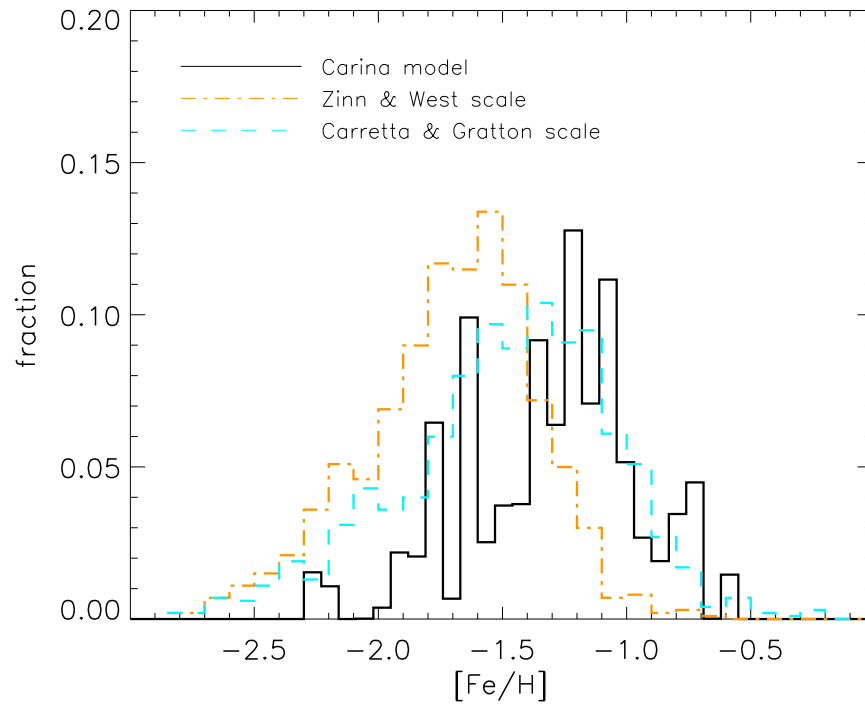


Figure 5.9: Same as Figure 5.6, but now employing the Kobayashi et al. (2006) SNeII yields, rather than those of Woosley & Weaver (1995). Shown is the predicted metallicity distribution function of the Carina dSph (black) compared with the observed MDF of Koch et al. (2006), (calibrated with two different metallicity calibrations: Carretta & Gratton (1997) in cyan, and Zinn & West (1984) in orange). The model has been convolved with a  $\sigma=0.28$  dex Gaussian to mimic the uncertainties associated with the observational data.

## CHAPTER 5

LIMS yields from Karakas (2010), yields from Kobayashi et al. (2006) for SNeII (for  $m < 20 M_{\odot}$ ) and hypernovae (for  $m > 20 M_{\odot}$ ), and pre-supernovae yields for massive stars (for He, C, N, and O) from the Geneva group (Ekström et al. 2008). Again though, we must stress that this mixing-and-matching of stellar physics is not an ideal situation, but one forced upon by the lack of a singularly consistent set of yields.

We note here, in advance, that due to the similarities encountered, for the different yield selections for the next two galaxies presented in this chapter (Sculptor: §5.5 and Fornax: §5.6), we will only present the models using the default Woosley & Weaver (1995) yields.

### 5.4.5 Discussion

Chemical evolution models for Carina have also been presented by Lanfranchi et al. (2006); their framework differs from that described here, in that the star formation is *not* constrained directly by the CMD. Compared to our fiducial model, their predicted  $\alpha$ -element abundances are typically  $\sim 0.5$  dex lower than our predictions, at higher metallicities ( $[\text{Fe}/\text{H}] > -1$ ). Beyond the  $\alpha$ -elements, the neutron capture patterns, within the Lanfranchi et al. framework, have been presented by Lanfranchi et al. (2008). They find good agreement with observations, however their predicted evolution of  $[\text{Ba}/\text{Fe}]$  does not show the same ‘upturn’ near  $[\text{Fe}/\text{H}] \sim -2$ , as seen in the data of Venn et al. (2012).

Broadly speaking, our model predictions are a fair match to the observational data; having said that, the model has two clear failings:

1. The final gas fraction of the model dSph does not match that observed. Our models have final gas fractions of  $> 90\%$ , while the fraction observed is  $< 1\%$  (Mateo 1998). If we include a simple model for stripping where any gas that is not required for star formation is stripped away, we do obtain a final gas

fraction more in line with observations. However, this comes at a cost, as the predicted metallicity is too low and we are unable to match the observed abundance patterns. One solution for this would be to force the infalling gas onto Carina to have a higher metallicity (currently it is assumed to be pristine), thereby ensuring the overall metallicity of the system to remain ‘high’. Supporting this, Koch et al. (2006) make the argument that the episodic star formation history of Carina could not have been caused by the repeated infall of pristine gas. Another solution to the problem would be to implement a more sophisticated model for the stripping, taking into account the orbit of Carina. Pasetto et al. (2011) show details of the orbital history of Carina; allowing stripping to occur only during epochs associated with peri-Galacticon passages might prove enlightening.

2. The neutron capture abundance patterns do not match those observed (Venn et al. 2012). A new, homogeneous, set of neutron capture yields is of the utmost importance for the next version of `GETool`. A first step in this direction is provided by, for example, Karakas et al. (2012), who calculates s-process yields self-consistently, rather than *a posteriori*, as in the current version of `GETool`. We await the release of a comprehensive grid of models spanning a wide range of mass and metallicity, before undertaking this next phase of our work.

## 5.5 Sculptor

At a distance of  $\sim 80$  kpc from the Milky Way, and a mass of  $\sim 6 \times 10^6 M_{\odot}$ , Sculptor possesses basic characteristics similar (within a factor of two) to that of Carina (Mateo 1998). Sculptor, like Carina, alas has a very low HI gas fraction ( $< 1\%$  of the galaxy mass). It appears that Sculptor has two HI clouds associated with it (e.g.

## CHAPTER 5

Carignan 1999; Bouchard et al. 2003), although debate remains as to whether they were present when Sculptor formed or have been expelled subsequently.

The star formation history of Sculptor (Fig 5.10) is comprised of a significant burst at early times (declining exponentially thereafter), with little or no recent star formation; again using its spatially-resolved CMD, de Boer et al. (2012a) went beyond a singular star formation history and derived the spatially-resolved star formation history of Sculptor. The inner regions show a more extended history of star formation, consistent with its metallicity (Tolstoy et al. 2004) and age (de Boer et al. 2011) gradients (which show higher metallicity and younger stars in the central region and older and lower metallicity stars as one moves towards the outskirts of the galaxy).

The chemical evolution model for Sculptor presented here is an update to that presented originally by Fenner et al. (2006). The star formation history has been updated to reflect the newer work of de Boer et al. (2012a). As described in §5.3.1, the AGB stellar yields have also been updated from those of Karakas & Lattanzio (2007) to those of Karakas (2010) (to reflect progress made in refining the underlying reaction rate uncertainties; a minor effect for most elements, with the exception of sodium, which is dramatically reduced (and in better agreement with observations now)).

### 5.5.1 Inflows and Outflows

We now show the inferred temporal evolution of the total gas surface density (equation 5.1) of Sculptor (inset panel to Fig 5.11), after Figure 5.3. Where Carina (Fig 5.3) was dominated by the effects of the infalling gas, Sculptor is dominated by the star formation (yellow curve in Fig 5.11). This is also reflected in the predicted final gas fraction of Sculptor (67%) being  $\sim 30\%$  lower than that of the Carina model. In nature, dSphs have present day gas fractions  $< 1\%$ ; to obtain present-day gas

## CHAPTER 5

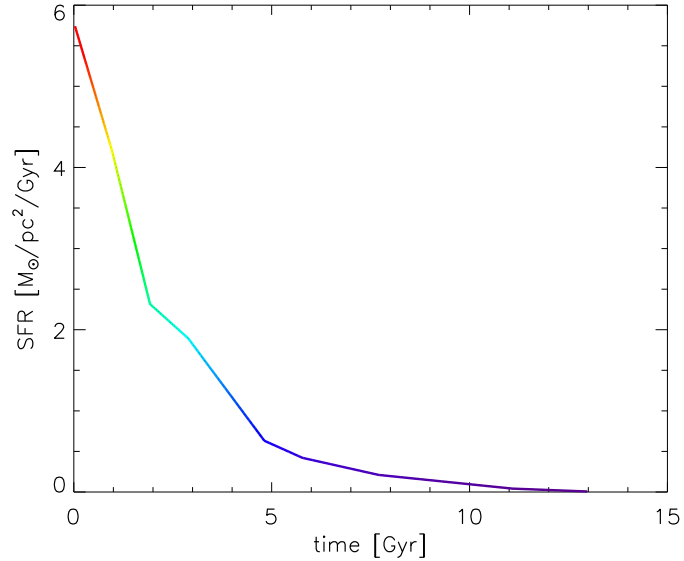


Figure 5.10: The star formation history of the Sculptor dSph derived from its colour-magnitude diagram (de Boer et al. 2012a). Colour-coding reflects the magnitude of star formation, with red representing higher rates, and blue, lower rates.

fractions of this level, we again need to implement gas stripping within the model.

As the infalling gas is tied to the star formation history (de Boer et al. 2012a) via equation 5.2, Sculptor has only one brief phase of gas infall (during the first  $\sim 300$  Myrs of the model: cyan curve of Fig 5.11); this is also reflected in the stellar ejecta returned from dying stars (red curve of Fig 5.11) which again is higher at earlier times and slowly decreases over time (reflecting, obviously, the star formation history).

Next, we show the individual components contributing to the stellar winds (red curve of Fig 5.11). Following equations 5.3, 5.4, and 5.5, the SNIa, SNeII, and ISM all contribute to the material lost to the SNe-driven wind. As for Carina, the ISM component carried along by the SNe-driven winds dominates. That said, while dominating, the final gas fraction predicted by the model (in the absence of ram pressure stripping) remains excessive relative to that observed.

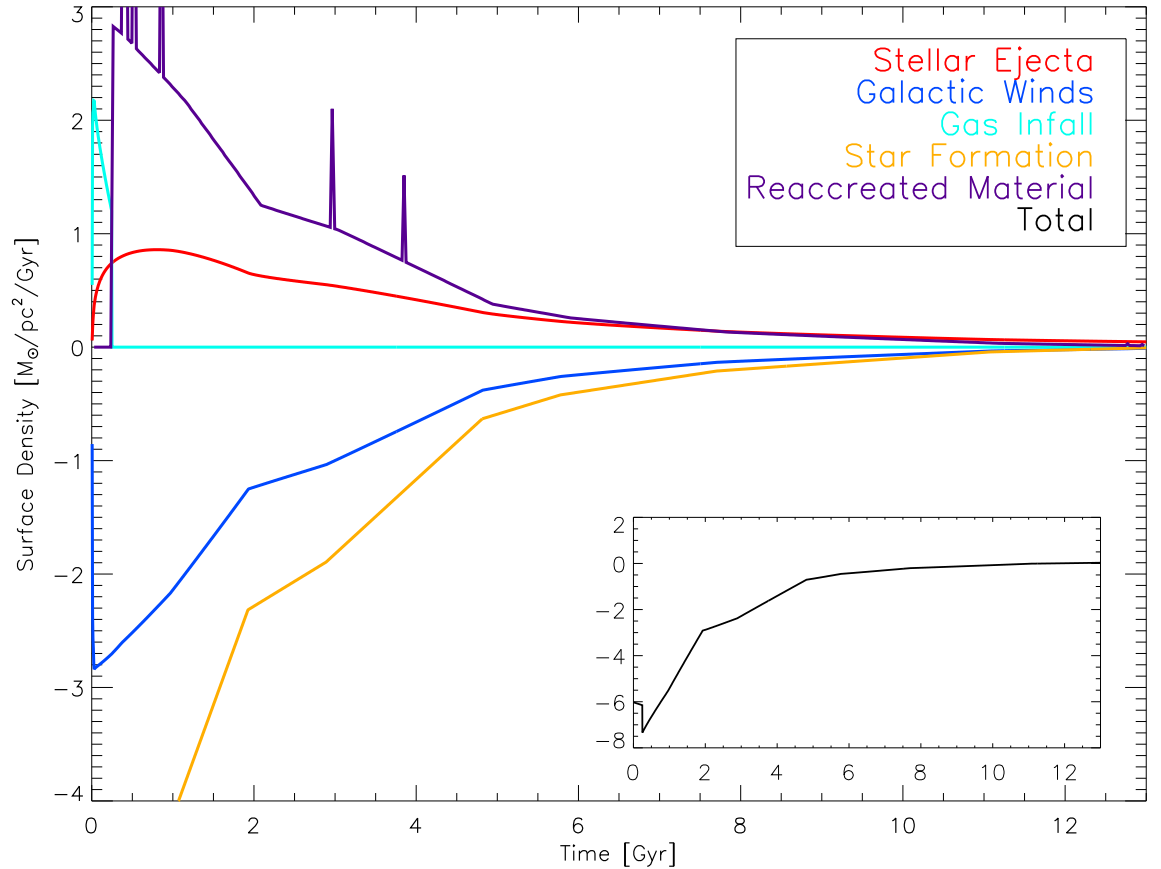


Figure 5.11: The evolution of the surface density of gas for the Sculptor dSph model. In red is shown the material returned to the system from dying stars, as a function of time. Dark blue represents the amount of gas removed by the galactic winds. Yellow shows the amount of gas used up in star formation. Cyan corresponds to the gas infalling to the system. Purple shows the amount of gas being reaccreted back onto the galaxy. The inset to the panel shows the sum of the four sources of gas. Unlike Carina, Sculptor is dominated by the underlying star formation.

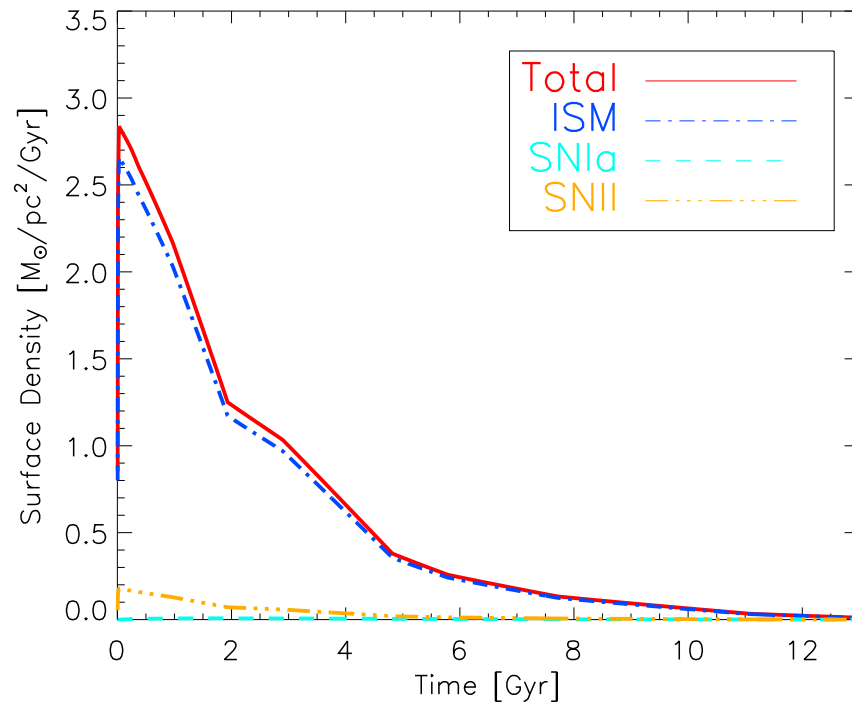


Figure 5.12: The three components that contribute to the stellar winds in the Sculptor dSph model (i.e., the dark blue curve in Fig 5.11): the red curve shows the total, the dark blue dash-dotted curve shows the contribution from the ISM being carried out with the SN winds; the yellow dash-triple-dotted curve shows the contribution from SNeII; the cyan dashed curve shows the contribution from SNeIa.

### 5.5.2 Abundance Patterns

The abundance patterns for six representative elements for the fiducial model of Sculptor is shown in Fig 5.13. The methodology and presentation is as was done for Carina (§5.4.2), where the colour-coding is by star formation rate (Fig 5.10), red (purple) corresponding to high (low) rates. In black, the observational data of Tolstoy et al. (2009) is shown in triangles, and that of Geisler et al. (2005), in diamonds.

One immediate difference between Sculptor and Carina is that the star formation rate in the former is highest at low metallicities, rather than high. As was the case with Carina, the main issue in matching the model to observations comes from the neutron capture elements. The  $[\text{Ba}/\text{Fe}]$  in Sculptor is low compared with observations, and the scatter at a given  $[\text{Fe}/\text{H}]$  appears too small. Our  $[\text{Na}/\text{Fe}]$  is in good agreement with the data of Tolstoy et al. (2009). At metallicities above  $[\text{Fe}/\text{H}]=-1.5$  the predictions for  $[\text{Mg}/\text{Fe}]$  are in good agreement with the data, but below that metallicity, our model underpredicts  $[\text{Mg}/\text{Fe}]$  relative to that observed. The predicted  $[\text{Ca}/\text{Fe}]$  is slightly high, but the slope of the trend with  $[\text{Fe}/\text{H}]$  matches that observed remarkably well. Our  $[\text{O}/\text{Fe}]$  distribution is satisfactory, but the limited data available makes a more concrete comparison difficult.

Sculptor is the only dSph where the ‘knee’ in the  $[\alpha/\text{Fe}]-[\text{Fe}/\text{H}]$  plane has been identified (near  $[\text{Fe}/\text{H}]\sim-1.8$ : Tolstoy et al. 2009). Battaglia et al. (2008) demonstrated that this knee in abundance ‘space’ can also be identified in Sculptor’s kinematic and spatial properties. Our predicted location of the knee in oxygen and magnesium match that observed. The downturn at metallicities above the knee is more significant than that seen in Carina.

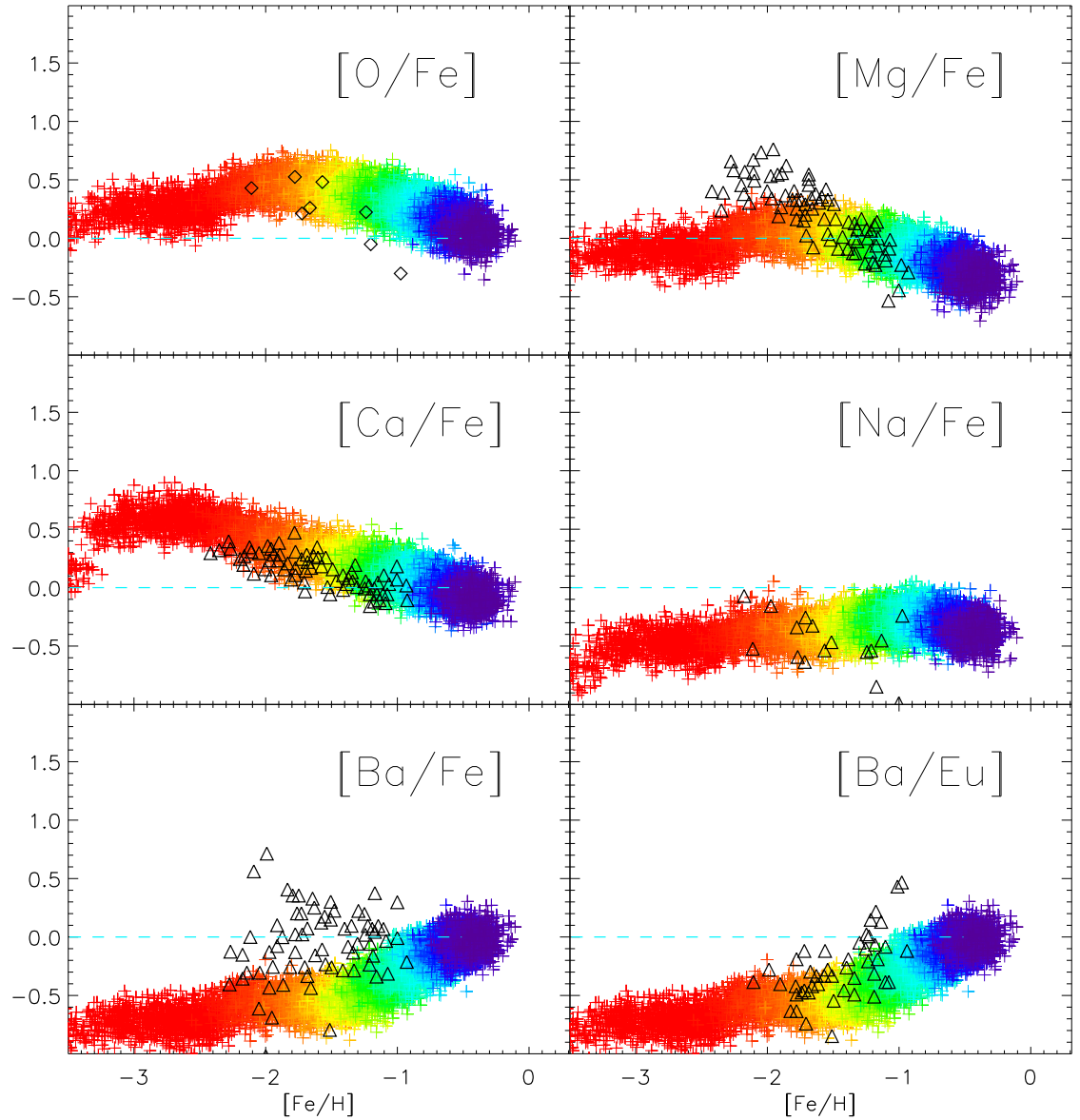


Figure 5.13: Predicted abundance ratios for the chemical evolution model of Sculptor. Colour-coding is according to star formation rate (recall Fig 5.10), with red (purple) corresponding to higher (lower) rates. Black symbols correspond to observations: triangles, from Tolstoy et al. (2009), and diamonds from Geisler et al. (2005).

### 5.5.3 Metallicity Distribution Function

Lastly, we examine the predicted MDF from our chemical evolution of Sculptor (Fig 5.14). As was the case for Carina, the raw MDF has been convolved with a  $\sigma=0.28$  dex Gaussian, to mimic the observational uncertainties. In orange, we show the observed MDF from de Boer et al. (2012a), which peaks at  $[\text{Fe}/\text{H}]\sim-2$ , while the predicted MDF peaks at the much more metal-rich value of  $[\text{Fe}/\text{H}]\sim-0.6$ .<sup>2</sup>

To decrease the metallicity of the system, without making changes to the yields or decoupling the inflows and outflows from the star formation history, we can restrict the re-accretion of gas. For gas to re-accrete within our formalism, the gas originally lost from the system first has to cool, the time for which depends upon the metallicity of the gas (e.g. Kawata & Gibson 2003). Figure 5.15 shows the surface density of gas that is re-accreted, compared to the surface density of the gas that is lost. Recalling Fig 5.12, the majority of the stellar wind ejecta is re-accreted; this re-accreted material is metal-enhanced and invariably drives the metallicity higher than observations suggest.

If we eliminate all re-accretion from the modelling, the system (not surprisingly) does not reach the same high values seen above (i.e., a peak near  $[\text{Fe}/\text{H}]\sim-0.6$ ). Fig 5.16 shows the effect on the MDF, in the absence of re-accretion. The peak is lowered by  $\sim 0.6$  dex, to  $[\text{Fe}/\text{H}]\sim-1.2$ , closer to that observed by de Boer et al. (2012a), but still a factor of  $\sim 5\times$  too high.

Recall from above that an apparent metallicity gradient exists in Sculptor; the empirical MDF used here is a composite, constructed from the summation of the five MDFs associated with the inner five annuli around Sculptor (de Boer et al.

---

<sup>2</sup>The dearth of stars with  $[\text{Fe}/\text{H}]<-1.5$  in the MDF *today* is not inconsistent with the apparent surplus of stars *forming* in this metallicity range (red symbols in Fig 5.13). The lifetimes of the G- and K- dwarfs at low metallicities are  $<10$  Gyrs (Schaller et al. 1992) and, as such, while plotted in Fig 5.13, are no longer ‘alive’ today to be included in the MDF (which have been chosen to only include  $0.85-1.25 M_{\odot}$  stars, to better reflect the observational biases).

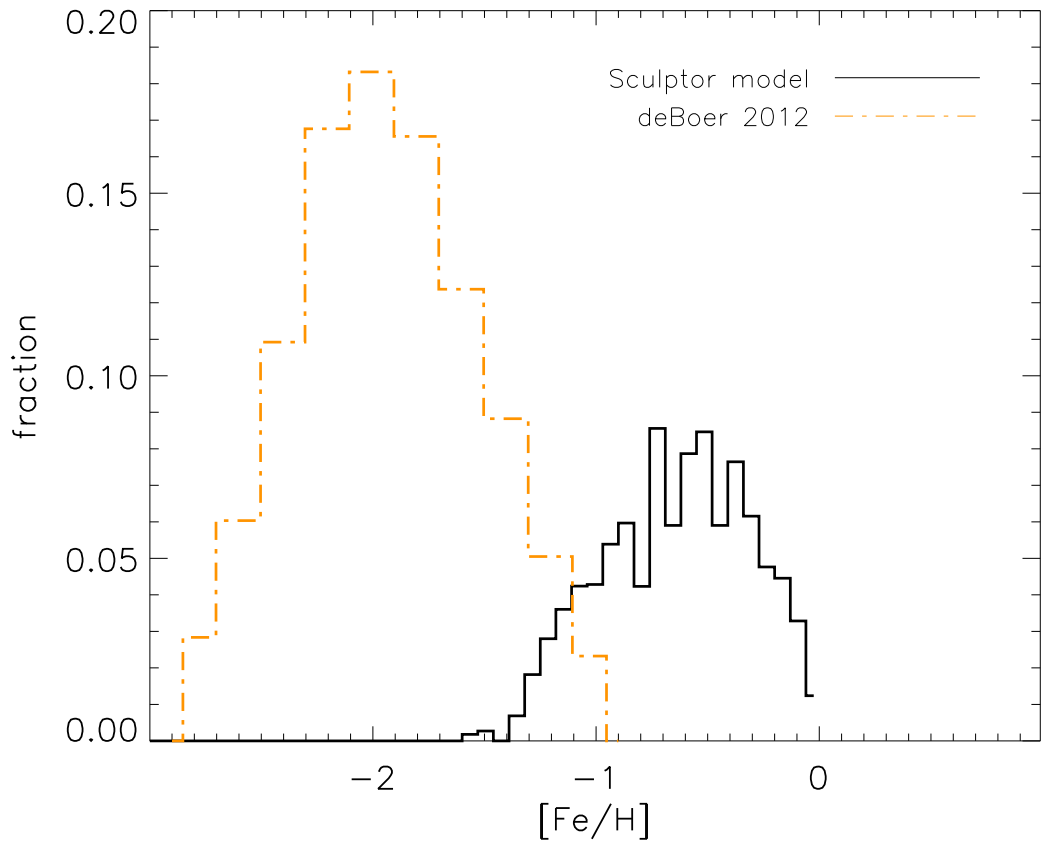


Figure 5.14: The predicted metallicity distribution function (MDF) for the chemical evolution model of Sculptor (black line). The MDF has been convolved with a  $\sigma=0.28$  dex Gaussian, to mimic the observational uncertainties. In orange, we show the observed MDF from de Boer et al. (2012a).

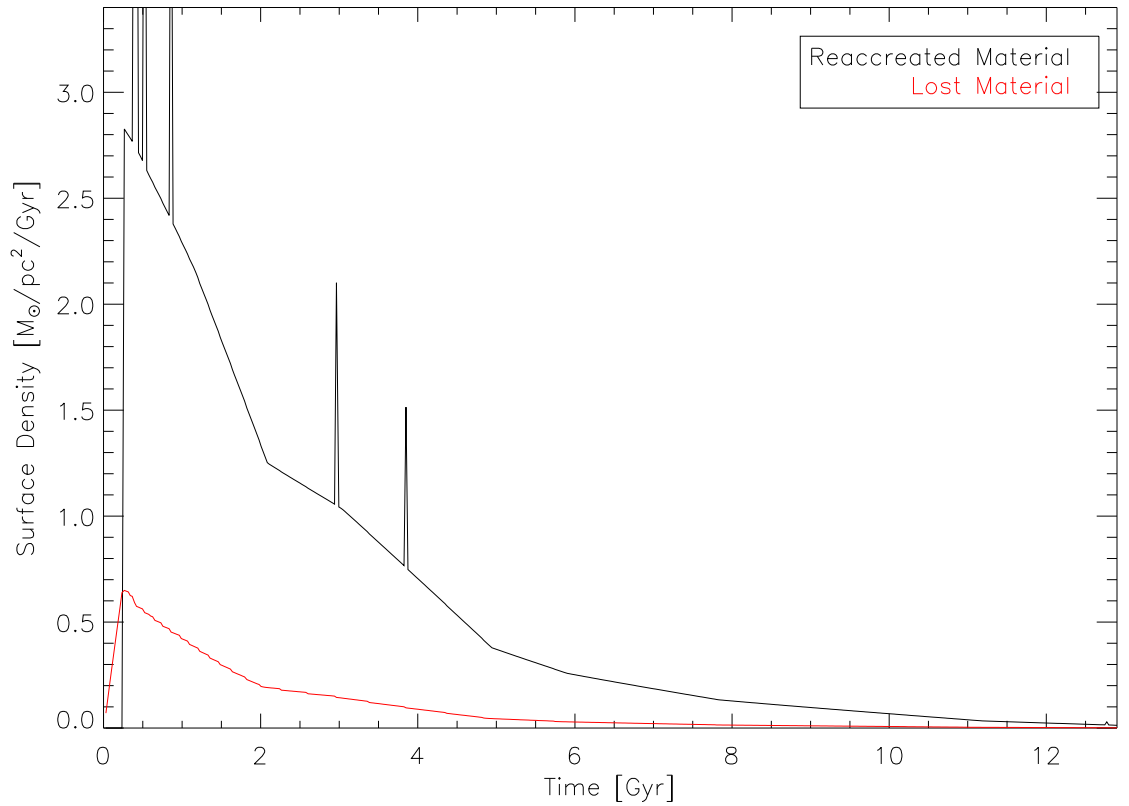


Figure 5.15: The surface density of gas that is re-accreted onto the Sculptor dSph (black line), in the context of our chemical evolution model, in addition to that of the material lost from the galaxy (red line). The peaks in the re-accretion curve correspond to the cooling time required before material is allowed to re-accrete.

2012a). The innermost annuli of Sculptor show a peak nearer to  $[\text{Fe}/\text{H}] \sim -1.4$ , not dissimilar to that which we find for our *one-zone* chemical evolution model of the dwarf. Because of the spatial structure in the metallicity distribution in Sculptor, it is likely the case that our one-zone assumption is a poor one here; instead, if we were to compare only with the innermost annuli of Sculptor, the apparent mismatch between model and observation would be somewhat ameliorated.

## CHAPTER 5

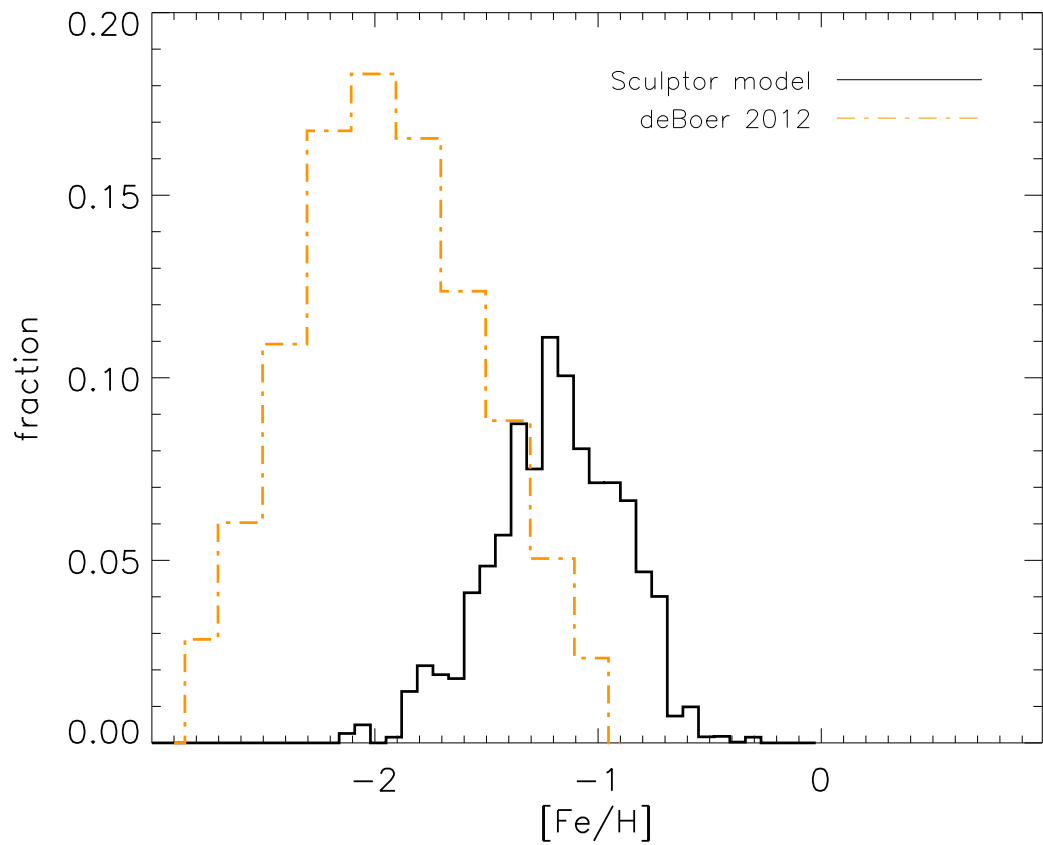


Figure 5.16: Similar to Fig 5.14, but now in the absence of re-accreted ejected material. The black curve corresponds to the predicted MDF of the Sculptor dSph model, and the orange dot-dashed line is that of the empirical MDF from de Boer et al. (2012a).

### 5.5.4 Discussion

The chemical evolution model of Sculptor presented here is an update to that presented by Fenner et al. (2006). The model here includes new AGB yields from Karakas (2010) and an improved star formation history from de Boer et al. (2012a). We find in general a good match to the observed properties of Sculptor, however as in our models of Carina, we find ourselves unable to match the neutron capture elements. This again suggests an update to the neutron capture yields is needed.

The main downfall of the Sculptor dSph model is the mismatch between the MDFs, in the sense of our predicted MDF being too metal-rich. We show two models - with and without re-accretion of ejected gas - not surprisingly, impeding re-accretion helps to reduce the metal overproduction. Alternate (plausible) routes to reducing the metallicity might include increasing the strength of the stellar winds and/or ram pressure stripping of the ISM.

As de Boer et al. (2012a) show, there is a metallicity gradient in Sculptor (in the sense of the inner regions being more metal-rich than the outskirts). By construction, our framework is ‘one-zone’, and therefore, detailed comparisons with a system such as Sculptor which possesses spatial variations in chemistry and kinematics must be approached with care. A multi-zone and/or full chemo-dynamical approach (e.g. Kawata et al. 2006) is merited.

## 5.6 Fornax

With a mass of  $\sim 70 \times 10^6 M_{\odot}$  and Galactocentric distance of  $\sim 140$  kpc from (Mateo 1998), Fornax is the final dSph (and most massive and distant) we examine here. As with Carina and Sculptor, Fornax does not have any significant HI component.

Fornax differs from Carina and Sculptor in that its star formation extends to more recent times (see Fig 5.17). Indeed, Fornax appears to have formed stars

## CHAPTER 5

up until the last  $\sim$ Gyr (de Boer et al. 2012b), unusual for typical dSphs. Fornax also differs from many dSphs by having an associated globular cluster population. Letarte et al. (2006) shows these globular clusters have similar abundance patterns to those in the Milky Way, suggesting similar formation scenarios. To explain the dynamics of these globular clusters, it has been suggested that Fornax formed from the merger of two smaller dSphs (e.g. Coleman et al. 2004; Yozin & Bekki 2012).

Recently, Tafelmeyer et al. (2010) identified extremely metal poor stars (EMPs) in Fornax (i.e., stars with  $[\text{Fe}/\text{H}] < -3$ ), joining Sculptor and Sextans as other Local Group dSphs possessing a populations of EMPs. This suggests that the extreme metal-poor tails of the MDFs of dSphs and the Milky Way halo are not dissimilar, as explored specifically by Pilkington et al. (2012b).

Here, we use the inferred star formation history from de Boer et al. (2012b) as input to our chemical evolution model for Fornax. Following the procedure outlined in §5.5 and §5.4, we now present our predicted abundance ratio distributions, MDF, and inflow/outflow characteristics for Fornax.

### 5.6.1 Inflows and Outflows

First, we show the predicted temporal evolution of the surface density of gas inflows and outflows for the Fornax chemical evolution model. As with Figures 5.3 and 5.11, the evolution of the total gas surface density is shown in the inset panel (in black). The sub-components to this gas density are shown in the primary panel: infalling gas is shown in cyan, gas returned from dying stars is in red, gas locked up due to star formation is in yellow, that recreated back onto the galaxy is in purple, and that removed via SN-driven winds is in blue.

The overall evolution of the gas surface density is dominated by the infall of pristine gas, albeit the degree of dominance is not as extreme as for Carina. The effect of this is to reduce the final gas fraction from  $>90\%$  in Carina, to  $\sim 50\%$  in the

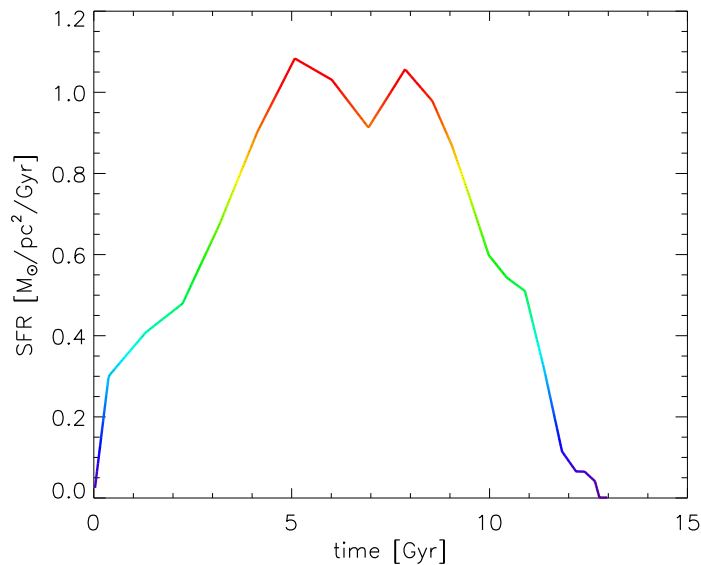


Figure 5.17: CMD-derived star formation history for the Fornax dSph (de Boer et al. 2012b).

case of Fornax, although this is still 1–2 orders of magnitude greater than observed. As for the other dSphs studied here, this suggests the need for additional gas removal processes - i.e., our galactic winds, in and of themselves, are not sufficient to remove residual gas at the level required to match present-day dSph gas fractions. Within the context of our framework, ram pressure stripping must be invoked, to result in gas fractions  $<1\%$ .

As with Carina and Sculptor, the amount of ISM carried along with the SN-driven wind is much greater than that directly associated with the SNeIa or SNeII (see Fig 5.19).

## 5.6.2 Abundance Patterns

As in Figures 5.5 and 5.13 we show the abundance patterns for six representative elements for our Fornax chemical evolution model in Fig 5.20. Colour-coding is as described in §5.4.2, corresponding to the magnitude of star formation (Fig 5.17),

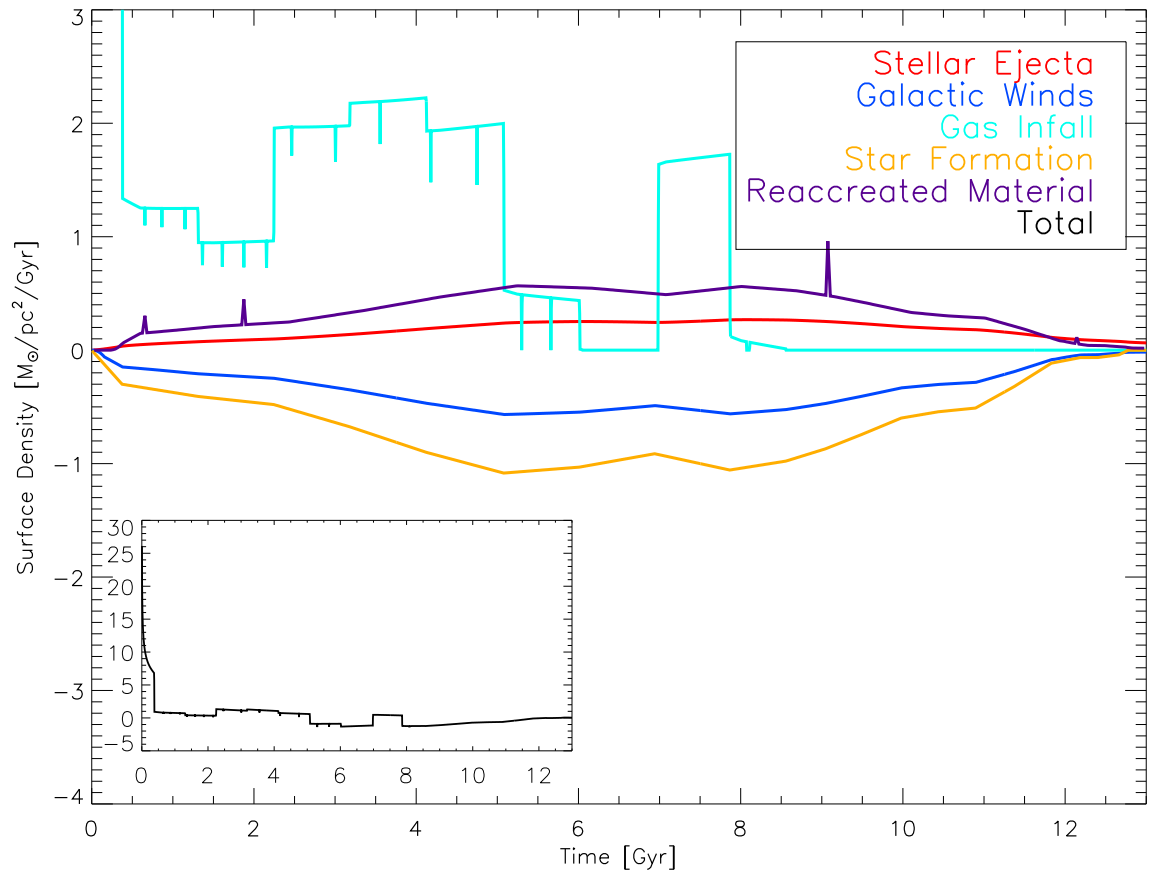


Figure 5.18: Predicted gas inflow and outflow rates for the chemical evolution model of Fornax. In red is shown the material returned to the system by dying stars; dark blue shows the gas removed by galactic winds; yellow shows the gas locked up due to star formation; cyan shows the infalling gas to the system. Purple shows the amount of gas being reacreated back onto the galaxy. The inset to the panel shows the sum of these four sub-components; like Carina, Fornax is dominated by the infall of gas, especially during the initial phases.

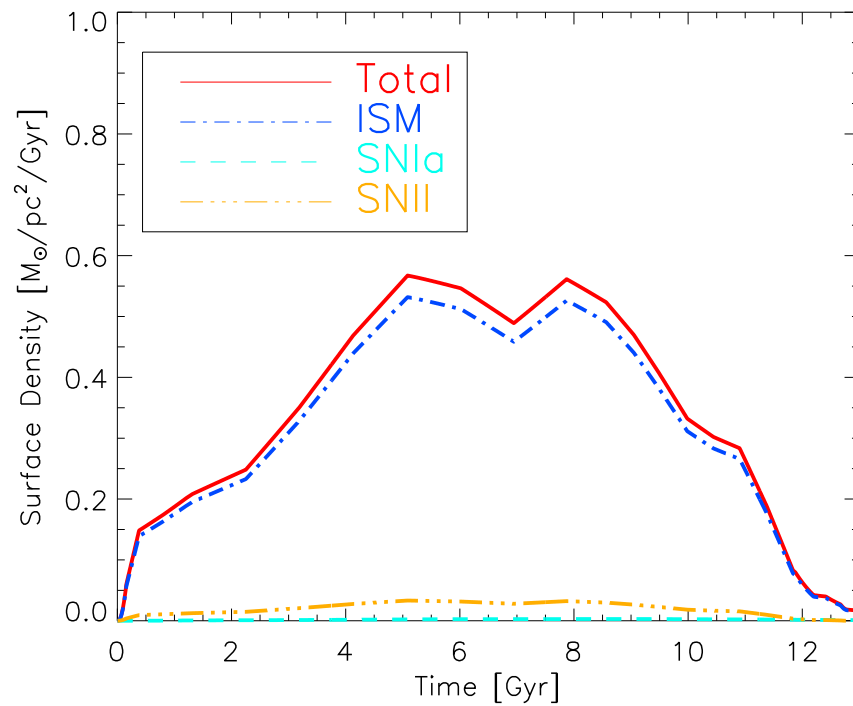


Figure 5.19: The contributions to the SN-driven winds for the chemical evolution model of Fornax. The red line shows the total of the three contributions (this is the same as the dark blue line in Fig 5.18); the cyan dashed line shows the contribution from SNeIa; the yellow triple-dotted-dashed line shows the contribution from SNeII; the dark blue dotted-dashed line shows the amount of the ISM expelled with the winds.

## CHAPTER 5

with red (purple) being associated with time of high (low) star formation. The observational data from Tolstoy et al. (2009) are represented by black triangles in each panel.

Our Fornax models appear to agree well with the empirical data for many of the  $\alpha$ -elements, including [Mg/Fe]. Our model [Ca/Fe] is slightly higher than the data, as we saw for the case of Sculptor (Fig 5.13); the predicted [Na/Fe] distribution also sits somewhat high, relative to the data, although the models are fairly consistent between the three dSphs (the difference here being that the empirical [Na/Fe] distribution in Fornax appears lower than in either Carina or Sculptor).

Again, as for Carina and Sculptor, the predicted distribution of neutron capture elements does not match well the empirical data (although, as before, the [Ba/Eu] distribution does appear consistent, including its trend with metallicity, but the absolute production of barium and europium is underproduced in the same direction and conspires to give an excellent fit in [Ba/Eu]).

### 5.6.3 Metallicity Distribution Function

Finally, we show the predicted metallicity distribution function for the Fornax chemical evolution model. As we found with Sculptor, allowing re-accretion results in an overly metal-rich population. Figure 5.21 shows the MDF for our model, in black, in the absence of re-accretion. The empirical MDF from de Boer et al. (2012b) is shown in orange; as before the model MDF has been convolved with a  $\sigma=0.28$  dex Gaussian, to mimic the observational uncertainties. Both the model and empirical MDF peak near  $[\text{Fe}/\text{H}]\sim-1.1$ ; including re-accretion within the model would shift the predicted MDF peak to  $[\text{Fe}/\text{H}]\sim-0.4$ .

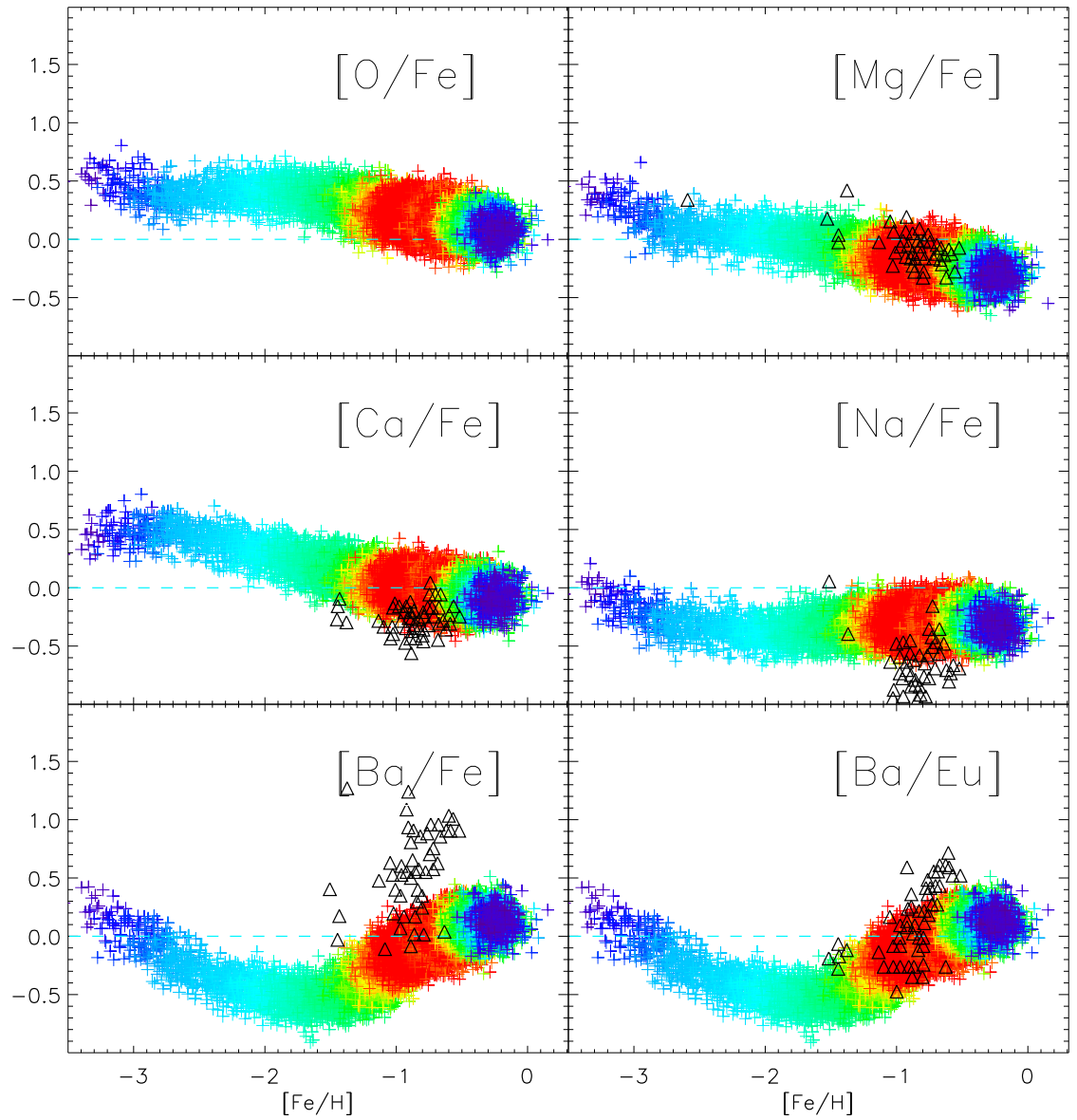


Figure 5.20: Predicted abundance patterns for the chemical evolution model of Fornax. Colour-coding is by star formation, with red (purple) corresponding to high (low) rates. The black triangles correspond to the observational data of Tolstoy et al. (2009).

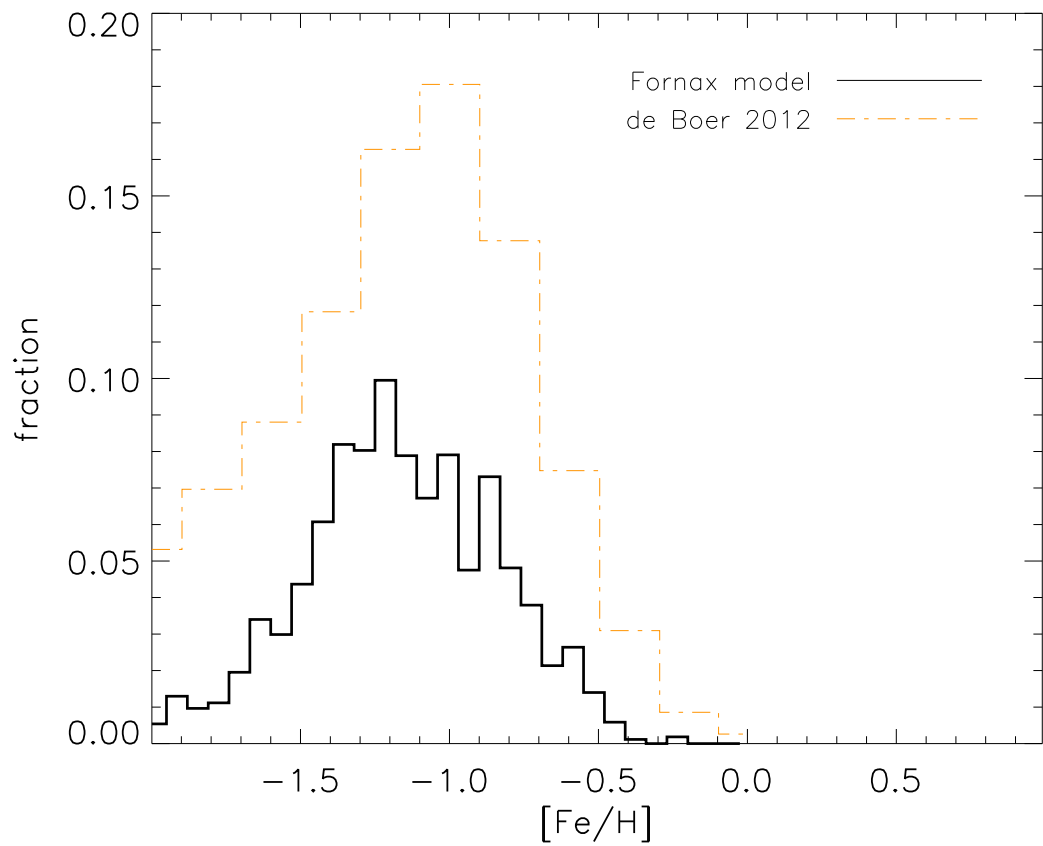


Figure 5.21: Predicted (black) and empirical (orange: from de Boer et al. 2012b) metallicity distribution functions for the Fornax dSph. The model has been convolved with a  $\sigma=0.28$  dex Gaussian, to mimic the observational uncertainties.

### 5.6.4 Discussion

Broadly speaking, our chemical evolution of Fornax is a good match to the empirical constraints. The abundance ratios are fairly insensitive to the inclusion of re-accretion, although the mean metallicity can vary by a factor of  $\sim 5$  with its inclusion (in the sense of being too metal-rich when re-accretion is allowed).

As was the case for Sculptor, de Boer et al. (2012b) found an age gradient in Fornax, in the sense of younger, more metal-rich, stars being preferentially situated in the centre of the galaxy. A multi-zone and/or full chemo-dynamical approach should be a natural next step in the modelling of Fornax.

## 5.7 Conclusions

This chapter has explored the chemical evolution of three Local Group dSphs: Carina, Sculptor, and Fornax. The chemical evolution models were constrained by empirically-derived star formation histories, with the complex interplay of infall and SN-driven outflows being further constrained by the requirement that the systems always adhere to a Kennicutt star formation law. The main conclusions can be summarised as:

1. We show that an infall rate determined by inverting the Kennicutt star formation law ( $\psi \propto \sigma^{1.4}$ ), with a CMD-inferred star formation history, can successfully match many of the chemical properties of the dSphs, without the need for additional ‘fine-tuning’ of the basic chemical evolution properties.
2. Most elemental abundance patterns are consistent with those observed, save (primarily) for the neutron capture elements. The need for an updated, and homogeneous, implementation of neutron capture nucleosynthesis is apparent.

## CHAPTER 5

3. Without invoking some form of parameterised ram pressure stripping, we inevitably over-predict the final gas fraction by two orders of magnitude. Updating `GEtool` to include a detailed parameterised stripping of gas, taking into account the orbital characteristics of each dSph about the Milky Way, would be useful.
4. The models of Sculptor and Fornax produce results that better match the observations without invoking the re-accreration of lost gas. Carina, however, is better modelled with the inclusion of such re-accretion.
5. The ratio of inflows to outflows within these chemical evolution models is consistent with the findings of Brook et al (in prep) where using SPH simulations of LMC size galaxies they find a inflow to outflow ratio of between 1:1 to 2:1.
6. Extending the one-zone models presented here to either multi-zone models or full chemo-dynamical simulations, would allow one to make use of the constraints provided by empirical determinations each system's age and metallicity gradient (if one exists).
7. Extending our work to the cover the entire sample of Local Group dwarfs with CMD-inferred star formation histories, including samples such as those of LCID (<http://http://www.iac.es/proyecto/LCID/>), is one of the next steps in this work.

# Chapter 6

## Conclusions

Galaxy simulations are key to our understanding of galaxy formation. Simulations can be used to make predictions on specific aspects of galaxy evolution such as kinematics or chemistry. Secondly galaxy simulations can be used to test the underlying physics of observations, so we can truly understand what is happening.

The focus of this thesis has been on the analysis of the gaseous and chemical properties of simulated late-type galaxies. The approach taken has been done in an attempt to constrain the underlying physics shaping galaxy formation and evolution, including the feedback and diffusion of energy and chemical elements throughout the interstellar medium, as well as the respective roles of gas infall and supernovae-driven outflows. Both dwarfs and massive discs have been considered, in order to target specific problems, some of which are relevant to the former (metallicity distribution functions and the turbulent structure of the interstellar medium) and some to the latter (spatially-resolved abundance gradients and metallicity distribution functions).

In addition to some of the constraints on galaxy simulations this thesis has provided, it also has an impact on observations. The work in chapter 4 shows an attempt to constrain feedback within simulations but it also highlights the importance of observations to our work. Although not the focus of chapter 3 our work

on MDF's in particular those in the bulge help quantify recent observations of the Milky Way's bulge MDF (e.g. Bensby et al. 2011; Hill et al. 2011). Finally chapter 5 begins to quantify the infows and outflows needed in local group dwarf spheroidal galaxies to obtain the chemical patterns we have seen in observations.

Here, the primary results are summarised, and several potential avenues for future research itemised.

## 6.1 The Chemistry and Cold Gas Content of Bulgeless Dwarf Galaxies

This chapter is an amalgam of work presented in Pilkington et al. (2011) and Pilkington et al. (2012c), the conclusions of which can be summarised as:

- We analyse the HI and chemical properties of five bulgeless dwarf galaxies drawn primarily from the work of Governato et al. (2010), supplemented with new realisations undertaken with the same feedback prescription. These simulations were the first, within a cosmological framework, to result in the successful reproduction of a dwarf galaxy with no associated stellar bulge.
- We first showed that each of the simulated dwarfs sit on the HI-luminosity, mass-metallicity, and luminosity-metallicity scaling relations (Figures 2.1, 2.20, and 2.21).
- Cold gas surface densities within the dwarfs are too high (apart from DG1LT, a realisation for which a conservative feedback scheme was adopted, consistent with others in the literature, but for which the resulting morphology does not resemble a late-type disc) when compared to galaxies in nature (e.g. Bigiel et al. 2008, Figure 2.4). We speculate that the inclusion of molecular  $H_2$  cooling may ameliorate (if not solve) this problem.

## CHAPTER 6

- The velocity dispersions of the dwarfs (again, apart from DG1LT), taking into account a thermal broadening term, are consistent with those observed in nature (Tamburro et al. 2009), although the radial trends do not resemble those observed, showing no anisotropies in the distribution (see Fig 2.9).
- Each of the dwarf galaxy simulations - from this generation of realisations - show an overproduction of extremely metal-poor stars metal poor stars (Fig 2.23), relative to observations of the metallicity distribution functions of nearby dwarfs. This overproduction can be (in large part) traced to the adopted metal diffusion being overly inefficient, a point to which we returned more quantitatively in §3.5.
- Broadly speaking, the predicted abundance ratio patterns and metallicity distribution functions (MDFs) agree with those seen in Local Group dwarfs (e.g. Tolstoy et al. 2009; Kirby et al. 2011a, Figures 2.24 and 2.22); a more quantitative comparison of simulated and empirical MDFs was seen in §3.5.

## 6.2 The Distribution of Metals in Cosmological Simulations of Dwarf Disk Galaxies

This chapter is based upon work first presented in Pilkington et al. (2012b), the conclusions of which can be summarised as:

- We demonstrated graphically the power of the extreme metal-poor tail of the metallicity distribution function (MDF) to constrain the efficiency with which metals diffuse within the interstellar medium (Fig 3.5).
- The simulated age-metallicity relations are very tight and highly correlated, unlike those observed in nature (e.g. Holmberg et al. 2009, see Fig 3.4); we speculate that while the efficient feedback employed is required to produce a

realistic late-type disc, a consequence of this strong feedback (coupled with efficient metal diffusion) is an ISM that appears overly homogeneous at any given time.

- Neglecting metal diffusion (as is typically done in particle-based hydrodynamical simulations) results in the classical metal-poor star overproduction problem, which is reflected in predicted MDF skewness and kurtosis values which are not consistent with those observed in nature.

### 6.3 Metallicity Gradients in Disk Galaxies

This chapter is based on work first presented by Pilkington et al. (2012a), Pilkington & Gibson (2012b), and Pilkington et al. (2012d). The main conclusions can be summarised as:

- All of the galaxy simulations analysed exhibit inside-out formation of the disk with varying degrees of centrally concentrated star formation. The radial star formation rate dependence directly influences the resulting metallicity gradient (see Figures 4.3 and 4.1).
- We observe vertical metallicity gradients in the simulated galaxies that are of comparable values to those in nature (e.g. Marsakov & Borkova 2005). The resolution of the simulations is not sufficient though to discriminate between thin and thick disks (see Figure 4.5).
- Each of the simulated galaxies possess present-day metallicity gradients similar to those observed in nature; the temporal evolution of this gradient though varies *dramatically* from galaxy-to-galaxy.
- The temporal evolution of the metallicity gradients is ultimately controlled by the treatment of sub-grid physics with the various codes employed (rather

than any fundamental numerical difference between, say, particle- or grid-based hydrodynamics approaches). Where energy feedback is distributed more efficiently to the surrounding ISM, the abundance gradients are both flatter and evolve little with time. This is perhaps one of the most important results of this work - specifically, the demonstration that uncertainties in feedback can be constrained via direct observation of spatially-resolved gas-phase metallicity gradients at high-redshift; this important conclusion (the first recognition of such, to our knowledge) receives additional support in §6.5.

- We found little evidence in our simulations for azimuthal abundance or age gradients.

## 6.4 Chemical Evolution Models of Local Group Dwarf Spheroidal Galaxies

This chapter is a significant extension to the work first presented by Pilkington & Gibson (2012a), the conclusions for which can be summarised as:

- Employing a model framework in which the star formation history of several Local Group dwarf spheroidals is used as (fixed) input, chemical evolution models of Carina, Sculptor, and Fornax are derived. A unique aspect of our modelling effort is that while varying the degree of gas infall and supernovae-driven wind outflows, the surface density of gas in the system is constrained to adhere to a Kennicutt star formation law (something *not* enforced in other models in the literature).
- The distribution of  $\alpha$ -elements and sodium for the three models is not dissimilar to that observed in the three Local Group dwarfs under study.

- Chemically speaking, the primary problem our models encounter relate to the distribution of neutron capture elements. While the predicted ratio of s- to r-process elements, and its trend with metallicity, resembles that observed, the absolute values for both do not. A homogeneous grid of neutron capture yields, spanning a range of masses and metallicities, is needed.
- The final predicted gas fractions for our dSph models are all 1-2 orders-of-magnitude in excess of those observed, suggesting the need for a treatment of ram pressure stripping.

## 6.5 Future Work

The work conducted as part of this thesis leads naturally to a number of subsequent studies, several of which are in their initial phases. Here, we outline the current state of these follow-up projects, each of which have arisen from the work described here.

- **The Cold Gas Content of Massive Spirals:** A natural extension to our work on the turbulent nature of the cold ISM of late-type dwarfs (Chapter 2) is in the application of comparable techniques to the massive discs in our MUGS (Chapter 4) and MaGICC (Brook et al. 2011, 2012b,c). Recent observation work by Dutta et al. (2013) presents vertical scaleheight and ISM power spectra for 18 massive discs in the THINGS sample, finding fundamental differences in the distribution of structural power between the ISM in dwarf vs massive discs. Further, Ianjamasimanana et al. (2012) has extended THINGS, providing high-resolution velocity dispersion profiles for the full sample of massive discs in THINGS. These studies provide excellent and unique data against which to compare our simulations.

## CHAPTER 6

- **Halos of Spirals:** Empirical evidence suggests that the halo of the Milky Way can be sub-divided (chemically and kinematically) into two distinct sub-components (e.g. Beers et al. 2012). We will examine the stellar halos of the MUGS and MaGICC simulations, to search for any evidence of such chemo-kinetic sub-structure; should we find it, we will identify its origin (e.g., accreted vs in situ).
- **Radial Metallicity Gradients as a Function of Scaleheight:** Following on from the observational work of Carrell et al. (2012), and as a natural extension to the work of Pilkington et al. (2012d), we will examine the radial metallicity gradients of the MaGICC (Brook et al. 2011, 2012b,c) disc galaxies and how they change as a function of distance from the mid-plane. This will allow us to search for signatures of the thin and thick disc, and determine the rate at which the gradient flattens as a function of scaleheight (which should be driven by the complex interplay between star formation, assembly/accretion, and radial migration).
- **Radial and Azimuthal Metallicity Dispersions:** Sanders et al. (2012) has shown recently that for M31, the radial metallicity gradient shows scatter at a given radius significantly in excess of observational uncertainties ( $\sim 0.1-0.3$  dex). As an extension to our earlier work (Pilkington et al. 2012d), we will quantify the degree of intrinsic scatter at a given radius and, more importantly, determine its source (e.g., azimuthal variations, vertical gradients, radial gas flows, etc.). This links to our cursory ‘azimuthal variation’ work in §4.8.
- **Chemical Evolution of the Galactic Bulge:** We have undertaken a cursory examination of the bulge MDFs associated with the MUGS discs (Calura et al. 2012) and dwarf discs (Pilkington et al. 2012b), but an extraordinary

## CHAPTER 6

wealth of information regarding chemical abundance patterns and kinematics of bulge stars in the Milky Way has become available only recently (Bensby et al. 2013, 2011; Hill et al. 2011). Revisiting the chemistry of the bulges of both the MUGS and MaGICC simulations would be most timely.

- **The Galactic Terrestrial Zone:** We are currently expanding upon our earlier Galactic Habitable Zone work (Lineweaver et al. 2004), by defining what we call the Galactic Terrestrial Zone (GTZ). The mineralogy of terrestrial planets can be linked to the chemistry of the proto-stellar cloud out of which they and their host star formed (Bond et al. 2010). In particular, the ratios of C/O and Mg/Si prove to be powerful delineators of (for example) carbide-rich planets, as opposed to pyroxene- or olivine-rich planets. We will make use of our chemical evolution models of both the Milky Way and Local Group dwarfs to characterise the temporal evolution of the GTZ.
- **Chemical Evolution of Local Group Dwarfs:** Following the work described in Chapter 5, we will extend our analysis to the complete set of Local Group dwarfs. The primary work which is needed though relates to the underlying stellar yields; we will update shortly the yields currently within `GEtool` with unpublished `NuGRID` yields that have been made available to us (Pignatari et al., in prep). This is the most pressing ‘technical’ work required within our chemical and chemo-dynamical codes.

# Bibliography

- Aaronson, M. 1983, *Astrophys. J. Letters*, 266, L11
- Abadi, M. G., Navarro, J. F., Steinmetz, M., & Eke, V. R. 2003a, *Astrophys. J.*, 591, 499
- Abadi, M. G., Navarro, J. F., Steinmetz, M., & Eke, V. R. 2003b, *Astrophys. J.*, 597, 21
- Afflerbach, A., Churchwell, E., & Werner, M. W. 1997, *Astrophys. J.*, 478, 190
- Alibés, A., Labay, J., & Canal, R. 2001, *Astron. Astrophys.*, 370, 1103
- Amorisco, N. C. & Evans, N. W. 2012, *Astrophys. J. Letters*, 756, L2
- Aoki, W., Arimoto, N., Sadakane, K., et al. 2009, *Astron. Astrophys.*, 502, 569
- Arcones, A. & Thielemann, F.-K. 2013, *Journal of Physics G Nuclear Physics*, 40, 013201
- Asplund, M., Grevesse, N., Sauval, A. J., & Scott, P. 2009, *Ann. Rev. Astron. Astrophys.*, 47, 481
- Babusiaux, C., Gómez, A., Hill, V., et al. 2010, *Astron. Astrophys.*, 519, A77+
- Bailin, J., Kawata, D., Gibson, B. K., et al. 2005, *Astrophys. J. Letters*, 627, L17
- Baldry, I. K. & Glazebrook, K. 2003, *Astrophys. J.*, 593, 258

- Bartašiūtė, S., Aslan, Z., Boyle, R. P., et al. 2003, *Baltic Astronomy*, 12, 539
- Battaglia, G., Helmi, A., Tolstoy, E., et al. 2008, *Astrophys. J. Letters*, 681, L13
- Beers, T. C., Carollo, D., Ivezić, Ž., et al. 2012, *Astrophys. J.*, 746, 34
- Belokurov, V., Walker, M. G., Evans, N. W., et al. 2010, *Astrophys. J. Letters*, 712, L103
- Bensby, T., Adén, D., Meléndez, J., et al. 2011, *Astron. Astrophys.*, 533, A134
- Bensby, T., Yee, J. C., Feltzing, S., et al. 2013, *Astron. Astrophys.*, 549, A147
- Bigiel, F., Leroy, A., Walter, F., et al. 2010, *Astron. J.*, 140, 1194
- Bigiel, F., Leroy, A., Walter, F., et al. 2008, *Astron. J.*, 136, 2846
- Blanton, M. R., Geha, M., & West, A. A. 2008, *Astrophys. J.*, 682, 861
- Bond, J. C., O'Brien, D. P., & Lauretta, D. S. 2010, *Astrophys. J.*, 715, 1050
- Bono, G., Stetson, P. B., Walker, A. R., et al. 2010, *Pub. Astron. Soc. Pac.*, 122, 651
- Booth, C. M., Theuns, T., & Okamoto, T. 2007, *Mon. Not. Roy. Astron. Soc.*, 376, 1588
- Bouchard, A., Carignan, C., & Mashchenko, S. 2003, *Astron. J.*, 126, 1295
- Bovy, J., Rix, H.-W., & Hogg, D. W. 2012, *Astrophys. J.*, 751, 131
- Brewer, B. J., Dutton, A. A., Treu, T., et al. 2012, *Mon. Not. Roy. Astron. Soc.*, 422, 3574
- Brook, C. B., Governato, F., Roškar, R., et al. 2011, *Mon. Not. Roy. Astron. Soc.*, 415, 1051

- Brook, C. B., Kawata, D., Gibson, B. K., & Freeman, K. C. 2004, *Astrophys. J.*, 612, 894
- Brook, C. B., Stinson, G., Gibson, B. K., et al. 2012a, *Mon. Not. Roy. Astron. Soc.*, 419, 771
- Brook, C. B., Stinson, G., Gibson, B. K., Wadsley, J., & Quinn, T. 2012b, *Mon. Not. Roy. Astron. Soc.*, 424, 1275
- Brook, C. B., Stinson, G. S., Gibson, B. K., et al. 2012c, *Mon. Not. Roy. Astron. Soc.*, 426, 690
- Brooks, A. M., Governato, F., Booth, C. M., et al. 2007, *Astrophys. J. Letters*, 655, L17
- Brooks, A. M., Solomon, A. R., Governato, F., et al. 2011, *Astrophys. J.*, 728, 51
- Burbidge, E. M., Burbidge, G. R., Fowler, W. A., & Hoyle, F. 1957, *Reviews of Modern Physics*, 29, 547
- Cacciari, C. 2009, *Memorie della Societ Astronomia Italiana*, 80, 97
- Caimmi, R. 2008, *New Astron.*, 13, 314
- Calura, F., Gibson, B., & et al. 2012, *Mon. Not. Roy. Astron. Soc.*, submitted
- Calura, F., Lanfranchi, G. A., & Matteucci, F. 2008, *Astron. Astrophys.*, 484, 107
- Calzetti, D., Kennicutt, Jr., R. C., Bianchi, L., et al. 2005, *Astrophys. J.*, 633, 871
- Canterna, R. 1975, *Astrophys. J. Letters*, 200, L63+
- Carignan, C. 1999, *Pub. Astron. Soc. Australia*, 16, 18
- Carollo, D., Beers, T. C., Lee, Y. S., et al. 2007, *Nature*, 450, 1020

- Carrell, K., Chen, Y., & Zhao, G. 2012, *Astron. J.*, 144, 185
- Carrera, R., Gallart, C., Aparicio, A., et al. 2008, *Astron. J.*, 136, 1039
- Carretta, E. & Gratton, R. G. 1997, *Astron. Astrophys. Suppl.*, 121, 95
- Casagrande, L., Schönrich, R., Asplund, M., et al. 2011, *Astron. Astrophys.*, 530, A138+
- Ceverino, D. & Klypin, A. 2009, *Astrophys. J.*, 695, 292
- Chabrier, G. 2003, *Pub. Astron. Soc. Pac.*, 115, 763
- Chen, L., Hou, J. L., & Wang, J. J. 2003, *Astron. J.*, 125, 1397
- Chiappini, C., Matteucci, F., & Romano, D. 2001, *Astrophys. J.*, 554, 1044
- Cioni, M.-R. L., Clementini, G., & et al. 2011, *Astron. Astrophys.*, 527, A116
- Cohen, J. G. & Huang, W. 2009, *Astrophys. J.*, 701, 1053
- Cohen, J. G. & Huang, W. 2010, *Astrophys. J.*, 719, 931
- Coleman, M., da Costa, G. S., Martínez-Delgado, D., & Bland-Hawthorn, J. 2004, in *Astronomical Society of the Pacific Conference Series*, Vol. 327, *Satellites and Tidal Streams*, ed. F. Prada, D. Martinez Delgado, & T. J. Mahoney, 173
- Cooper, M. C., Tremonti, C. A., Newman, J. A., & Zabludoff, A. I. 2008, *Mon. Not. Roy. Astron. Soc.*, 390, 245
- Cresci, G., Mannucci, F., Maiolino, R., et al. 2010, *Nature*, 467, 811
- Crosthwaite, L. P., Turner, J. L., & Ho, P. T. P. 2000, *Astron. J.*, 119, 1720
- Crosthwaite, L. P., Turner, J. L., Hurt, R. L., et al. 2001, *Astron. J.*, 122, 797
- de Boer, T. J. L., Tolstoy, E., Hill, V., et al. 2012a, *Astron. Astrophys.*, 539, A103

- de Boer, T. J. L., Tolstoy, E., Hill, V., et al. 2012b, *Astron. Astrophys.*, 544, A73
- de Boer, T. J. L., Tolstoy, E., Saha, A., et al. 2011, *Astron. Astrophys.*, 528, A119
- de Rossi, M. E., Tissera, P. B., & Scannapieco, C. 2007, *Mon. Not. Roy. Astron. Soc.*, 374, 323
- Dib, S., Bell, E., & Burkert, A. 2006, *Astrophys. J.*, 638, 797
- Dobbs, C. L. & Pringle, J. E. 2010, *Mon. Not. Roy. Astron. Soc.*, 409, 396
- Doherty, C. L. & Lattanzio, J. C. 2006, *Memorie della Societ Astronomia Italiana*, 77, 828
- Dolphin, A. E., Saha, A., Skillman, E. D., et al. 2003, *Astron. J.*, 126, 187
- Dolphin, A. E., Weisz, D. R., Skillman, E. D., & eHoltzman, J. A. 2005, ArXiv Astrophysics e-prints
- Dopita, M. A. & Ryder, S. D. 1994, *Astrophys. J.*, 430, 163
- Dubois, Y. & Teyssier, R. 2008, *Astron. Astrophys.*, 477, 79
- Dutta, P., Begum, A., Bharadwaj, S., & Chengalur, J. N. 2013, *New Astron.*, 19, 89
- Ekström, S., Meynet, G., Chiappini, C., Hirschi, R., & Maeder, A. 2008, *Astron. Astrophys.*, 489, 685
- Erb, D. K., Shapley, A. E., Pettini, M., et al. 2006, *Astrophys. J.*, 644, 813
- Fenner, Y., Campbell, S., Karakas, A. I., Lattanzio, J. C., & Gibson, B. K. 2004, *Mon. Not. Roy. Astron. Soc.*, 353, 789
- Fenner, Y. & Gibson, B. K. 2003, *Pub. Astron. Soc. Australia*, 20, 189

- Fenner, Y., Gibson, B. K., Gallino, R., & Lugaro, M. 2006, *Astrophys. J.*, 646, 184
- Ferland, G. J., Korista, K. T., Verner, D. A., et al. 1998, *Pub. Astron. Soc. Pac.*, 110, 761
- Few, C. G., Courty, S., Gibson, B. K., et al. 2012a, *Mon. Not. Roy. Astron. Soc.*, 424, L11
- Few, C. G., Gibson, B. K., Courty, S., et al. 2012b, *Astron. Astrophys.*, 547, A63
- Franx, M. & Illingworth, G. 1990, *Astrophys. J. Letters*, 359, L41
- Frebel, A., Kirby, E. N., & Simon, J. D. 2010, *Nature*, 464, 72
- Freeman, K. 2012, Structure and Evolution of the Milky Way, ed. A. Miglio, J. Montalbán, & A. Noels, 137
- Fu, J., Hou, J. L., Yin, J., & Chang, R. X. 2009, *Astrophys. J.*, 696, 668
- Geisler, D., Smith, V. V., Wallerstein, G., Gonzalez, G., & Charbonnel, C. 2005, *Astron. J.*, 129, 1428
- Gibson, B. K. 1994, *JRASC*, 88, 383
- Gibson, B. K., Giroux, M. L., Penton, S. V., et al. 2001, *Astron. J.*, 122, 3280
- Gibson, B. K., Loewenstein, M., & Mushotzky, R. F. 1997, *Mon. Not. Roy. Astron. Soc.*, 290, 623
- Gibson, B. K., Pilkington, K., Brook, C. B., Stinson, G. S., & Bailin, J. 2013, ArXiv e-prints
- Gilmore, G. & Reid, N. 1983, *Mon. Not. Roy. Astron. Soc.*, 202, 1025
- Gilmore, G., Wilkinson, M. I., Wyse, R. F. G., et al. 2007, *Astrophys. J.*, 663, 948

- Gilmore, G. & Wyse, R. F. G. 1991, *Astrophys. J. Letters*, 367, L55
- Gilmore, G., Wyse, R. F. G., & Norris, J. E. 2002, *Astrophys. J. Letters*, 574, L39
- Gingold, R. A. & Monaghan, J. J. 1977, *Mon. Not. Roy. Astron. Soc.*, 181, 375
- Governato, F., Brook, C., Mayer, L., et al. 2010, *Nature*, 463, 203
- Governato, F., Mayer, L., Wadsley, J., et al. 2004, *Astrophys. J.*, 607, 688
- Governato, F., Willman, B., Mayer, L., et al. 2007, *Mon. Not. Roy. Astron. Soc.*, 374, 1479
- Grand, R. J. J., Kawata, D., & Cropper, M. 2012, *Mon. Not. Roy. Astron. Soc.*, 421, 1529
- Grebel, E. K. 1998, *Highlights of Astronomy*, 11, 125
- Greggio, L. & Renzini, A. 1983, *Astron. Astrophys.*, 118, 217
- Grieco, V., Matteucci, F., Pipino, A., & Cescutti, G. 2012, ArXiv e-prints
- Guseva, N. G., Papaderos, P., Meyer, H. T., Izotov, Y. I., & Fricke, K. J. 2009, *Astron. Astrophys.*, 505, 63
- Haardt, F. & Madau, P. 1996, *Astrophys. J.*, 461, 20
- Hartwick, F. D. A. 1976, *Astrophys. J.*, 209, 418
- Haywood, M. 2001, *Mon. Not. Roy. Astron. Soc.*, 325, 1365
- Heckman, T. M., Lehnert, M. D., Strickland, D. K., & Armus, L. 2000, *Astrophys. J. Supple.*, 129, 493
- Helmi, A., Irwin, M. J., Tolstoy, E., et al. 2006, *Astrophys. J. Letters*, 651, L121

- Hensler, G., Köppen, J., Pflamm, J., & Rieschick, A. 2004, in IAU Symposium, Vol. 217, Recycling Intergalactic and Interstellar Matter, ed. P.-A. Duc, J. Braine, & E. Brinks, 178
- Hill, V., Lecureur, A., Gómez, A., et al. 2011, *Astron. Astrophys.*, 534, A80
- Hirschi, R., Meynet, G., & Maeder, A. 2005, *Astron. Astrophys.*, 433, 1013
- Holmberg, E. 1941, *Astrophys. J.*, 94, 385
- Holmberg, J., Nordström, B., & Andersen, J. 2007, *Astron. Astrophys.*, 475, 519
- Holmberg, J., Nordström, B., & Andersen, J. 2009, *Astron. Astrophys.*, 501, 941
- Holtzman, J. A., Gallagher, III, J. S., Cole, A. A., et al. 1999, *Astron. J.*, 118, 2262
- Hopkins, P. F., Quataert, E., & Murray, N. 2011, *Mon. Not. Roy. Astron. Soc.*, 417, 950
- House, E. L., Brook, C. B., Gibson, B. K., et al. 2011, *Mon. Not. Roy. Astron. Soc.*, 415, 2652
- Ianjamasimanana, R., de Blok, W. J. G., Walter, F., & Heald, G. H. 2012, *Astron. J.*, 144, 96
- Iwamoto, K., Brachwitz, F., Nomoto, K., et al. 1999, *Astrophys. J. Supple.*, 125, 439
- Jimenez, R., Flynn, C., MacDonald, J., & Gibson, B. K. 2003, *Science*, 299, 1552
- Jones, T., Ellis, R., Jullo, E., & Richard, J. 2010, *Astrophys. J. Letters*, 725, L176
- Jonsson, P., Groves, B. A., & Cox, T. J. 2010, *Mon. Not. Roy. Astron. Soc.*, 403, 17

- Kannan, R., Macciò, A. V., Pasquali, A., Moster, B. P., & Walter, F. 2012, *Astrophys. J.*, 746, 10
- Karakas, A. & Lattanzio, J. C. 2007, *Pub. Astron. Soc. Australia*, 24, 103
- Karakas, A. I. 2010, *Mon. Not. Roy. Astron. Soc.*, 403, 1413
- Karakas, A. I., García-Hernández, D. A., & Lugaro, M. 2012, *Astrophys. J.*, 751, 8
- Kawata, D., Arimoto, N., Cen, R., & Gibson, B. K. 2006, *Astrophys. J.*, 641, 785
- Kawata, D. & Gibson, B. K. 2003, *Mon. Not. Roy. Astron. Soc.*, 340, 908
- Kawata, D., Gibson, B. K., & Windhorst, R. A. 2004, *Mon. Not. Roy. Astron. Soc.*, 354, 387
- Kennicutt, Jr., R. C. 1983, *Astrophys. J.*, 272, 54
- Kennicutt, Jr., R. C. 1998, *Astrophys. J.*, 498, 541
- Kewley, L. J., Geller, M. J., & Barton, E. J. 2006, *Astron. J.*, 131, 2004
- Kewley, L. J., Rupke, D., Jabran Zahid, H., Geller, M. J., & Barton, E. J. 2010, *Astrophys. J. Letters*, 721, L48
- Kirby, E. N., Lanfranchi, G. A., Simon, J. D., Cohen, J. G., & Guhathakurta, P. 2011a, *Astrophys. J.*, 727, 78
- Kirby, E. N., Martin, C. L., & Finlator, K. 2011b, *Astrophys. J. Letters*, 742, L25
- Kirby, E. N., Simon, J. D., Geha, M., Guhathakurta, P., & Frebel, A. 2008, *Astrophys. J. Letters*, 685, L43
- Klypin, A., Kravtsov, A. V., Bullock, J. S., & Primack, J. R. 2001, *Astrophys. J.*, 554, 903

- Klypin, A., Kravtsov, A. V., Valenzuela, O., & Prada, F. 1999, *Astrophys. J.*, 522, 82
- Kobayashi, C. & Nakasato, N. 2011, *Astrophys. J.*, 729, 16
- Kobayashi, C., Tsujimoto, T., & Nomoto, K. 2000, *Astrophys. J.*, 539, 26
- Kobayashi, C., Umeda, H., Nomoto, K., Tominaga, N., & Ohkubo, T. 2006, *Astrophys. J.*, 653, 1145
- Koch, A., Grebel, E. K., Gilmore, G. F., et al. 2008, *Astron. J.*, 135, 1580
- Koch, A., Grebel, E. K., Wyse, R. F. G., et al. 2006, *Astron. J.*, 131, 895
- Koch, A., Matteucci, F., & Feltzing, S. 2012, 1480, 190
- Köppen, J., Weidner, C., & Kroupa, P. 2007, *Mon. Not. Roy. Astron. Soc.*, 375, 673
- Kormendy, J. & Djorgovski, S. 1989, *Ann. Rev. Astron. Astrophys.*, 27, 235
- Korobkin, O., Rosswog, S., Arcones, A., & Winteler, C. 2012, *Mon. Not. Roy. Astron. Soc.*, 426, 1940
- Kotoneva, E., Flynn, C., Chiappini, C., & Matteucci, F. 2002, *Mon. Not. Roy. Astron. Soc.*, 336, 879
- Kroupa, P. 2001, *Mon. Not. Roy. Astron. Soc.*, 322, 231
- Kroupa, P. 2002, *Mon. Not. Roy. Astron. Soc.*, 330, 707
- Kroupa, P., Tout, C. A., & Gilmore, G. 1993, *Mon. Not. Roy. Astron. Soc.*, 262, 545
- Lai, D. K., Lee, Y. S., Bolte, M., et al. 2011, *Astrophys. J.*, 738, 51

- Lanfranchi, G. A. & Matteucci, F. 2007, *Astron. Astrophys.*, 468, 927
- Lanfranchi, G. A. & Matteucci, F. 2010, in IAU Symposium, Vol. 262, IAU Symposium, ed. G. Bruzual & S. Charlot, 370–371
- Lanfranchi, G. A., Matteucci, F., & Cescutti, G. 2006, *Astron. Astrophys.*, 453, 67
- Lanfranchi, G. A., Matteucci, F., & Cescutti, G. 2008, *Astron. Astrophys.*, 481, 635
- Larson, R. B. 1974, *Mon. Not. Roy. Astron. Soc.*, 169, 229
- Lee, H., Skillman, E. D., Cannon, J. M., et al. 2006, *Astrophys. J.*, 647, 970
- Lee, Y. S., Beers, T. C., An, D., et al. 2011, *Astrophys. J.*, 738, 187
- Lemasle, B., Hill, V., Tolstoy, E., et al. 2012, *Astron. Astrophys.*, 538, A100
- Lépine, J. R. D., Cruz, P., Scarano, Jr., S., et al. 2011, *Mon. Not. Roy. Astron. Soc.*, 417, 698
- Lequeux, J., Peimbert, M., Rayo, J. F., Serrano, A., & Torres-Peimbert, S. 1979, *Astron. Astrophys.*, 80, 155
- Letarte, B., Hill, V., Jablonka, P., et al. 2006, *Astron. Astrophys.*, 453, 547
- Lineweaver, C. H., Fenner, Y., & Gibson, B. K. 2004, *Science*, 303, 59
- Lucy, L. B. 1977, *Astron. J.*, 82, 1013
- Mac Low, M. 2009, in Revista Mexicana de Astronomia y Astrofisica, vol. 27, Vol. 36, Revista Mexicana de Astronomia y Astrofisica Conference Series, 121–127
- Macciò, A. V., Stinson, G., Brook, C. B., et al. 2012, *Astrophys. J. Letters*, 744, L9
- Maciel, W. J., Costa, R. D. D., & Uchida, M. M. M. 2003, *Astron. Astrophys.*, 397, 667

- Marcolini, A., Brighenti, F., & D'Ercole, A. 2003, *Mon. Not. Roy. Astron. Soc.*, 345, 1329
- Marigo, P. 2001, *Astron. Astrophys.*, 370, 194
- Marigo, P., Girardi, L., Bressan, A., et al. 2008, *Astron. Astrophys.*, 482, 883
- Marsakov, V. A. & Borkova, T. V. 2005, *Astronomy Letters*, 31, 515
- Marsakov, V. A. & Borkova, T. V. 2006, *Astronomy Letters*, 32, 376
- Martin, C. L., Kobulnicky, H. A., & Heckman, T. M. 2002, *Astrophys. J.*, 574, 663
- Mateo, M. L. 1998, *Ann. Rev. Astron, Astrophys.*, 36, 435
- Mathews, W. G. & Baker, J. C. 1971, *Astrophys. J.*, 170, 241
- Matteucci, F. & Brocato, E. 1990, *Astrophys. J.*, 365, 539
- Matteucci, F. & Greggio, L. 1986, *Astron. Astrophys.*, 154, 279
- McClure-Griffiths, N. M., Ford, A., Pisano, D. J., et al. 2006, *Astrophys. J.*, 638, 196
- McConnachie, A. W., Arimoto, N., Irwin, M., & Tolstoy, E. 2006, *Mon. Not. Roy. Astron. Soc.*, 373, 715
- McConnachie, A. W. & Irwin, M. J. 2006, *Mon. Not. Roy. Astron. Soc.*, 365, 1263
- McWilliam, A., Preston, G. W., Sneden, C., & Searle, L. 1995, *Astron. J.*, 109, 2757
- Michel-Dansac, L., Lambas, D. G., Alonso, M. S., & Tissera, P. 2008, *Mon. Not. Roy. Astron. Soc.*, 386, L82
- Miller, G. E. & Scalo, J. M. 1979, *Astrophys. J. Supple.*, 41, 513

- Minniti, D. & Zoccali, M. 2008, in IAU Symposium, Vol. 245, IAU Symposium, ed. M. Bureau, E. Athanassoula, & B. Barbuy, 323–332
- Mollá, M. & Díaz, A. I. 2005, *Mon. Not. Roy. Astron. Soc.*, 358, 521
- Mollá, M., Ferrini, F., & Diaz, A. I. 1997, *Astrophys. J.*, 475, 519
- Mollá, M., Hardy, E., & Beauchamp, D. 1999, *Astrophys. J.*, 513, 695
- Monaghan, J. J. 1992, *Ann. Rev. Astron, Astrophys.*, 30, 543
- Monelli, M., Bernard, E. J., Gallart, C., et al. 2012, *Mon. Not. Roy. Astron. Soc.*, 422, 89
- Mould, J. & Aaronson, M. 1983, *Astrophys. J.*, 273, 530
- Nagamine, K. 2002, *Astrophys. J.*, 564, 73
- Navarro, J. F., Abadi, M. G., Venn, K. A., Freeman, K. C., & Anguiano, B. 2011, *Mon. Not. Roy. Astron. Soc.*, 89
- Ness, M., Freeman, K., Athanassoula, E., et al. 2012, *Astrophys. J.*, 756, 22
- Nichols, M. & Bland-Hawthorn, J. 2011, *Astrophys. J.*, 732, 17
- Nomoto, K., Iwamoto, K., Nakasato, N., et al. 1997, *Nuclear Physics A*, 621, 467
- Nordström, B., Mayor, M., Andersen, J., et al. 2004, *Astron. Astrophys.*, 418, 989
- O’Brien, J. C., Freeman, K. C., & van der Kruit, P. C. 2010, *Astron. Astrophys.*, 515, A62+
- Oey, M. S. & Clarke, C. J. 1997, *Mon. Not. Roy. Astron. Soc.*, 289, 570
- Oh, S., Brook, C., Governato, F., et al. 2011, *Astron. J.*, 142, 24

- Okamoto, T., Eke, V. R., Frenk, C. S., & Jenkins, A. 2005, *Mon. Not. Roy. Astron. Soc.*, 363, 1299
- Okamoto, T., Nemmen, R. S., & Bower, R. G. 2008, *Mon. Not. Roy. Astron. Soc.*, 385, 161
- Oort, J. H. 1974, in IAU Symposium, Vol. 58, The Formation and Dynamics of Galaxies, ed. J. R. Shakeshaft, 375–396
- Pagel, B. E. J. & Patchett, B. E. 1975, *Mon. Not. Roy. Astron. Soc.*, 172, 13
- Pasetto, S., Grebel, E. K., Berczik, P., Chiosi, C., & Spurzem, R. 2011, *Astron. Astrophys.*, 525, A99
- Pasetto, S., Grebel, E. K., Zwitter, T., et al. 2012, *Astron. Astrophys.*, 547, A71
- Peletier, R. F., Davies, R. L., Illingworth, G. D., Davis, L. E., & Cawson, M. 1990, *Astron. J.*, 100, 1091
- Perez, J., Michel-Dansac, L., & Tissera, P. B. 2011, *Mon. Not. Roy. Astron. Soc.*, 417, 580
- Persic, M., Salucci, P., & Stel, F. 1996, *Mon. Not. Roy. Astron. Soc.*, 281, 27
- Petric, A. O. & Rupen, M. P. 2007, *Astron. J.*, 134, 1952
- Pilkington, K., Few, C. G., Gibson, B. K., et al. 2012a, *Astron. Astrophys.*, 540, A56
- Pilkington, K. & Gibson, B. K. 2012a, ArXiv e-prints
- Pilkington, K. & Gibson, B. K. 2012b, in Astronomical Society of the Pacific Conference Series, Vol. 458, Galactic Archaeology: Near Field Cosmology and the Formation of the Milky Way, ed. W. Aoki, 241

- Pilkington, K., Gibson, B. K., Brook, C. B., et al. 2012b, *Mon. Not. Roy. Astron. Soc.*, 425, 969
- Pilkington, K., Gibson, B. K., Calura, F., et al. 2011, *Mon. Not. Roy. Astron. Soc.*, 417, 2891
- Pilkington, K., Gibson, B. K., Calura, F., et al. 2012c, in JENAM 2010, Joint European and National Astronomy Meeting
- Pilkington, K., Gibson, B. K., & Jones, D. H. 2012d, in From the First Structures to the Universe Today, ed. P. S. E. De Rossi, M. W. & L. J. Pellizza, AAA Workshop Series - Argentine Astronomical Society, in press
- Pilyugin, L. S. & Ferrini, F. 2000, *Astron. Astrophys.*, 358, 72
- Piontek, R. A. & Ostriker, E. C. 2007, *Astrophys. J.*, 663, 183
- Pohlen, M. & Trujillo, I. 2006, *Astron. Astrophys.*, 454, 759
- Pontzen, A., Governato, F., Pettini, M., et al. 2008, *Mon. Not. Roy. Astron. Soc.*, 390, 1349
- Pontzen, A. & Pettini, M. 2009, *Mon. Not. Roy. Astron. Soc.*, 393, 557
- Portinari, L. & Chiosi, C. 1999, *Astron. Astrophys.*, 350, 827
- Prantzos, N. & Boissier, S. 2000, *Mon. Not. Roy. Astron. Soc.*, 313, 338
- Qian, Y.-Z. & Wasserburg, G. J. 2012, Proceedings of the National Academy of Science, 109, 4750
- Queyrel, J., Contini, T., Kissler-Patig, M., et al. 2011, ArXiv e-prints
- Rahimi, A., Kawata, D., Allende Prieto, C., et al. 2011, *Mon. Not. Roy. Astron. Soc.*, 725

- Rahimi, A., Kawata, D., Brook, C. B., & Gibson, B. K. 2010, *Mon. Not. Roy. Astron. Soc.*, 401, 1826
- Raiteri, C. M., Villata, M., & Navarro, J. F. 1996a, *Astron. Astrophys.*, 315, 105
- Raiteri, C. M., Villata, M., & Navarro, J. F. 1996b, *Memorie della Societ Astronomia Italiana*, 67, 817
- Rasera, Y. & Teyssier, R. 2006, *Astron. Astrophys.*, 445, 1
- Recchi, S., Hensler, G., Angeretti, L., & Matteucci, F. 2006, *Astron. Astrophys.*, 445, 875
- Recchi, S., Matteucci, F., D'Ercole, A., & Tosi, M. 2004, *Astron. Astrophys.*, 426, 37
- Renda, A., Kawata, D., Fenner, Y., & Gibson, B. K. 2005, *Mon. Not. Roy. Astron. Soc.*, 356, 1071
- Revaz, Y. & Jablonka, P. 2012, *Astron. Astrophys.*, 538, A82
- Revaz, Y., Jablonka, P., Sawala, T., et al. 2009, *Astron. Astrophys.*, 501, 189
- Rich, R. M., Origlia, L., & Valenti, E. 2007, *Astrophys. J. Letters*, 665, L119
- Richardson, J. C., Irwin, M., McConnachie, A. W., et al. 2011, *Astrophys. J.*, 732, 76
- Robertson, B., Yoshida, N., Springel, V., & Hernquist, L. 2004, *Astrophys. J.*, 606, 32
- Robertson, B. E. & Kravtsov, A. V. 2008, *Astrophys. J.*, 680, 1083
- Robin, A. C., Luri, X., Reyl e, C., et al. 2012, *Astron. Astrophys.*, 543, A100

- Romano, D., Karakas, A. I., Tosi, M., & Matteucci, F. 2010, *Astron. Astrophys.*, 522, A32
- Roškar, R., Debattista, V. P., Quinn, T. R., Stinson, G. S., & Wadsley, J. 2008, *Astrophys. J. Letters*, 684, L79
- Rupke, D. S. N., Kewley, L. J., & Barnes, J. E. 2010a, *Astrophys. J. Letters*, 710, L156
- Rupke, D. S. N., Kewley, L. J., & Chien, L. 2010b, *Astrophys. J.*, 723, 1255
- Ryan, S. G. & Norris, J. E. 1991, *Astron. J.*, 101, 1865
- Saitoh, T. R., Daisaka, H., Kokubo, E., et al. 2008, *Pub. Astron. Soc. Japan*, 60, 667
- Salpeter, E. E. 1955, *Astrophys. J.*, 121, 161
- Sánchez-Blázquez, P., Courty, S., Gibson, B. K., & Brook, C. B. 2009, *Mon. Not. Roy. Astron. Soc.*, 398, 591
- Sánchez-Blázquez, P., Ocvirk, P., Gibson, B. K., Perez, I., & Peletier, R. F. 2011, *Mon. Not. Roy. Astron. Soc.*, 415, 709
- Sánchez-Gil, M. C., Jones, D. H., Pérez, E., et al. 2011, *Mon. Not. Roy. Astron. Soc.*, 415, 753
- Sanders, N. E., Caldwell, N., McDowell, J., & Harding, P. 2012, *Astrophys. J.*, 758, 133
- Sawala, T., Scannapieco, C., Maio, U., & White, S. 2010, *Mon. Not. Roy. Astron. Soc.*, 402, 1599
- Scalo, J. M. 1986, in IAU Symposium, Vol. 116, Luminous Stars and Associations in Galaxies, ed. C. W. H. De Loore, A. J. Willis, & P. Laskarides, 451–466

- Scannapieco, C., Tissera, P. B., White, S. D. M., & Springel, V. 2008, *Mon. Not. Roy. Astron. Soc.*, 389, 1137
- Schaller, G., Schaerer, D., Meynet, G., & Maeder, A. 1992, *Astron. Astrophys. Suppl.*, 96, 269
- Schlesinger, K. J., Johnson, J. A., & et al. 2012, ArXiv e-prints
- Schmidt, M. 1959, *Astrophys. J.*, 129, 243
- Schönrich, R. & Binney, J. 2009, *Mon. Not. Roy. Astron. Soc.*, 396, 203
- Schörck, T., Christlieb, N., Cohen, J. G., et al. 2009, *Astron. Astrophys.*, 507, 817
- Searle, L. & Zinn, R. 1978, *Astrophys. J.*, 225, 357
- Shaver, P. A., McGee, R. X., Newton, L. M., Danks, A. C., & Pottasch, S. R. 1983, *Mon. Not. Roy. Astron. Soc.*, 204, 53
- Shen, S., Wadsley, J., & Stinson, G. 2010a, *Mon. Not. Roy. Astron. Soc.*, 1043
- Shen, S., Wadsley, J., & Stinson, G. 2010b, *Mon. Not. Roy. Astron. Soc.*, 407, 1581
- Shetrone, M., Venn, K. A., Tolstoy, E., et al. 2003, *Astron. J.*, 125, 684
- Shetrone, M. D., Bolte, M., & Stetson, P. B. 1998, *Astron. J.*, 115, 1888
- Shetrone, M. D., Côté, P., & Sargent, W. L. W. 2001, *Astrophys. J.*, 548, 592
- Siebert, A. 2012, in SF2A-2012: Proceedings of the Annual meeting of the French Society of Astronomy and Astrophysics, ed. S. Boissier, P. de Laverny, N. Nardetto, R. Samadi, D. Valls-Gabaud, & H. Wozniak, 121–127
- Silk, J. 2003, *Mon. Not. Roy. Astron. Soc.*, 343, 249
- Simpson, J. P., Colgan, S. W. J., Rubin, R. H., Erickson, E. F., & Haas, M. R. 1995, *Astrophys. J.*, 444, 721

- Skillman, E. D., Kennicutt, R. C., & Hodge, P. W. 1989, *Astrophys. J.*, 347, 875
- Skillman, E. D., Tolstoy, E., Cole, A. A., et al. 2003, *Astrophys. J.*, 596, 253
- Smecker-Hane, T. A., Stetson, P. B., Hesser, J. E., & Vandenberg, D. A. 1996, in *Astronomical Society of the Pacific Conference Series*, Vol. 98, *From Stars to Galaxies: the Impact of Stellar Physics on Galaxy Evolution*, ed. C. Leitherer, U. Fritze-von-Alvensleben, & J. Huchra, 328
- Sommer-Larsen, J. & Fynbo, J. P. U. 2008, *Mon. Not. Roy. Astron. Soc.*, 385, 3
- Sommer-Larsen, J., Toft, S., Rasmussen, J., et al. 2003, *Astrophys. Space Sci.*, 284, 693
- Soubiran, C., Bienaymé, O., Mishenina, T. V., & Kovtyukh, V. V. 2008, *Astron. Astrophys.*, 480, 91
- Spitoni, E., Matteucci, F., & Marcon-Uchida, M. M. 2013, ArXiv e-prints
- Springel, V., Wang, J., Vogelsberger, M., et al. 2008, *Mon. Not. Roy. Astron. Soc.*, 391, 1685
- Stanghellini, L. & Haywood, M. 2010, *Astrophys. J.*, 714, 1096
- Stanimirovic, S., Staveley-Smith, L., Dickey, J. M., Sault, R. J., & Snowden, S. L. 1999, *Mon. Not. Roy. Astron. Soc.*, 302, 417
- Stinson, G., Brook, C., Prochaska, J. X., et al. 2012, ArXiv e-prints
- Stinson, G., Seth, A., Katz, N., et al. 2006, *Mon. Not. Roy. Astron. Soc.*, 373, 1074
- Stinson, G. S., Bailin, J., Couchman, H., et al. 2010, *Mon. Not. Roy. Astron. Soc.*, 408, 812
- Stinson, G. S., Brook, C., Macciò, A. V., et al. 2013, *Mon. Not. Roy. Astron. Soc.*, 428, 129

- Stinson, G. S., Dalcanton, J. J., Quinn, T., et al. 2009, *Mon. Not. Roy. Astron. Soc.*, 395, 1455
- Stinson, G. S., Dalcanton, J. J., Quinn, T., Kaufmann, T., & Wadsley, J. 2007, *Astrophys. J.*, 667, 170
- Sutherland, R. S. & Dopita, M. A. 1993, *Astrophys. J. Supple.*, 88, 253
- Tafelmeyer, M., Jablonka, P., Hill, V., et al. 2010, *Astron. Astrophys.*, 524, A58
- Tamburro, D., Rix, H., Leroy, A. K., et al. 2009, *Astron. J.*, 137, 4424
- Tasker, E. J. & Bryan, G. L. 2008, *Astrophys. J.*, 673, 810
- Teyssier, R. 2002, *Astron. Astrophys.*, 385, 337
- Thacker, R. J. & Couchman, H. M. P. 2001, *Astrophys. J. Letters*, 555, L17
- Thielemann, F., Nomoto, K., & Yokoi, K. 1986, *Astron. Astrophys.*, 158, 17
- Thielemann, F.-K., Arcones, A., Käppeli, R., et al. 2011, *Progress in Particle and Nuclear Physics*, 66, 346
- Tinsley, B. M. 1979, *Astrophys. J.*, 229, 1046
- Tinsley, B. M. 1980, *Fundamentals of Cosmic Physic*, 5, 287
- Tissera, P. B., White, S. D. M., & Scannapieco, C. 2012, *Mon. Not. Roy. Astron. Soc.*, 420, 255
- Tollerud, E. J., Beaton, R. L., Geha, M. C., et al. 2012, *Astrophys. J.*, 752, 45
- Tolstoy, E., Hill, V., & Tosi, M. 2009, *Ann. Rev. Astron, Astrophys.*, 47, 371
- Tolstoy, E., Irwin, M. J., Helmi, A., et al. 2004, *Astrophys. J. Letters*, 617, L119
- Tolstoy, E., Venn, K. A., Shetrone, M., et al. 2003, *Astron. J.*, 125, 707

- Toomre, A. & Toomre, J. 1972, *Astrophys. J.*, 178, 623
- Tosi, M. 1996, in Astronomical Society of the Pacific Conference Series, Vol. 98, From Stars to Galaxies: the Impact of Stellar Physics on Galaxy Evolution, ed. C. Leitherer, U. Fritze-von-Alvensleben, & J. Huchra, 299–+
- Travaglio, C., Galli, D., Gallino, R., et al. 1999, *Astrophys. J.*, 521, 691
- Travaglio, C., Gallino, R., Arnone, E., et al. 2004, *Astrophys. J.*, 601, 864
- Tremonti, C. A., Heckman, T. M., Kauffmann, G., et al. 2004, *Astrophys. J.*, 613, 898
- Tumlinson, J., Thom, C., & et al. 2011, *Science*, 334, 948
- van den Bergh, S. 1994, *Astrophys. J.*, 428, 617
- van den Bosch, F. C. 2001, *Mon. Not. Roy. Astron. Soc.*, 327, 1334
- van den Bosch, F. C., Abel, T., Croft, R. A. C., Hernquist, L., & White, S. D. M. 2002, *Astrophys. J.*, 576, 21
- van den Hoek, L. B. & Groenewegen, M. A. T. 1997, *Astron. Astrophys. Suppl.*, 123, 305
- van Zee, L., Salzer, J. J., Haynes, M. P., O’Donoghue, A. A., & Balonek, T. J. 1998, *Astron. J.*, 116, 2805
- Venn, K. A. & Hill, V. M. 2008, *The Messenger*, 134, 23
- Venn, K. A., Irwin, M., Shetrone, M. D., et al. 2004, *Astron. J.*, 128, 1177
- Venn, K. A., Shetrone, M. D., Irwin, M. J., et al. 2012, *Astrophys. J.*, 751, 102
- Vera-Ciro, C. A., Helmi, A., Starkenburg, E., & Breddels, M. A. 2012, ArXiv e-prints

- Verheijen, M. A. W., Deshev, B., van Gorkom, J., et al. 2010, in ISKAF2010 Science Meeting
- Wadsley, J. W., Stadel, J., & Quinn, T. 2004, *New Astronomy*, 9, 137
- Walter, F., Brinks, E., de Blok, W. J. G., et al. 2008, *Astron. J.*, 136, 2563
- Wang, P. & Abel, T. 2009, *Astrophys. J.*, 696, 96
- White, S. D. M. 1978, *Mon. Not. Roy. Astron. Soc.*, 184, 185
- White, S. D. M. & Rees, M. J. 1978, *Mon. Not. Roy. Astron. Soc.*, 183, 341
- Whiting, A. B., Hau, G. K. T., & Irwin, M. 1999, *Astron. J.*, 118, 2767
- Wiersma, R. P. C., Schaye, J., & Theuns, T. 2011, *Mon. Not. Roy. Astron. Soc.*, 415, 353
- Winnick, R. A. 2003, PhD thesis, YALE UNIVERSITY
- Winteler, C., Käppeli, R., Perego, A., et al. 2012, *Astrophys. J. Letters*, 750, L22
- Woosley, S. E. & Weaver, T. A. 1995, *Astrophys. J. Supple.*, 101, 181
- Wyse, R. F. G., Gilmore, G., Norris, J. E., et al. 2006, *Astrophys. J. Letters*, 639, L13
- Yanny, B., Rockosi, C., Newberg, H. J., et al. 2009, *Astron. J.*, 137, 4377
- Yoachim, P. & Dalcanton, J. J. 2006, *Astron. J.*, 131, 226
- Yozin, C. & Bekki, K. 2012, *Astrophys. J. Letters*, 756, L18
- Yuan, T.-T., Kewley, L. J., Swinbank, A. M., Richard, J., & Livermore, R. C. 2011, *Astrophys. J. Letters*, 732, L14+
- Zahid, H. J., Kewley, L. J., & Bresolin, F. 2011, *Astrophys. J.*, 730, 137

- Zaritsky, D., Colucci, J. E., Pessev, P. M., Bernstein, R. A., & Chandar, R. 2012, *Astrophys. J.*, 761, 93
- Zaritsky, D., Kennicutt, Jr., R. C., & Huchra, J. P. 1994, *Astrophys. J.*, 420, 87
- Zinn, R. & West, M. J. 1984, *Astrophys. J. Supple.*, 55, 45
- Zoccali, M., Hill, V., Barbuy, B., et al. 2009, *The Messenger*, 136, 48
- Zoccali, M., Hill, V., Lecureur, A., et al. 2008, *Astron. Astrophys.*, 486, 177
- Zolotov, A., Willman, B., Brooks, A. M., et al. 2009, *Astrophys. J.*, 702, 1058
- Zolotov, A., Willman, B., Brooks, A. M., et al. 2010, *Astrophys. J.*, 721, 738
- Zucker, D. B., de Silva, G., Freeman, K., Bland-Hawthorn, J., & Hermes Team. 2012, in *Astronomical Society of the Pacific Conference Series*, Vol. 458, *Galactic Archaeology: Near-Field Cosmology and the Formation of the Milky Way*, ed. W. Aoki, M. Ishigaki, T. Suda, T. Tsujimoto, & N. Arimoto, 421